

UNREINFORCED MASONRY WALLS SUBJECTED TO
OUT-OF-PLANE SEISMIC ACTIONS

JAROSLAV VACULIK

A thesis submitted to
The University of Adelaide
School of Civil, Environmental & Mining Engineering
in fulfilment of the requirements for the degree of
Doctor of Philosophy

April, 2012.

Chapter 1

INTRODUCTION

1.1 OUT-OF-PLANE WALLS

When an unreinforced masonry (URM) building is subjected to horizontal shaking during a seismic event, most of its walls inevitably experience a combination of in-plane and out-of-plane response. Past research into seismic response of URM structures has focused primarily on walls' in-plane shear behaviour, since it provides the primary load path for transfer of the building's lateral seismic force to its foundation (Figure 1.1) [e.g. König *et al.*, 1988; Anthoine *et al.*, 1994; Andreaus, 1996; Magenes and Calvi, 1997; Tomaževič and Klemenc, 1997; Paquette and Bruneau, 2003; Vasconcelos and Lourenço, 2009]. However, whilst out-of-plane action is not typically considered to be part of the building's seismic load path, walls still require sufficient capacity to avoid out-of-plane collapse; as even local failure can pose significant danger to life safety, and furthermore, failure of loadbearing walls could potentially trigger partial or complete collapse of the overall structure by compromising its gravity or lateral in-plane load resistance paths.

Post-earthquake studies have identified out-of-plane wall collapse as one of the predominant modes of failure in URM construction, including during the 1989 Newcastle earthquake [Page, 1992], as well as in more recent events such as 2009 L'Aquila, Italy [Bazzurro *et al.*, 2009; Oyarzo-Vera and Griffith, 2009], and 2010–2011 Christchurch, New Zealand [Ingham and Griffith, 2011a,b]. Studies have also found, however, that a large proportion of out-of-plane collapse during earthquakes occurred in instances where the walls were not designed to withstand such actions, and furthermore, that failure was preventable if the walls were properly designed and constructed according to the relevant design codes [Scrivener, 1993; Page, 1995].

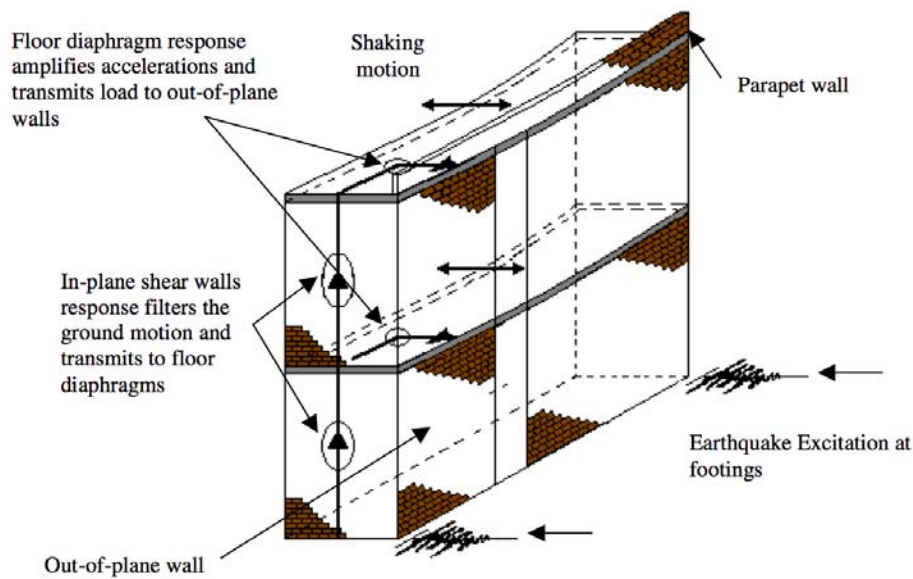


Figure 1.1: Seismic load path in URM buildings [from *Doherty, 2000*]. (Graphics used with permission from K. Doherty.)

Nonetheless, the topic of seismic out-of-plane response is one that is still not fully understood; *Paulay and Priestley [1992]* describing it as “one of the most complex and ill-understood areas of seismic analysis”, and numerous others highlighting the need for further research into the seismic behaviour of URM buildings [*Bruneau, 1994; Brunsdon, 1994; Calvi, 1999; Maffei et al., 2000; Abrams, 2001*]. Considering Australia’s large amount of seismically vulnerable URM building stock, it is therefore of significant interest both nationally and internationally that we conduct research to improve our understanding of seismic out-of-plane wall response, and facilitate development of the corresponding design and assessment techniques.

When a wall is subjected to out-of-plane face loading due to either earthquake or wind, it undergoes flexure (bending). Orientation of the internal stresses within the wall and the resulting crack pattern developed is dictated by the position of its supported edges, as shown by Figure 1.2. One-way spanning walls (Figure 1.2a) undergo uniaxial bending, which can be classified as either vertical or horizontal depending on the orientation of the span.¹ This results in cracks that run parallel to the panel’s supports and the axis of internal bending. Behaviour of two-way spanning walls (Figure 1.2b), which include any class of walls supported on at

¹The traditional naming convention for vertical and horizontal bending is based on the orientation of principal flexural stresses generated by the applied bending moment. Vertical bending causes flexural stresses acting perpendicularly to the bed joints (see Figure 1.3a), whilst horizontal bending causes flexural stresses acting perpendicularly to the perpend joints (Figure 1.3b). For clarity, it should be noted that the crack direction is opposite to that suggested by the name—vertical bending is associated with horizontal cracks and conversely, horizontal bending with vertical cracks.

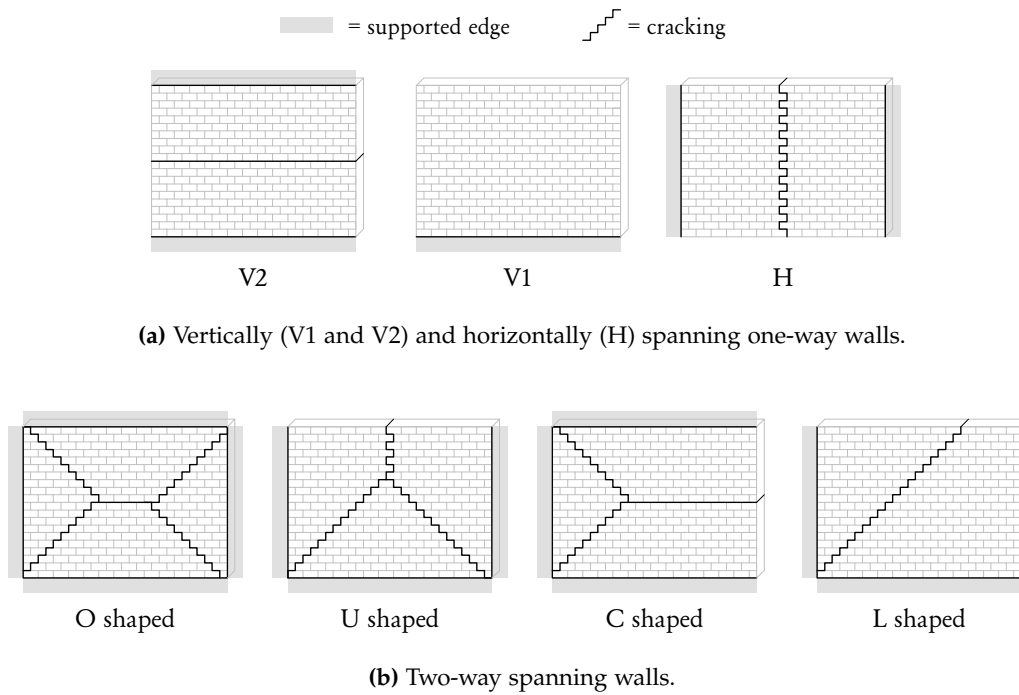


Figure 1.2: Various types of wall support shapes and the associated out-of-plane flexure cracking patterns.

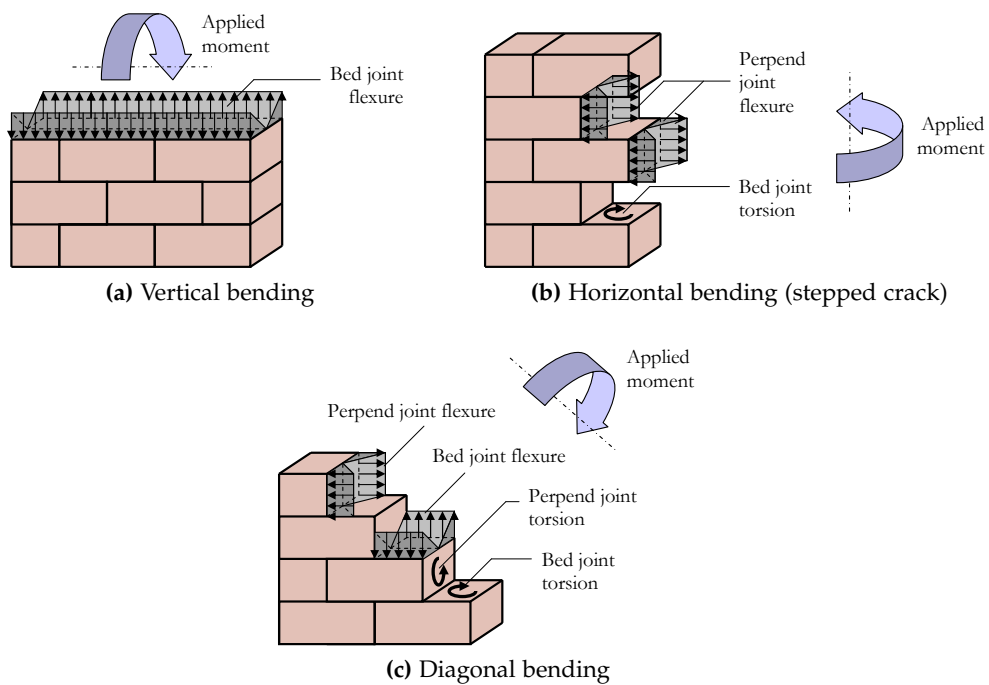


Figure 1.3: Mechanics of internal moment resistance for the different types of bending.

least one vertical edge and one horizontal edge, is especially complex, due to the anisotropic nature of the masonry material and the structural indeterminacy of the wall configurations [Drysdale *et al.*, 1994]. Such walls undergo biaxial bending, whereby the internal flexural stresses act in both the horizontal and vertical directions. As a result, two-way panels characteristically develop crack patterns exhibiting a combination of vertical, horizontal and diagonal crack lines. In turn, the internal moments along the different types of crack lines can consist of a combination of flexure (normal stress) and torsion (shear stress) (Figure 1.3).

The majority of past experimental and theoretical research dealing with seismic out-of-plane response has been focused on vertically spanning URM walls [Ewing and Kariotis, 1981; Doherty *et al.*, 2002; Griffith *et al.*, 2004]. By contrast, two-way URM walls have received only limited attention [e.g. Jaramillo, 2002], even though they are most commonly encountered in practice. This topic will hence form the primary focus of this thesis.

1.2 SHORTCOMINGS OF CURRENT DESIGN METHODOLOGY

To highlight the flaws of the current seismic design approach, a brief description of typical load-displacement (F - Δ) behaviour of a URM wall subjected to out-of-plane loading will firstly be presented (Figure 1.4). When an uncracked URM wall is loaded, it initially deforms in a linear elastic manner until the internal stresses begin to exceed the material's tensile strength and cracking starts to occur. With continued deformation, progressive cracking of joints occurs and the panel loses stiffness. Typically, the wall reaches its ultimate load capacity at a deformation between approximately 5–15 mm. As the wall is displaced further, it continues to lose strength and stiffness until it eventually becomes fully cracked. After this, the wall can still maintain some load resistance due to gravity effects; however, this load resistance reduces with increased deformation due to P-Delta destabilisation. The wall finally reaches its ultimate displacement capacity when the internal resisting moments become balanced by the destabilising moments, which typically occurs as the deformation approaches the wall thickness (110 mm for single leaf walls built with standard Australian clay brick units). Beyond this point, the wall becomes unstable and requires a centring applied load to prevent it from collapsing.

Under cyclic loading, fully cracked vertically spanning walls behave as rocking blocks and possess nonlinear but elastic load-displacement (F - Δ) behaviour (as shown by the dotted line in Figure 1.4) [Ewing and Kariotis, 1981; Griffith *et al.*, 2004]. By contrast, two-way spanning walls obtain the additional benefit of increased strength and displacement capacities, as well as frictional energy dissipation under

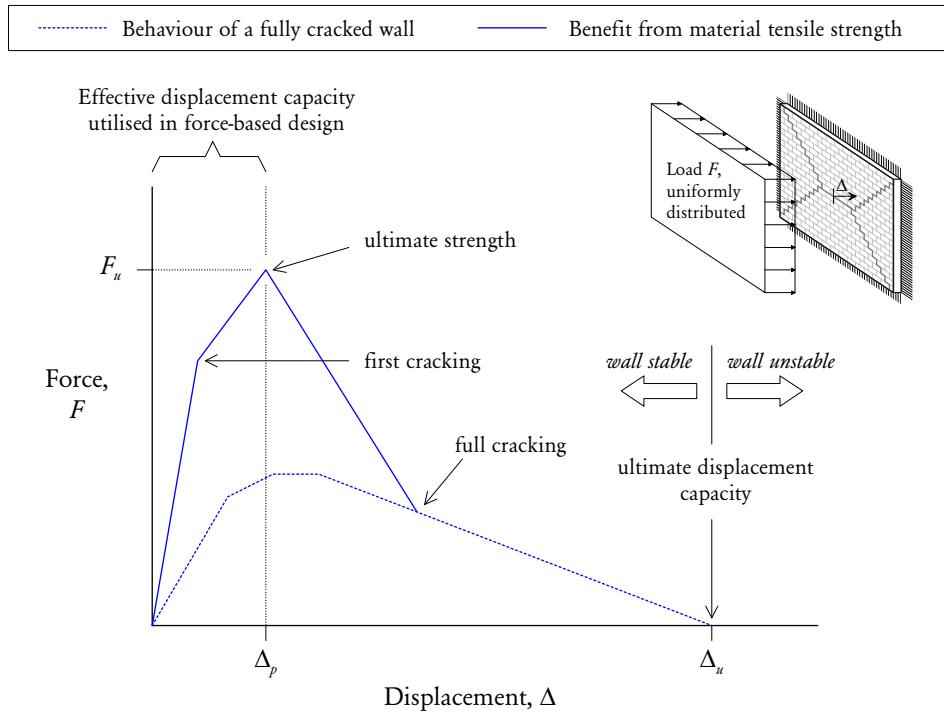


Figure 1.4: Generalised F - Δ response of URM walls subjected to out-of-plane bending.

cyclic loading—characteristics that are all favourable to seismic performance. This has been demonstrated by both preliminary studies [Vaculik *et al.*, 2004] and also the experimental work performed as part of this research.

The current Australian provisions for ultimate limit state design (prevention of collapse) of URM walls against out-of-plane seismic actions use a force-based (FB) capacity check—that is, the designer must ensure that a wall’s load capacity (F_c) exceeds its seismic load demand (F_d):

$$F_c > F_d. \quad (1.1)$$

The load demand is determined according to the Australian earthquake loading code AS 1170.4 [Standards Australia, 2007], where the wall is treated as a non-structural component (i.e. it is assumed to not be a part of the building’s overall seismic load path). According to the code, the force demand is calculated as

$$F_d = a_{\text{floor}} \frac{I_c a_c}{R_c} M, \quad (1.2)$$

where a_{floor} is the effective floor acceleration at the level in the building where the wall is situated; M is the mass of the wall; and I_c , a_c and R_c are factors accounting for component importance, attachment amplification and component

ductility, respectively, which are all taken as 1.0 for a URM wall subjected to out-of-plane actions. The wall's load capacity (F_c) is in turn determined according to the Australian masonry code AS 3700 [Standards Australia, 2001] using the virtual work (VW) method. Therefore, in order for the wall to be deemed as adequate, its effective static acceleration capacity (load capacity divided by wall mass) must exceed the maximum acceleration of the motion that the wall is subjected to; or

$$F_c/M > a_{\text{floor}}. \quad (1.3)$$

The shortcomings of the presently-used seismic design approach, together with the associated aims of this research are as follows:

1. Whilst a FB design approach is suitable for preventing collapse due to static loading such as wind, it has the potential to become overly conservative for seismic design of ductile systems [Priestley, 1985; Abrams et al., 1996; Magenes and Calvi, 1997; Priestley, 2000], as wall collapse only occurs once its deformation exceeds its ultimate displacement capacity (Δ_u in Figure 1.4). Since the current design approach is aimed to ensure that the ultimate load capacity of the wall is not exceeded, it effectively limits the maximum allowable wall deformation to relatively small values (Δ_p in Figure 1.4). Hence, there is a large range of 'reserve' displacement capacity that goes unutilised in conventional FB design.

An innovative alternative to FB design is *displacement-based* (DB) seismic design, whose objective is to ensure that the imposed displacements are kept within acceptable limits. The philosophy of DB design is based on the notion that structural deformations, rather than forces, provide a reliable indicator of damage incurred under seismic loading, which is an especially attractive concept from the point of view of performance-based seismic engineering [Priestley, 2000; Fajfar, 2000; Abrams, 2001; Bertero and Bertero, 2002; Xue and Chen, 2003]. DB methods have gained widespread acceptance in recent years and have been developed for various types of ductile systems [Priestley, 1997; Magenes and Calvi, 1997; Medhekar and Kennedy, 2000; Kowalsky, 2002], including vertically spanning URM walls subjected to out-of-plane actions [Doherty et al., 2002]. The ultimate aim of the present research is to develop a generalised DB design methodology for walls subjected to out-of-plane loading, with particular emphasis on two-way walls.

2. A further issue of the current FB design approach is that the ultimate load capacity (peak of the solid line in Figure 1.4), calculated according to AS 3700, is heavily dependent upon the masonry's tensile strength properties which

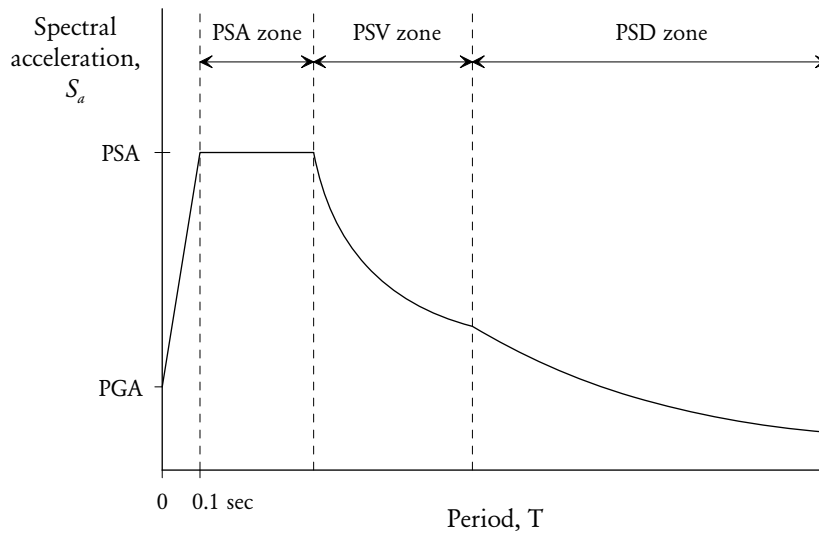


Figure 1.5: General form of the AS 1170.4 design acceleration spectrum.

have a large range of variability. While this is a natural aspect of **URM**, it does make seismic assessment of existing masonry buildings problematic, as it is difficult to reliably quantify these material properties in-situ.

By contrast, it is intended that the developed **DB** methodology will be based upon the wall's capacity curve after cracking (dotted line in Figure 1.4), which does not rely upon tensile strength data but rather on the geometry of the wall. In particular, it is already well established that the ultimate out-of-plane displacement capacity Δ_u is dependent primarily on the wall's thickness [e.g. *Doherty et al., 2002*]²—information that is much easier to obtain in existing buildings.

3. The current AS 1170.4 provisions used to determine the seismic load demand [as per Eq. (1.2)] effectively assume that the wall is rigid (has a zero vibrational period) and therefore responds at the peak acceleration of the excitation motion. For example, if the wall is situated at the ground level, then the design acceleration a_{floor} used in the design check [Eq. (1.3)] is taken as the peak ground acceleration (**PGA**) in the design acceleration spectrum (Figure 1.5). This, however, can be a highly unconservative assumption since the wall is, to some degree, flexible (has a period greater than zero) and can therefore amplify accelerations through its own vibration. Hence, if the **FB** design procedure is to be used, it may be more prudent to use the peak spectral acceleration (**PSA**) region of the acceleration spectrum rather than the **PGA**.²

²An alternative way to rectify this problem would be for AS 1170.4 to stipulate the component amplification factor a_c in Eq. (1.2) as a value > 1 . Presently the only such value (2.5) is specified for

For comparison, the ratio of the PSA/PGA for the AS 1170.4 prescribed design spectra ranges between 2.8 and 3.3.

As described by the above points, the current FB design approach appears to be overly conservative in certain parts (point 1) and unconservative in others (point 3). Hence, there is significant scope for the development of an alternative design methodology to address these deficiencies. Of the above limitations, this thesis will focus primarily on points 1 and 2, through development of a DB design approach. While the third point remains valid, it can be effectively addressed through DB design using the capacity spectrum method [e.g. as described by *Freeman, 2004*] and will therefore not be explicitly dealt with in this thesis.

1.3 RESEARCH OBJECTIVES, SCOPE AND OUTLINE

As discussed in the previous section, the primary objective of this research is the development of a displacement-based seismic design approach for URM walls subjected to two-way bending. As a secondary objective, it is also of interest to further develop the presently-used force-based methodology, in particular, analytical techniques for predicting: (i) the ultimate strength which accounts for the material tensile strength of the masonry (solid line in Figure 1.4), and (ii) the strength of a wall after cracking (dashed line in Figure 1.4). It is anticipated that the resulting FB and DB methodologies can ultimately be assimilated into a multi-tiered design procedure.

The URM typology forming the main focus for this research is single-leaf, half-overlap stretcher bonded, clay brickwork (as illustrated in Figure 1.3), which has widespread prevalence in both new and existing Australian construction. While multi-leaf interlocked and cavity construction is also common, it is beyond the scope of this thesis. Furthermore, as stated previously, two-way spanning walls (Figure 1.2b) represent the main type of wall configuration considered in this work; although, where forming a specific case of the developed methodology, one-way spanning walls (Figure 1.2a) are also considered. It is the author's intention that within this scope, the findings of this research are kept as general as possible, so that they may be applied toward the design of new buildings as well as the assessment of existing buildings alike.

To achieve the aforementioned objectives, the content of this thesis is divided into three parts: Part I reports the experimental work undertaken and includes Chapters 2 and 3. Part II reports the development of the associated analytical

"flexible spring-type mounting systems for mechanical equipment".

methodologies and includes Chapters 4, 5, 6 and 7. Part III includes various supporting appendices relating to the individual chapters.

The following is a synopsis of each chapter:

- Chapter 2 reports experimental tests in which eight full-scale walls were subjected to quasistatic cyclic loading using airbags.
- Chapter 3 reports a companion study where five half-scale walls were tested using a shaketable.
- Chapter 4 provides further developments of the present state-of-the-art method for prediction of the ultimate load capacity of two-way walls, which considers contributions from the tensile strength of the masonry.
- Chapter 5 develops a probabilistic approach to horizontal bending, with application toward the ultimate moment capacity and expected likelihood of the different types of failure modes.
- Chapter 6 develops an analytical method for predicting the wall's load capacity by assuming that the masonry possesses zero bond strength. The resulting approach becomes based primarily on the geometric properties of the wall.
- Chapter 7 continues the development of the approach in the previous chapter by extending it to the prediction of the wall's overall load-displacement capacity. It also describes a prototype DB analysis using the proposed model.
- Chapter 8 concludes this thesis by summarising its main outcomes and providing recommendations for future research.

Part I

EXPERIMENTAL WORK

Chapter 2

QUASISTATIC CYCLIC TESTING

Abstract

An experimental programme was conducted in which eight full-scale unreinforced masonry walls were subjected to quasistatic cyclic face loading using a system of airbags. Of the tested walls, six contained a window opening and four were subjected to vertical precompression. Combined supports at the vertical and horizontal edges ensured that under face loading the walls underwent two-way bending. The walls were found to possess good post-peak strength and displacement capacity as well as reasonable energy dissipation characteristics. Significant strength and stiffness degradation and non-symmetry of strength in the positive and negative displacement directions were also evident. Discussion of the causes of the aforementioned trends and their implications towards the seismic response of masonry walls is provided.

2.1 INTRODUCTION

This chapter presents an experimental study in which a set of eight full-scale unreinforced masonry (URM) walls were subjected to cyclic out-of-plane loading. The panels were two-way spanning, in that they were supported at their horizontal and vertical edges, and thus responded in biaxial bending when subjected to face loads. Displacement-controlled quasistatic loading was administered using a set of inflatable airbags positioned against the opposite faces of the walls. The boundary support conditions remained constant for all wall specimens and incorporated moment connections at the walls' vertical edges. Parameters varied across the eight walls include the panel aspect ratio, amount of vertical precompression, and the presence of a window opening. The panel configurations are described in greater detail in Section 2.3.2.

The aims of this study were:

- To record the cyclic load-displacement ($F-\Delta$) behaviour of the walls, for the purposes of: (i) studying it with respect to the walls' expected seismic performance, (ii) comparing the walls' static strength to analytical predictions made using the virtual work (VW) method (dealt with in Chapter 4), (iii) quantifying values of key hysteretic properties including stiffness and damping, and (iv) providing a basis for the development of a nonlinear $F-\Delta$ model (dealt with in Chapter 7).
- To study the walls' cracking patterns and measure their deformation profiles, and assess the accuracy of idealised failure mechanisms used in the various analytical methods.
- To contribute to the available pool of experimental data for full-scale URM walls with precompression and fixity at the vertical edges, which is surprisingly lacking in the available literature.

To achieve these aims, every wall was tested in two distinct stages, as follows:

ULTIMATE STRENGTH TEST The first stage of the test involved subjecting the wall to monotonic loading using airbags until it reached its ultimate load capacity. In most of the walls, this corresponded to deformations of approximately 20 to 40 mm, which caused sufficient cracking to define a failure mechanism. During this phase of testing, the face of the wall was heavily instrumented using an array of displacement transducers to monitor displacements at different locations along the wall.

CYCLIC TESTING After the initial ultimate strength test was completed, airbags were placed on both sides of the wall and cyclic loading was administered. The amplitude of the applied displacement was sequentially increased at increments of 10 mm, with typically two cycles being performed at each level of displacement. During this phase the walls were subjected to maximum central displacements close to the wall's thickness of 110 mm.

The test study undertaken is believed to provide a significant contribution to the existing pool of experimental work, by filling several research gaps identified through a review of literature (reported in Section 2.2). Among the unique aspects of this study are the boundary support conditions imposed on the test walls. To the author's knowledge, no prior experimental work has been conducted where full rotational fixity was implemented along the vertical edges of the wall by means of return walls, a restraint condition that is commonly encountered in practice. In this study, vertical edges were restrained against both translation and rotation and were therefore considered to be fixed-supported. By contrast, the top and bottom horizontal edges were simply-supported, with the exception of one wall which remained free at the top edge. Another significant aspect of the tests was subjecting some of the walls to precompression, in order to simulate loadbearing walls that act as part of the gravity load path. In addition, six of the eight walls tested in this study contained a window opening, and furthermore, because most of the walls with openings encountered in past literature contained concentrically positioned openings, this study included four walls with asymmetrically positioned openings. Finally and most importantly, to the author's knowledge, no prior experimental work has been performed where the primary aim was to study the cyclic response of two-way URM walls under quasistatic loading conditions.

The outline of this chapter is as follows: A review of past experimental research is presented in Section 2.2. A detailed account of the main test programme, including the material properties, wall configurations, the test arrangements and test procedure, is provided in Section 2.3. Results of the experimental study are then presented in three parts: The walls' load-displacement behaviour is studied in Section 2.4, the observed damage and crack patterns are discussed in Section 2.5, and a study of the wall deformation profiles is presented in Section 2.6. The chapter concludes by summarising the key observations and lessons derived from the experimental programme in Section 2.7.

Supporting appendices are also provided in relation to the work in this chapter: Appendix A reports details of material testing, and Appendix B provides other miscellaneous details.

2.2 REVIEW OF PAST EXPERIMENTAL RESEARCH

2.2.1 Comparison of Testing Methods

The general aim of cyclic testing, which may include any method of testing where the structure is subjected to repeated reversals of loading direction, is to study the seismic performance of structural systems. Such tests can be further categorised according to the loading rate as either *quasistatic* or *dynamic*.

Quasistatic cyclic tests involve administering a cyclic loading pattern at a slow rate, usually in displacement control. The primary advantage of this mode of testing is to allow the load versus displacement (hysteresis) behaviour to be studied under predefined displacement histories. These generally involve alternating direction of the applied displacement at sequentially increasing levels, with multiple cycles at each level of displacement. This can be used to quantify the system's cyclic load-displacement envelope as well as its degradation and energy dissipation characteristics.

Dynamic shaketable testing is fundamentally different to quasistatic loading, because it subjects the structure to a series of accelerations. Whilst this mode of testing doesn't afford the same level of control over the imposed structural deformations, it does recreate the true dynamic nature of seismic response by incorporating inertial and viscous damping forces. It also allows for the structure to be subjected to realistic earthquake motions. A further aspect of shaketable testing is that the structure is inherently subjected to loading spatially distributed according to its mass, which is an experimental design aspect that needs to be explicitly taken into account in quasistatic testing if it is to be used for seismic resistance assessment.

Calvi et al. [1996] provides a good discussion of the relative merits of the different testing methods with respect to masonry structures. He notes that since *URM* exhibits rate-dependent behaviour whereby crack propagation can occur during application of a constant load, quasistatic tests tend to indicate lower load resistance than dynamic tests and are thus generally considered to be conservative for seismic assessment. Furthermore, he and other researchers [e.g. *Abrams, 1996*] have also argued that since typical displacement histories used in quasistatic cyclic tests involve a large number of displacement cycles, which are more severe than monotonic or random earthquake histories, quasistatic cyclic tests tend to be even further conservative in terms of the measured strength for structural systems such as *URM*, where degradation is affected by the number of cycles.

2.2.2 Monotonic Loading

In the past four decades, a substantial amount of monotonic testing has been performed on two-way masonry walls, with significant contributions made in Australia, Canada and the United Kingdom. The general aim of these studies has been to measure the static load capacity of various types of wall configurations in response to a uniformly distributed pressure, typically administered using airbags. An extensive review of these works has led to the compilation of a database incorporating over 400 individual tests. Table 2.1 summarises the main aspects of the published test data, including: the type of masonry (unreinforced or reinforced¹), specimen scale (full or reduced), type of material (clay or concrete), types of edge support geometries, and the number of walls featuring openings or precompression.

The review conducted indicates a notable lack of available test data for walls with precompression. As seen from Table 2.1, of the eight reported tests with precompression, only five involved unreinforced clay brick masonry walls. The shortage of data for such walls is somewhat surprising, considering that loadbearing walls are very common in typical masonry construction. The review also shows a lack of data for two-way spanning walls with rotational fixity along the vertical edges (not indicated in the table). As a contribution to the available data pool, the experimental programme in this chapter focuses on walls featuring both precompression and vertical edge fixity.

2.2.3 Cyclic Loading

Whilst a relatively large amount of experimental work has been performed involving monotonic loading (as reported in Section 2.2.2), only a handful of studies have administered cyclic loading, be it quasistatic or dynamic. Furthermore, the majority of such studies have focused only on vertically spanning walls. These include tests on unstrengthened URM panels [Ewing and Kariotis, 1981; Dafnis *et al.*, 2002; Griffith *et al.*, 2004], as well as URM panels strengthened using various retrofit systems such as fibre-reinforced polymer (FRP) strips [Ehsani *et al.*, 1999], expansive epoxy [Zeiny, 2003] and timber backup framing [Paquette *et al.*, 2001; Reneckis *et al.*, 2004].

Experimental research on two-way panels is especially limited in the available literature. Benedetti *et al.* [1998] performed shaketable tests on 24 half-scale two-storey masonry buildings; however, the study focused primarily on the overall

¹Although unreinforced masonry walls are the primary focus of this research, several tests on reinforced masonry walls and concrete masonry walls are included in Table 2.1, as these formed part of a data set used by Lawrence and Marshall [2000] to validate the accuracy of the VW method for calculation of the ultimate load capacity.

Table 2.1: Summary of past experimental work involving out-of-plane tests on single leaf walls.

Source	Note	Country	Total no. walls	Reo *	Scale †	Material‡		Support shape §					No. walls with		
						clay	conc.	O	U	C	L	V2	H	openings	precomp.
<i>Satti [1972]</i>	a.	UK	19	U	1/6	19	-	6	13	-	-	-	-	-	-
<i>Anderson [1976]</i>		UK	6	U	1	-	6	-	6	-	-	-	-	-	-
<i>BCRA (1977 - 1986)</i>	b.	UK	239	U	1	176	51	12	11	209	9	-	2	8	15
<i>Gairns [1983]</i>		Australia	9	R	1	-	9	-	4	5	-	-	-	-	-
<i>Lawrence [1983]</i>		Australia	32	U	1	32	-	-	21	11	-	-	-	-	-
<i>Baker [1984]</i>		Australia	4	R	1	-	4	-	4	-	-	-	-	-	-
<i>Anderson [1985]</i>		UK	9	U	1	5	4	-	8	-	1	-	-	-	8
<i>Tapp [1985]</i>	c.	UK	6	U	1	6	-	-	6	-	-	-	-	-	5
<i>Gairns and Scriver [1987]</i>		Australia	7	U	1	2	5	-	7	-	-	-	-	-	-
<i>Drysdale and Essary [1988]</i>		Canada	21	R	1	-	21	-	12	3	-	-	3	3	3
<i>Southcombe and Tapp [1988]</i>		UK	5	U	1	5	-	-	-	5	-	-	-	-	5
<i>Candy et al. [1989]</i>		Australia	9	U	1	2	7	-	-	8	-	1	-	-	6
<i>Chong [1993]</i>		UK	16	U	1	13	3	-	2	10	4	-	-	-	11
<i>Abrams et al. [1996]</i>		USA	8	U	1/2	6	2	-	8	-	-	-	-	-	-
<i>Edgell and Kjar [2000]</i>		UK	37	U	1	22	15	-	14	12	11	-	-	-	11
<i>Griffith [2000]</i>		Australia	2	U	1	2	-	-	1	1	-	-	-	-	1
<i>Chen [2002]</i>	d.	Canada	8	U	1	-	8	-	8	-	-	-	-	-	7
<i>Korany [2004]</i>		Canada	4	U	1	4	-	-	2	2	-	-	-	-	1
Total no. walls:			441			294	135	12	108	291	25	1	5	11	69
															8

*Unreinforced or reinforced. The reinforced masonry walls reported here are included only for completeness, as they were used by *Lawrence and Marshall [1996]* in validating the virtual work method.

†Specimen scale factor.

‡Unit material, as either clay brick, concrete block (including AAC and various types of aggregate concrete), or calcium silicate (CS) brick.

§The various codes (O, U, C, L, V2, H) are indicated by Figure 1.2.

a. As reported by *Hendry [1973]*.

b. Tests conducted by the British Ceramic Research Association have been reported throughout numerous publications, including *West et al. [1977]*; *Haselstine et al. [1978]*; *West et al. [1979b,a]*; *Hodgkinson et al. [1982b]*; *West et al. [1986]*; *de Vekey et al. [1986]*; *Haselstine and Titt [1986]*.

c. As reported by *Chong [1993]*.

d. As reported by *Baker et al. [2005]*; *Choharath and El Mandouh Galal [2004]*.

building response and only limited attention was given to the out-of-plane flexural response of the two-way walls which were present. *Jaramillo [2002]* conducted a rare study involving shaketable testing of two-way spanning walls. He tested two full-scale wall specimens supported along the bottom edge and both vertical edges, whilst being free at top edge.

Cyclic tests on two-way walls using quasistatic load application have also been very limited, but some research has been performed, including previous work by the author [*Vaculik et al., 2003, 2004*] involving airbag tests on half-scale dry-stack masonry walls; and tests by *Ghobarah and El Mandooh Galal [2004]* using carbon-FRP retrofitted concrete block masonry walls. However, in both of these studies the wall specimens were tested by unloading and reloading in the same direction and since the direction of loading was not reversed, the loading would not be considered truly 'cyclic'.

Review of the available literature indicates a surprising lack of experimental work on regular non-retrofitted, two-way URM panels subjected to cyclic loading, be it quasistatic or dynamic. In order to fill these gaps, two test studies have been conducted as part of this research: (i) the quasistatic cyclic tests on eight full-scale panels, as reported in the current chapter; and (ii) shaketable tests on five half-scale panels, reported in Chapter 3.

2.3 TEST PROGRAMME AND METHODOLOGY

2.3.1 Materials

All brickwork used in this study, including the eight full-scale URM panels and small-scale material test specimens, was constructed by qualified bricklayers under controlled laboratory conditions to ensure the best possible quality control. The masonry units comprised standard Australian clay bricks with nominal dimensions $230 \times 110 \times 76$ mm ($l_u \times t_u \times h_u$), perforated with two rows of five holes (Figure 2.1). The nominal weight density γ of this type of masonry is 19×10^{-6} N/mm³. To minimise variability in the material properties, all masonry was constructed using brick units originating from the same batch at manufacture.

Mortar joints were constructed to a standard thickness of 10 mm using 1:2:9 mortar (portland cement, lime and sand). The clay content of the sand was determined to be 8.2%. Quality control measures were undertaken during the mixing of the mortar to ensure consistency. This included bucket batching of the ingredients and ensuring that all sand was air-dried prior to mixing. Water was added to the mix of cement and lime inside the mortar mixer to provide a desired

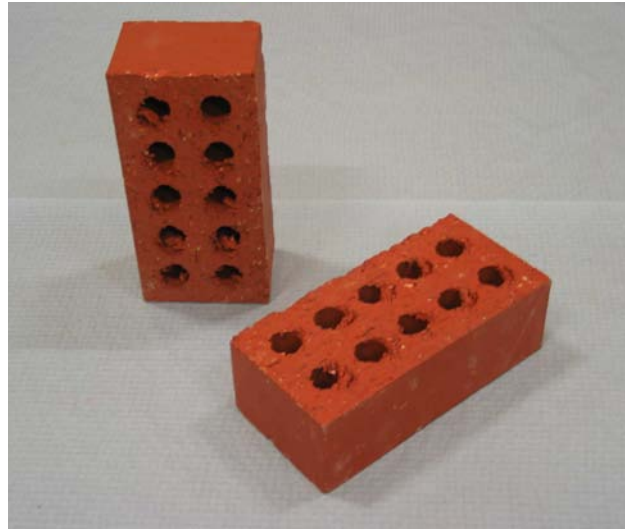


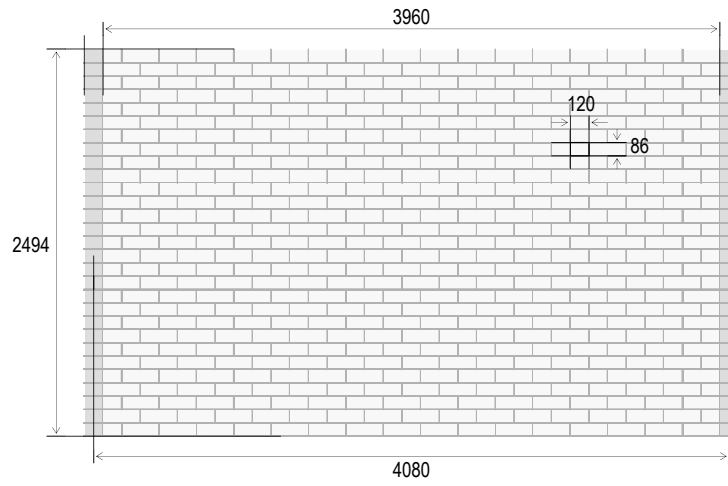
Figure 2.1: Perforated clay masonry units with $230 \times 110 \times 76$ mm dimensions.

Table 2.2: Material properties of brick units.

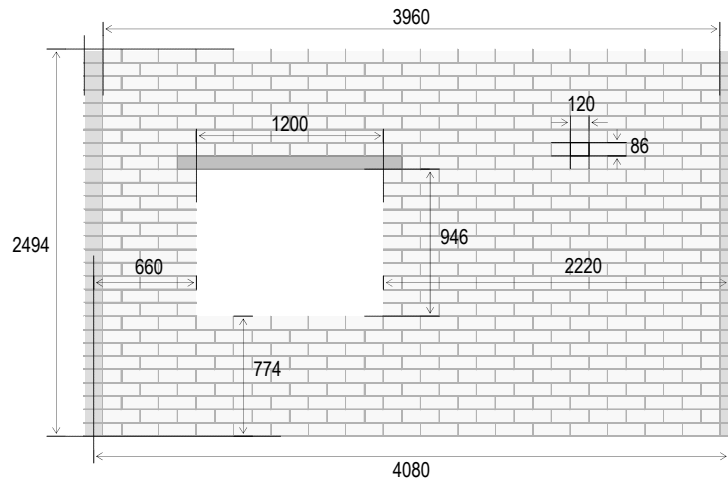
	Lateral modulus of rupture f_{ut} [MPa]	Young's modulus E_u [MPa]
Mean	3.55	52,700
CoV	0.27	0.35

workability based on the bricklayers' experience. All water additions were recorded. The average volumetric water content of the mortar was 19.9%, with a coefficient of variation (CoV) of 0.13.

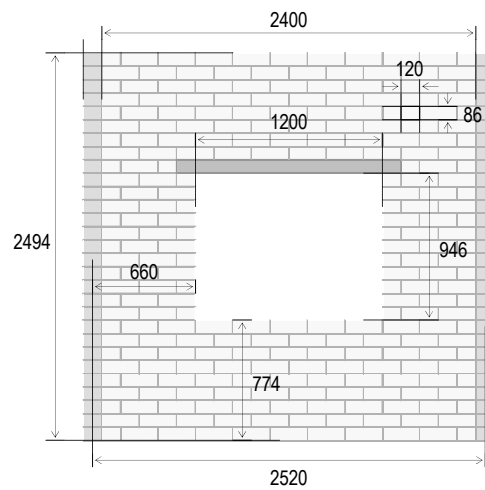
Tests on small masonry specimens were conducted in accordance with the guidelines given in the Australian masonry code AS 3700 [*Standards Australia, 2001*], to determine values of key material properties for use in subsequent analytical studies. A detailed report of the test procedures used and the associated results is given in Appendix A. Mean material properties for the brick units are summarised in Table 2.2, including the lateral modulus of rupture f_{ut} and Young's modulus of elasticity E_u . Mean material properties for the masonry are summarised in Table 2.3 for the respective walls, including the flexural tensile strength f_{mt} , compressive strength f_{mc} and Young's modulus of elasticity E_m . Note that the f_{mt} presented in this table was determined as the average of the mean values for the mortar batches used in each wall (refer to Appendix A.2). The values of material properties determined are considered typical for the type of masonry used.



(a) Walls s1 and s2.



(b) Walls s3, s4, s5 and s6.



(c) Walls s7 and s8.

Figure 2.2: Detailed wall dimensions (in millimetres).

Table 2.3: Material properties of masonry.

Wall	Flexural tensile strength f_{mt} [MPa]	Compressive strength f_{mc} [MPa]	Young's modulus E_m [MPa]
s1	0.721	17.6	3,190
s2	0.520	13.6	2,240
s3	0.499	15.1	3,030
s4	0.635	16.8	5,580
s5	0.655	17.4	3,990
s6	0.496	15.8	2,740
s7	0.682	15.1	4,130
s8	0.714	16.1	3,060
Mean	0.614	16.0	3,540
CoV	0.19	0.14	0.41

2.3.2 Panel Configurations

Configurations of the eight test walls are presented in Table 2.4, with their dimensions shown in Figure 2.2. The walls comprised of three different geometries, as follows:²

LONG SOLID WALLS (s1, s2) These walls had dimensions of 4080×2494 mm ($L \times H$) and did not contain any openings (Figure 2.2a). They were tested under precompression of 0.10 and 0 MPa, respectively.

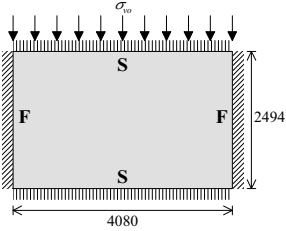
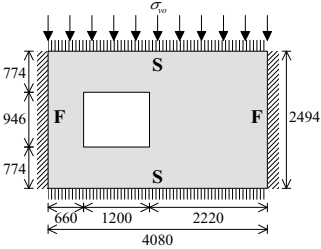
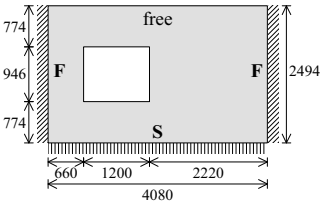
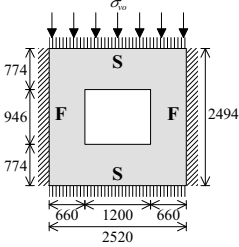
LONG WALLS WITH OPENINGS (s3, s4, s5, s6) These walls had dimensions of 4080×2494 mm ($L \times H$) and each contained an eccentrically positioned window opening (Figure 2.2b). Walls s3–s5 were supported at the top horizontal edge and tested under precompression of 0.10, 0.05 and 0 MPa, respectively. The fourth wall, s6, was unique to this study in that it was left unsupported at the top edge.

SHORT WALLS WITH OPENINGS (s7, s8) These walls had dimensions of 2520×2494 mm ($L \times H$) and contained a concentrically positioned window opening (Figure 2.2c). They were tested under precompression of 0.10 and 0 MPa, respectively.

All walls were constructed entirely using half-overlap stretcher bonded masonry. Short return walls spanning two brick units in length (480 mm) were provided at the vertical edges, as shown by Figure 2.3, which were also engaged into the main leaf of the wall using the half-overlap stretcher bond. The purpose of the

²Note that the given wall lengths refer to the length between the centre-to-centre of the return walls supporting the vertical edges. For the clear lengths between the supports refer to Table 2.5 and Figure 2.2.

Table 2.4: Test wall configurations.

Panel dimensions [mm] and support arrangement	Wall	σ_{vo} [MPa]
	S1	0.10
	S2	0
	S3	0.10
	S4	0.05
	S5	0
	S6	–
	S7	0.10
	S8	0

Note: F = Fixed support, S = Simple support

Table 2.5: Detailed wall dimensions and properties.

Walls	Wall dimensions			Opening dimensions				Area		Weight	
	$L_{w\ sup}$ [mm]	$L_{w\ clear}$ [mm]	H_w [mm]	x_o [mm]	y_o [mm]	L_o [mm]	H_o [mm]	A_w [m ²]	W_w [kN]		
s1, s2	4080	3960	2494	–	–	–	–	9.876	20.64		
s3, s4, s5, s6	4080	3960	2494	660	774	1200	946	8.741	18.27		
s7, s8	2520	2400	2494	660	774	1200	946	4.850	10.14		

Note: The area and weight of the wall were calculated using the clear wall length between the supports, $L_{w\ clear}$.

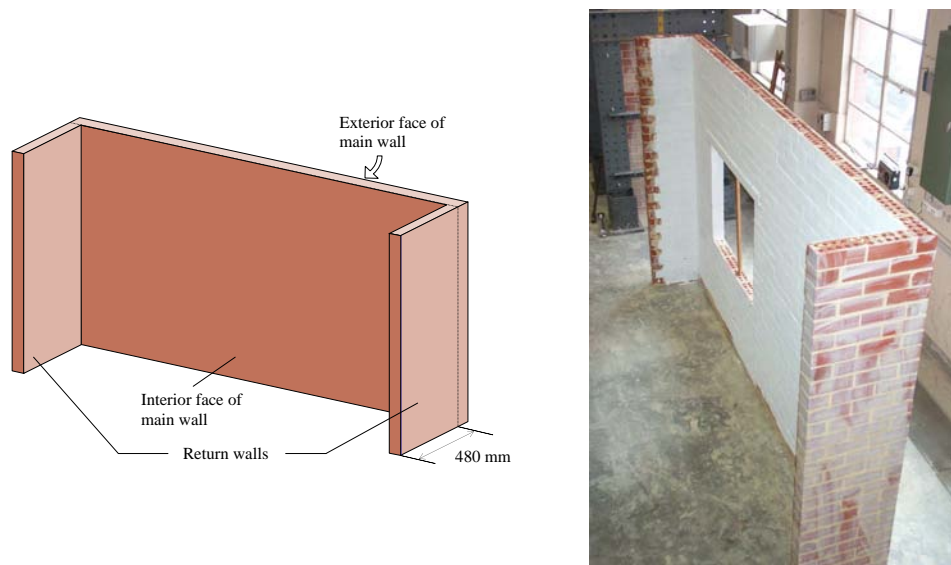


Figure 2.3: Overall test wall geometry.

return walls was to stabilise the walls against overturning and to provide means for implementing rotational fixity at the vertical edges. The naming convention used for reference to the interior and exterior faces of the wall is also shown on Figure 2.3, which is used throughout this chapter.

The dimensions of each class of wall are summarised in Table 2.5, including the wall length $L_{w\text{ sup}}$ measured between the centre-to-centre of the vertical supports, wall length $L_{w\text{ clear}}$ taken as the clear span between the return walls, wall height H_w , and coordinates of the opening as x_o , y_o , L_o and H_o (horizontal offset, vertical offset, length and height, respectively). The net face area A_w and net weight W_w of the main face of the wall are also provided in the table, which were used in subsequent calculations for converting the measured force resistance to pressure. Note that these values were calculated using the clear length of the wall, $L_{w\text{ clear}}$, since this corresponds to the area over which the airbag loading acted.

2.3.3 Wall Support Conditions

The methods of restraint used at the edges of the walls incorporated simple translational support at the top and bottom edges, and both translational and rotational restraint at the vertical edges. The detailing used to provide these support conditions and the implications toward wall behaviour will now be discussed.

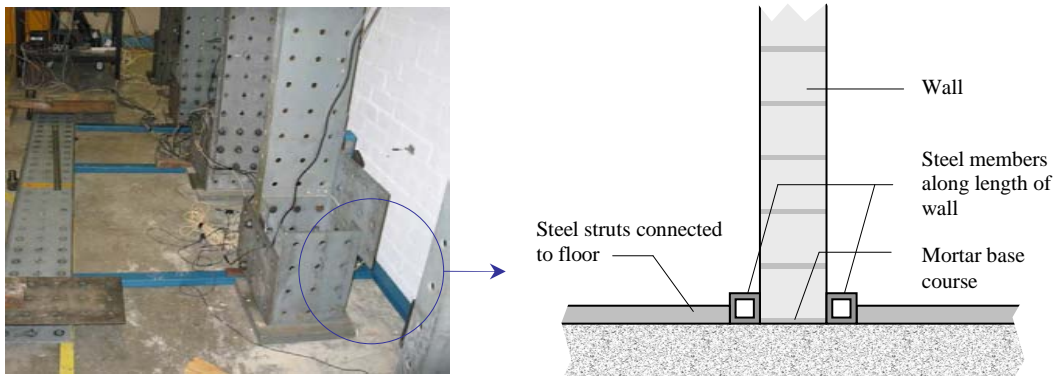


Figure 2.4: Bottom edge support details.

Bottom Edge

During construction, a mortar base joint was used to bond the walls to the concrete floor of the laboratory. Whilst this provided sufficient translational restraint during testing of panel s1 which was subjected to 0.10 MPa precompression, significant sliding along the base occurred during the initial push of wall s2, an identical wall with no precompression. This is most likely to have resulted from the lack of additional frictional restraint in wall s2. It was decided that whilst it is possible for such behaviour to occur in practice when the base connection is weak, for example in the case of a damp proof course connection, additional support at the bottom edge would be provided in order to facilitate two-way bending response.

An improved restraint method was thus implemented in all subsequent tests, consisting of a steel member that ran adjacent to the entire length of the bottom edge and was fastened to the laboratory floor using steel struts (Figure 2.4). This system was implemented on both sides of the wall during the cyclic test phase.

Although each wall was mortar-bonded to the floor using a base joint, previous studies have shown that horizontal cracks in two-way walls generally form prior to the attainment of the ultimate load capacity [Lawrence and Marshall, 2000]. Consequently, the cohesion along the base joint does not contribute to the ultimate strength of the wall. Nonetheless, the bottom edge still possesses the capacity to provide some degree of rotational restraint following crack formation, due to the restoring moment from self-weight. Although this level of moment resistance has been shown to be generally negligible when considering the ultimate strength of a wall, it becomes significant when considering the wall's residual strength after cracking [Vaculik et al., 2003].

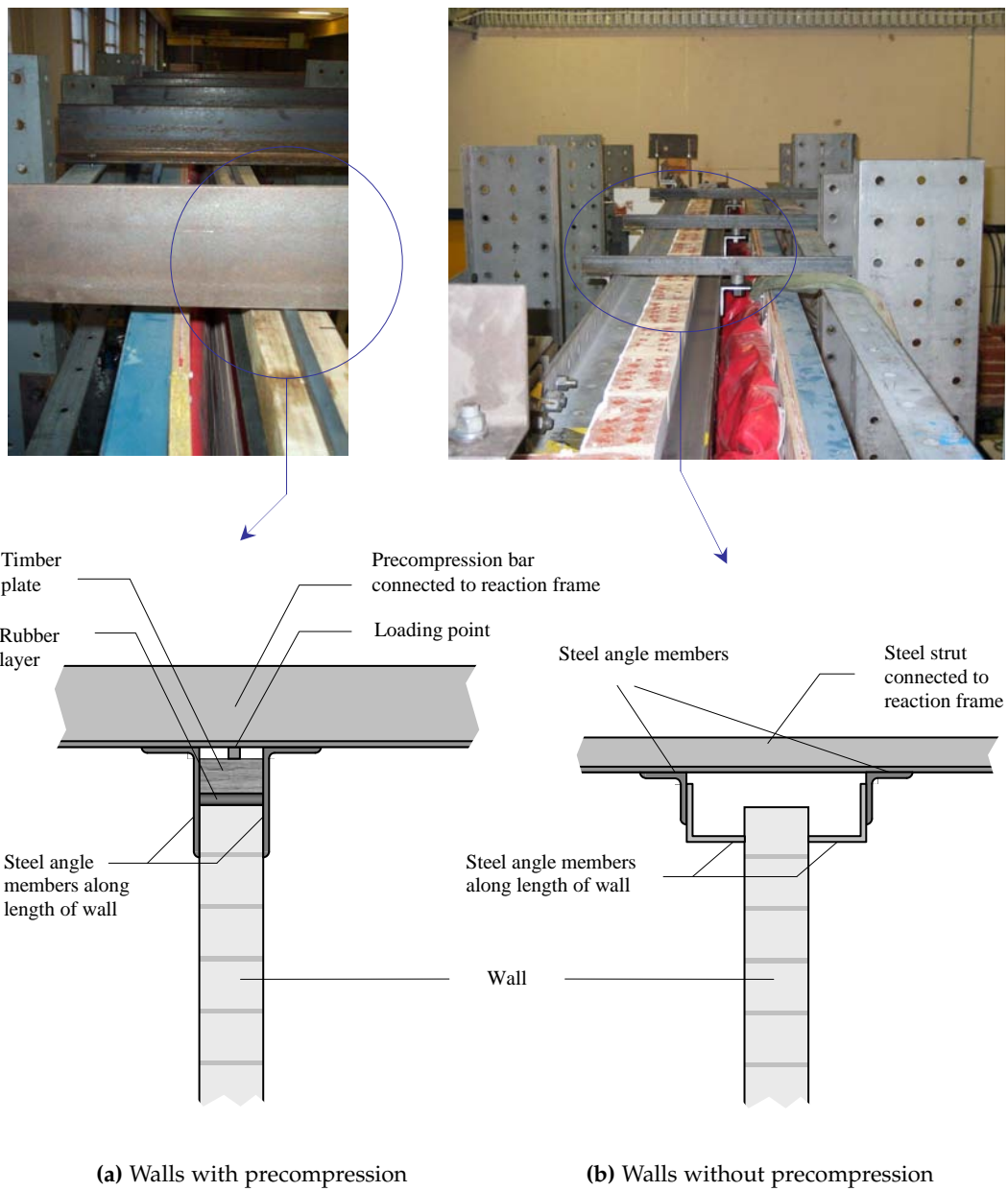


Figure 2.5: Top edge support details.

Top Edge

The methods used to provide translational restraint along the top edge of the panels are shown in Figure 2.5. In walls with axial loading (Figure 2.5a), the top edge was restrained using steel angles that were clamped onto the horizontal precompression bars, with further restraint also resulting from friction. In the absence of axial loading (Figure 2.5b), the edge was restrained by angled steel members that ran along the entire length of the wall, and were further stiffened using steel struts.

Because both connection methods provided translational restraint but were unable to transfer any bending moment, the top edge in all test walls (except s6) was considered to be simply-supported. It should also be noted that in the presence of axial precompression, the load was transferred to the wall through a thin steel bar which was positioned at the mid-thickness of the wall (Figure 2.5a), and thus provided no restoring moment to contribute to the wall's out-of-plane load resistance.

Vertical Edges

The degree of rotational restraint along the vertical edges can significantly influence the out-of-plane strength of two-way walls calculated using the AS 3700 [*Standards Australia, 2001*] method [*Griffith, 2000*]. Special care was therefore taken in the detailing of the connections at the vertical edges, to ensure that the degree of fixity was a controlled quantity. To achieve this, connections were detailed to produce full translational and rotational restraint—boundary conditions which would be representative of typical masonry construction; for example, where a wall is built into an engaged pier, or at the intersection of two orthogonal walls at the corner of a building.

The detailing used to restrain the vertical edges of the walls is shown by Figure 2.6. Full moment connections were achieved at the vertical edges of the main wall face, by encasing the return walls along their height using steel channel members which were in turn braced back to the reaction frame. Because this provided lateral out-of-plane restraint to the vertical edges of the return walls themselves, any face load acting on the main wall face generated a horizontal bending moment at the boundary between the main wall and the return wall. Consequently, the vertical edges of the wall can be treated as fixed moment connections, which require cracks to form in order for the wall to develop a collapse mechanism.

2.3.4 Vertical Precompression

For the purpose of simulating typical loadbearing walls, vertical precompression of up to 0.10 MPa was applied to four of the test specimens (walls s1, s3, s4 and s7). The vertical load was administered using a series of horizontal steel members pinned at one end to a support frame and cantilevered over the test wall along the main panel as well as at the return walls, as shown in Figure 2.7. In order to apply axial loading in a realistic manner, the steel members were positioned along the test wall at spacing representative of typical roof beams (details in Figure B.1, Appendix B.1). Weights were suspended from the ends of the horizontal bars to achieve the

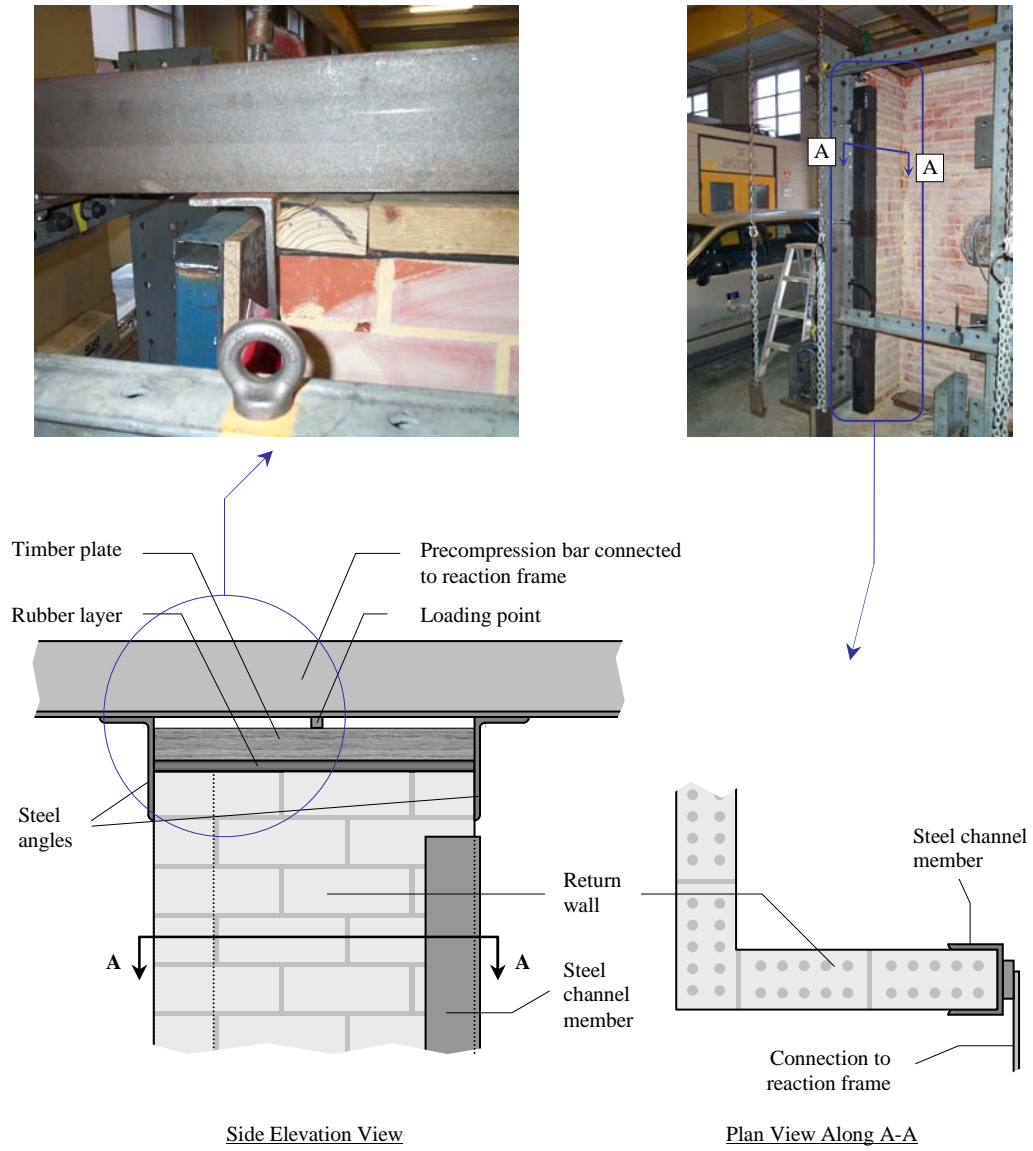


Figure 2.6: Vertical edge support details.

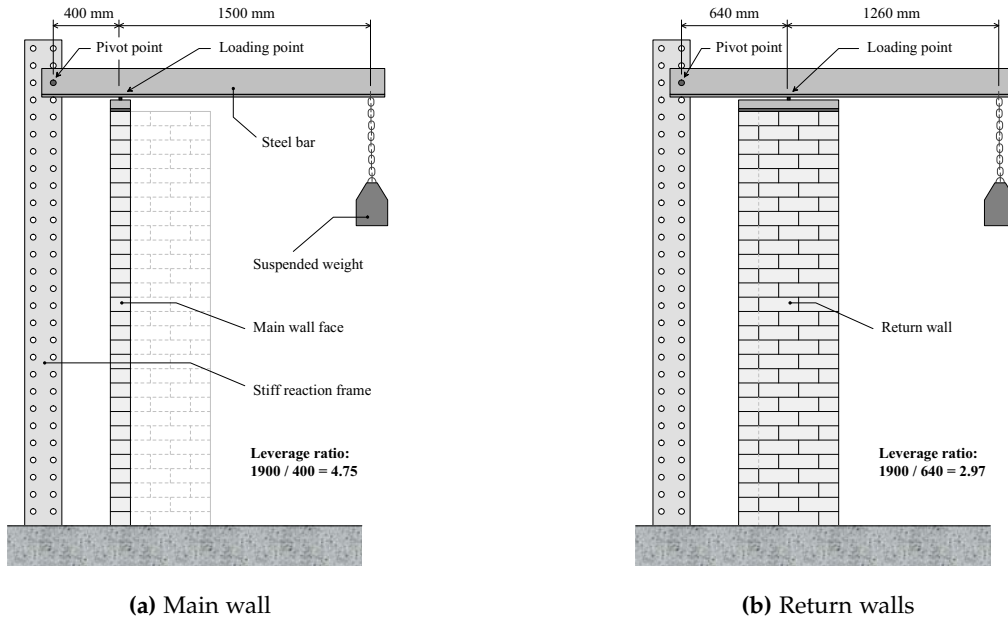


Figure 2.7: Vertical precompression loading arrangement.

intended precompression stress (σ_{vo}) at the top of each wall, particularly 0.10 MPa in walls s1, s3 and s7, and 0.05 MPa in wall s4. The force was transferred to the wall through a loading pin positioned along the centre line of the wall's thickness, with a timber top-plate and a rubber layer used to disperse the load more uniformly (Figure 2.5a).

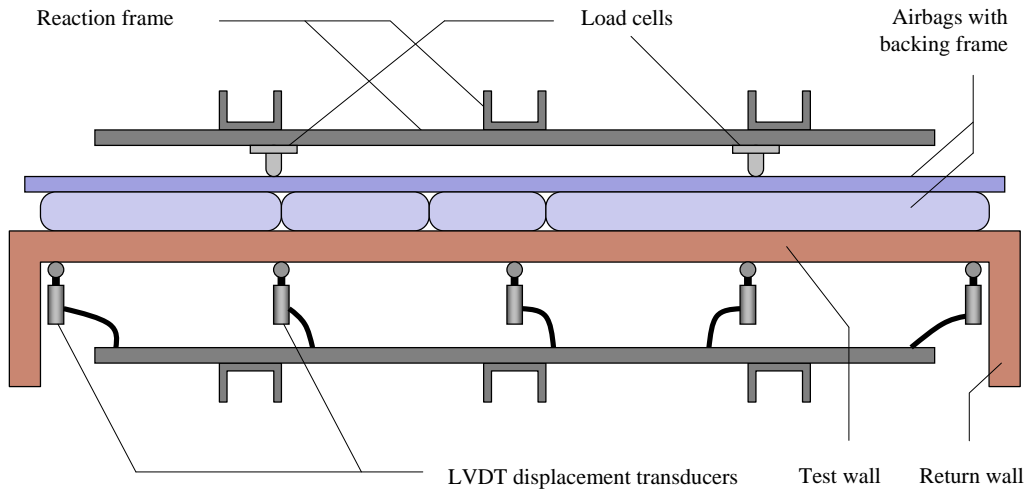
2.3.5 Test Procedure

Each wall was tested in two distinct stages which are described herein. A diagram of the loading and instrumentation arrangement used during each stage is shown in Figure 2.8.

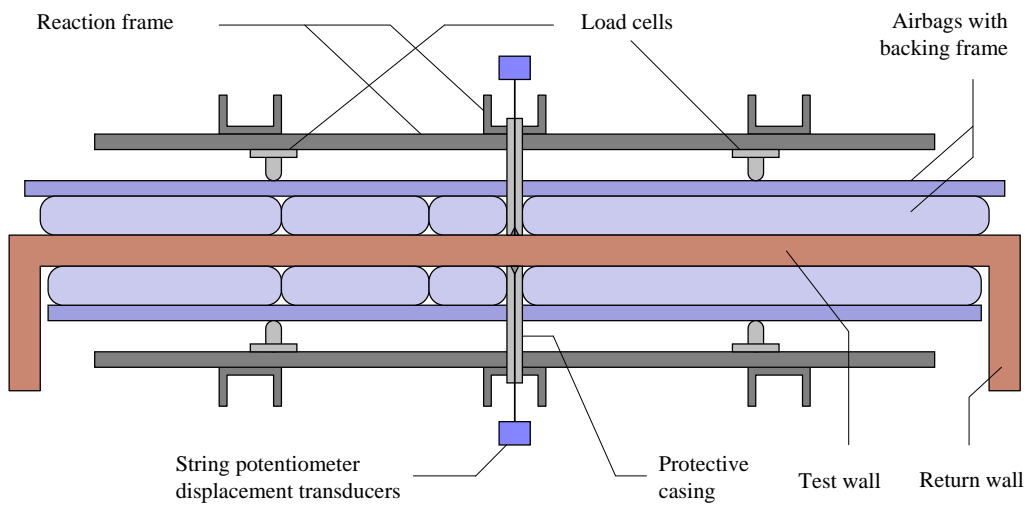
Ultimate Strength Test

The first phase of testing involved subjecting the initially uncracked wall to a monotonic load until it reached its ultimate load capacity. In the majority of tests, this involved displacements of approximately 20–40 mm, during which sufficient cracking occurred along the panel to define the failure mechanism. Once it was deemed that a wall had attained its peak strength, the applied load was released.

Figure 2.8a illustrates various aspects of the test arrangement schematically, whilst Figure 2.9 shows a photograph of a panel during this phase of testing. The



(a) Arrangement for ultimate strength test



(b) Arrangement for cyclic testing

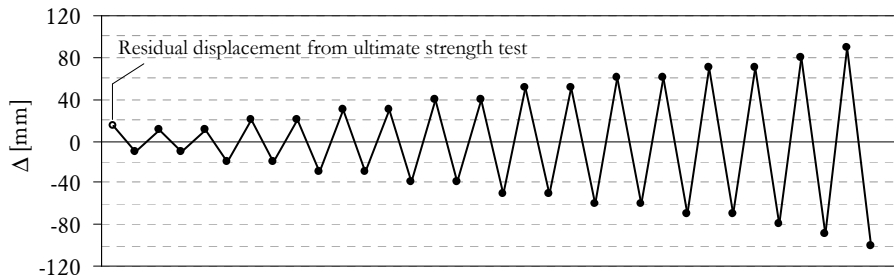
Figure 2.8: Plan view of the instrumentation and loading arrangement.



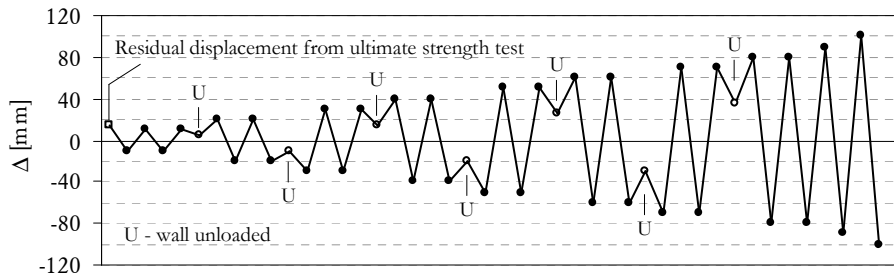
Figure 2.9: Photograph of the overall test setup, including precompression arrangement (wall s1 shown).

mechanism used to apply a uniformly distributed pressure onto the panel consisted of a series of inflatable airbags mounted on a stiffened backing frame, which was in turn supported by load cells connected to the reaction frame. Because of the differently sized airbags available, their arrangement was chosen so as to provide the best possible coverage along the face of the wall, in order to distribute the load evenly (details in Figure B.2, Appendix B.1). Pressure was applied to the test wall by slowly inflating the airbags using an electronically regulated air pump. The exact force exerted on the wall was measured by the load cells and conveyed to a data acquisition system. It was noted during the tests that the face pressure measured using the load cells was typically 75–80% of the air pressure recorded in the airbags, which is common for this type of loading technique.

The deformation profile along the wall was monitored using an array of displacement transducers (Figure B.4, Appendix B.1). A 3×3 grid was used to measure the displacement along the wall's quarter- and mid-span locations. Movement of the walls along their vertical and horizontal edges was also monitored using displacement transducers, and where movement along these boundaries took place, the wall deformation data was adjusted accordingly such that the displacements were measured relative to the wall edges.



(a) Type A, used for walls s1–s3.



(b) Type B, used for walls s4–s8.

Figure 2.10: Cyclic loading patterns.

Cyclic Testing

After completing the ultimate load capacity test, which essentially corresponded to the first half-cycle of loading, the walls were subjected to cyclic loading using airbags positioned on both sides of the wall (Figure 2.8b). Due to the presence of the airbags, it was impractical to record displacements at multiple locations over the face of the wall as was done in the ultimate load capacity tests; so instead, displacement transducers were used only at key positions (Figure B.5, Appendix B.1), including the location of the maximum displacement during the initial push. To achieve this, string potentiometer displacement transducers were attached to the wall through holes in the airbag backing frame and encased in protective tubing to prevent contact between the string and the airbags (Figure 2.8b).

Idealised representations of the applied displacement histories are shown in Figure 2.10 (Figures B.16–B.23 in Appendix B.3 show the precise histories imposed on each wall). Initiating from the residual displacement from the initial push, the applied displacement was alternated between the positive and negative directions, with its amplitude being increased by 10 mm increments. Two loading cycles were generally performed at each amplitude, except at larger displacements where only one cycle was performed. The tests were concluded when the walls were deemed to

be sufficiently damaged based on visual inspection and measured strength, which typically corresponded to deformations of approximately 100 mm.

Two types of loading patterns were employed: type A loading, used for walls s1–s3 (Figure 2.10a); and type B loading, used for walls s4–s8 (Figure 2.10b). In type A loading, the displacement was consistently alternated between the positive and negative directions for two complete cycles, before increasing the amplitude by 10 mm. By contrast, in type B loading, each time the displacement amplitude was increased to a higher level, the wall was unloaded (denoted by ‘U’ in Figure 2.10b) and then reloaded in the same direction as the previous displacement excursion. This allowed for observations of hysteretic behaviour caused by unloading/reloading in the same direction, which was not possible under type A loading, since unloading was always followed by loading in the opposite direction. It was thought that type B loading could provide additional information regarding the hysteretic behaviour that might prove useful in subsequent development of a hysteresis model.

2.4 LOAD-DISPLACEMENT BEHAVIOUR

Using the recorded data, load-displacement graphs were generated for the initial push to ultimate strength (Figures 2.11–2.13) and cyclic tests (Figures 2.14–2.21). It should be noted that the positive displacement and load direction in these graphs corresponds to the applied load pushing the wall inwards, thereby imposing a compressive reaction onto the return walls.

The primary axes of the graphs plot the wall’s face pressure q versus displacement Δ . The pressure resistance was calculated as

$$q = \frac{F}{A_w}, \quad (2.1)$$

where F is the lateral force acting on the wall, obtained as the total of the load cell measurements, and A_w is the net face area (given in Table 2.5 for each wall).³

The secondary axes of the provided graphs display the displacement and load using the non-dimensional λ - δ format. The normalised displacement δ is defined as

$$\delta = \frac{\Delta}{t_u}, \quad (2.2)$$

where t_u is the wall thickness (in these tests 110 mm). The non-dimensional load (or load multiplier) λ is defined the ratio of the wall’s lateral force resistance and

³The net area was calculated as $A_w = L_w \times H_w - A_o$, where L_w and H_w are the length and height of the wall along which the load was applied and A_o is the area of any openings present.

Table 2.6: Results of the initial push.

Wall	Measured Strength			K_{ini} [kN/mm]	Percentage of Δ_{max} recovered
	F_{ult} [kN]	q_{ult} [kPa]	λ_{ult}		
s1	47.0	4.76	2.28	42.1	66%
s2	30.0	3.04	1.45	6.71	62%
s3	44.2	5.05	2.42	45.1	83%
s4	34.2	3.91	1.87	35.2	77%
s5	31.4	3.59	1.72	16.6	52%
s6	17.2	1.97	0.94	3.85	75%
s7	42.2	8.71	4.17	28.7	60%
s8	41.3	8.52	4.08	24.6	70%

self-weight⁴ (given in Table 2.5 for each wall); or

$$\lambda = \frac{F}{W_w} = \frac{q}{\gamma t_u}, \quad (2.3)$$

where γ is the weight density of the masonry (in these tests 19×10^{-6} N/mm³). Alternatively, λ may also be interpreted as the equivalent static acceleration in units of g 's. Of these three different measures of strength (F , q and λ), the pressure and load multiplier are most meaningful in terms of the wall's load resistance to seismic actions, as they account for the surface area of the wall, and therefore reflect the inertial nature of earthquake loading. Therefore, throughout the upcoming discussions the pressure capacity is used as the measure of the load capacity.

2.4.1 Initial Push

The walls' load-displacement response during the initial push up to the ultimate load capacity is graphed in Figures 2.11–2.13. Several key parameters were derived based on the measured response, as summarised in Table 2.6 for each wall. These include: the ultimate strength, reported as a force (F_{ult}), pressure (q_{ult}) and load multiplier (λ_{ult}); and the initial uncracked stiffness (K_{ini}), determined as the slope of the F - Δ loading branch up to 40% of the wall's ultimate strength.⁵ The percentage of displacement recovered upon unloading is also provided; however, since the maximum displacement imposed upon the walls during these tests was somewhat arbitrary, these values should only be treated as indicative of the walls' self-centring

⁴The wall's net weight is calculated as $W_w = A_w t_u \gamma$, where A_w is the net area.

⁵All walls except for s2 were originally uncracked at the time the ultimate strength test was conducted. In addition, wall s6 had its return walls insufficiently restrained in the in-plane direction during these tests. Hence, it is likely that the strength and stiffness of these two walls may have been reduced relative to their 'true' values.

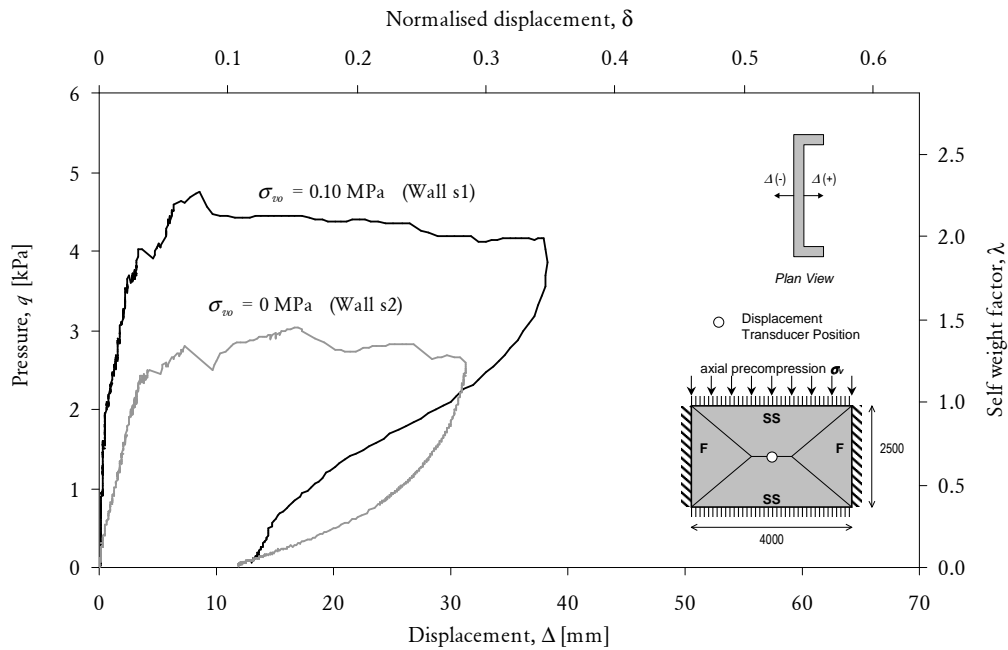


Figure 2.11: Load-displacement response for long solid walls (s1, s2) during initial push.

ability. Graphs demonstrating the derivation of each of these parameters from the load-displacement curves are provided in Appendix B.2 (Figures B.6–B.13).

The upcoming sections discuss the behaviour of individual walls, followed by a summary of the general trends observed from the initial ultimate strength tests.

Long Solid Walls (s1, s2)

Solid walls s1 and s2 differed only in that wall s1 was loaded with 0.10 MPa precompression, whilst wall s2 had no axial loading. From inspection of the load-displacement response shown in Figure 2.11 and Table 2.6, it can be seen that wall s1 was stronger (4.76 kPa for wall s1 compared to 3.04 kPa for wall s2) and significantly stiffer (42.1 kN/mm for wall s1 relative to 6.71 kN/mm for wall s2).

Whilst the increased strength of wall s1 may be explained by the presence of vertical precompression, the difference in stiffness is thought to be due to previous cracking undergone by wall s2 during an initial failed test attempt. In the first loading attempt, the wall underwent sliding between its base course and the floor, due to insufficient restraint along the bottom edge. This caused the wall to respond primarily in one-way horizontal bending, resulting in a vertical crack along its mid-length (photograph in Figure B.33, Appendix B.5). Following this failed test, the restraint at the bottom edge was revised to the arrangement shown by Figure 2.4,

which subsequently caused the wall to respond in two-way bending, as intended.

Both walls maintained a relatively constant load resistance for displacements ranging from 5 mm to in excess of 30 mm. The shapes of the curves are also consistent with those reported by *Lawrence* [1983] for similarly supported walls incorporating fixed vertical edges. This apparent 'ductility' is thought to be due to redistribution of internal resistance from diagonal bending along the inclined cracks to horizontal bending along the vertical edges at the return walls. Consequently, at the point where the ultimate load capacity is first reached, the horizontal bending restraint along the vertical edges has additional capacity to accept transfer of load from the diagonal bending mechanisms. This argument is supported by the crack patterns exhibited by the walls during this phase of testing (refer to Figure 2.23), showing that the diagonal cracks were fully developed but vertical cracks along the edges were only partially developed. Further support to this hypothesis is given by analytical calculations of wall strength, reported in Section 4.5, which suggest that at the point of the wall's ultimate load capacity, the full moment capacity of the vertical edge cracks is not yet reached. Due to the damage incurred by the walls, both unloaded inelastically and recovered approximately 60% of the imposed displacement.

Long Walls with Openings (s3, s4, s5, s6)

Walls s3, s4 and s5 each had translational support along their top edges, with precompression of 0.10, 0.05 and 0 MPa, respectively. From the load-displacement curves for these walls shown by Figure 2.12 and Table 2.6 it can be seen again that the walls with more vertical precompression were both stronger (5.05 kPa for wall s3, 3.91 kPa for wall s4 and 3.59 kPa for wall s5), and stiffer (45.1 kN/mm for wall s3, 35.2 kN/mm for wall s4 and 16.6 kN/mm for wall s5). By virtue of its free top edge, wall s6 had the lowest strength (1.97 kPa) and stiffness (3.85 kN/mm) of these four walls, particularly compared to wall s5 which differed from wall s6 only in that its top edge was restrained from translation.

The load-displacement curves for these walls also suggest an apparent plasticity over a range of displacements from 5 to 25 mm that is also believed to be due to the moment redistribution from moment along the diagonal cracks to the horizontal bending resistance along the vertical edge supports. The crack patterns for these walls also demonstrate that at the conclusion of this test phase, the diagonal cracks for these walls were well developed while no vertical cracks were visible at the return wall supports, except in wall s3 where they were just starting to appear (refer to Figure 2.23).

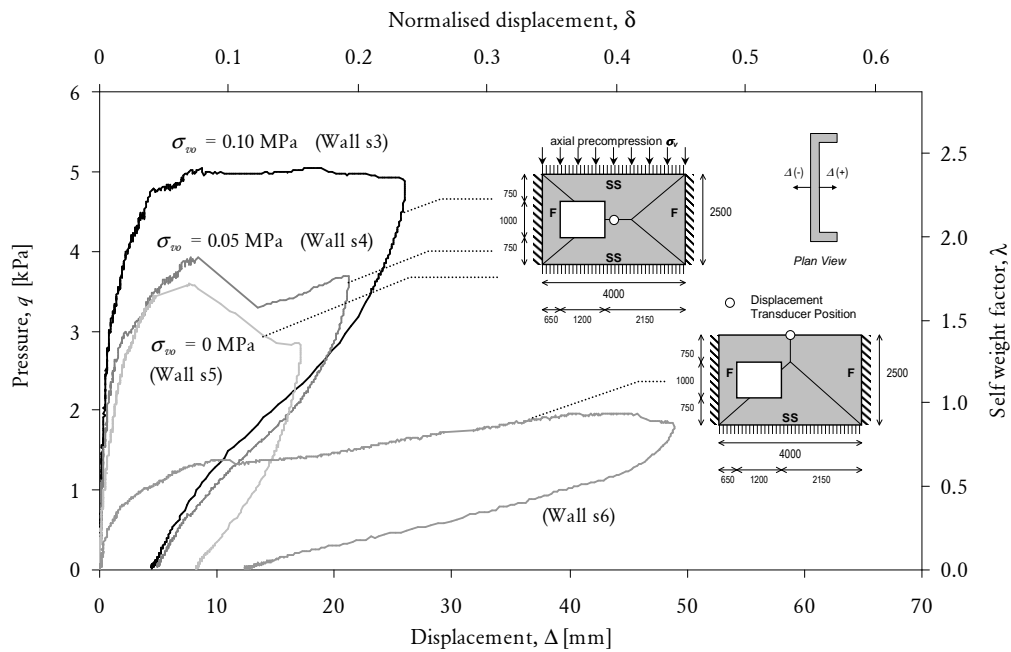


Figure 2.12: Load-displacement response for long walls with openings (s3–s6) during initial push.

Interestingly, walls s3 and s5 with openings had a greater pressure resistance capacity than the corresponding walls without openings (s1 and s2), as shown by the results in Table 2.6. This somewhat counterintuitive result is due to the fact that the space occupied by the windows was not loaded, which caused the total length of diagonal cracks contributing to the wall's overall load resistance to reduce only slightly, whilst the applied load applied reduced more significantly due to the applied pressure acting over a smaller area. Hence, this particular set of walls with openings would be expected to have a greater 'force-based' resistance toward seismic loading than the corresponding solid walls. Note, however, that this result is dependent on the size and position of the opening and should therefore not be generalised. By contrast, the same walls subjected to wind loading would generate uniform load distribution over its entire face including any openings and would therefore be expected to fail under a smaller pressure than the corresponding solid walls.

Short Walls with Openings (s7, s8)

Walls s7 and s8 were approximately square in shape with a symmetrically placed window opening, and subjected to vertical precompression loads of 0.10 and 0 MPa, respectively. Both panels, similarly to the previous panels, displayed

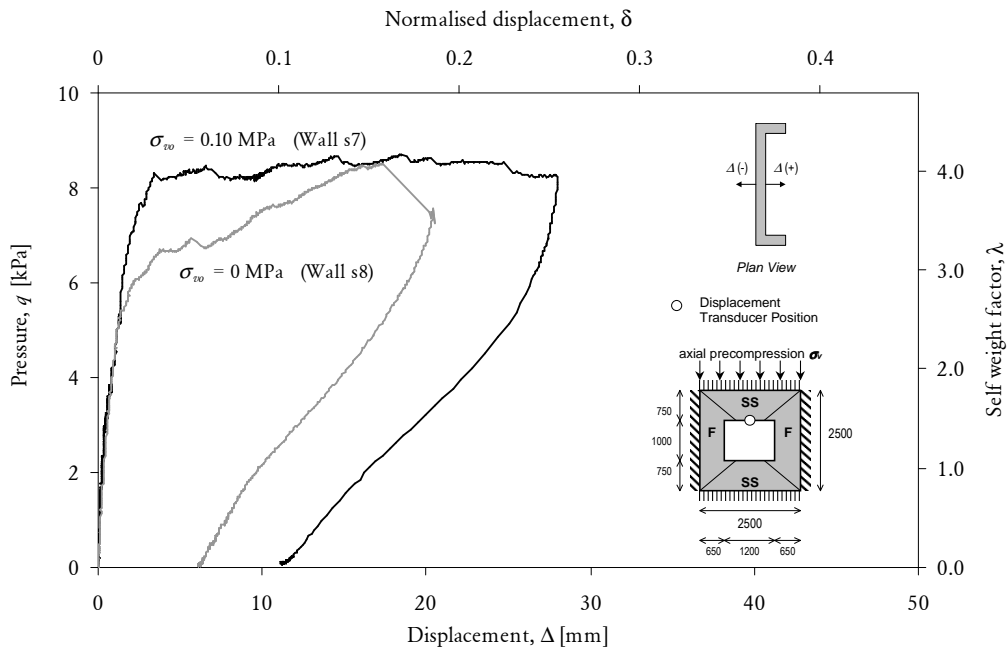


Figure 2.13: Load-displacement response for short walls with openings (s7, s8) during initial push.

a substantial amount of displacement capacity beyond their elastic range and recovered inelastically upon unloading (Figure 2.13). In contrast to the other walls tested, wall s7 had only a slight increase in strength (4.17 kPa relative to 4.08 kPa) and stiffness (28.7 kN/mm relative to 24.6 kN/mm) over wall s8.

At this stage of the test, the cracking pattern for wall s7 had fully developed diagonal crack lines and a nearly complete vertical crack mechanism in one of the return walls, whereas only diagonal cracking was visible for wall s8 (refer to Figure 2.23). This suggests that wall s7 had very nearly developed a full collapse mechanism at which point the strength would be expected to decrease rapidly.

Main Observations

The following generalisations can be made from the observed wall response during the initial push:

Both the ultimate strength and initial loading stiffness of the walls became enhanced with higher applied precompression. This is evident by comparing the F - Δ curves for walls s1 and s2 (Figure 2.11), walls s3, s4 and s5 (Figure 2.12) and walls s7 and s8 (Figure 2.13); as well as the associated F_{ult} and K_{ini} values provided in Table 2.6. The increase in ultimate strength results from increased flexural and

torsional resistance along cracks, which contribute to the internal moment capacity of the masonry.

Significantly, each of the walls demonstrated some degree of ductility in the region of the ultimate load capacity, as characterised by their ability to maintain a relatively constant load resistance with continued deformation. Such behaviour is considered desirable with respect to seismic resistance. As discussed previously, this apparent ductility is thought to have been due to gradual redistribution of internal bending moment from diagonal cracks to vertical cracks along the edges, and was therefore a consequence of the vertical edges having rotational restraint. This conclusion is also supported by the observed crack patterns at this phase of testing, in that the vertical edge cracks were only partially developed whilst the diagonal cracks were fully developed in most of the test walls (refer to Figure 2.23), and also by analytical predictions of wall strength reported in Section 4.5. It is worth noting that *Lawrence* [1983] observed similarly ductile response during tests on 15 walls that had comparable supports to the walls in the present study, including some degree of rotational restraint at the vertical edges. By comparison, *Lawrence* did not observe such strength plateaus in walls whose vertical edges were simply supported, thus indicating that the apparent ductility in the former set of walls was a result of the rotational restraint.

2.4.2 Cyclic Response

Cyclic F - Δ curves for the eight walls are plotted in Figures 2.14–2.21. Various key properties have been derived from the response, as summarised in Table 2.7. Note that all properties in the table were determined independently in the positive and negative loading directions (as denoted by superscripts + and –) and include the following: The ultimate force capacities in the two directions (F_{ult}^+ and F_{ult}^-) are given in the 3rd and 4th columns. Two alternative measures of the wall's ability to maintain its strength with increasing deformation were used, including: (i) the displacement range encompassing 80% of the ultimate strength ($\Delta_{0.8Fu}^+$ and $\Delta_{0.8Fu}^-$), as given in the 5th and 6th columns; and (ii) the residual strength and stiffness at $\delta = \pm 0.5$ (displacement equal to half the wall's thickness). The corresponding residual force capacities (F_{ht}^+ and F_{ht}^-) are provided in the 7th and 8th columns; the ratios of the respective residual strengths and the overall ultimate strength ($F_{ht}^+/F_{\text{ult}}^+$ and $F_{ht}^-/F_{\text{ult}}^-$) are in the 9th and 10th columns; and the effective secant stiffness (K_{ht}^+ and K_{ht}^-) are in the 11th and 12th columns. The 13th and 14th columns provide the equivalent viscous damping (ξ_{hyst}), calculated by the method of energy dissipated per cycle of loading. A detailed description of the methods used to derive the various properties from the data is provided in Appendix B.3, including a graphical

illustration in Figures B.16–B.23.

The main trends in the observed load-displacement behaviour will now be discussed with emphasis on their expected influence on the walls' seismic response.

Residual Strength and Displacement Capacity

The derived values of $\Delta_{0.8F_u}^+$ and $\Delta_{0.8F_u}^-$ (summarised in Table 2.7) indicate that the walls were generally able to maintain 80% of their ultimate strength up to displacements ranging between 20 to 40 mm in the positive direction and 30 to 50 mm in the negative direction. That the capacity in the negative direction appears higher is a result of the ultimate strength in that direction (F_{ult}^-) being lower than that in the positive direction (F_{ult}^+), as the walls were already cracked when they were first pushed in the negative direction. For the different walls, values of the ratios F_{ht}^+/F_{ult} and F_{ht}^-/F_{ult} provided in Table 2.7, range between 0.27 and 0.83 in the positive direction (0.54 average), and between 0.20 and 0.73 in the negative direction (0.47 average). This indicates that the walls still retained, on average, approximately half of their ultimate load carrying capacity at a deformation equal to half the wall thickness.

In Section 2.4.1, it was demonstrated that the F - Δ response in the vicinity of the ultimate strength exhibited a ductile plateau due to progressive cracking and an associated redistribution of moment from the diagonal cracks to the vertical edge cracks. However, from the cyclic tests it is evident that the walls still possessed significant residual strength and displacement capacity even after becoming fully cracked. The reasons for this are as follows:

1. Following the formation of a collapse mechanism, the walls undergo rocking block motion allowing them to reach significant displacement without collapse. It is already well established that vertically spanning walls possess a stability limit as the displacement approaches the wall thickness ($\delta = 1$) [Ewing and Kariotis, 1981; Doherty et al., 2002; Derakhshan et al., 2011, e.g.]. By contrast, two-way spanning walls are expected to possess even greater displacement capacity, due to the following points.
2. In two-way collapse mechanisms, a greater proportion of the wall undergoes rotation about the vertical axis. Mechanism sub-plates rotating about the vertical axis are not governed by stability mechanics, since the axis of rotation is parallel to the action of gravity. As a result, the overall wall becomes less destabilised by P-Delta effects, and the instability displacement increases.

Table 2.7: Summary of main results derived from cyclic tests. Properties with superscripts + and – refer to the positive and negative displacement directions.

Wall	σ_{c10} [MPa]	Ultimate Strength		Displacement range encompassing $F \geq 0.8F_{ult}$		Residual strength and effective stiffness at $\delta = 0.5$						Equivalent damping at $0.25 \leq \delta \leq 0.75$	
		F_{ult}^+ [kN]	F_{ult}^- [kN]	$\Delta_{0.8Fu}^+$ [mm]	$-\Delta_{0.8Fu}^-$ [mm]	F_{ht}^+ [kN]	F_{ht}^- [kN]	F_{ht}^+ / F_{ult}	F_{ht}^- / F_{ult}	K_{ht}^+ [kN/mm]	K_{ht}^- [kN/mm]	ξ_{hyst}^+	ξ_{hyst}^-
s1	0.1	47.0	-34.5	3.1 ~ 38.2	3.9 ~ 39.5	26.5	-24.3	0.56	0.52	0.481	0.442	0.13	0.14
s2	0	30.0	-18.4	3.8 ~ 31.3	7.3 ~ 41.5	12.3	-10.4	0.41	0.35	0.223	0.190	0.13	0.13
s3	0.1	44.2	-32.0	2.4 ~ 30.2	5.9 ~ 55.3	27.4	-25.6	0.62	0.58	0.498	0.466	0.14	0.14
s4	0.05	34.2	-29.9	3.1 ~ 38.6	8.0 ~ 48.0	21.7	-22.0	0.63	0.64	0.395	0.401	0.11	0.13
s5	0	31.4	-18.5	2.8 ~ 14.9	2.5 ~ 30.2	9.8	-7.4	0.31	0.24	0.177	0.134	0.17	0.20
s6	0	17.2	-15.1	23.8 ~ 60.1	16.4 ~ 59.9	14.2	-12.6	0.83	0.73	0.259	0.229	0.14	0.13
s7	0.1	42.2	-33.1	2.0 ~ 40.4	13.3 ~ 27.5	28.9	-21.3	0.69	0.51	0.526	0.388	0.15	0.15
s8	0	41.3	-24.7	5.3 ~ 20.5	4.5 ~ 30.2	11.0	-8.4	0.27	0.20	0.200	0.152	0.18	0.22

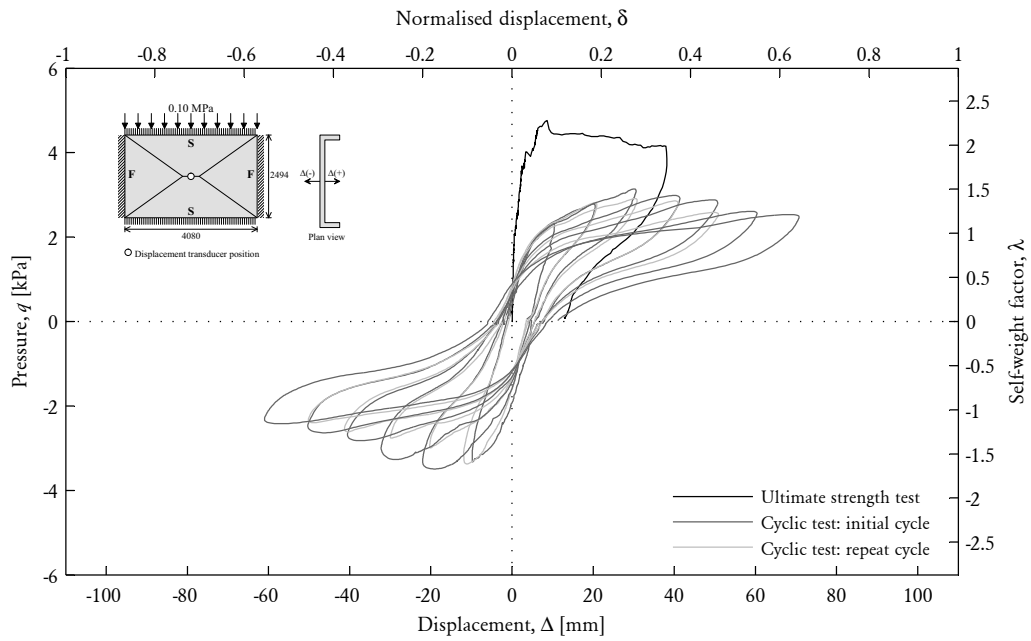


Figure 2.14: Cyclic load-displacement response for wall s1.

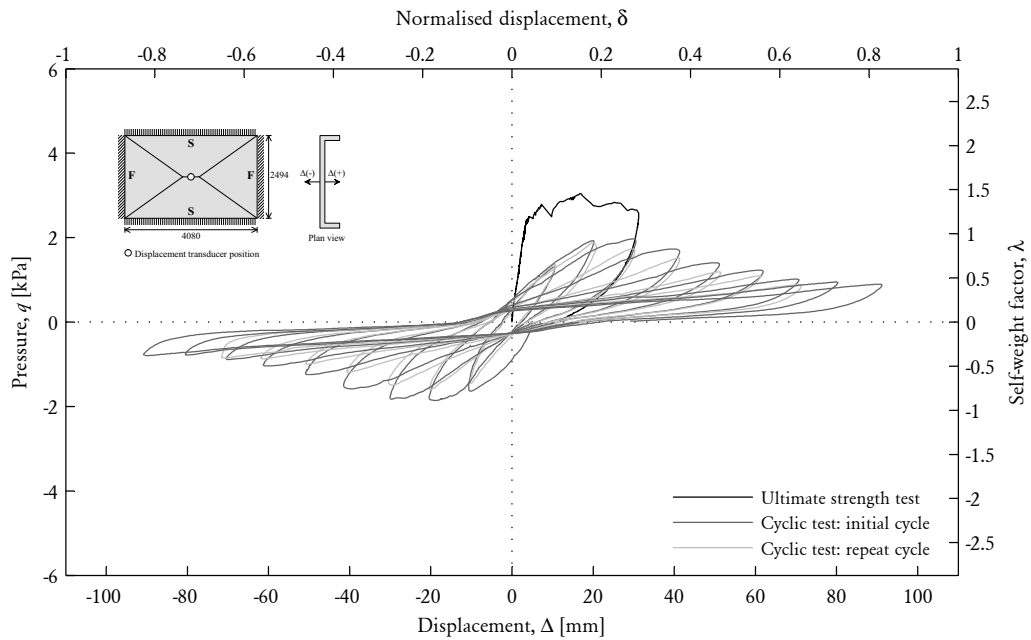


Figure 2.15: Cyclic load-displacement response for wall s2.

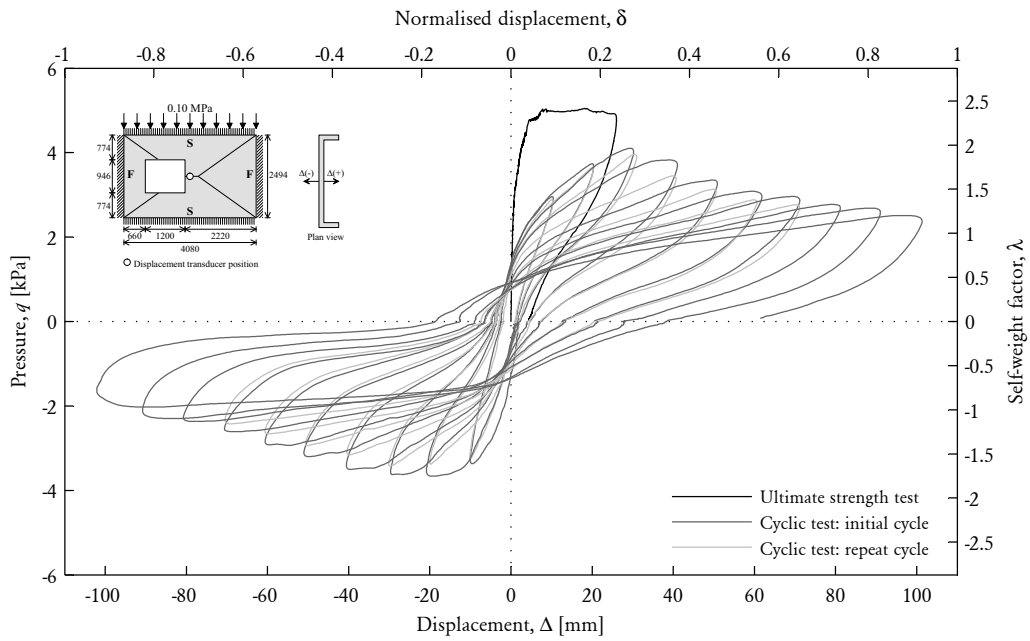


Figure 2.16: Cyclic load-displacement response for wall s3.

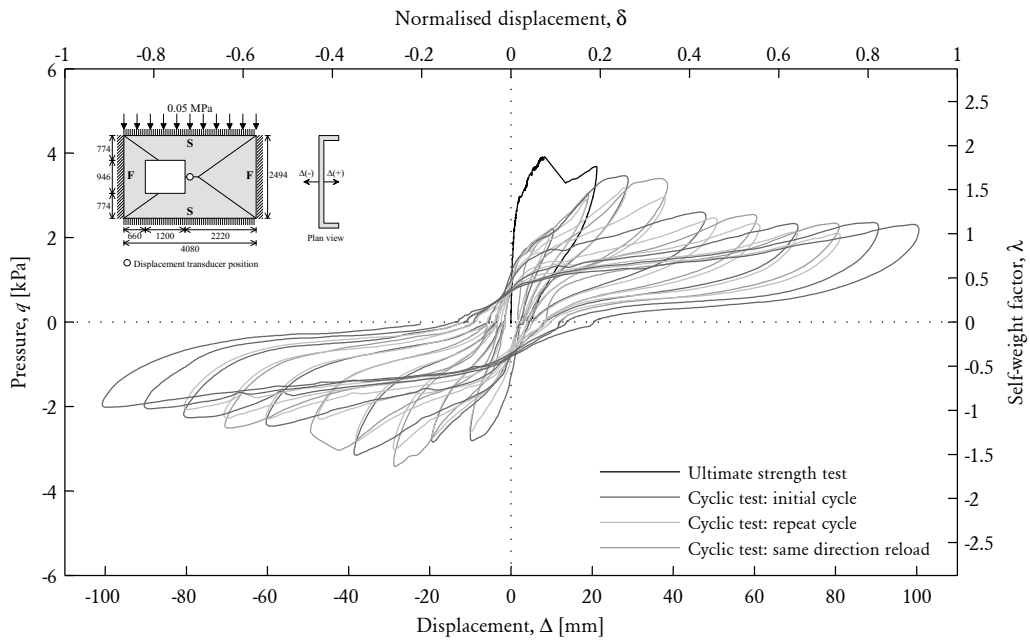


Figure 2.17: Cyclic load-displacement response for wall s4.

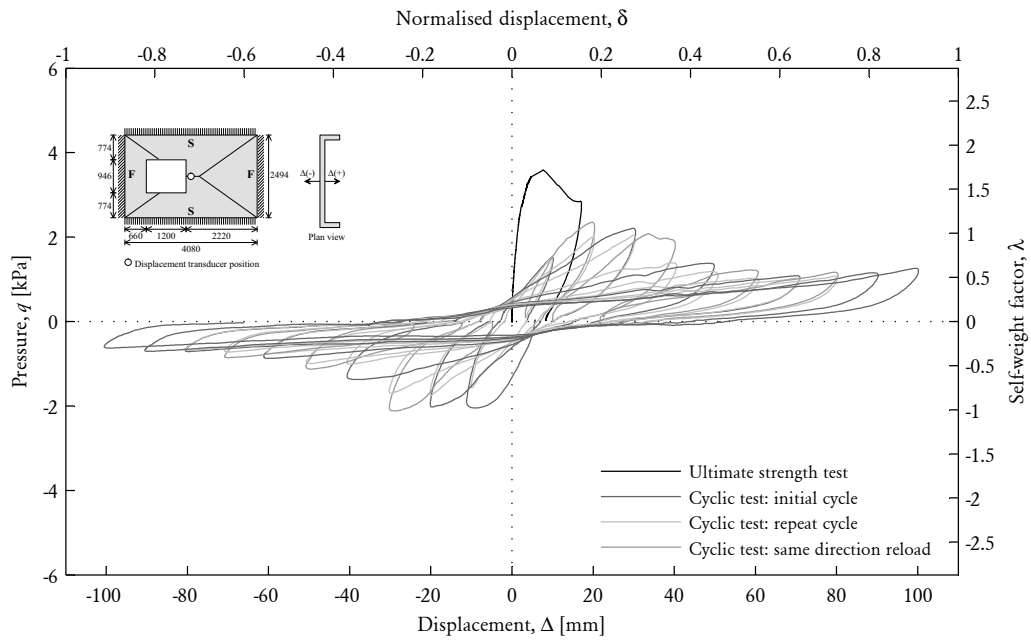


Figure 2.18: Cyclic load-displacement response for wall s5.

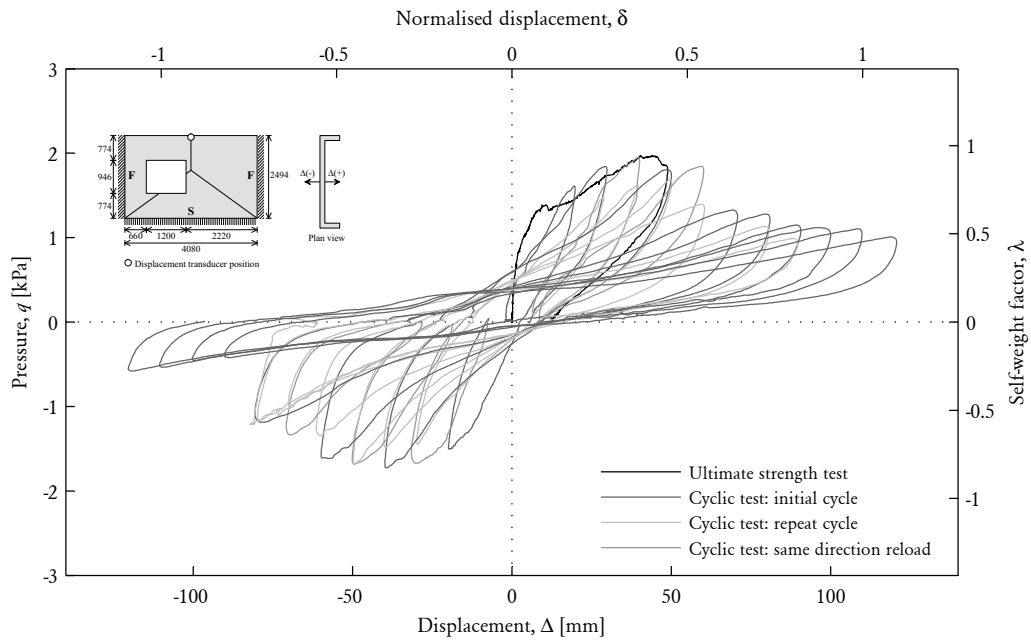


Figure 2.19: Cyclic load-displacement response for wall s6.

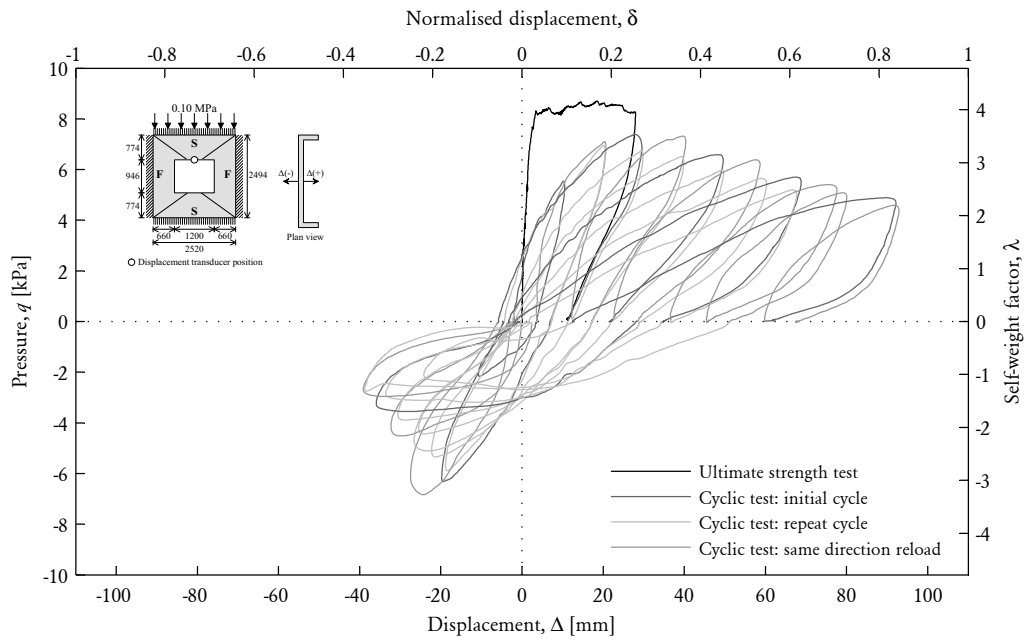


Figure 2.20: Cyclic load-displacement response for wall s7.

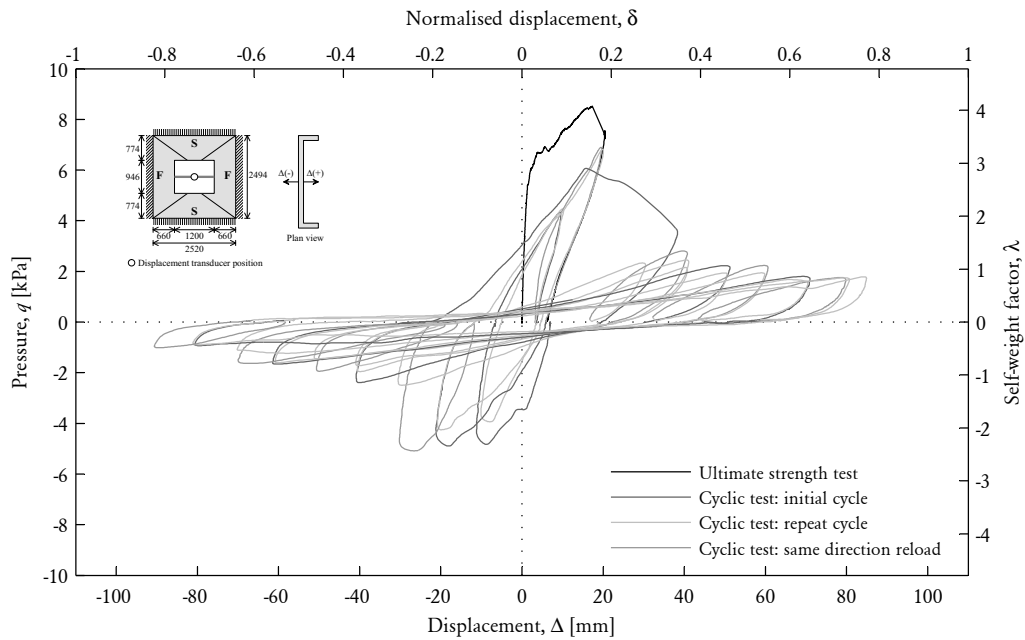


Figure 2.21: Cyclic load-displacement response for wall s8.

In fact, analytical methodology developed in Chapter 7 predicts the upper bound of the instability displacement for two-way mechanisms to be $\delta = 2$.

3. Furthermore, two-way walls obtain an additional benefit to their post-cracking strength from frictional modes of resistance along the already-formed crack lines; particularly, rotational friction along vertical cracks. Since friction is naturally ductile, it is expected that its influence can be active over a large range of the wall's displacement.
4. Another interesting feature of the F - Δ curves (Figures 2.14–2.21) is that the walls' load resistance increased with increasing displacement, as indicated by the positive stiffness of the loading branches. This trend is consistent for all panels tested and suggests that the walls underwent some degree of arching. It is likely that this included some combination of horizontal arching due to in-plane restraint provided by the vertical edge supports (Figure 2.6); as well as vertical arching caused by vertical confinement of the walls close to the return walls.

The two-way spanning walls tested in this study have been shown to exhibit substantial displacement capacity as most were subjected to displacements close to the wall thickness of 110 mm without collapse. These imposed displacements were well in excess of the displacement at which the walls reached their ultimate strength, as shown by the lower limit of $\Delta_{0.8F_u}^+$ in Table 2.7, where it is seen that most walls reached 80% of their ultimate load at a displacement between 2 and 5 mm. The walls' ability to undergo large displacements while still maintaining a reasonable amount of strength, is highly beneficial to their seismic resistance, and counter to the conventional wisdom that assumes URM components are non-ductile. Considering that traditional force-based (FB) design assumes failure to occur when the walls reach their ultimate strength, these tests have demonstrated a substantial reserve displacement capacity that is not recognised in FB design, suggesting the current seismic design provisions to be overly conservative (as discussed in Section 1.2).

Hysteretic Energy Dissipation

The 'fat' load-displacement hysteresis loops (Figures 2.14–2.21) demonstrate the cyclic behaviour of the walls to be highly inelastic, which is beneficial with regard to their seismic performance. This is in contrast to vertically spanning walls, whose response is well known to be nonlinear but elastic [e.g. Griffith *et al.*, 2004]. The reason for the additional energy dissipation capability in two-way walls is the

activation of frictional modes of internal resistance along the vertical and diagonal crack lines.

Equivalent viscous damping (ζ_{hyst}) was calculated for each half-cycle test run performed, based on the energy dissipated through hysteresis. The calculated values of damping were averaged for half-cycles whose displacement amplitude was within the range $0.25 \leq \delta \leq 0.75$ ($27.5 \text{ mm} \leq \Delta \leq 82.5 \text{ mm}$) and are summarised in Table 2.7. Average values of ζ_{hyst} for the eight walls are all between 0.11 and 0.22. Comparison of ζ_{hyst}^+ and ζ_{hyst}^- shows that there is minimal difference between the damping ratios in the two directions. Furthermore, damping values were observed to be relatively constant during the initial and repeat cycles at each amplitude of imposed displacement.

Asymmetry Effects

While it is not uncommon for structures to exhibit asymmetric cyclic response in relation to strength in the opposite loading directions, the load-displacement response of the eight test walls (Figures 2.14–2.21) was observed to be markedly asymmetric. Each wall tested was consistently weaker in the negative displacement direction; that is, when it was pushed in the direction away from the return walls (refer to Figure 2.3). This is demonstrated by the residual strength in the negative direction (F_{ht}^-) being consistently lower than in the positive direction (F_{ht}^+), by between 10–30%, and approximately 16% on average, as indicated in Table 2.7. The higher of these differences were observed for walls s1, s5 and s8.

The observed strength asymmetry is believed to be caused by the asymmetric orientation of the return walls, particularly with respect to their ability to provide a path for the transfer of lateral load from the main wall leaf to its vertical edges. As discussed later in Section 2.5.2, in certain instances, the occurrence of extensive cracking at the vertical edges was observed to reduce the amount of overlapping bed area between adjacent courses, especially when a large number of units underwent line failure (refer to Figure 2.26). This diminished the capacity of the vertical edge to transmit a lateral force by means of friction and hence reduced the ability of the return walls to provide a horizontal force reaction. Loading the interior face (away from the return walls) therefore caused the vertical cracks to open up, thus reducing the walls' strength in the negative displacement direction. Conversely, loading the exterior face closed the vertical cracks to restore some of the overlap and also caused bearing of the main wall against the return walls, thereby improving the wall's ability to transmit horizontal forces in the positive displacement direction.

Strength and Stiffness Degradation

A moderate degree of strength and stiffness degradation is evident from the F - Δ curves of all eight walls (Figures 2.14–2.21), which was symptomatic of the accumulated damage resulting from progressively increased displacements and repeated cyclic deformation. The overall degradation is likely to have resulted from numerous irreversible sources of damage, which are discussed in more detail in Section 2.5.2.

Generally, around a 10% reduction in strength was observed between the first and second cycle of loading for any given displacement amplitude, with a greater reduction for walls without precompression when expressed as a percentage of the resulting post-peak strength. However, because the walls with precompression had a higher post-peak strength, the loss in the absolute strength from cycle to cycle remained relatively constant. For example, consider walls s3, s4 and s5 and the initial and repeat cycles at a displacement amplitude Δ_{amp} of +60 mm.⁶ Wall s3 (0.10 MPa) experienced a first to second cycle strength drop of 1.8 kN (6.7%) (measured by the force amplitude F_{amp}), compared to 1.9 kN (8.5%) for wall s4 (0.05 MPa), and 1.6 kN (15.1%) for wall s5 (0 MPa). Similar trends are also evident for the two long walls without openings (s1 and s2) and the two short walls (s7 and s8).

Inspection of the load-displacement curves (Figures 2.14–2.21) indicates that the strength and stiffness degradation were also asymmetric. Comparison of the first pair of cycles between -10 and $+10$ mm shows that the load resistance was consistently higher in the negative direction. Note that this was overshadowed at larger displacements by the asymmetry in the strength capacity as discussed previously. However, this observation suggests that the initial push during the static strength test weakened the wall predominantly in the positive displacement direction. In fact, the peak of the cyclic strength envelope in the positive displacement range coincided closely with the maximum displacement excursion during the initial static test in the case of every wall tested. It is therefore necessary to treat the displacement excursion during the initial push as the first half-cycle in each panel's overall loading history.

The observed degradation asymmetry is likely to be linked to the progression of tensile crack formation during a wall's displacement history. Consider the state of the wall immediately after the initial push. During the initial ultimate strength test, in which the walls underwent positive displacement, cracks formed in the tensile fibres of the stressed regions and were unlikely to have spanned across the full wall

⁶Runs 23 and 25 for wall s3, runs 22 and 24 for wall s4, and runs 22 and 24 for wall s5, as referred to in Tables B.3, B.4 and B.5, in Appendix B.3.

thickness. Once the panel was unloaded and pushed in the negative direction (in the first half-cycle of the cyclic tests), the original cracks closed up in compression, and the opposite fibres then needed to crack in tension, thus requiring a higher load in the negative displacement direction. The next push in the positive direction would not require much additional cracking, since the tensile cracks had already formed during the static test. The strength of the wall in the positive direction during the first few half-cycles in cyclic testing was therefore not as high as in the negative direction.

From these tests it is difficult to establish the significance of this asymmetric degradation mechanism at larger displacements, because the cyclic loading histories imposed on the walls were symmetric (Figure 2.10). It is believed however, that the asymmetric effects of degradation become less significant at larger displacements, since a wall having undergone large deformation in either displacement direction is expected to exhibit extensive cracking across its thickness and thus be already weakened in both directions.

The most notable implication for the seismic response of URM walls with asymmetric strength and stiffness degradation characteristics is that walls could be particularly vulnerable to earthquake motions which contain acceleration pulses in a predominant direction. Such earthquake inputs may weaken a wall and encourage failure in a predominant direction.

Influence of Vertical Precompression

The most significant effect of vertical precompression on the behaviour of the walls was an enhancement of their load capacities. Whilst it is emphasised that the ultimate strength is dependent mainly on the flexural tensile strength of the masonry (f_{mt}), in which there was shown to be variation between the different walls tested (refer to Table 2.3), Figure 2.22 shows the influence of the vertical compressive stress, σ_v , on both their ultimate and residual strength. The plotted values of ultimate strength are the average of F_{ult}^+ and F_{ult}^- , and the plotted values of the residual strength are the average of F_{ht}^+ and F_{ht}^- , both as given in Table 2.7. The influence of the vertical stress on the ultimate strength has already been discussed in Section 2.4.1 and therefore the discussion here is limited to its effect on the residual strength.

It can be seen from the graphs in Figure 2.22 that panels with precompression significantly outperformed panels without precompression with regard to their residual strength. For example, in the long solid walls (s1, s2) there was over a two-fold increase in the residual strength (11.4 kN in wall s2 compared to 25.4 kN

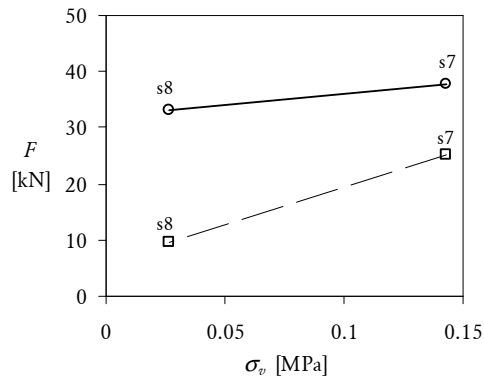
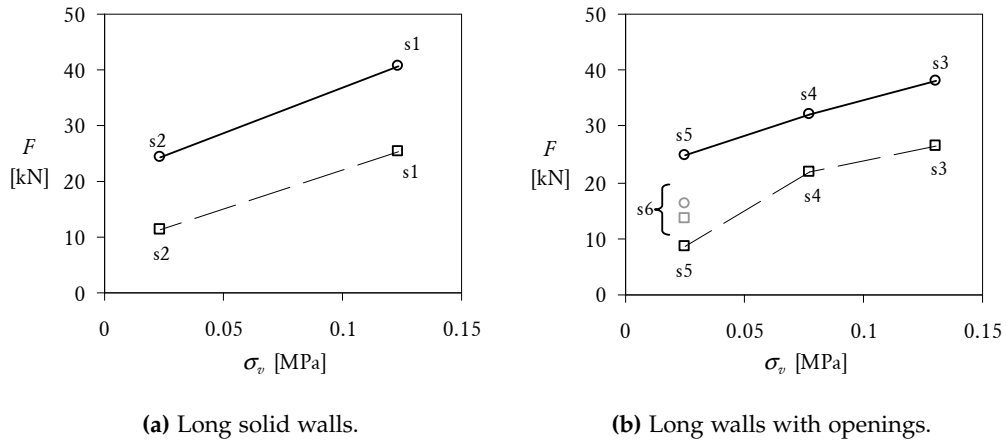


Figure 2.22: Influence of vertical precompression on wall strength. Circle markers (○) show the ultimate strength as an average of F_{ult}^+ and F_{ult}^- ; and square markers (□) show the residual strength as an average of F_{ht}^+ and F_{ht}^- . The value of σ_v is taken as the internal compressive stress at the mid-height of the wall.

in wall s1) due to an increase in precompression from zero to 0.10 MPa. There was a similar trend in the long walls containing an opening (s3, s4, s5), which had mean residual strength of 26.5, 21.9 and 8.6 kN, for precompression of 0.10, 0.05 and 0 MPa, respectively. The short walls containing an opening (s7, s8) further confirmed this trend, having mean residual strength of 25.1 and 9.7 kN, for precompression of 0.1 and 0 MPa, respectively.

The improvement in post cracking strength in panels subjected to vertical precompression is a result of an increase in the residual moment capacity along the already formed crack lines, which derive their strength from axial compression. These effects are recognised in analytical expressions for the residual moment capacities provided in Section 4.3.

2.5 OBSERVED DAMAGE AND CRACK PATTERNS

2.5.1 Initial Push

The cracking patterns exhibited by the test walls at the completion of ultimate load capacity tests are shown in Figure 2.23.

Comparisons of the observed crack pattern shapes with those assumed by the AS 3700 VW method for calculating the load capacity (see Figure 4.1), are favourable. For all walls tested, the generated patterns are synonymous with the crack patterns typically known to occur for two-way panels, characterised by diagonal cracks propagating from corners where two neighbouring supported edges intersect. Furthermore, diagonal cracks generally followed the natural diagonal slope of the masonry (i.e. one bed-joint across, one perpendicular joint up, and so on), as assumed by the VW approach. Differences between the idealised shapes and the observed ones are considered to be minor and where they did occur, the differences could be attributed to factors such as spatial variability of material properties, workmanship, and local stress concentrations.

One of the notable aspects of the crack patterns following the initial push up to the ultimate strength of the wall (Figure 2.23) is that only a limited amount of cracking was visible at the vertical edges, and where present, such cracks were only partially developed. For example, walls s1, s2, s3 and s7 exhibited a limited amount of cracking at the vertical edges whereas walls s4, s5, s6 and s8 showed no visible cracks at these edges at the conclusion of the initial push up to ultimate strength. By contrast, the diagonal cracks were relatively well developed in all panels. Furthermore, comparison of crack patterns after the initial ultimate load capacity tests (Figure 2.23) with those after the cyclic tests (Figure 2.24) shows that

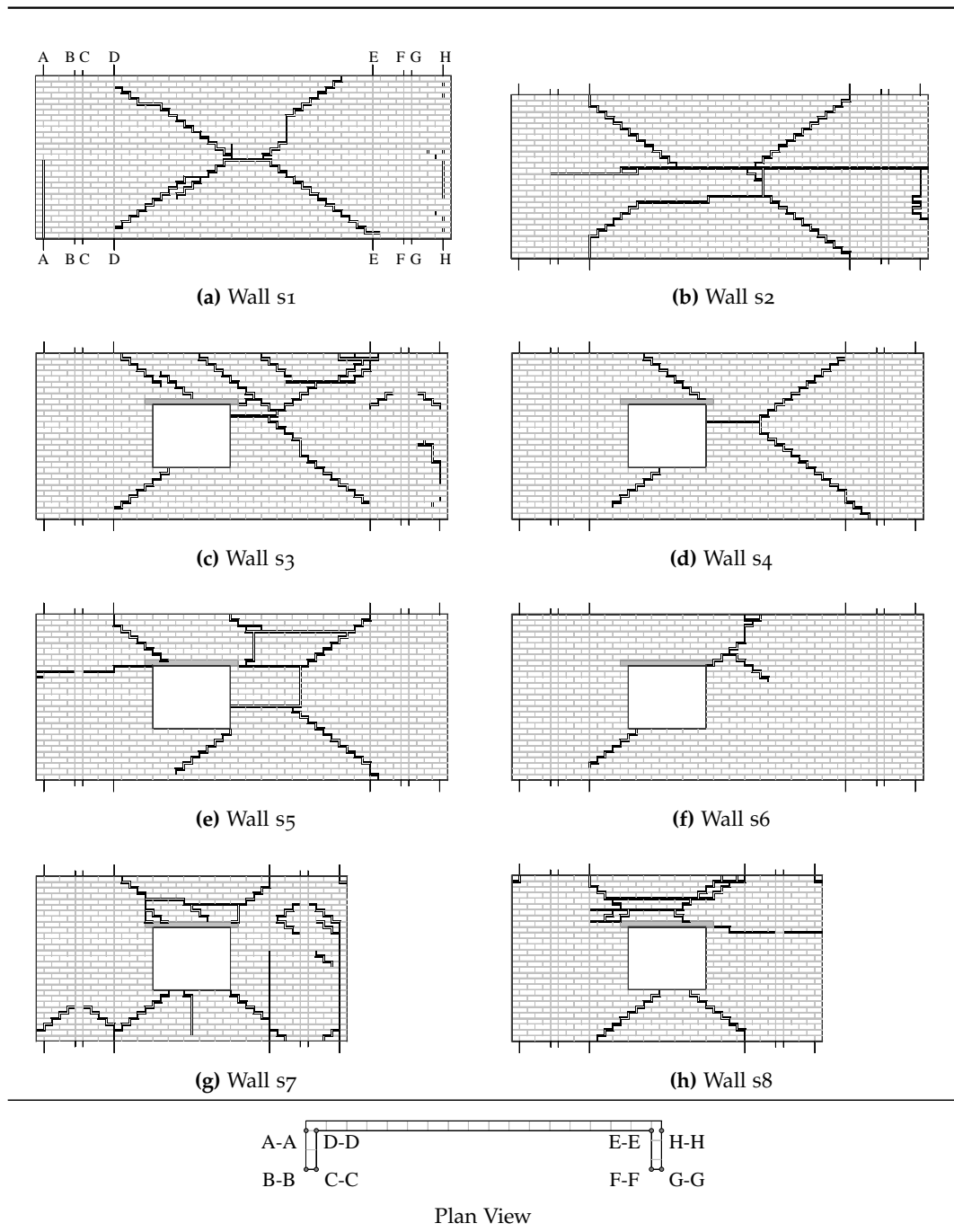


Figure 2.23: Cracking patterns at the conclusion of ultimate strength test, shown for the interior face of the wall.

the vertical edge cracks in all walls became fully developed during cyclic loading. These observations indicate that in the sequence of crack formation in two-way panels with full moment support at the vertical edges, diagonal cracks are formed prior to vertical edge cracks, and significantly, that such panels are likely to reach their ultimate load capacity prior to the vertical edge cracks reaching their full moment capacity. This finding has important implications toward the application of the *VW* method for ultimate load capacity analysis, as the method inherently assumes that the moment capacity in vertical bending and diagonal bending is reached simultaneously. This issue is further investigated in Section 4.5, whereby analytical calculations of ultimate load capacity indeed support this hypothesis.

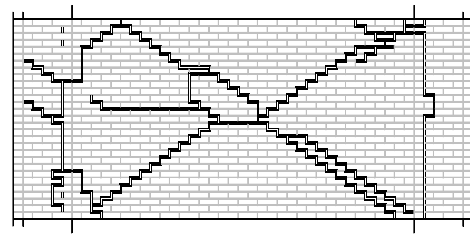
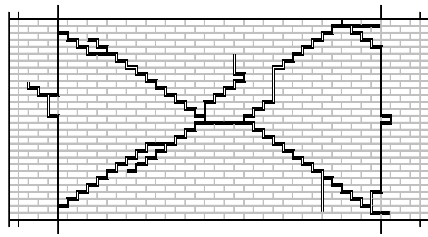
2.5.2 Cyclic Testing

After the conclusion of cyclic testing, the airbags were removed from both faces of the walls, and a visual inspection of the developed crack patterns was performed. The resulting crack patterns are illustrated in Figure 2.24, while corresponding photographs are also provided in Appendix B.5.

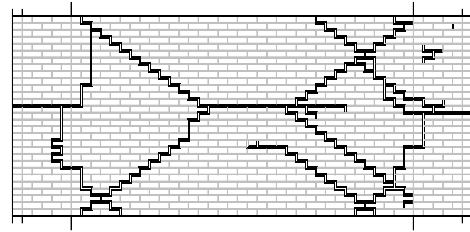
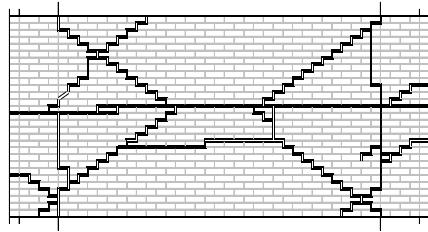
Comparisons of the crack patterns following the cyclic tests with those after the initial push (Figure 2.23) demonstrate that the walls underwent a large amount of additional damage during the rigorous cyclic loading histories to which they were subjected. Nonetheless, the overall shapes were still consistent with the idealised shapes assumed in the *VW* analysis, as already discussed in Section 2.5.1 with reference to the initial observed crack patterns.

Close inspection of the cracks present following the cyclic tests revealed various levels of damage, ranging from small hairline cracks to large cracks which exhibited severe damage and fallout of mortar. In Figure 2.24, the more severe cracks are highlighted as thick lines, whilst cracks with lesser damage are shown as thin lines. Notably, the cracks defining the typical two-way failure patterns along the walls exhibited moderate to severe damage, suggesting that they underwent large rotations.

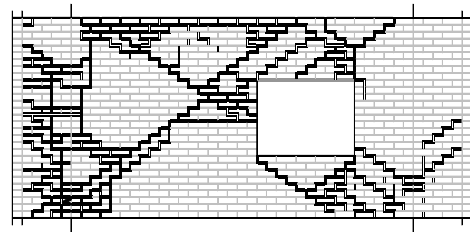
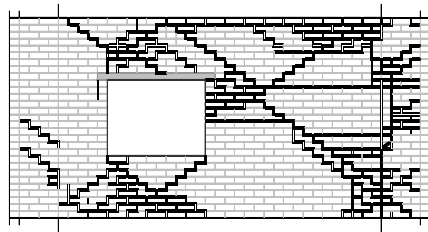
A common feature of the crack patterns at the completion of testing was that vertical cracks typically underwent line failure through brick rupture as opposed to stepped failure along the brick/mortar bond. Examples of vertical cracks exhibiting a combination of these two failure modes along the vertical edges of the walls are shown in Figure 2.25. This observation is in agreement with a developed probabilistic approach for the purpose of calculating the relative proportions of each type of failure mode, presented in Chapter 5. Predictions made by the new approach are reported in Section 5.7.2, which indeed show line failure to be the



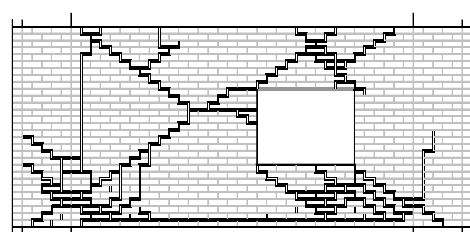
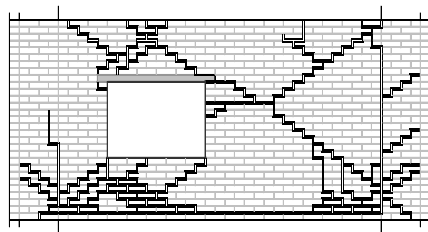
(a) Wall s1.



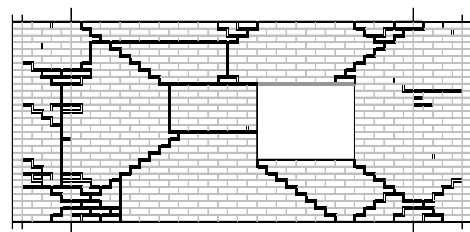
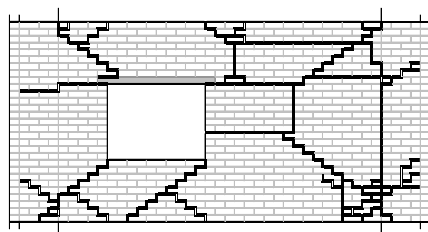
(b) Wall s2.



(c) Wall s3.

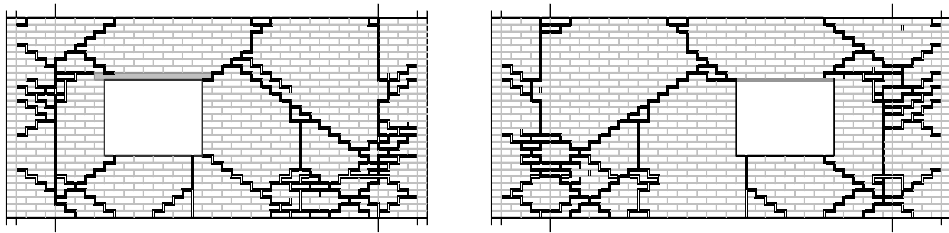


(d) Wall s4.

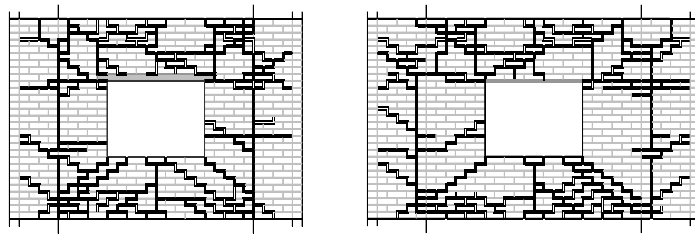


(e) Wall s5.

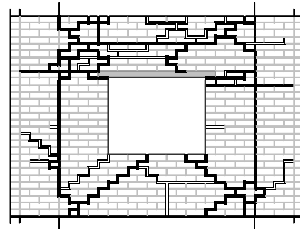
Figure 2.24: Cracking patterns at the conclusion of cyclic testing. The left diagram for each wall shows the inside face and the right diagram the outside face. The only exception is wall s8, for which only the outside face is shown, as it was deemed unsafe to remove the airbag from the outside face due to the wall's deteriorated state at the conclusion of the tests.



(f) Wall s6.



(g) Wall s7.



(h) Wall s8.

Figure 2.24: (cont'd).

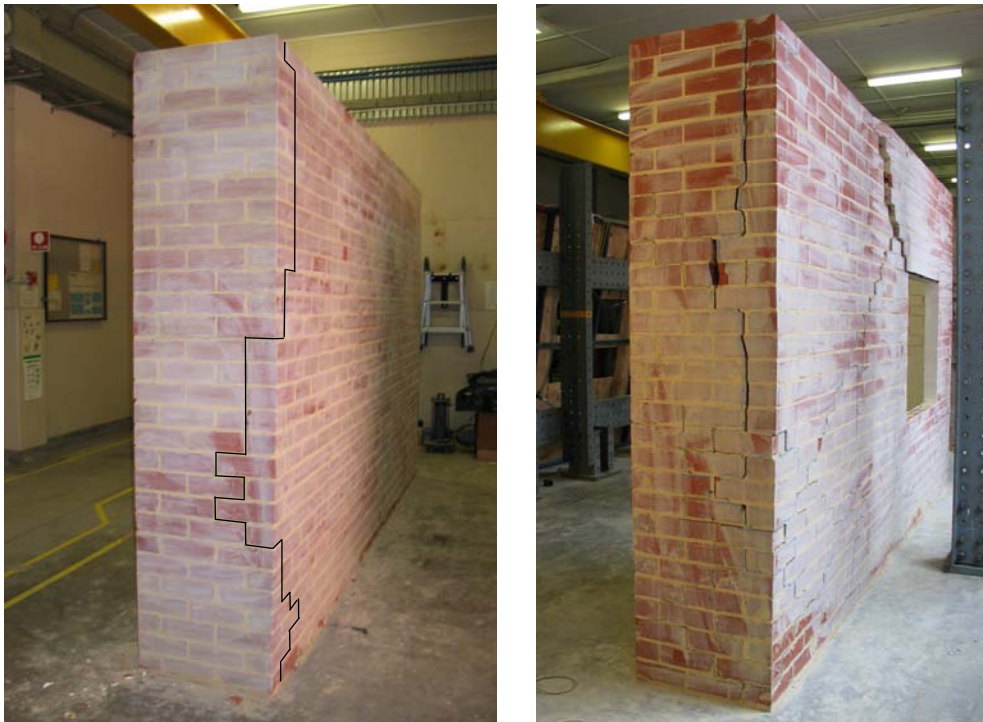


Figure 2.25: Examples of combined stepped and line failure along vertical edge cracks. Walls s2 and s6 shown.

slightly more dominant crack mode, based on the relative tensile strengths of the brick units and masonry bond that were measured through material testing. The predominance of line failure over stepped failure is detrimental to the post-cracking strength of the masonry walls, since line failure possesses zero post-cracking moment capacity; as opposed to stepped failure, which can provide significant reserve post-cracking moment capacity in horizontal bending due to rotational friction along the bed-joints (refer to Section 4.3.3).

A serious issue that may arise, which can significantly affect a wall's seismic performance, is that if an excessive amount of line failure occurs along the supported vertical edge of a wall, its ability to provide a load path for the applied face load may become diminished. In extreme cases, it is even possible for the main wall leaf to separate from the return walls, thus effectively making the wall unsupported at its vertical edges. If this occurs, the wall is likely to revert to a one-way vertical bending mode, which will reduce its strength and displacement capacity, as well diminish its energy dissipation capability due to the loss of internal friction. This type of failure was observed in some of the test walls and was most pronounced for walls s3, s7 and s8. A visual example is provided in Figure 2.26, in which wall s3 appears to approach instability at the largest imposed displacement of -110

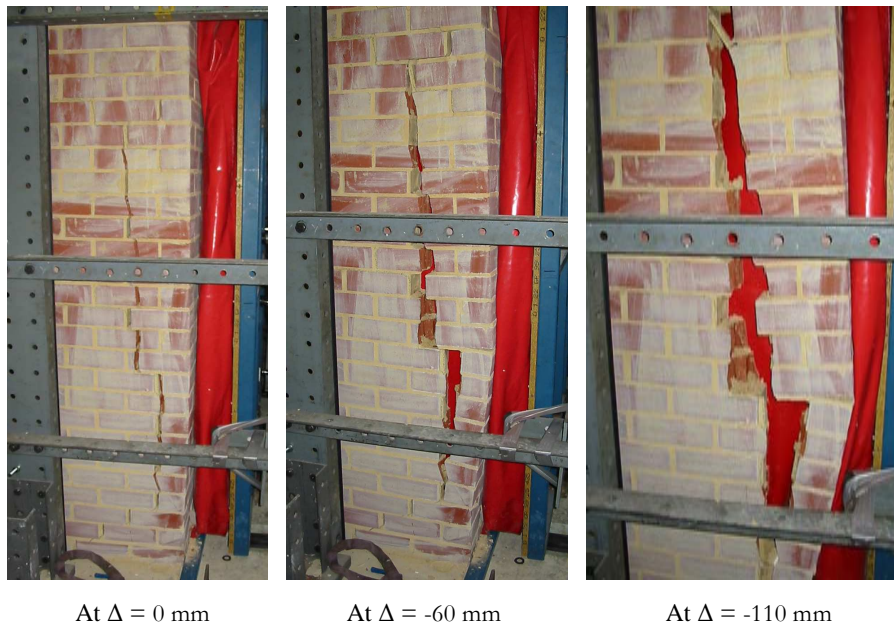


Figure 2.26: Wall approaching instability with increasing outward displacement after loss of vertical edge support due to excessive line failure. Wall s3 shown, at the far end from the window.



(a) Restoration of support at $\Delta = +70$ mm.

(b) Loss of support at $\Delta = -90$ mm.

Figure 2.27: Loss and restoration of the vertical edge support with alternating direction of loading (wall s8 shown). The support provides a bearing reaction when the wall is pushed toward the return wall as shown in (a); however, the reaction is lost when the wall is pushed away from the return wall, as shown in (b).



Figure 2.28: Examples of sliding between adjacent sub-plates within the mechanism.

mm. A second example is shown by Figure 2.27, where it is seen that when the wall was pushed inwards, the vertical edge provided a bearing reaction to transfer horizontal load from the main wall to the return wall. This caused the adjacent sub-plate in the main wall to undergo rotation about the vertical axis, consistently with two-way bending. However, when the wall was pushed outwards, support along the vertical edge effectively became lost and the wall appeared to undergo a rocking mechanism synonymous with simple vertically spanning walls.

The progressive damage accumulated by the walls during the course of the cyclic tests caused significant strength and stiffness degradation in the $F-\Delta$ behaviour (Figures 2.14–2.21). On the basis of visual observations, the following sources of irreversible damage are believed to have contributed to the overall degradation:

- Progressive tensile and shear cracking of brick/mortar joints;
- Line failure through units in horizontal bending, thus causing a reduction of internal frictional resistance due to reduced overlap;
- In certain walls, an inability of the vertical edges to provide a path for the

applied horizontal load due to excessive line failure (Figures 2.25 and 2.26);

- Crushing of bed joint mortar at large crack rotations, causing a reduction in the effective width of the bedded area; and
- Sliding between successive courses of adjacent sub-plates within the overall mechanism, thus further reducing the amount of overlapping bedded area (Figure 2.28).

It is difficult to evaluate the relative importance of each of these sources with regard to the overall degradation; however, their overall combined effects on the resulting F - Δ behaviour are discussed in Section 2.4.2.

2.6 WALL DEFORMATION PROFILES

One of the key assumptions of the **VW** method, used for predicting the ultimate load capacity of **URM** walls (refer to Chapter 4), is that at the instance that the ultimate load capacity is reached the wall's deformed shape closely resembles an idealised failure mechanism dependent on the configuration of its supported edges. The idealised displaced shapes consist of a series of rigid sub-plates bordered by crack lines along which rotations are concentrated. In Section 2.5, this assumption was shown to be reasonably accurate on the basis of visual comparison of the idealised shapes to the observed crack patterns. The accuracy of the assumption is further investigated here, by comparing the displacement profiles measured along the face of the wall with the idealised failure mechanisms employed by the **VW** method (refer to Figure 4.1). Details of the displacement transducer array layout used are given in Appendix B.1 (Figure B.4).

For the eight walls tested, displacement profiles along vertical slices at the 1/4-span, midspan and 3/4-span were determined by calculating the measured displacement at each gauge point relative to the wall boundaries. Representative plots of the deformation profiles for each class of wall tested are provided in Figures 2.29–2.32. The 'snapshots' plotted in these figures include: (i) the instance at which ultimate load capacity F_{ult} was reached, and (ii) the point at which the maximum displacement Δ_{max} was imposed on the wall during the initial push. The full set of plots for the eight walls are provided in Appendix B.4 (Figures B.24–B.31). For comparison, each graph also shows the displaced shapes according to the idealised collapse mechanisms used in the **VW** method. The observed displacement patterns will now be discussed for the different types of wall geometries tested.

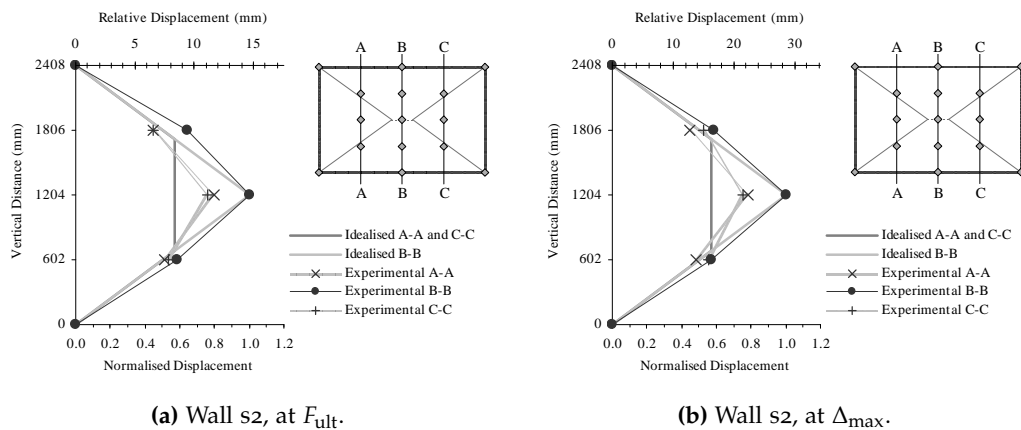


Figure 2.29: Typical displacement profiles for long solid walls (s1–s2).

2.6.1 Long Solid Walls, O-Shaped

Displacement profiles representative of the two long solid walls are shown by Figure 2.29 at (a) the point of peak load, and (b) at the point of maximum displacement applied to the wall during the static test. It can be seen that the displaced shape is quite symmetric, with the displacements at slice A–A being very comparable to the displacements at C–C. Further, the displacement profiles at A–A and C–C match reasonably well with the displacements predicted by the idealised shape. The displaced shape along central slice B–B is in very good agreement with the idealised shape, being nearly linear above and below the mid-height crack, especially at the point of maximum displacement (Figure 2.29b).

It was observed that for each of the walls tested, the measured displaced shape at the point of peak load was comparable to the shape at the point of maximum applied displacement, although the latter tended to be in slightly better agreement with the idealised failure mechanism. This is thought to be a result of the collapse mechanism being more fully developed in the latter case. Furthermore, it will be noted that the *VW* method is intrinsically concerned with predicting the peak load resistance of a wall, from which it can be reasoned that the displacement profile at the point of peak load is of primary importance. However, in most walls there was only a slight drop from the peak load to the load resisted at the point of maximum applied displacement (Figures 2.11–2.13) and hence, consideration of the displacement profile at a snapshot anywhere along this ‘strength plateau’ seems to be justified.

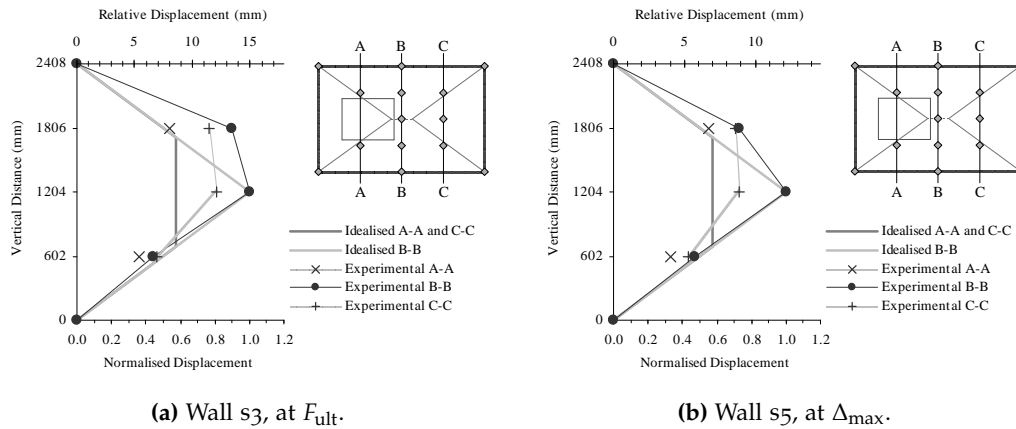


Figure 2.30: Typical displacement profiles for long walls with asymmetric opening and supported at all four edges (walls s3–s5).

2.6.2 Long Walls with Openings, O-Shaped

Typical displacement profiles for the long walls containing an asymmetric window opening and supported at all four edges (walls s3, s4 and s5) are shown by Figure 2.30. Asymmetry of the displaced shapes is clearly evident, with displacements at vertical slice C–C exceeding those at A–A for each wall in this category. This is believed to be a direct result of the stiffening effect of the lintel located at the top edge of the window opening, in addition to the relative values of stiffness of the local subpanels at each side of the opening. Because the subpanel to the left of the window opening (as seen from the inside face on Figure 2.30) has a shorter horizontal span (0.65 m) than the subpanel to the right of the window (2.15 m), it is expected to be stiffer; and therefore to undergo a smaller displacement, as indeed indicated by the plots.

In all cases, the experimentally observed displaced shapes of walls s3, s4 and s5 were fairly consistent with the shape of the idealised mechanism; the most notable difference being that the measured displacement at the 3/4-height along section B–B was consistently greater than the displacement predicted by the idealised mechanism. This discrepancy was most pronounced in wall s3 (Figure 2.30a), where the displacement at the 3/4-height was almost as large as the displacement at the mid-height. This trend suggests that the central horizontal crack formed above the expected mid-height location, as was indeed observed in the crack patterns for all three walls (Figure 2.23c, 2.23d, 2.23e). This phenomenon is believed to be a result of the reinforcing action of the lintel, which acted to inhibit propagation of the top-left diagonal crack and thus promote the formation of a central horizontal crack closer to the top of the wall. Interestingly, the **VW** method predictions reported in

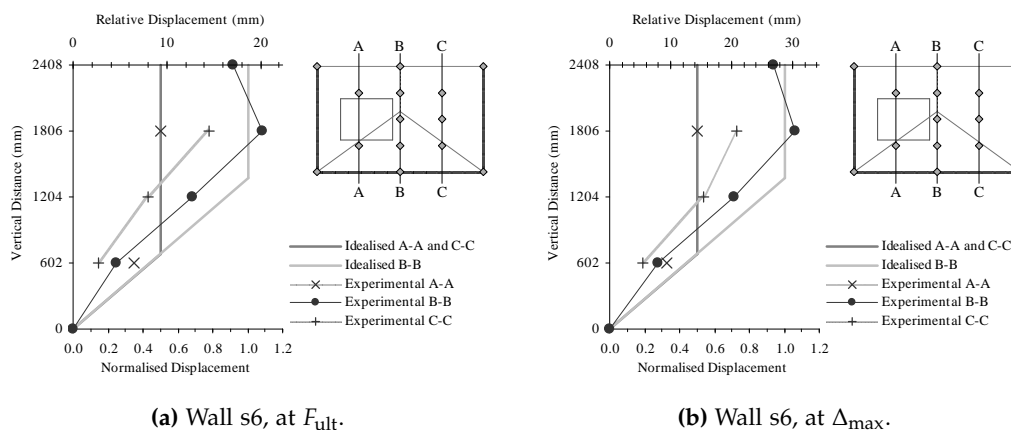


Figure 2.31: Displacement profiles for long wall with asymmetric opening and free top edge (wall s6).

Section 4.5 produce the greatest underestimation of the actual ultimate load for wall s3, in which the aforementioned effect was most pronounced. The author believes this to be a result of the deviation from the idealised collapse mechanism where the central horizontal crack is at mid-height of the wall, thus minimising the internal work term in the calculations. Because the central horizontal crack did not actually form at the mid-height, the internal work performed by the wall increased, hence increasing its load resistance.

2.6.3 Long Wall with Opening, U-Shaped

The displacement profile for the long wall with an asymmetric window opening and free on the top edge (wall s6) is shown in Figure 2.31. The displaced shapes are comparable at the point of peak load and at maximum displacement and are in good agreement with the shape predicted by the idealised collapse mechanism. While there is a discrepancy in the 'slope' of the displaced shape along slices A-A and C-C, the average displacement at these slices is fairly constant and the overall displaced shape of the wall can be considered to be symmetrical about the central vertical slice B-B. This symmetry is in contrast to the relatively asymmetric profiles observed for walls s3, s4 and s5, which had the same geometry, but were supported at the top edge, and is likely to be a result of the fact that the lintel did not intersect with any of the cracks, in neither the observed nor idealised failure mechanisms, which therefore remained unaltered by its presence.

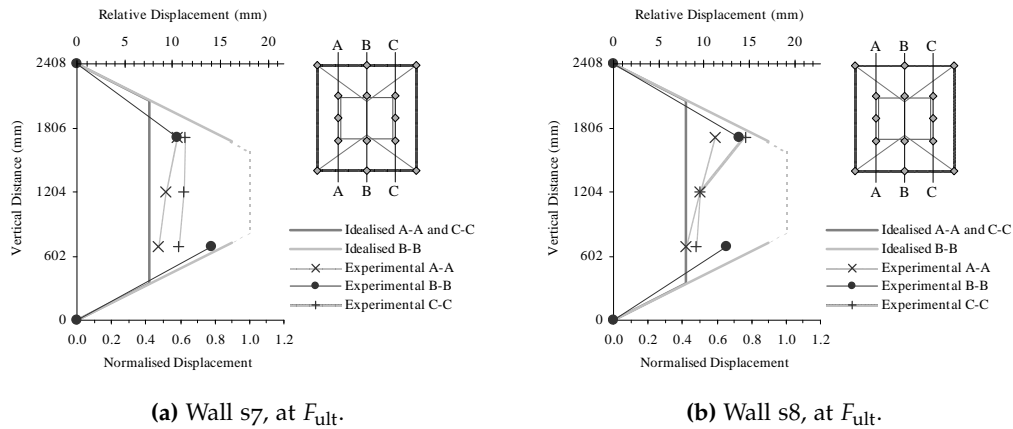


Figure 2.32: Displacement profiles for short walls with central opening (walls s7–s8).

2.6.4 Short Walls with Openings, O-Shaped

The displaced shapes of the short walls (s7 and s8) containing a centred window opening are shown in Figure 2.32. It can be seen that the observed displacement profiles suffer from the same discrepancy relative to the idealised displacement profiles, whereby in the observed shapes the displacements along slices A–A and C–C are quite similar in magnitude to the displacements at the central slice B–B, whereas in the idealised shape the displacements at B–B should be significantly greater than the displacements at A–A and C–C. This behaviour is believed to result from the stiffening effect of the lintel located at the top edge of the window, which provided a substantial amount of reinforcement in the $3/4$ -height region of the wall, but whose influence also appears to have extended to the $1/4$ -height region where the measured displacements at the three vertical slices A–A, B–B and C–C are also closely clustered.

2.7 CONCLUSIONS

The main outcome of these tests has been the demonstration that two-way spanning URM walls possess substantial post-cracking strength and displacement capacity, well beyond the displacement at which the peak strength is reached. The ability of the walls to maintain their strength at large deformations without collapsing is counter to the traditional view that URM components are non-ductile. This significant reserve displacement capacity is not taken into account in contemporary FB calculation procedures, suggesting that these methods may be overly conservative for ultimate limit state design against seismic actions, and thus warranting the development of displacement-based (DB) methodology.

Other trends identified from the walls' load-displacement response were as follows.

- The walls exhibited highly inelastic cyclic behaviour due to hysteretic energy dissipation. This behaviour results from the internal frictional resistance as a result of two-way action and is beneficial to the walls' seismic performance. Equivalent viscous damping was calculated to be within the range of 0.11–0.22.
- Loading branches after cracking were found to have a relatively constant and positive tangent stiffness, which can likely be attributed to horizontal arching within the walls.
- All specimens underwent a moderate degree of strength and stiffness degradation due to the damage accumulated from repeated cyclic deformation and increasing displacement excursions. The main forms of damage identified by visual observation included vertical line failure through units in the return walls, crushing of the bed-joint mortar, and sliding between adjacent sub-plates in the mechanism.
- The walls exhibited asymmetric strength in the positive and negative displacement directions and were consistently weaker when pushed away from the return walls. The difference between the post cracking strength in the two directions was approximately 16%, on average. This asymmetry could be a potentially significant issue with certain types of seismic excitations.
- The post-cracking strength was shown to be greatly enhanced by the presence of vertical precompression.

To verify the wall behaviour observed in the present study under true dynamic loading conditions, shaketable tests were performed on a set of five half-scale walls, as reported in the following chapter.

Chapter 3

SHAKETABLE TESTING

Abstract

To verify whether the wall behaviour observed in the quasistatic cyclic tests (Chapter 2) could be considered representative of response under true dynamic earthquake loading, a complimentary shaketable study was performed on five reduced-scale walls. These corresponded to half-scale replicas of specimens *s1–s5* from the previous study, with three walls being subjected to vertical precompression and three containing a window opening. Care was taken to ensure that the boundary conditions remained as close as possible to the original tests, in particular simple supports at the horizontal edges and fixed restraint along the vertical edges. Each wall was subjected to an extensive number of individual runs which included pulse loading, harmonic excitation and realistic earthquake motions. The tests confirmed the main behaviour trends observed in the quasistatic test study, including good post-peak strength, reasonable energy dissipation characteristics, strength and stiffness degradation, and very similar crack patterns.

3.1 INTRODUCTION

A key outcome of the quasistatic test study reported in Chapter 2 was the detailed characterisation of the load-displacement behaviour of unreinforced masonry (URM) walls subjected to two-way bending. This was enabled by the displacement-controlled nature of the loading to which the walls were subjected, accomplished using a series of airbags positioned on both sides of each wall. However, a natural limitation of that test method with regard to studying the walls' seismic response was that it could not recreate the true dynamic nature of seismic loading.

The present chapter reports a complimentary experimental study in which a set of five URM walls were subjected to dynamic loading by means of a shaketable. The test wall configurations employed were half-scale replicas of walls s1–s5 from the quasistatic tests. All walls had identical dimensions and boundary conditions, which included translational support at the top and bottom edges and full moment connections at the vertical edges. Parameters that were varied between the walls included the presence of an asymmetrically positioned window opening and the amount of vertical precompression applied at the top of the wall. Throughout the course of testing, each wall was subjected to an extensive number of individual runs comprising of pulse loading, harmonic excitation and realistic earthquake motions.

The aims of the dynamic tests were as follows:

- To establish whether the wall behaviour observed in the quasistatic tests (Chapter 2) could be considered representative of wall behaviour under true seismic loading. The main points of comparison included the walls' load-displacement behaviour as well as damage and crack patterns.
- To generate data to aid the development of a nonlinear time-history analysis (THA) for simulation of dynamic response. A finalised THA is not presented as part of this thesis; however, some preliminary work on development of such a model, including comparisons to the experimental data obtained from these tests, can be found in *Vaculik and Griffith [2008]*.
- To expand the available pool of experimental work on this topic. As outlined in Section 2.2, shaketable testing of two-way URM walls has been identified as a major gap in previous research.

It should be emphasised that these half-scale wall tests were not aimed at assessing the seismic resistance or code compliance of similar full-scale walls with respect

to any particular ‘design’ earthquake; but rather, at providing data for the development of a numerical model used to simulate the dynamic response of walls to arbitrary seismic motions. It is intended to be the role of the subsequent analytical model to generate data that can be used to make predictions regarding the seismic adequacy of particular masonry walls, and to draw recommendations regarding future code provisions for seismic assessment and design.

The outline of this chapter is as follows: Section 3.2 describes the test methodology, including material properties, wall configurations and test procedure. Section 3.3 describes the processing of the test data to derive various properties relating to the wall’s dynamic behaviour. The load-displacement behaviour of the walls is discussed in Section 3.4 and the observed damage and crack patterns in Section 3.5. The chapter concludes by summarising the key observations and lessons derived in Section 3.6. Several appendices are also provided relating to this experimental study: Tests to determine the material properties of the masonry are reported in Appendix A; data analysis methods and detailed results in Appendix C; and an investigation relating to a performance issue of the shaketable is reported in Appendix D.

3.2 TEST PROGRAMME AND METHODOLOGY

3.2.1 Materials

All brickwork used in this study, including the five test walls and small material test specimens, were constructed by qualified bricklayers under controlled laboratory conditions in order to ensure the best possible quality control (Figure 3.1). Because reduced-scale brick units were unavailable from professional manufacturers, the units used throughout this study were obtained by manually cutting solid clay pavers lengthwise to produce several half-scale units. The resulting brick units had average dimensions of $110 \times 50 \times 39$ mm ($l_u \times t_u \times h_u$). As a result of this process, all units were solid and lacked any perforations. All mortar joints within the brickwork were made to a standard thickness of 5 mm, using 1:2:9 mortar (portland cement, lime and sand). Quality control measures were undertaken during the mixing of the mortar to ensure consistency, including bucket batching of the ingredients and ensuring that the sand was air-dried prior to mixing. The ingredients were combined together in a mortar mixer and water was added to ensure a desired mortar workability based on the bricklayers’ experience.

In order to quantify values of key material properties of the brickwork, a series of material tests were conducted on small specimens constructed from the same



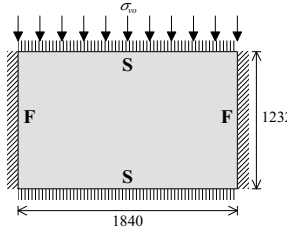
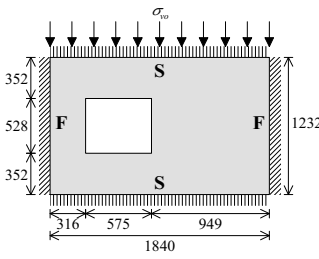
Figure 3.1: The test walls during construction.

Table 3.1: Material properties of the masonry.

Parameter	Mean	CoV
Flexural tensile strength of the masonry, f_{mt} [MPa]	0.415	0.53
Modulus of elasticity of the masonry, E_m [MPa]	9,180	0.15
Modulus of elasticity of the brick units, E_u [MPa]	32,100	0.16
Modulus of elasticity of the mortar joints, E_j [MPa]	1,410	0.20
Unconfined compressive strength of the masonry, f_{mc} [MPa]	25.9	0.09
Friction coefficient across the broken bond interface, μ_m	0.576	0.10

materials as the actual test walls. These tests were performed in accordance with the guidelines given in the Australian masonry code AS 3700 [*Standards Australia, 2001*]. The procedures and detailed results are reported in Appendix A. Mean values of the material properties as well as their coefficients of variation (CoV) are summarised in Table 3.1. In addition, the weight density γ of the masonry was experimentally measured as 21.17×10^{-6} N/mm³.

Table 3.2: Test wall configurations.

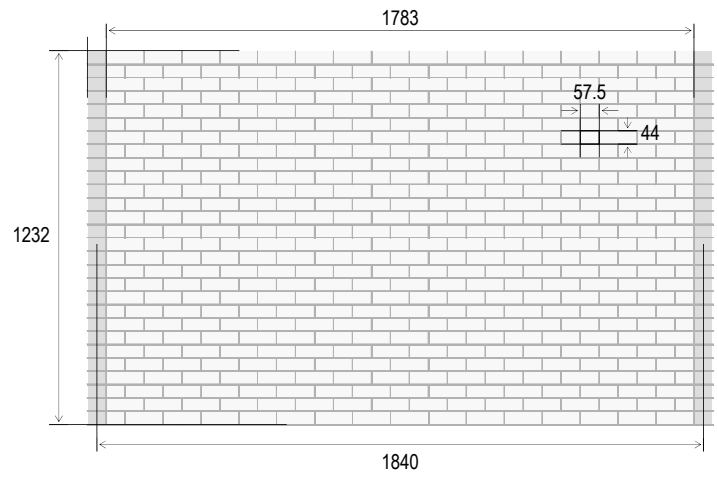
Panel dimensions [mm] and support arrangement	Wall	σ_{vo} [MPa]
	D1	0.10
	D2	0
	D3	0.10
	D4	0.05
	D5	0

Note: F = Fixed support, S = Simple support

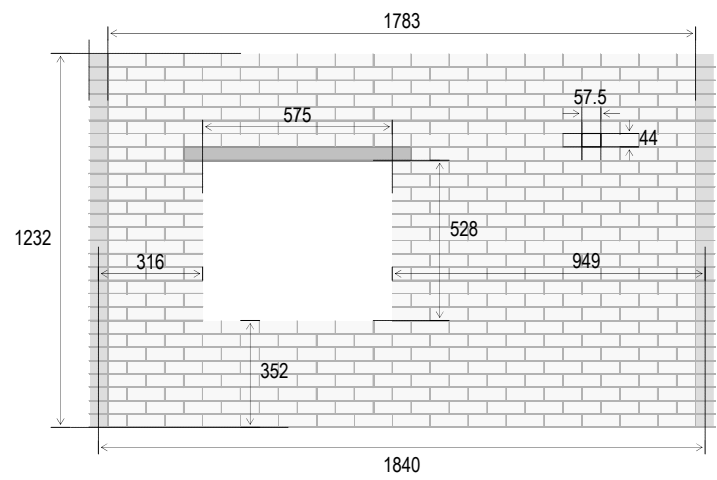
Table 3.3: Detailed wall dimensions and properties.

Walls	Wall dimensions			Opening dimensions				Area A_w [m ²]	Weight W_w [kN]
	$L_{w\ sup}$ [mm]	$L_{w\ clear}$ [mm]	H_w [mm]	x_o [mm]	y_o [mm]	L_o [mm]	H_o [mm]		
D1, D2	1840	1783	1232	–	–	0	0	2.267	2.400
D3, D4, D5	1840	1783	1232	316	352	575	528	1.963	2.079

Note: The area and weight of the wall were calculated using the wall length measured between the centres of the return walls, $L_{w\ sup}$.



(a) Walls D1 and D2.



(b) Walls D3, D4 and D5.

Figure 3.2: Detailed wall dimensions (in millimetres).

3.2.2 Panel Configurations

Configurations of the five walls tested are presented in Table 3.2, with their dimensions shown in Figure 3.2. The walls comprised two different geometries:¹

LONG SOLID WALLS (D1, D2) Serving as half-scale replicas of walls s1 and s2 in Chapter 2, these walls had dimensions of 1840×1232 mm ($L \times H$) and did not contain any openings (Figure 3.2a). They were tested under varied axial precompression of 0.10 and 0 MPa, respectively.

LONG WALLS WITH OPENINGS (D3, D4, D5) Intended as half-scale versions of walls s3, s4 and s5 in Chapter 2, these walls had dimensions of 1840×1232 mm ($L \times H$) and contained an eccentrically positioned window opening (Figure 3.2b). They were tested under varied axial precompression of 0.10, 0.05 and 0 MPa, respectively.

The wall construction method was identical to that used for the full-scale specimens in the quasistatic tests (Chapter 2). This included the use of half-overlap stretcher bond and inclusion of short return walls spanning two bricks in length (230 mm) at the vertical edges, for the purpose of stabilising the walls against overturning and providing a means for implementing rotational fixity at these edges. The walls were constructed upon reinforced concrete slabs, as shown by Figure 3.1, which enabled them to be lifted onto the shaketable using the laboratory crane. For the three walls with a window opening (walls D3, D4 and D5), the lintel consisted of a standard equal angle steel section (EA $50 \times 50 \times 3$) spanning 6 brick units (720 mm) in length.

The dimensions of the walls are summarised in Table 3.3, including the wall length $L_{w\text{sup}}$, measured between the centre-to-centre of the return walls; wall length $L_{w\text{clear}}$, taken as the clear span between the return walls; wall height H_w ; and coordinates of the window opening as x_o , y_o , L_o and H_o (horizontal offset², vertical offset³, length and height, respectively). The net face area A_w and net weight W_w of the main face of the wall are also provided in the table, which were used in subsequent calculations for converting the measured acceleration to the force resisted by the wall. Note that these values were calculated using the length of the wall between the centre-to-centre of the vertical supports, $L_{w\text{sup}}$.

¹Note that the given wall lengths refer to the length between the centre-to-centre of the return walls supporting the vertical edges. For the clear lengths between the supports, refer to Table 3.3 and Figure 3.2.

²Horizontal offset measured relative to the centre line of the return wall, as shown in Figure 3.2b.

³Vertical offset measured relative to the bottom of the wall, as shown in Figure 3.2b.

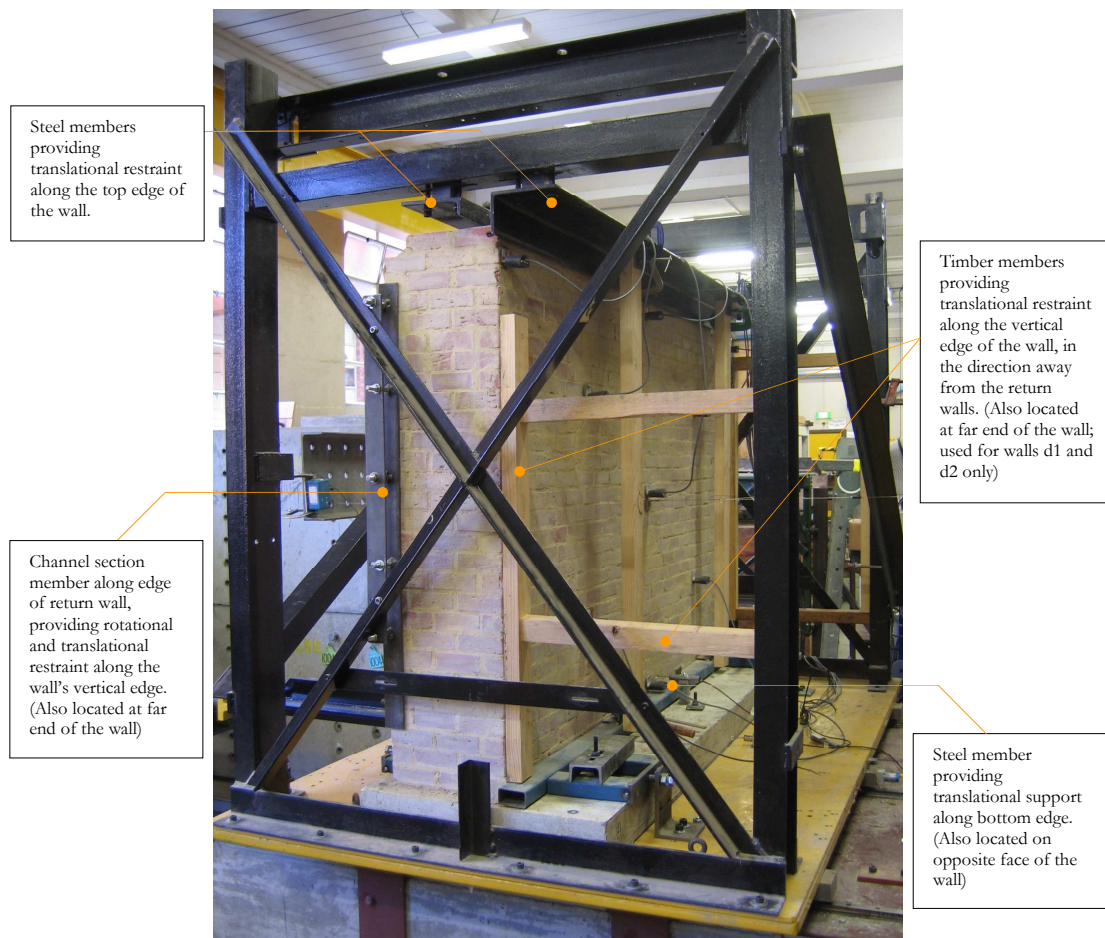
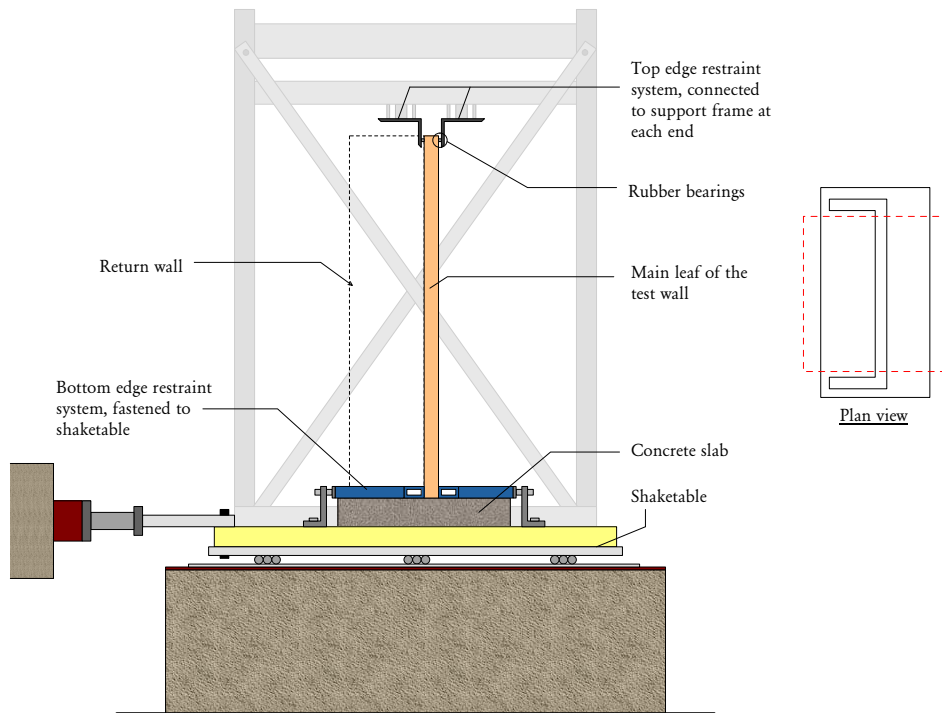


Figure 3.3: Photograph of the overall arrangement, showing various aspects of the wall restraint system. Wall D2 shown.

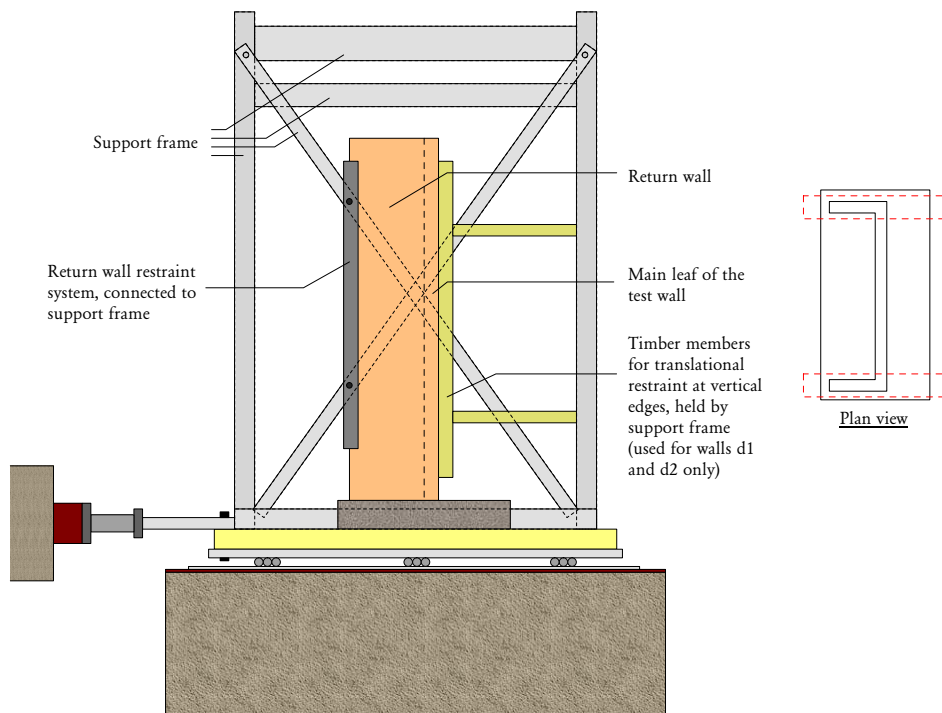
3.2.3 Wall Support Conditions

The support conditions used to restrain the edges of the test walls were intended to replicate as close as possible those used for the full-scale walls in the quasistatic tests (Section 2.3.3), which included simple translational support at the top and bottom edges, and full translational and rotational restraint at the vertical edges. The overall wall restraint system, as shown in Figures 3.3 and 3.4, utilised a stiff frame mounted on the shaketable with an in-plane stiffness similar to that expected for a masonry wall acting in-plane to the seismic excitation.⁴ The various components of the detailing used to provide the aforementioned support conditions are discussed further in this section.

⁴The support frame was originally designed to meet this criterion in previous experimental work by *Doherty* [2000], involving vertically spanning URM walls.



(a) Restraint along the top and bottom edges of the wall.



(b) Restraint along the vertical edges of the wall.

Figure 3.4: Arrangements used to restrain the wall's edges.

Bottom Edge

Despite the presence of a base mortar joint between the bottom course of the wall and the slab, additional restraint was provided along the bottom edge of the wall to ensure that sliding could not occur between the wall and the slab. This consisted of steel members located adjacent to both faces of the wall and fastened to the shaketable with steel struts, as shown in Figures 3.3 and 3.4a. This arrangement was identical to that used for the full-scale walls in the quasistatic tests, shown in Figure 2.4.

Top Edge

Translational restraint along the top edge of the wall was achieved using a pair of angled steel members, with one present on each side of the wall, as shown by Figures 3.3 and 3.4a. Rubber bearings glued onto the steel members were used to transmit the reaction force between the face of the wall along its top course and the steel members, which in turn were connected to the support frame. Whilst this arrangement was slightly different to that used in the quasistatic tests, shown by Figure 2.5, both are believed to have provided a very similar connection. The main difference between the two methods of support was the inclusion of the rubber bearing in the shaketable test walls, which were intended to soften any impacts that may have occurred during the shaking and to provide a more uniform distribution of the reaction force along the wall's top edge.

Vertical Edges

The connection arrangement used to achieve translational and rotational restraint along the vertical edges of the walls consisted of two components, illustrated in Figures 3.3 and 3.4b. The first component was a steel channel member encasing the vertical edges of the return walls. This connection was identical to that previously used for the quasistatic test walls, shown by Figure 2.6, which provided rotational restraint as well as lateral restraint when the wall was loaded toward the return walls. The second component consisted of a vertical timber member propped against the steel support frame using a pair of horizontal timber struts, in order to prevent translation in the direction away from the return walls. Note, however, that this was only used for walls D1 and D2 (the last two walls tested) after it was observed that the walls were undergoing rigid body rocking.⁵

⁵For wall D2, the arrangement was implemented for test run d2_20_H_12Hz_0.1mm and onwards.

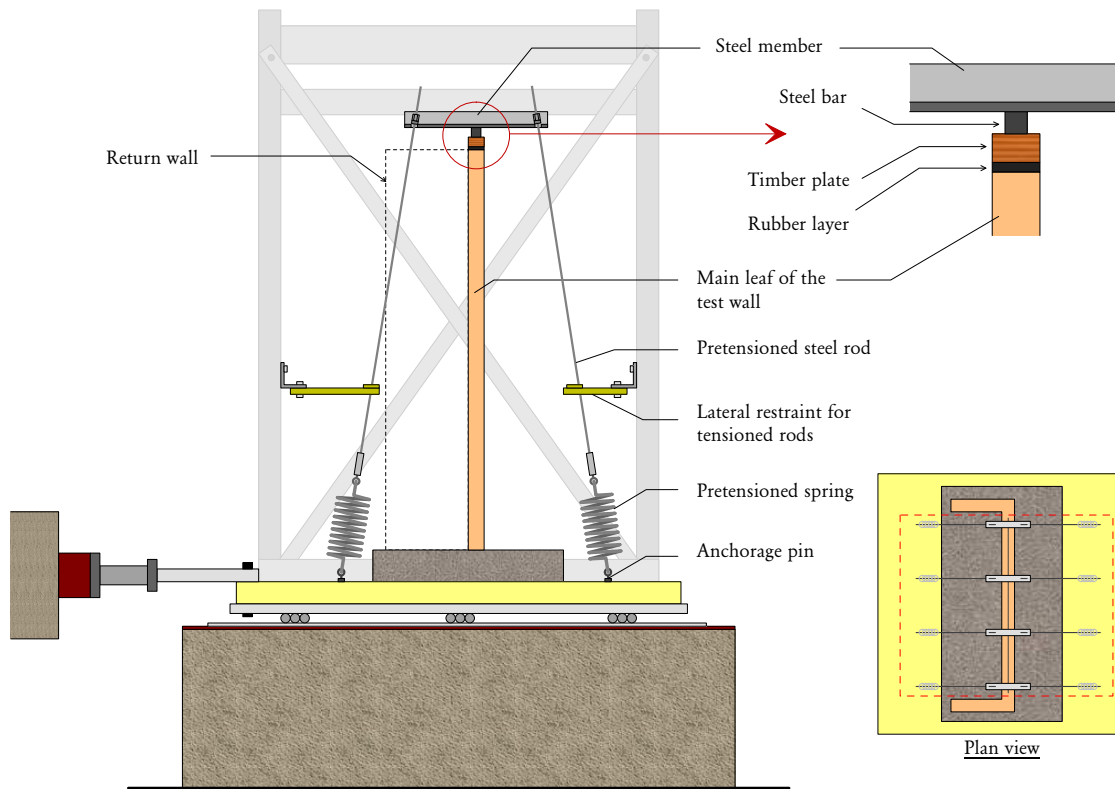


Figure 3.5: Arrangement used to impose vertical precompression.

3.2.4 Vertical Precompression

As mentioned in Section 3.2.2, walls D1, D3 and D4 were subjected to vertical precompression, in order to emulate loadbearing walls. The arrangement used to implement the precompression, shown by Figure 3.5, consisted of four pairs of pretensioned steel rods anchored onto the shaketable which applied compressive vertical reactions at the top of the wall. These loading points were equally spaced along the wall at intervals that could be considered representative of typical roof beams. The rods were tensioned using springs whose extension was manually controlled using bolts at the top ends of the rods. Each pair of pretensioned rods were connected to the opposite ends of a horizontal steel member which transferred the compressive force onto the top of the wall through a steel loading pin located along the central line of the wall's thickness. The loading pin further transmitted the force through a timber plate and a rubber layer which were intended to distribute the force more evenly within the wall. The desired compressive stress of either 0.10 MPa or 0.05 MPa was generated by adjusting the extension of the springs to a pre-calculated deflection based on previous calibration. It is also worth noting that the springs were designed to operate at large deformations, so that small changes

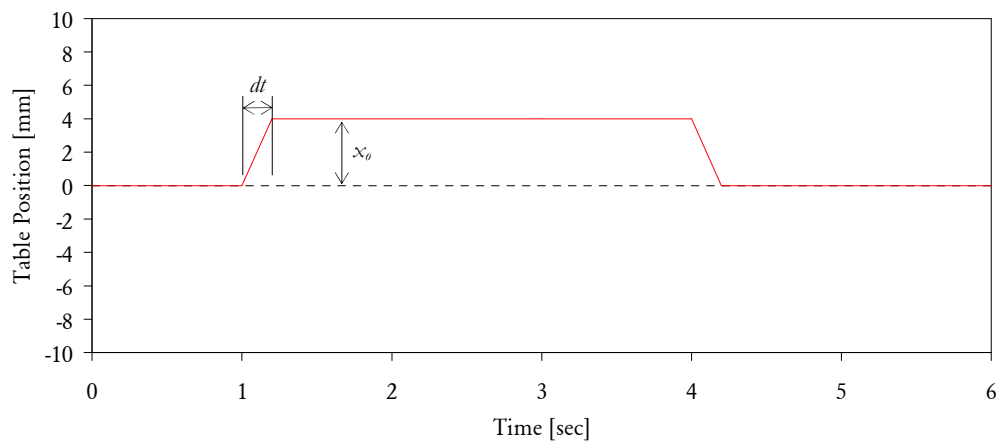


Figure 3.6: Table displacement step function used for pulse tests. Each run consisted of a pair of pulses: one forward and one backward. The function is defined by the table displacement x_0 and time interval dt over which it moves from $x = 0$ to $x = x_0$ at constant velocity.

in the height of the wall due to ‘rigid block’ rotation resulted in minimal influence on their tension.⁶

3.2.5 Test Procedure

The walls were fitted with an array of instrumentation, including accelerometers and displacement transducers, in order to acquire data for determination of their load-displacement response. Details of the instrumentation positioning along the walls are provided in Appendix C.3 (Figure C.5).

Throughout the course of testing, each wall was subjected to a large number of individual test runs comprising of three basic types of input motions:

PULSE TESTS In these tests, the table movement was defined by a simple displacement step function, as shown by Figure 3.6. The primary role of these tests was to generate an impulse for the purpose of causing the wall to undergo free vibration response. Each time these tests were performed, they were run at three different intensities: (i) 4 mm step in 0.2 sec, (ii) 4 mm step in 0.1 sec, and (iii) 8 mm step in 0.1 sec.

⁶The springs were designed such that the increase in compressive stress did not exceed 0.005 MPa (5% for the 0.10 MPa walls and 10% for the 0.05 MPa wall) in the most extreme scenario of the wall reaching a lateral displacement equal to its thickness of 50 mm. Since the wall displacements reached during the tests were considerably lower than this, it is believed that the change in compression which occurred was negligible.

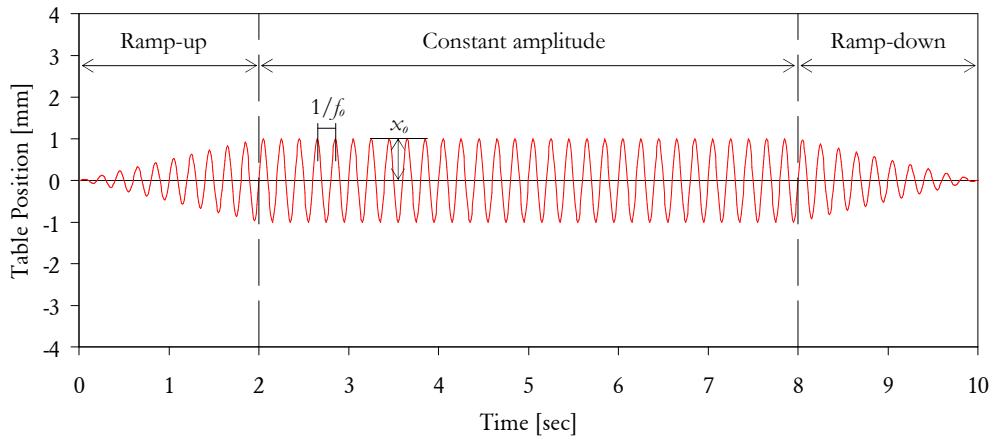


Figure 3.7: Sinusoidal table displacement function used for harmonic tests, as defined by excitation frequency f_0 and displacement amplitude x_0 .

HARMONIC TESTS These tests involved a sinusoidal input motion with a constant frequency and table displacement amplitude (Figure 3.7). Harmonic tests were used primarily for causing the wall to crack at the early stages of testing; and also at other points in testing, to generate hysteresis curves with a cyclic response due to the symmetric nature of the input motion.

EARTHQUAKE TESTS These tests involved earthquake-like motions with a broad frequency content. The main seismic motion used was the well known Kern County 1952 (Taft) earthquake, which was sped up by a factor of $\sqrt{2}$ in order to preserve frequency similitude in the reduced-scale masonry specimens in comparison to equivalent full-scale prototypes. In addition, several synthetically generated earthquake motions were also used. The time and frequency domain representations of these motions are provided in Appendix C.2 (Figures C.1–C.4). In the overall test sequence, these tests were performed in pairs—For example, an earthquake test run with a peak ground displacement (PGD) of +60 mm was always followed by a run with a PGD of –60 mm. This was done to reduce the effects of any directional offset in the walls' residual displacement that may have occurred due to the asymmetry of the motions.

Whilst the overall test sequence performed was different for each wall, the general strategy to testing each wall consisted of two stages: Firstly, the initially uncracked wall was subjected to a free vibration pulse test to determine its natural frequency. The wall was then subjected to harmonic sinusoidal input at increasing intensity until it cracked and developed a failure mechanism. Once the wall was cracked, the second phase of testing was undertaken, in which the wall

was subjected to earthquake motions at sequentially increasing intensities. Free vibration pulse tests were conducted regularly to observe any changes in the natural frequency of the wall as a result of cumulative damage. A description of the nomenclature used for naming the individual test runs, which is used throughout this chapter, is provided in Appendix C.1. The full sequence of tests performed on each wall is detailed in Appendix C.3 (Table C.6).

It should be noted that a problem was encountered during the course of testing, whereby the shaketable experienced unexpected ‘impacts’ while running earthquake input motions at higher levels of intensity. This resulted in large acceleration spikes in the table’s acceleration that were not present in the original input motion. Appendix D presents the results of a diagnostic study that was undertaken in order to identify the causes of these impacts, and to determine whether measures could be taken to prevent the impacts from occurring. The study found that the impacts resulted from a velocity limitation of the shaketable’s hydraulic actuator and that they could not be prevented from occurring with the resources available. In many instances, the acceleration spikes generated corresponded to the peak displacement and acceleration response of the wall. The test runs in which these impacts occurred are identified in Appendix C.3 (Table C.6).

3.3 DATA PROCESSING

The data acquired during the tests was processed in two stages: Firstly, the time domain vector data measured by the accelerometers and displacement transducers was used to calculate other vector data of interest, such as the wall’s load and displacement response and the motion of the supports. Secondly, the wall’s load-displacement data was used to quantify key cyclic response properties including stiffness, damping and vibrational frequency. The methods used to perform these two components of data processing are described in Sections 3.3.1 and 3.3.2, respectively.

3.3.1 Time Domain Response

Using the raw acceleration and displacement data acquired during the tests, numerous additional time domain response vectors were calculated. The variables of particular interest were those relating to: (i) the motion of the wall itself, and (ii) motion of the wall’s supports, which effectively served as the wall’s excitation. The most relevant of these variables are outlined in this section. A detailed description of these and other vector variables calculated is presented within Appendix C.3.1.

Support Motion

The motion of the wall's supports was of significant interest, as it defined the wall's excitation. The average support position was calculated as the mean of the measurements at the top and bottom supports:

$$x_{\text{sup.avg}} = \frac{x_{\text{sup.bot}} + x_{\text{sup.top}}}{2}. \quad (3.1)$$

The average support acceleration was taken as a weighted average of the accelerometer measurements along the slab (50% contribution), and the top left and right corners of the wall (25% contribution each):

$$a_{\text{sup.avg}} = 0.5 a_{\text{slab}} + 0.25 a_{\text{w.tl.corner}} + 0.25 a_{\text{w.tr.corner}}. \quad (3.2)$$

Wall Displacement

The wall's central displacement⁷ $\Delta_{\text{w.cent}}$ was calculated as the difference between the position at the centre of the wall and the average of the wall's supports:

$$\Delta_{\text{w.cent}} = x_{\text{w.cent}} - x_{\text{sup.avg}}. \quad (3.3)$$

Since the wall typically exhibited some displacement offset at the end of a test run relative to the start of the run, an alternative displacement response vector $\Delta_{\text{w.cent}0}$ was also used, which was zeroed at the start of the run.

To facilitate comparisons of displacement response between the half-scale walls in this study and the full-scale walls in Chapter 2, in the upcoming discussions the wall displacement (Δ) will generally be referred to in its normalised form, δ , defined [according to Eq. (2.2)] as

$$\delta = \frac{\Delta}{t_u}, \quad \text{rep. (2.2)}$$

where t_u is the wall thickness.

Wall Load Resistance

Load related response variables, including the force and pressure of the wall were determined from the measured accelerations. Two acceleration response vectors were of particular interest: (i) the central wall acceleration $a_{\text{w.cent}}$, which

⁷Unless otherwise stated, throughout this chapter, 'wall displacement' refers to the displacement at the centre of the wall.

was directly measured during testing, and (ii) the average wall acceleration $a_{w,avg}$, calculated as the weighted average of the various accelerometers along the face of the wall.

The significance of the wall's central acceleration is that it was believed to have provided a more accurate representation of the wall's flexural mode of vibration in comparison to the wall's average acceleration, with the latter appearing to have captured some contribution from higher vibrational modes such as twisting of the wall specimens. This opinion is based on visual inspection of hysteresis curves plotted using both methods (presented in Appendix C.6 for each test run), which indicate a much 'cleaner' relationship between $a_{w,cent}$ and δ , as opposed to $a_{w,avg}$ and δ . Additionally, Fourier spectra of the respective acceleration vectors exhibited a higher frequency content in the average acceleration, suggesting interference from these higher modes. On this basis, hysteresis curves based on $a_{w,cent}$ were deemed to provide a more reliable representation of the true loop shape for the flexural mode of vibration, and were therefore used in the computation of the equivalent viscous damping ζ_{hyst} (reported in Section 3.3.2). By contrast, $a_{w,avg}$ was believed to be more accurate in terms of the size of the force resisted by the wall, as the peak accelerations determined from $a_{w,cent}$ were typically much larger than those from $a_{w,avg}$, by approximately a factor of two. Consequently, the wall's force and pressure resistance was calculated using the average acceleration.

Based on the equation of motion, if velocity-proportional damping forces are assumed to be negligible, then the force and pressure resisted by the wall become directly proportional to the wall's average acceleration. Using this assumption, the wall's pressure resistance was calculated as

$$q_w = -\frac{\gamma t_u}{g} a_{w,avg}, \quad (3.4)$$

where γ is the weight density of the wall, t_u is the wall's thickness and g is gravitational acceleration. The wall's force resistance was taken as

$$F_w = -M_w a_{w,avg}, \quad (3.5)$$

where M_w is the mass of the wall⁸, calculated from the wall's net area A_w , such that

$$M_w = \frac{\gamma t_u A_w}{g}. \quad (3.6)$$

Because of the proportionality between the wall's acceleration, force and pressure,

⁸Note that the mass of the lintel used in walls D3, D4 and D5 composed less than 1% of the mass of the wall and was therefore omitted from this calculation.

as defined by the above equations, these response variables can be used somewhat interchangeably when considering the wall's load resistance. Throughout this chapter, hysteresis curves are generally presented in the non-dimensional a versus δ format⁹ in order to make them directly comparable to the corresponding graphs presented in Chapter 2.

3.3.2 Cyclic Properties

After the load and displacement data was calculated in the time domain as outlined in Section 3.3.1, an advanced analysis procedure was performed to derive values of several properties related to the wall's cyclic response. This procedure was performed on the data from each test run and consisted of three steps:

1. A cycle detection algorithm was implemented to find and isolate individual cycles of the wall's response in the time domain. Details of this procedure are provided in Appendix C.4.1.
2. The cyclic response properties of interest (described below) were calculated for each valid cycle found.¹⁰
3. Average values of the cyclic properties were calculated for specific ranges of displacement response, including at small displacements and near the maximum response occurring within the test run. The load and displacement amplitudes for the largest response cycles were also determined for the purpose of generating envelope curves for each wall.

The following properties were determined from each loop (cycle), as illustrated by Figure 3.8:

DISPLACEMENT AMPLITUDE Since the displacement response for the cycle was not necessarily symmetric about zero displacement ($\Delta = 0$), its amplitude Δ_{amp} was taken as

$$\Delta_{\text{amp}} = \frac{\Delta_{\text{max}} - \Delta_{\text{min}}}{2}, \quad (3.7)$$

where Δ_{max} and Δ_{min} are the maximum and minimum displacements occurring in a cycle.

⁹In this chapter, acceleration is generally quantified in units of g 's, thus making it analogous to the non-dimensional force λ defined by Eq. (2.3), since $\lambda = a/g$.

¹⁰For a cycle to be classified as valid, satisfaction of certain criteria was required, including: (i) sufficient centring around zero displacement, and (ii) being sufficiently 'closed'. This is discussed in greater detail in Appendix C.4.1.

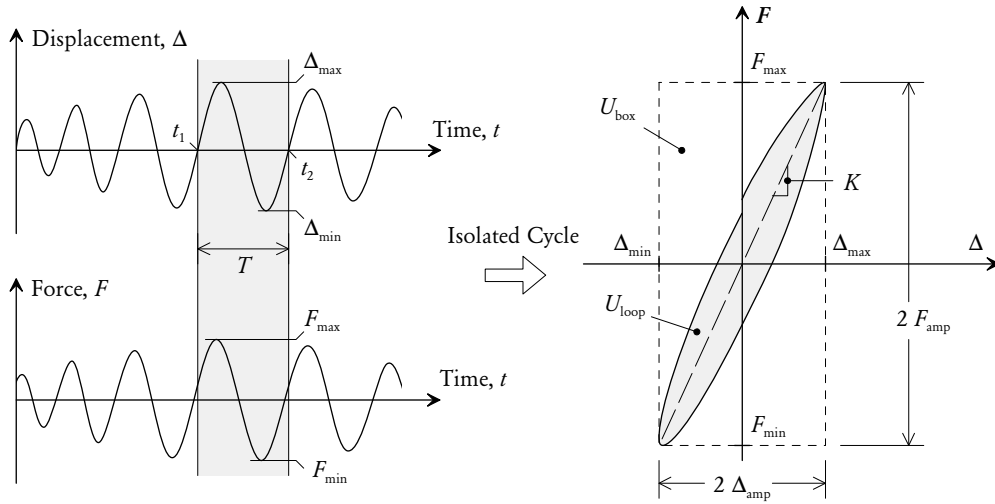


Figure 3.8: Isolated hysteresis loop and the properties derived.

FORCE AND ACCELERATION AMPLITUDE Due to the direct proportionality between the wall's restoring force F_w and average acceleration $a_{w,avg}$ [as per Eq. (3.5)], these two variables were used interchangeably when calculating other cyclic properties such as equivalent damping and frequency. The cycle acceleration amplitude a_{amp} was taken as

$$a_{amp} = \frac{a_{max} - a_{min}}{2}, \quad (3.8)$$

where a_{max} and a_{min} are the maximum and minimum accelerations occurring in the cycle. Similarly, for force:

$$F_{amp} = \frac{F_{max} - F_{min}}{2}. \quad (3.9)$$

EFFECTIVE STIFFNESS The effective secant stiffness of the cycle, K , defined as the slope of the cycle's force-displacement curve, was obtained as the slope of a straight line passing through the corner points of the loop's bounding box, as shown in Figure 3.8. This is equivalent to

$$K = \frac{F_{amp}}{\Delta_{amp}}. \quad (3.10)$$

EQUIVALENT VISCOUS DAMPING The equivalent viscous damping ζ_{hyst} was calculated using the area-based approach, according to the expression

$$\zeta_{hyst} = \frac{2}{\pi} \frac{U_{loop}}{U_{box}}, \quad (3.11)$$

where U_{loop} is the energy dissipated during the cycle and corresponds to the area enclosed within the hysteresis loop; and U_{box} is the area inside the loop's bounding box, which is proportional to the internal strain energy of the equivalent linear system (both quantities shown by Figure 3.8). It is emphasised that the energies U_{loop} and U_{box} were calculated based on the wall's central acceleration ($a_{\text{w.cent}}$) and not the average acceleration ($a_{\text{w.avg}}$), since $a_{\text{w.cent}}$ was believed to provide a more reliable representation of the fundamental mode of vibration corresponding to out-of-plane flexure, as previously discussed in Section 3.3.1.

PERIOD AND FREQUENCY The approach used to determine the cycle's period T depended on whether the cycle was classified as closed or open (as described in Appendix C.4.1). For closed cycles, the period was taken as the duration between its start and end boundaries as determined from the cycle isolation algorithm. For open cycles, the period was taken as twice the duration between its peak and trough vertices. The corresponding frequency was calculated as $f = 1/T$.

For each test run performed, average values of the aforementioned cyclic properties were calculated for specific ranges of the displacement response, including:

- *Short displacement range*, incorporating cycles having a displacement amplitude within the range $0.5 \text{ mm} \leq \Delta_{\text{amp}} \leq 3 \text{ mm}$. This was intended to capture the response along the initial loading branch of the load-displacement curve.
- *Peak response range*, incorporating cycles with a displacement amplitude between 70% and 100% of the maximum displacement amplitude occurring during the test run.

Further details are provided in Appendix C.4, including a description of the cycle detection algorithm, methods used to calculate the cyclic response properties, graphical examples of analysis output and summary of results for each test run. It is noted that prior to the analysis being conducted, the data used was digitally filtered in the frequency domain in order to improve functionality of the cycle detection algorithm. Test data from pulse and earthquake tests was filtered using a lowpass filter with the cutoff frequency generally set between 30 and 50 Hz, depending on the cleanliness of the original data. Data from harmonic tests was filtered using a comb filter which passed the spectral content at the first three harmonics of the excitation frequency. Further details of the filtering methods used are presented in Appendix C.5. The various cyclic properties as determined from the analysis are presented graphically in Figures 3.9–3.13 for each wall. Detailed results for individual test runs are provided in Appendix C.4 (Table C.7).

Table 3.4: Legend for Figures 3.9, 3.10, 3.11, 3.12 and 3.13.

Background colour	Meaning (Type of test)
■	Pulse test
■	Harmonic test
■	Earthquake test

Data series style	Meaning
—●—	Maximum measured value of the respective properties.
○	Mean result from cyclic response analysis, calculated in the large response range (70–100% of max response).
+	Mean result from cyclic response analysis, calculated in the small response range (0.5–3.0 mm).
-----	Represents the secant stiffness calculated as max force excursion divided by max displacement excursion.

3.4 LOAD-DISPLACEMENT BEHAVIOUR

This section presents results related to the walls' measured load-displacement response. Figures 3.9–3.13 provide a sequential plot of properties determined from each test run (using the procedures described in Section 3.3), including the load (or acceleration), displacement, effective stiffness, equivalent viscous damping and frequency.

3.4.1 Graphical Examples

Typical visual examples of the measured load-displacement response, as well as the corresponding response in the time and frequency domains, are shown by Figures 3.14, 3.15 and 3.16 for a pulse test, harmonic test and earthquake test, respectively. Plots of the load-displacement response for all individual test runs performed during the course of this test study are provided in Appendix C.6. It may be seen that the response observed through the shaketable tests is not as 'smooth' as that observed under quasistatic cyclic loading (Figures 2.14–2.21); however, this is known to be a typical aspect of dynamic testing.

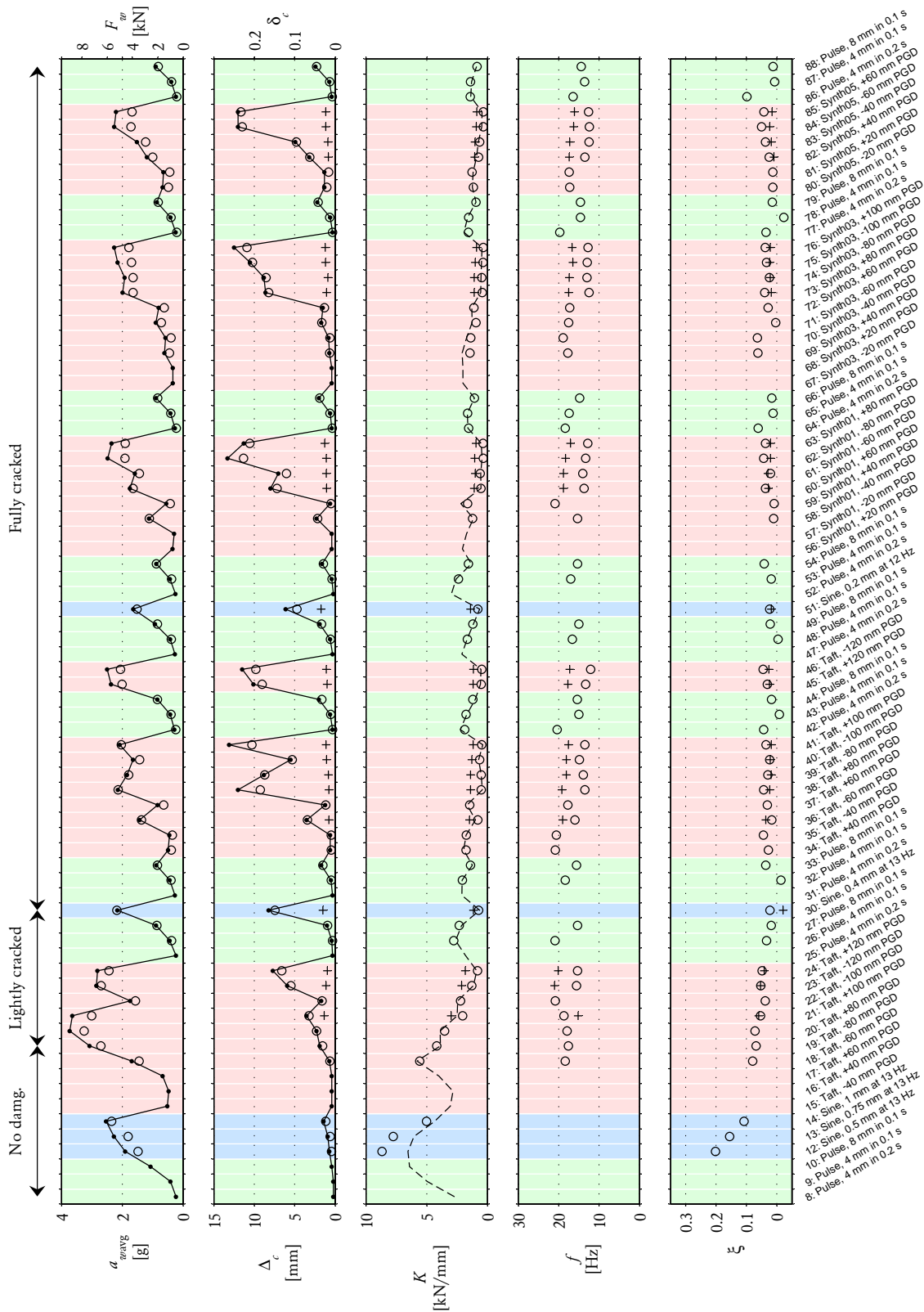


Figure 3.9: Test sequence and key results for wall D1. Legend in Table 3.4.

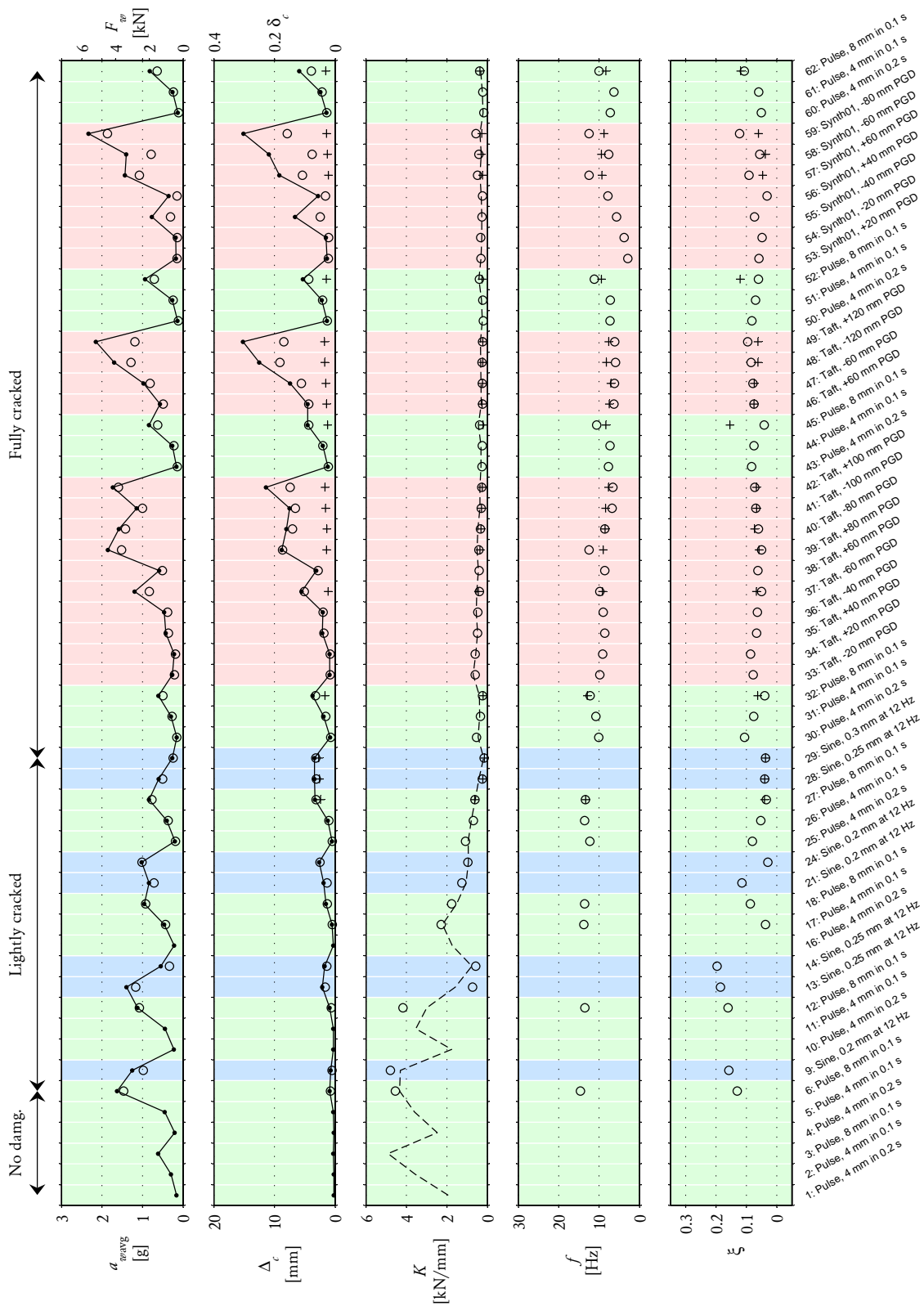


Figure 3.10: Test sequence and key results for wall D2. Legend in Table 3.4.

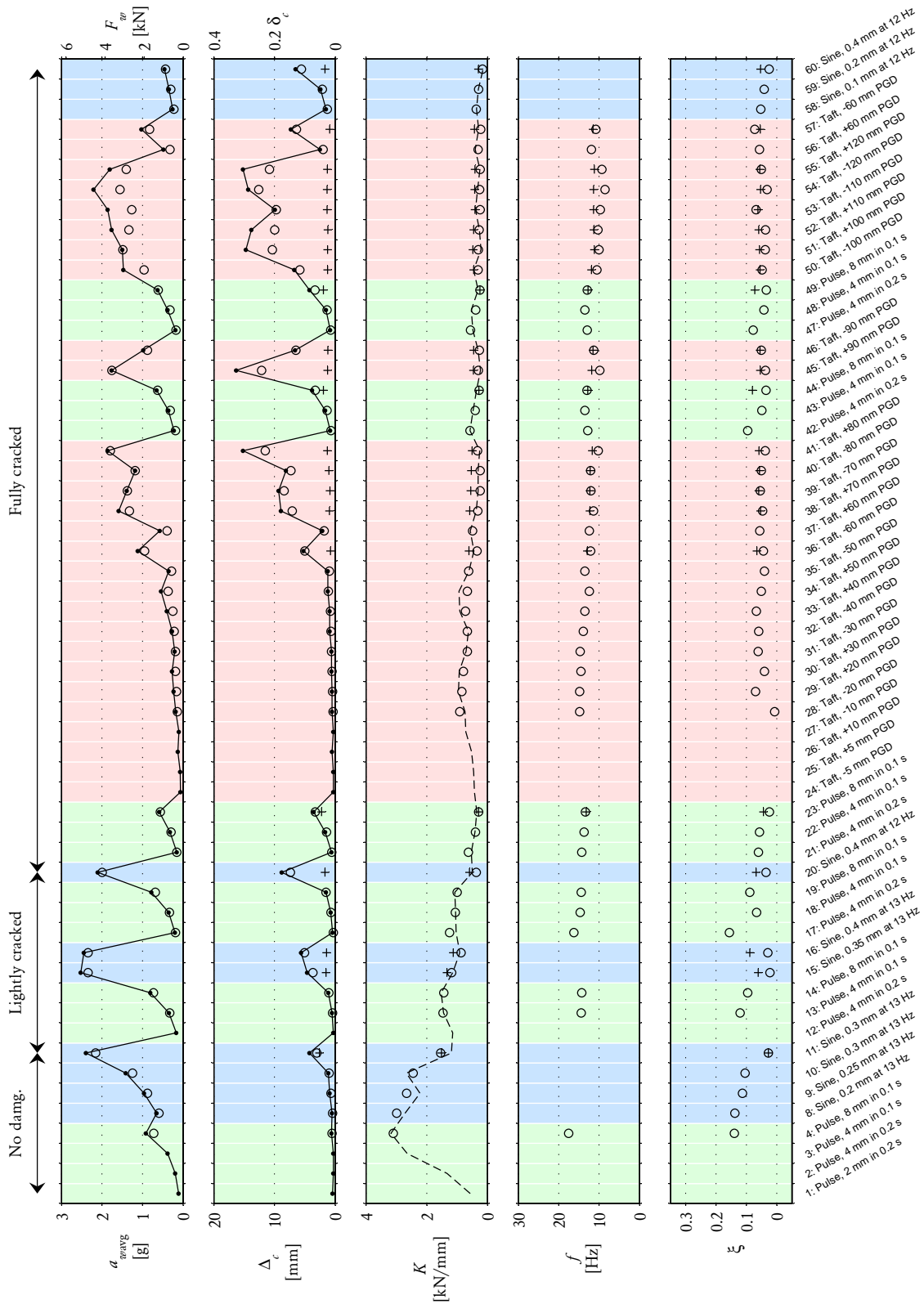


Figure 3.11: Test sequence and key results for wall D3. Legend in Table 3.4.

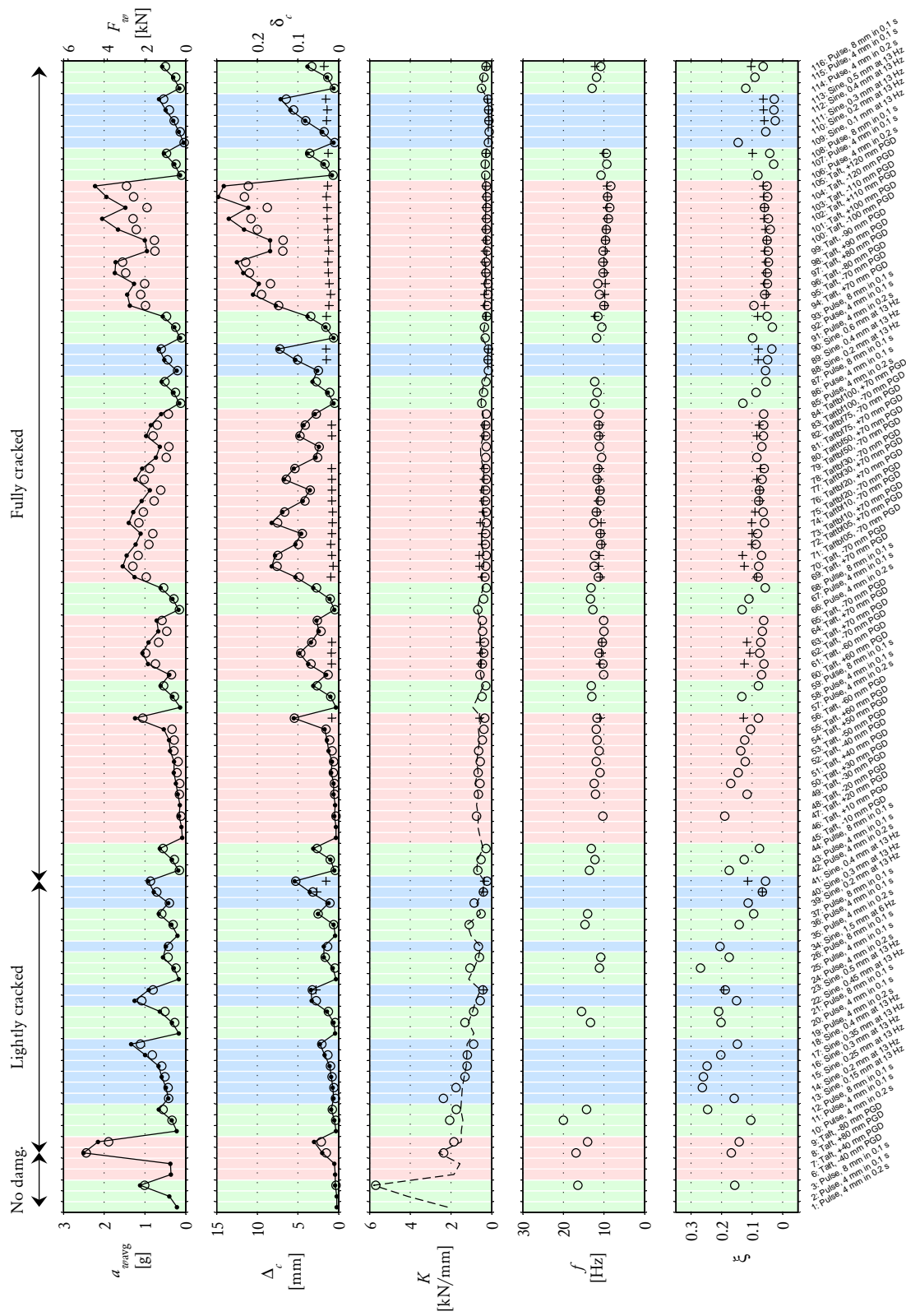


Figure 3.12: Test sequence and key results for wall D4. Legend in Table 3.4.

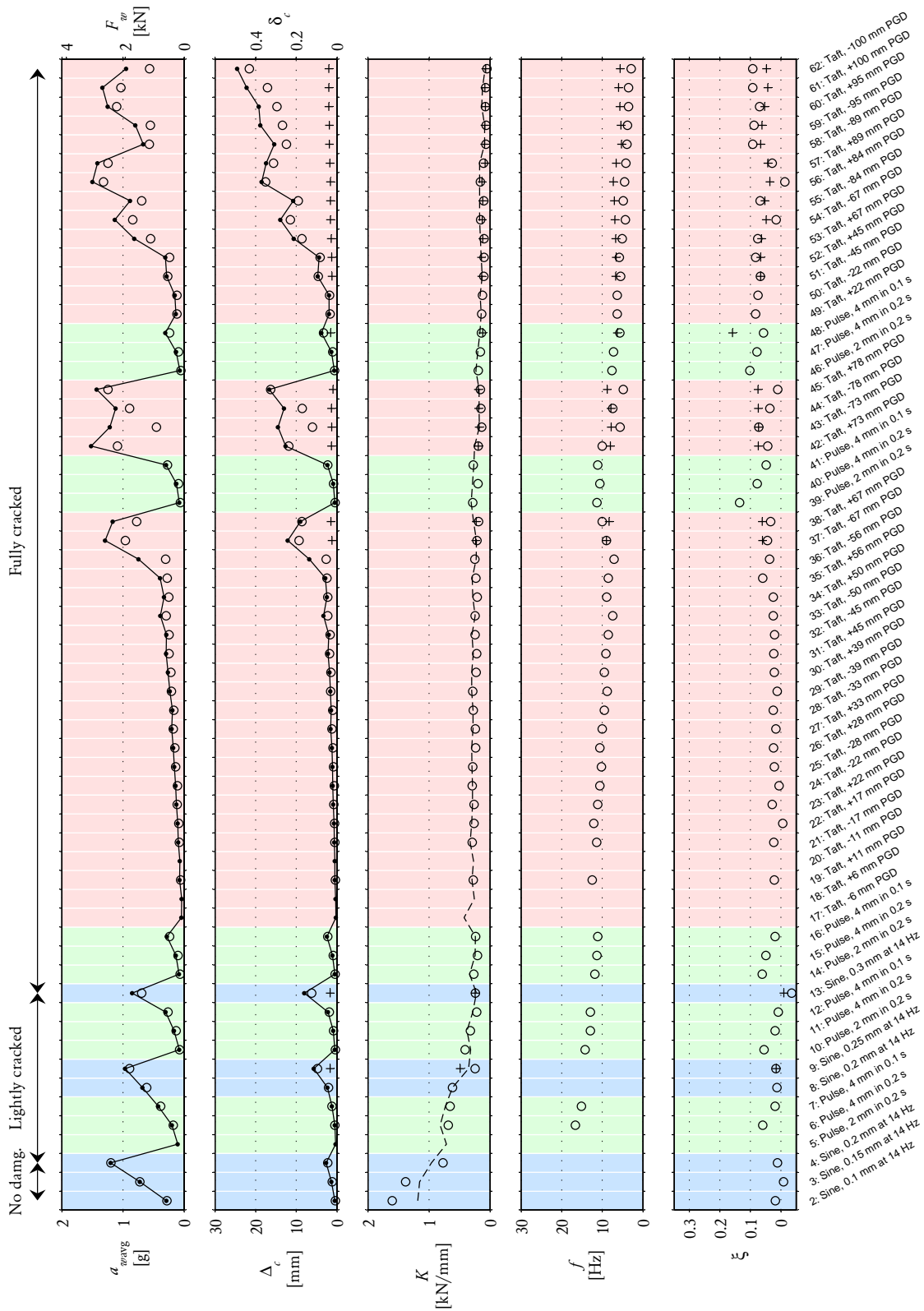


Figure 3.13: Test sequence and key results for wall D5. Legend in Table 3.4.

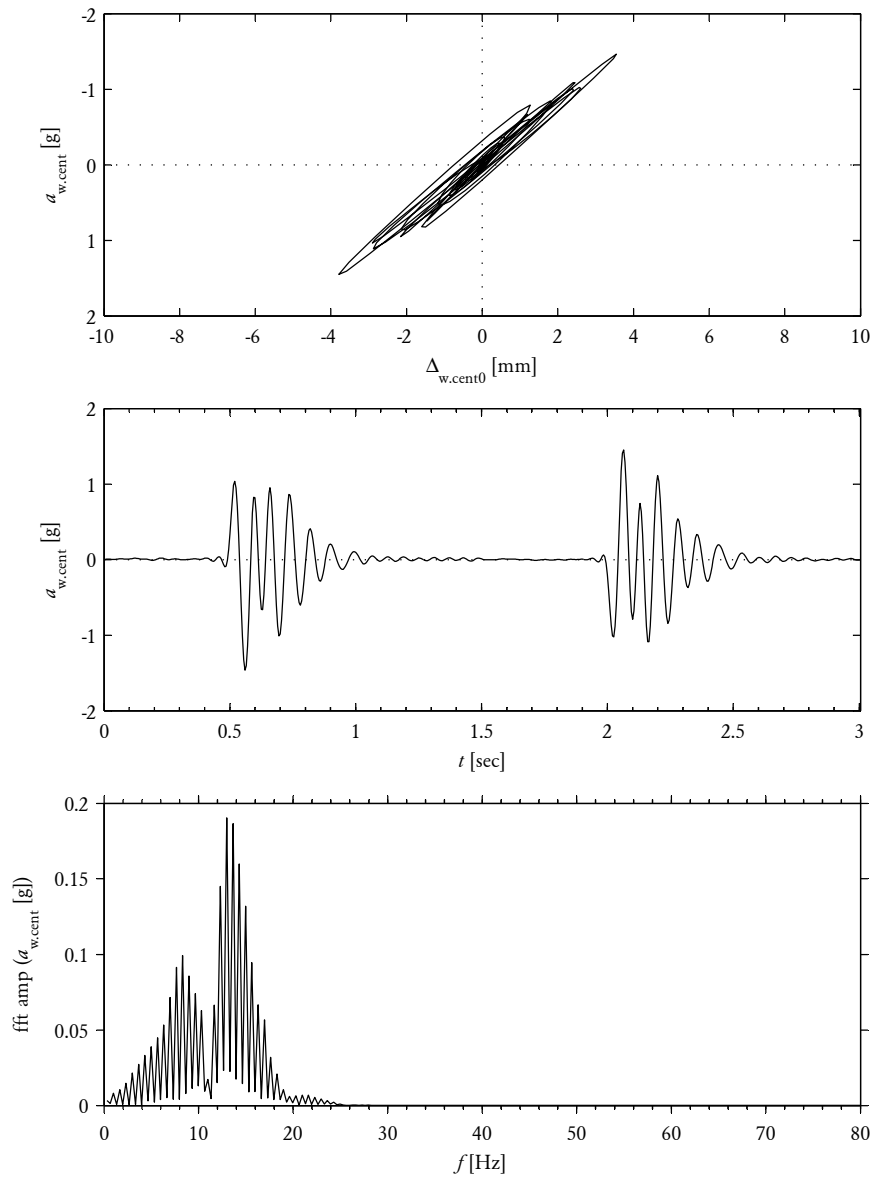


Figure 3.14: Typical response during pulse test, including hysteresis plot (top), time domain response (middle) and frequency domain response (bottom). Shown for test run d2_32_R_8mm_100ms incorporating high frequency filter.

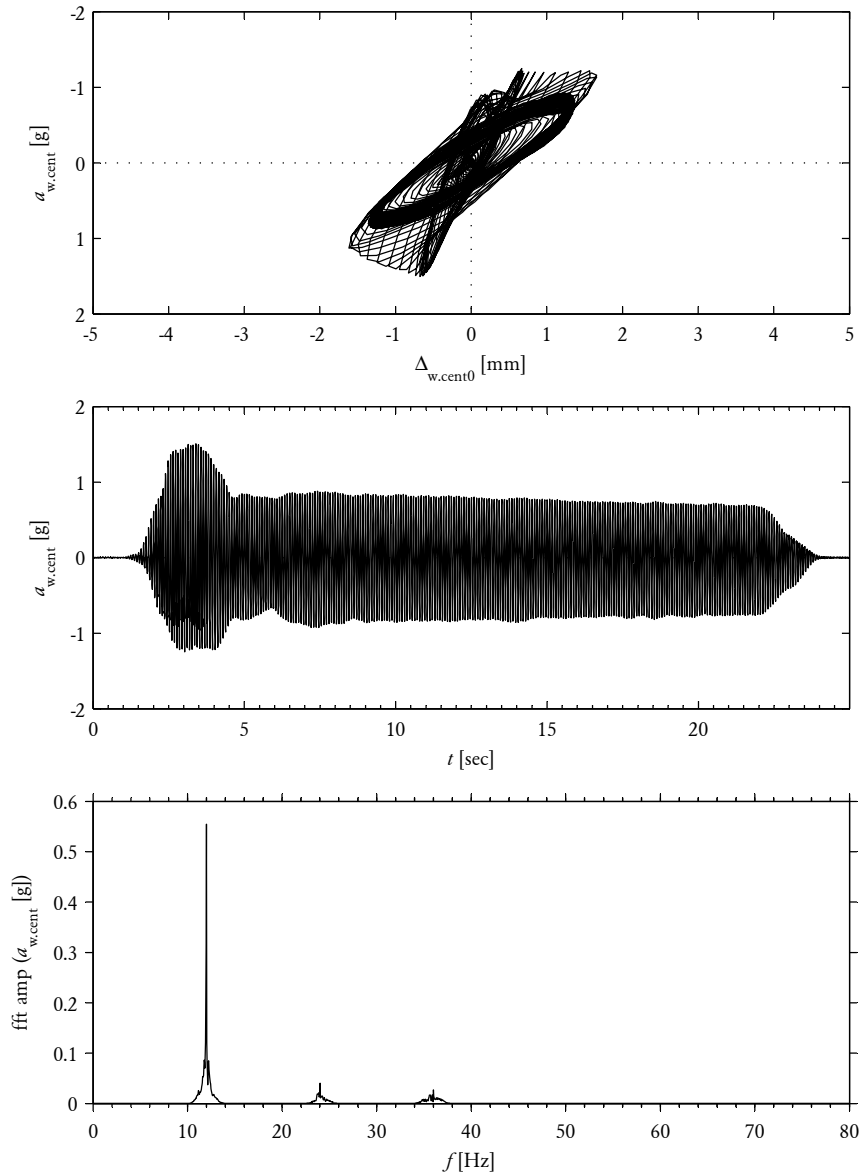


Figure 3.15: Typical response during harmonic test, including hysteresis plot (top), time domain response (middle) and frequency domain response (bottom). Shown for test run d2_13_H_12Hz_0.25mm incorporating high frequency filter.

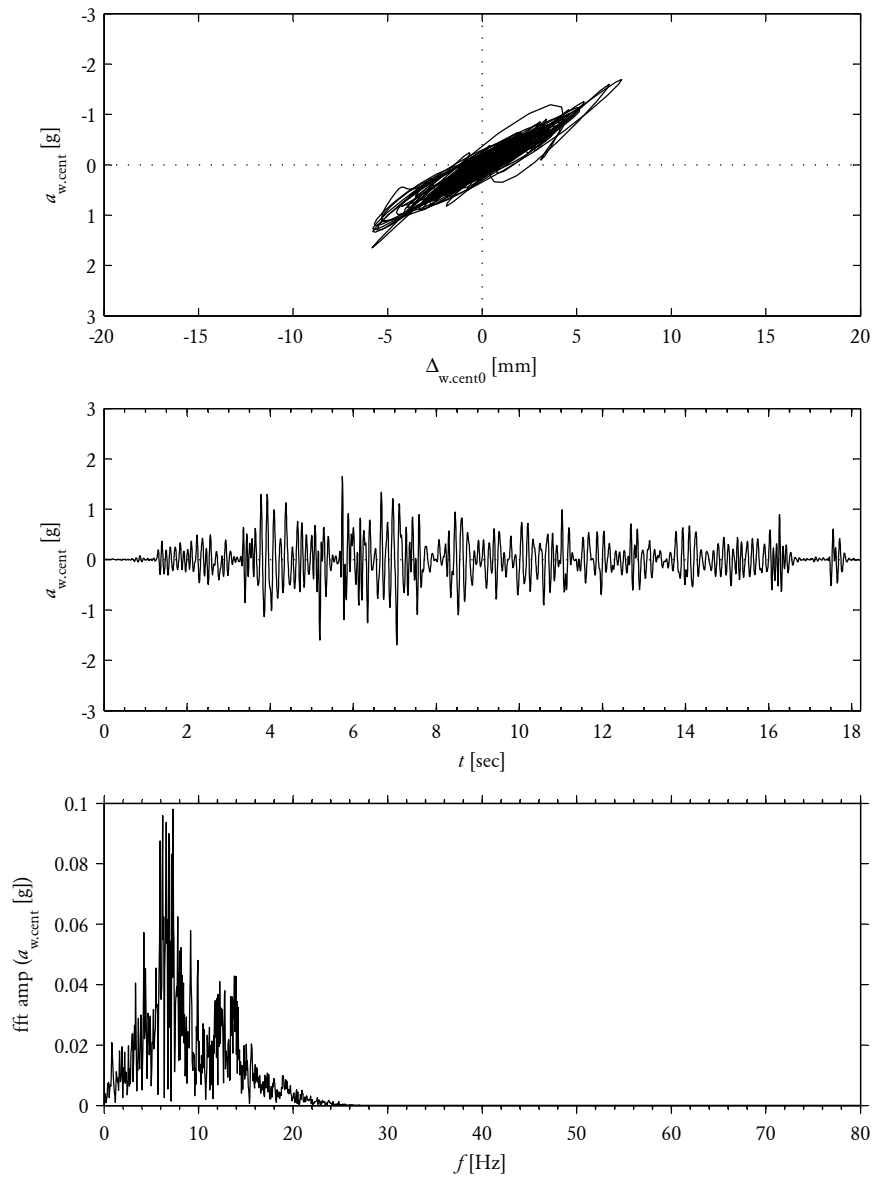


Figure 3.16: Typical response during earthquake test, including hysteresis plot (top), time domain response (middle) and frequency domain response (bottom). Shown for test run d2_41_EQ_Taft_-100mm incorporating high frequency filter.

Table 3.5: Peak measured response of key variables.

Wall	Ultimate strength			Max imposed displacement		
	$a_{w.avg}$ [g]	q_w [kPa]	F_w [kN]	$a_{w.cent}$ [g]	$\Delta_{w.cent}$ [mm]	$\Delta_{w.cent0}$ [mm]
D1	3.73	3.95	8.96	6.40	14.1	13.3
D2	2.33	2.47	5.60	3.83	14.4	15.2
D3	2.52	2.67	5.25	5.49	17.2	16.3
D4	2.51	2.65	5.21	5.56	16.7	14.8
D5	1.52	1.61	3.16	4.95	22.6	24.5

Table 3.6: Legend for Figures 3.17, 3.18, 3.19, 3.20 and 3.21.

Colour	Meaning (Type of test)
●	Pulse test
●	Harmonic test
●	Earthquake test

Marker	Meaning (Damage state)
□	Wall uncracked
○	Wall lightly cracked
×	Wall fully cracked

3.4.2 Peak Response

Table 3.5 summarises the peak values of the main response variables measured throughout the tests on each wall. Columns 2–4 provide different but interchangeable measures of the ultimate strength, in terms of the average wall acceleration $a_{w.cent}$, pressure q_w and force F_w . Column 5 provides the maximum measured central wall acceleration $a_{w.cent}$. Columns 6 and 7 give the largest displacement imposed on the walls during testing, in terms of $\Delta_{w.cent}$ and $\Delta_{w.cent0}$; however, it is emphasised that these values provide only a lower bound estimate of the wall's displacement capacity, since none of the walls were tested to collapse. Peak values of these variables occurring during individual runs are provided in Appendix C.3.2 (Table C.6). The corresponding peak values of $\Delta_{w.cent0}$ and $a_{w.avg}$ are also shown graphically in Figures 3.9–3.13.

3.4.3 Envelope Curves

Figure 3.17 presents envelope curves for each wall's load-displacement response in the a - δ format, by plotting the amplitude of displacement and average wall acceleration for the largest cycles occurring in each test run. It can be seen that the plots for each wall share several common features:

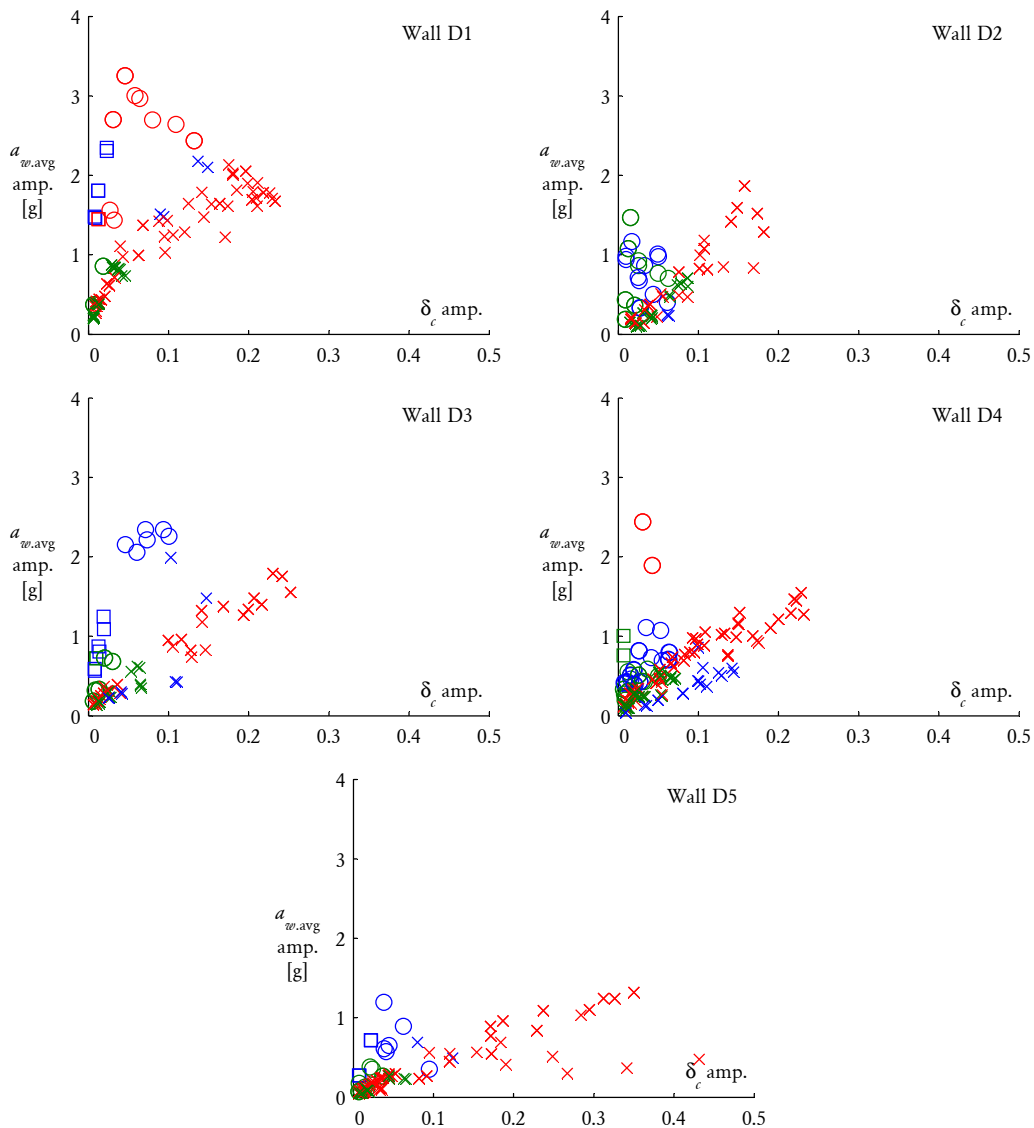


Figure 3.17: Average wall acceleration versus central displacement (amplitudes). Data points correspond to the largest cycles identified in each test run. Legend in Table 3.6.

- Each initially uncracked wall underwent first cracking and reached its ultimate strength at fairly small displacements (typically $\delta < 0.1$).
- With increasing deformation and number of cycles imposed on the wall, the progressive cracking and damage resulted in degradation of both strength and stiffness. This is also evident from Figures 3.9–3.13, which show a continual reduction in the stiffness with an increasing number of test runs.
- Even after full cracking, each wall still maintained its load capacity at increasing levels of displacement, which can be attributed to rigid body rocking and internal friction. It is noted that due to performance limitations of the

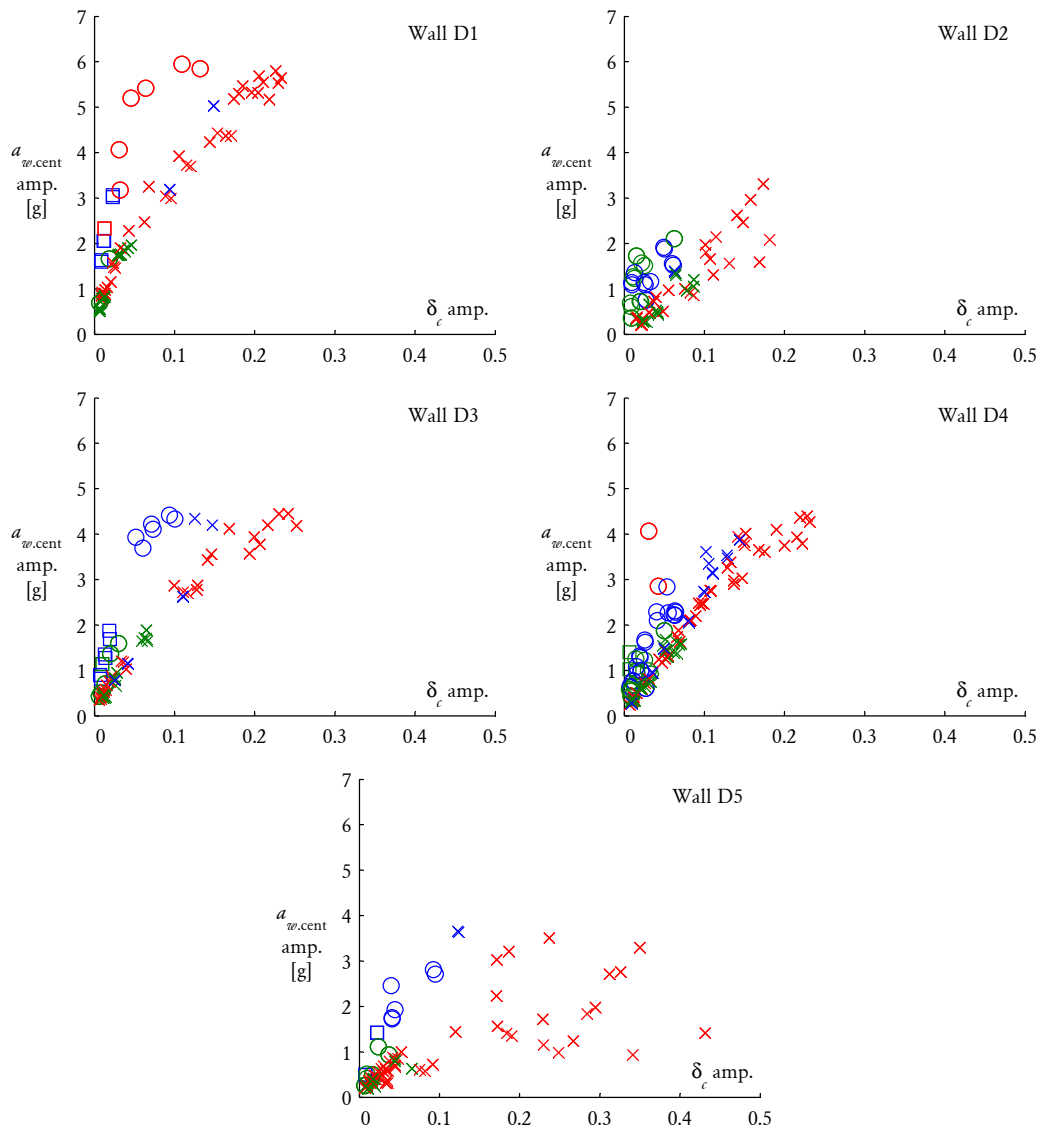


Figure 3.18: Central wall acceleration versus central displacement (amplitudes). Data points correspond to the largest cycles identified in each test run. Legend in Table 3.6.

shaketable, the maximum displacements reached (max δ between 0.2 and 0.4) were smaller than those achieved in the quasistatic tests (max δ approximately 1). Nonetheless, the envelope curves indicate that the walls still retained a significant proportion of their strength at the maximum imposed displacements.

These behavioural trends are considered consistent with those observed for the full-scale walls subjected to quasistatic cyclic loading as reported in Chapter 2.

Figure 3.18 provides alternative envelope curves, by plotting the wall's central acceleration versus displacement for the largest cycles occurring in each test run.

Whilst the values of acceleration in these graphs are not considered to be representative of the load resistance in terms of the magnitude (since they use the central acceleration and not the average acceleration), the plots suggest a more direct relationship between the wall's central acceleration and displacement, as opposed to the average acceleration and displacement (Figure 3.17). In particular, for the three walls with vertical precompression (walls D1, D3 and D4), the post-cracking envelope appears to be somewhat bilinear in shape. This trend is not surprising considering that the central acceleration was able to better capture the response of the fundamental flexural mode of vibration, compared to the average acceleration, which as discussed previously, is believed to have received some interference from higher vibrational modes such as twisting.

3.4.4 Hysteretic Damping

Equivalent viscous damping due to hysteretic energy dissipation (refer to Section 3.3.2) is plotted against the displacement amplitude in Figure 3.19. It can be seen that whilst there is a large degree of scatter in the measured values of ζ_{hyst} , the main cluster of points resides between approximately 0.02 and 0.10, for all walls tested. By comparison, values of damping at similar displacement amplitudes (i.e. $\delta < 0.3$) for the equivalent full-scale walls from Chapter 2 were generally between 0.09 and 0.15 (based on detailed results provided in Appendix B.3, particularly Tables B.1–B.5 and Figures B.16–B.20). That the measured hysteretic damping was higher for the full-scale walls can likely be attributed to the half-scale brickwork having a lower friction coefficient due to the bricks being solid, as opposed to the full-scale bricks which were perforated and therefore likely to have provided better interlock.

3.4.5 Vibration Frequency

Figure 3.20 plots the wall's vibrational frequency against displacement amplitude in the peak response range, using results obtained by the cyclic response analysis (outlined in Section 3.3.2). Despite a high level of scatter, the graphs suggest a somewhat inverse relationship between the frequency and displacement amplitude. An interesting correlation becomes apparent when the square of the angular frequency, ω^2 , (whereby $\omega = 2\pi f$) is plotted against the effective stiffness K (Figure 3.21). Whilst the resulting graphs still exhibit scatter, they do suggest a linear relationship between the two parameters, as would be expected for a linear dynamic system according to the fundamental relationship $\omega^2 = K/M$ (where M is the mass of the system). For the range of tests conducted, these graphs

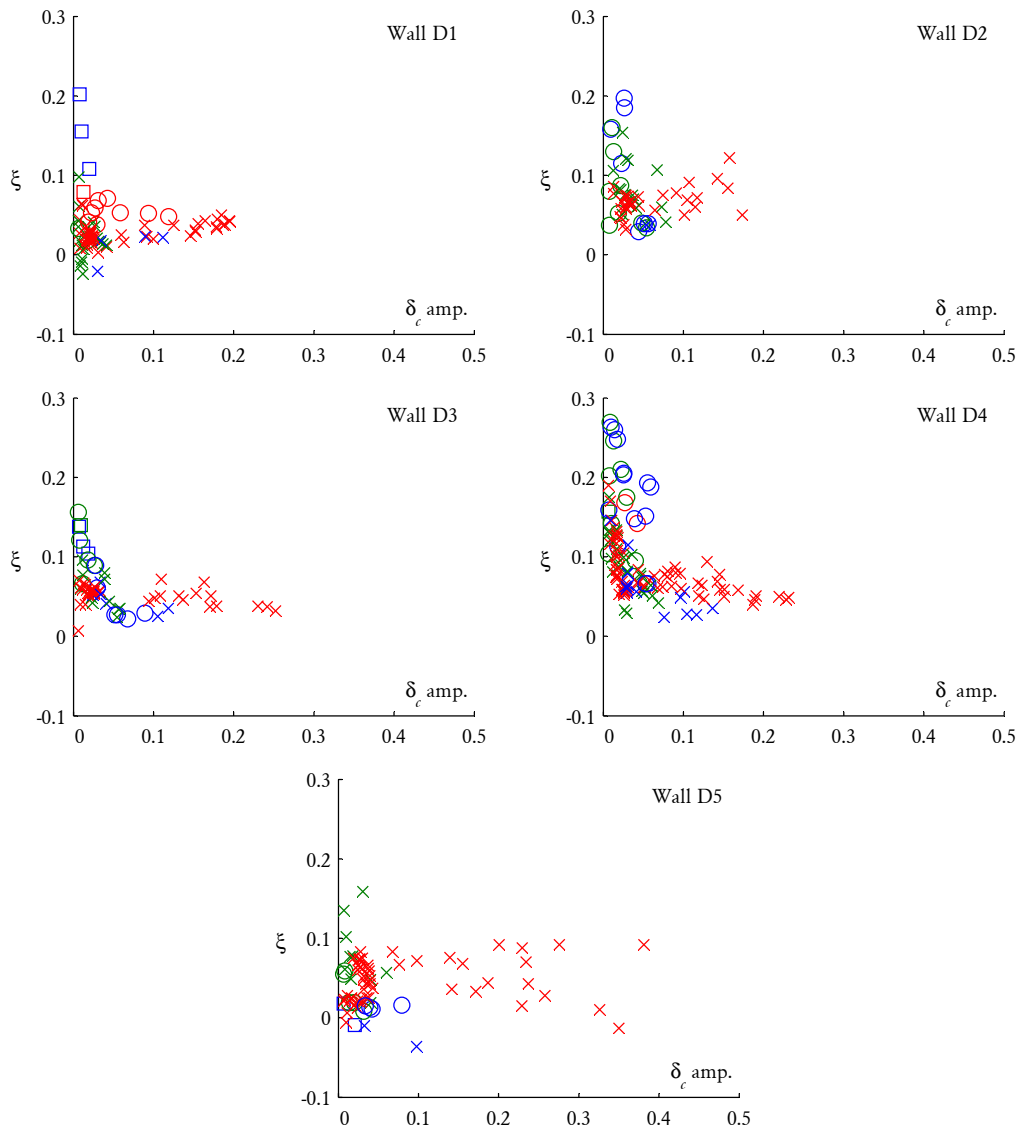


Figure 3.19: Equivalent viscous damping from hysteresis plotted against central displacement amplitude. Data points correspond to the average values calculated in the peak response range of each test run. Legend in Table 3.6.

also demonstrate that both stiffness and frequency were generally lower in walls without precompression (D2, D5) and higher in walls with precompression (D1, D3, D4).

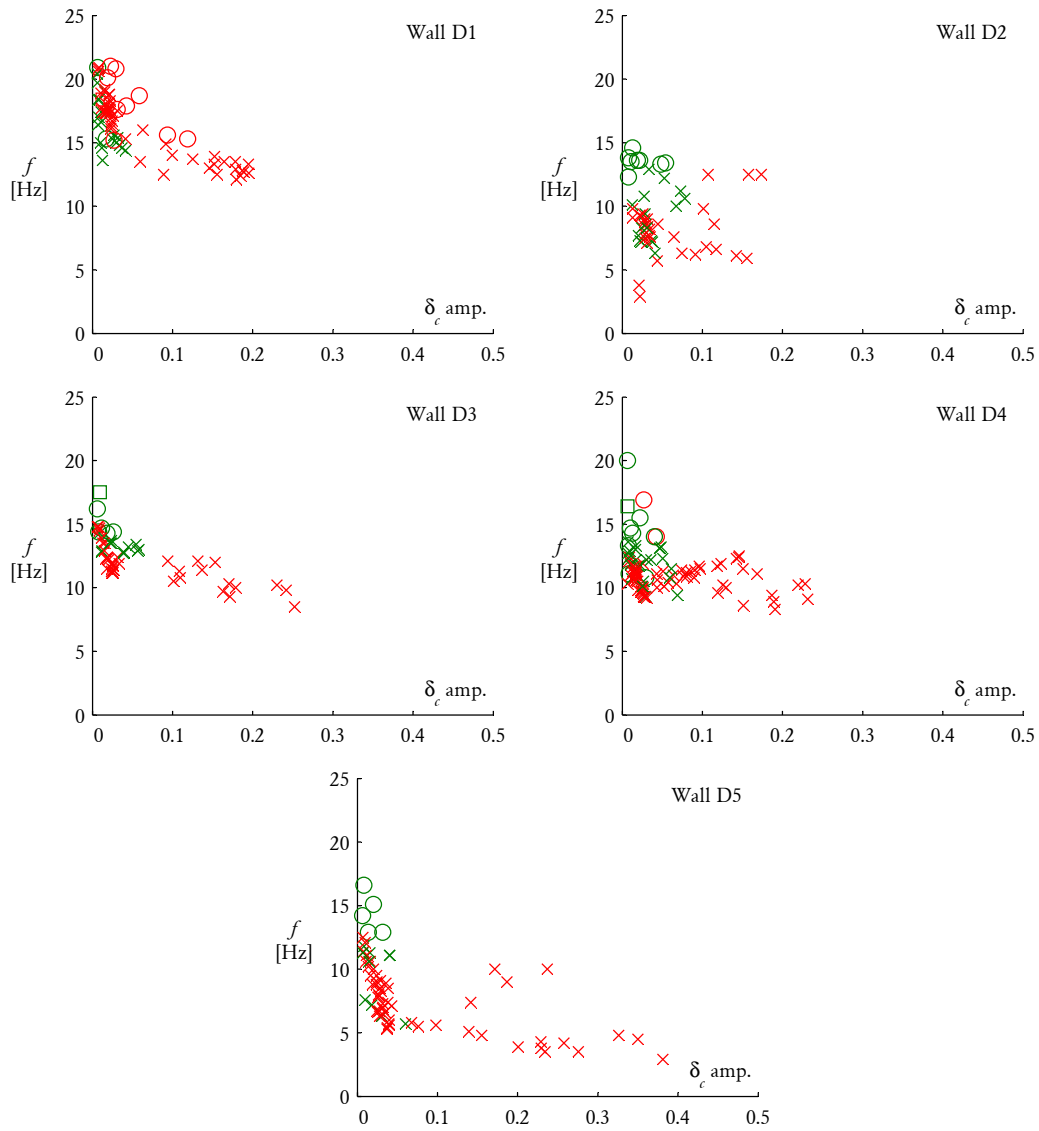


Figure 3.20: Cycle frequency plotted against central displacement amplitude. Data points correspond to the average values calculated in the peak response range of each test run. Legend in Table 3.6.

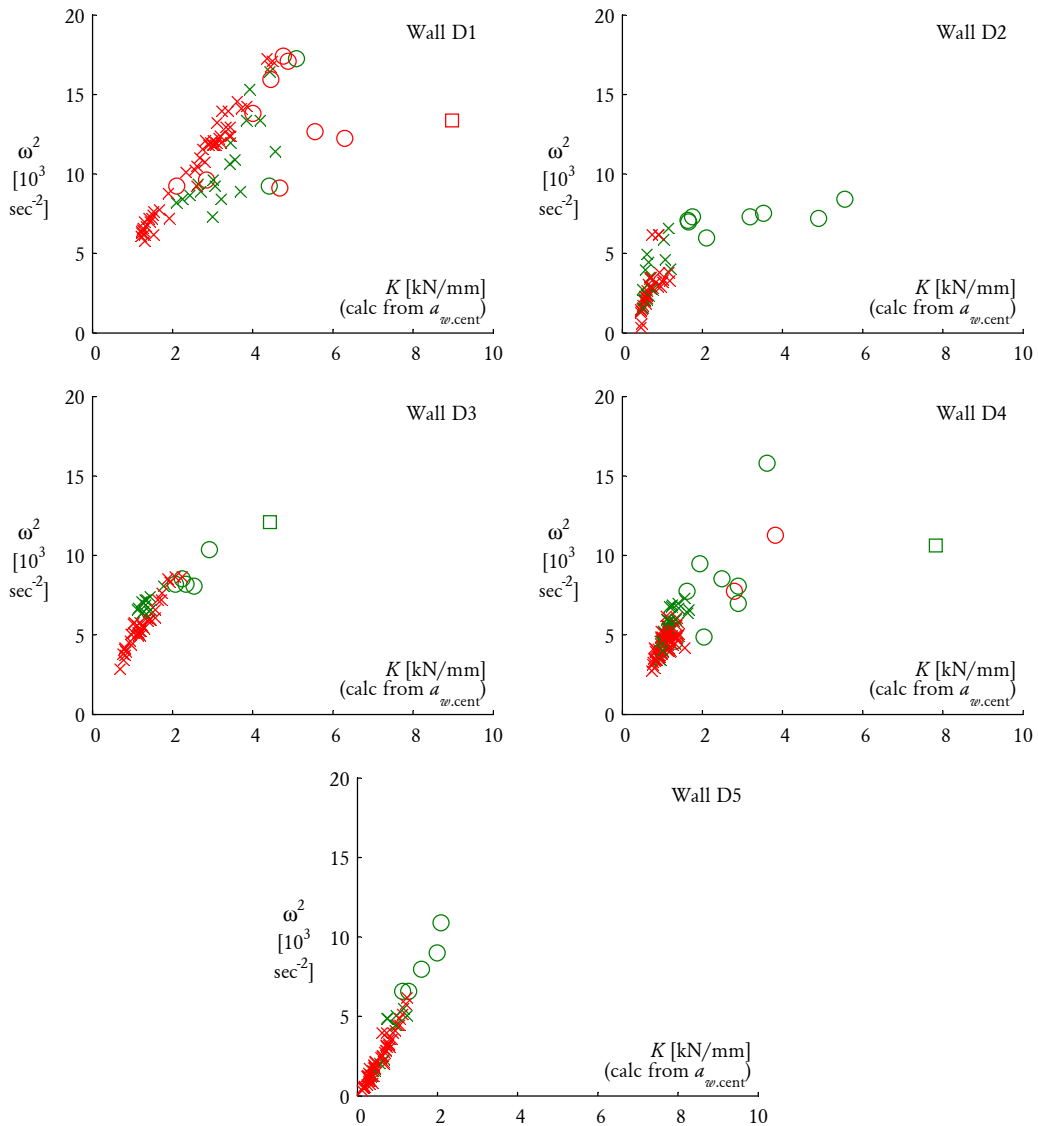


Figure 3.21: Cycle angular frequency squared [$\omega^2 = (2\pi f)^2$] plotted against effective stiffness. Data points correspond to the average values calculated in the peak response range of each test run. Effective stiffness is derived from the wall's central acceleration. Legend in Table 3.6.

3.5 OBSERVED DAMAGE AND CRACK PATTERNS

Diagrams of the failure patterns exhibited by the walls at the conclusion of testing are shown by Figure 3.22. Photographs showing the damage are also presented in Figures 3.23–3.27.

3.5.1 Crack Pattern Shapes

The observed cracking patterns are consistent with the failure patterns typically associated with walls in two-way bending, which are used in the AS 3700 virtual work (VW) method for prediction of the ultimate load capacity (refer to Figure 4.1).¹¹ These patterns are characterised by diagonal cracks propagating from corners where adjacent supported edges intersect, in addition to a short horizontal crack forming at the centre of the wall.

There were, however, some differences between the observed and expected behaviour: One such case was wall D2, which did not develop diagonal cracks propagating from the top corners; instead, it developed a vertical crack along the midspan that ran toward the top edge, with the overall pattern resembling that of a wall free along the top edge. The reason for this is believed to be that the top edge support did not provide a sufficient reaction at small displacements during which the wall first cracked, due to the presence of a short horizontal gap between the wall and the rubber spacer mounted onto the horizontal restraint members (refer to Figure 3.4a). However, once the wall became cracked and underwent horizontal movement at the top edge, it would make contact with the top edge support member causing the horizontal reaction to become restored. A second example is wall D5, which also did not develop a top diagonal crack along its longer subpanel. It is emphasised, however, that the differences between the observed and expected behaviour are not believed to be a result of the dynamic nature of the imposed loading, but rather, a consequence of the detailing used along the top edge support being unable to provide a sufficient horizontal reaction at the time that the walls first cracked.

3.5.2 General Observations

The damage exhibited by the walls at the conclusion of testing is shown by Figures 3.23–3.27.

¹¹Idealised versions of the expected failure patterns for the corresponding full-scale walls (S1–S5) are illustrated in Figures 2.14–2.18.

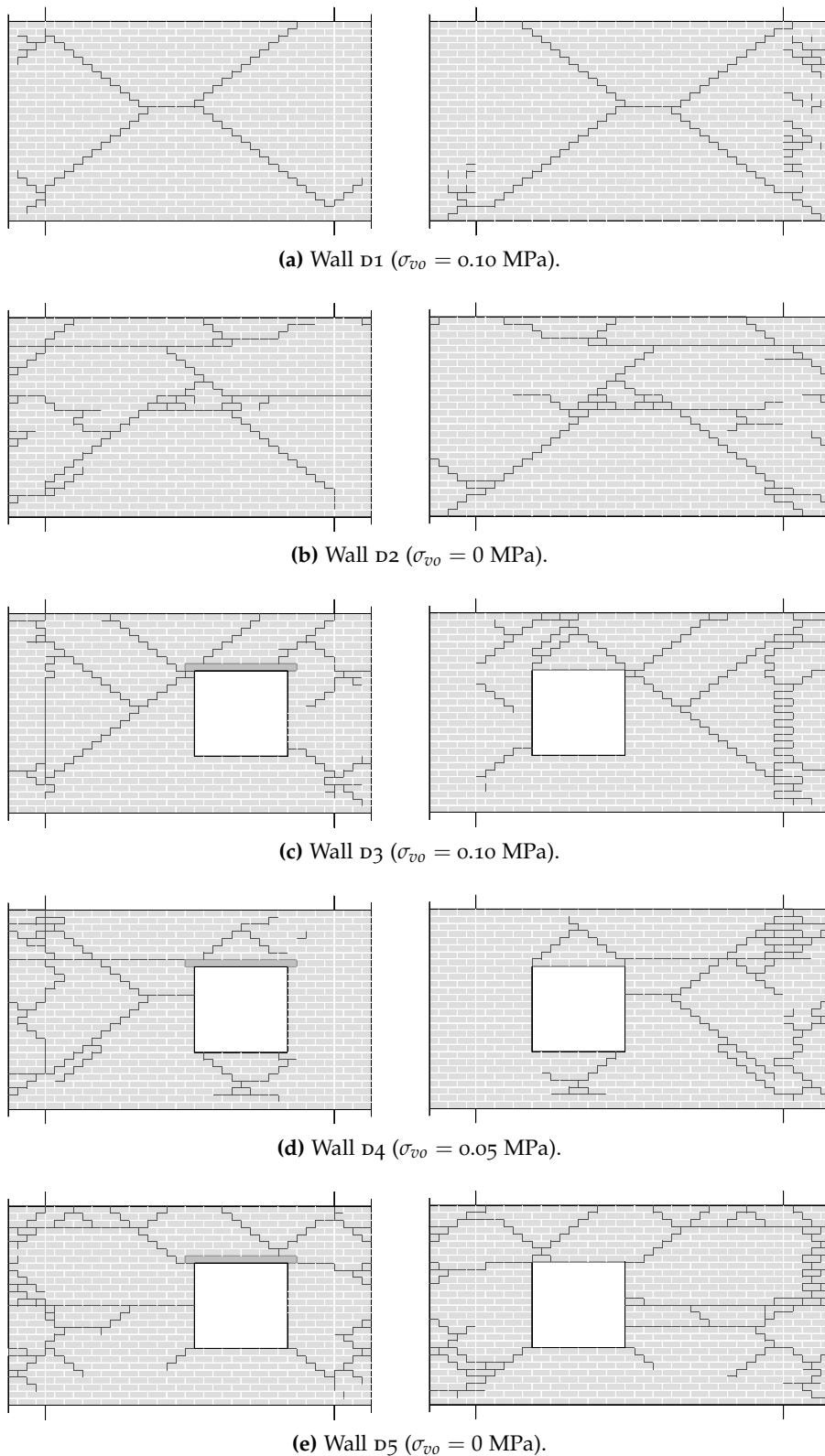


Figure 3.22: Cracking patterns exhibited by the walls at the conclusion of testing. The inside and outside faces of each wall are shown by the left and right diagrams, respectively. Note that the illustrations show the unfolded view of the walls (see Figure 2.23 for plan view).



Figure 3.23: Wall D1 at the conclusion of testing.



Figure 3.24: Wall D2 at the conclusion of testing.



Figure 3.25: Wall D3 at the conclusion of testing.

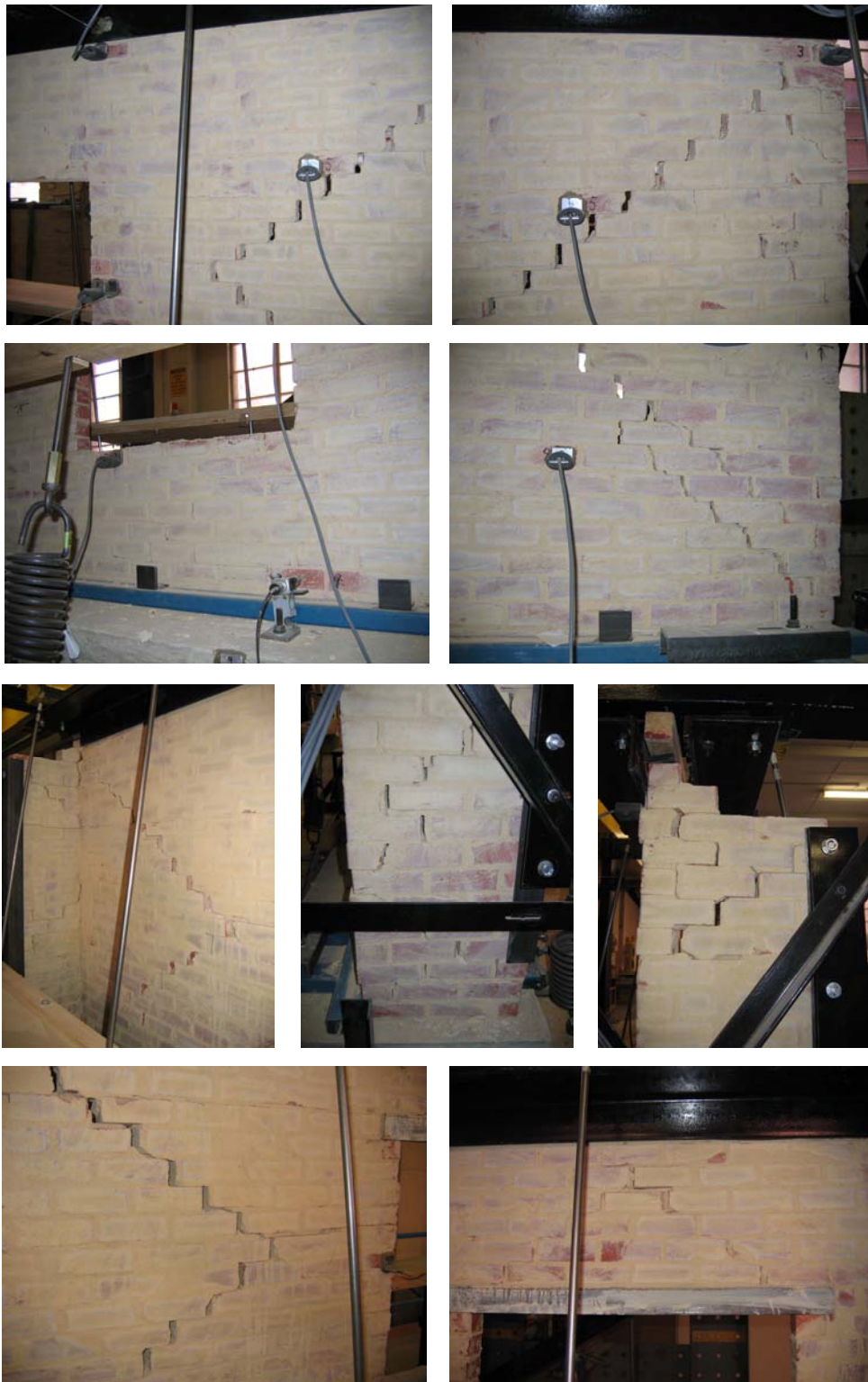


Figure 3.26: Wall D4 at the conclusion of testing.

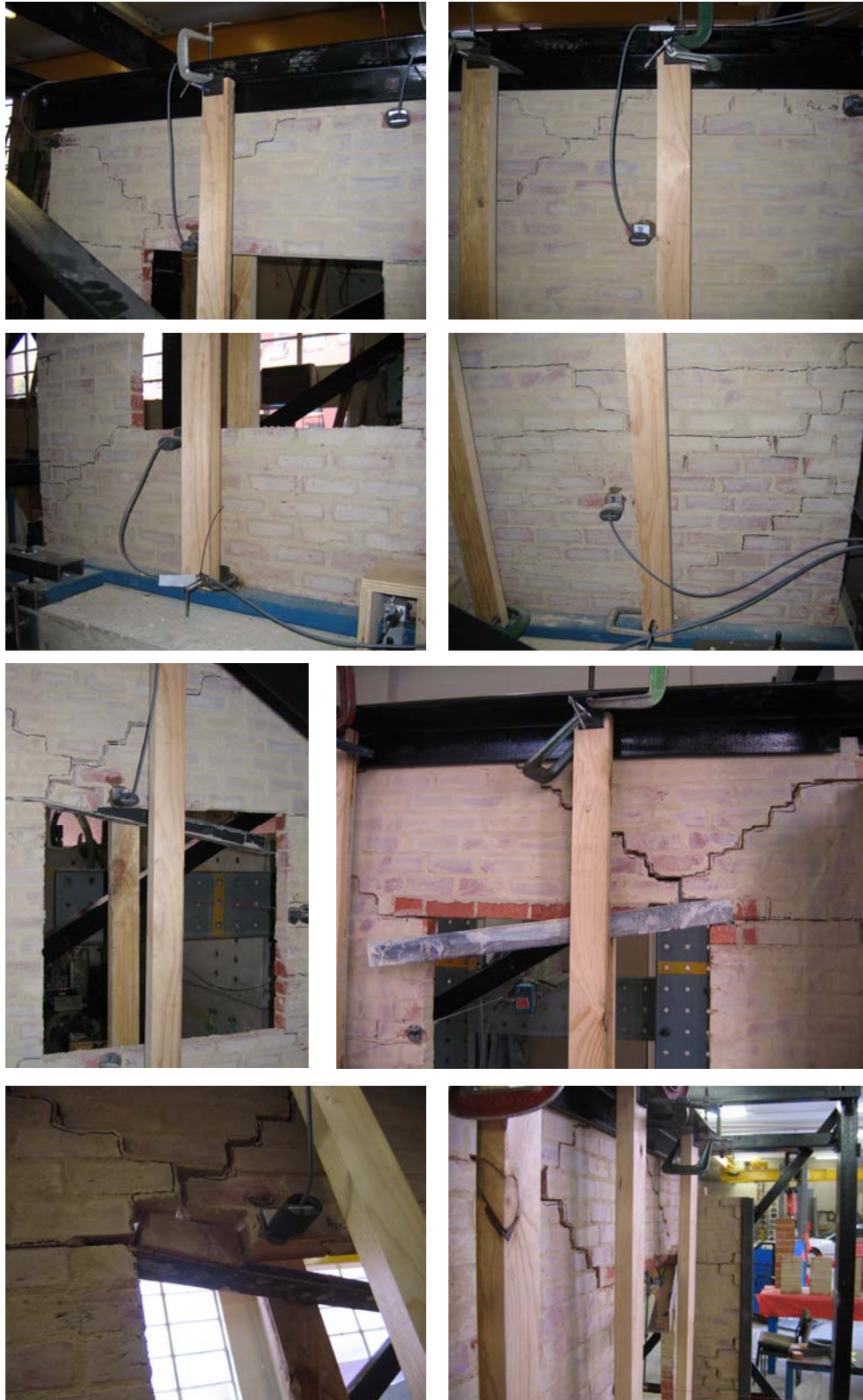


Figure 3.27: Wall D5 at the conclusion of testing.

Stepped Failure Versus Line Failure

Stepped failure was shown to be the exclusive mode of failure along vertical cracks in horizontal bending, with no line failure being observed in any of the walls tested. This is in contrast to the quasistatic test walls, where line failure was the slightly more dominant failure mode (refer to Section 2.5). The difference in the observed behaviour between the two sets of tests is believed to result from the different types of brickwork used—particularly, perforated brick units in the quasistatic tests (Figure 2.1) and solid brick units in the dynamic tests (Figure 3.1). The solid brickwork had a lower tensile bond strength than the perforated brickwork, as verified by material testing (reported in Appendix A.2). In addition, the solid brick units are likely to have had a higher modulus of rupture due to the lack of perforations (even though the modulus of rupture was not measured in these tests). Both of these factors are likely to have contributed to stepped failure being the more dominant mechanism in the reduced-scale test walls.

Importance of Wall Integrity Toward Seismic Performance

As stated in Section 3.1, one of the aims of this study was to verify whether the type of behaviour observed in the quasistatic test study was comparable to response produced under true dynamic conditions. In particular, it was speculated that the airbags positioned on both sides of the wall during the quasistatic cyclic tests (refer to Figure 2.8b) may have acted to confine the wall, thereby improving its integrity. Indeed, the shaketable tests have demonstrated that under seismic loading it is possible for a wall to undergo several types of premature local failure if its overall integrity is poor.

A common observation of the walls' response during seismic loading was localised shear sliding along the cracks between adjacent sub-plates forming the overall mechanism. Examples of this have been demonstrated to some extent by all five walls tested, with solid walls D1 and D2 being the most notable cases (Figures 3.23 and 3.24). In fact, for both of these walls, the largest measured slip between the subpanels was approximately 20 mm (40% of the wall's thickness). Such sliding could potentially cause a wall to lose flexural strength due to a reduction in internal overlap, or in the more extreme scenario to undergo local failure if the shear sliding becomes excessive. It should be noted, however, that the walls in this study were subjected to a very large number of deformation cycles throughout the course of testing, and that the number of deformation cycles expected during realistic earthquakes would be considerably lower. Furthermore, the brickwork used in this study may have been particularly susceptible to this kind of sliding behaviour due

to a weak tensile bond strength and low friction coefficient (mean value of 0.576) as a result of the flat surface of the bricks. By contrast, perforated brickwork, such as that used in the quasistatic cyclic tests, would be expected to benefit from the additional interlock between mortar and the bricks and hence be more resistant to this type of failure.

Another example of localised failure was demonstrated by wall D5, in which the steel lintel became disengaged from the wall at one of its ends (Figure 3.27). This is believed to have occurred due to a loss of the lintel's vertical confinement, caused by large rotations and excessive fallout of mortar adjacent to the lintel's support. A further factor likely to have contributed to the failure was the smooth surface of the lintel, which consisted of an equal angle steel section. This highlights the need for a strong connection between the lintel and wall. Resistance against this type of failure could be improved, for example, by using a lintel with a corrugated surface to generate better interlock with the brickwork.

As was observed during the quasistatic cyclic tests and discussed in some detail in Section 2.5.2, excessive line failure along the vertical edges of a wall can lead to separation between the main wall and the return walls. Whilst line failure did not occur in any of the shaketable test walls as discussed previously, it was nonetheless possible for the main wall to become disengaged from the return walls due to shear sliding, had the frictional interlock been insufficient. This did not occur in any of the test walls; however, it needs to be clarified that the restraint conditions implemented along the return walls for walls D1 and D2 would have prevented this type of premature failure, since the return walls were restrained in the outward direction (refer to Figures 3.3 and 3.4b).¹² Whilst some minor separation between the main wall and the return wall was observed in walls D3, D4 and D5 (for example, as shown by Figure 3.26, third row from top, middle and right photos), the frictional resistance along the cracks was still sufficient to provide a path for the horizontal load. These observations once again underline the importance of the brickwork having a high modulus of rupture (f_{ut}) in order to promote stepped cracks, thereby enabling frictional mechanisms to provide residual resistance following cracking and improving the overall seismic performance.

3.6 CONCLUSIONS

Shaketable tests have been performed on a set of five half-scale URM walls. The walls were intended to serve as half-scale replicas of walls from the quasistatic

¹²Whilst it is recognised that the type of connection provided for walls D1 and D2 was not entirely realistic, it was deemed necessary in order to prevent rocking of the test specimens (observed during testing of wall D2) and to facilitate two-way bending response instead.

cyclic loading tests in Chapter 2. As such, they were subjected to the same set of boundary conditions as in the previous study, including translational restraint at the top and bottom edges and full moment connections along both vertical edges. The specimens comprised panels with openings, as well as loadbearing walls with vertical precompression up to 0.1 MPa. During the course of testing, each wall was subjected to a large number of individual test runs that included pulse tests, harmonic tests and realistic earthquake motions.

The tests successfully verified the most significant behaviour characteristics observed in the quasistatic cyclic test study, including the following:

- The walls exhibited significant post-cracking strength as well as displacement capacity. Due to shaketable's performance limitations, the imposed wall displacements (max δ between approximately 0.2 and 0.4) were lower than those reached in the quasistatic test study (max $\delta \approx 1$). Nonetheless, they still significantly exceeded the deformations at which initial cracking and the ultimate strength were attained.
- Under cyclic deformation, the observed load-displacement behaviour was highly inelastic and exhibited a significant degree of hysteretic energy dissipation, due to the frictional resistance mechanisms associated with two-way bending.
- The walls' strength and stiffness degraded as a result of damage accumulated during the continued cyclic deformation and increasing displacements.
- Walls with precompression outperformed those without precompression with respect to their ultimate and post-cracking strength. Furthermore, the loadbearing walls exhibited a higher post-cracking stiffness and frequency of vibration compared to the equivalent non-loadbearing walls.
- The observed damage and cracking patterns were in reasonably good agreement with those typically associated with two-way walls, which were also observed in the quasistatic test study.

The tests have also demonstrated, however, that walls without good overall integrity could become susceptible to various modes of premature failure which could reduce their overall seismic resistance. This includes sliding of adjacent subplates along cracks; and in walls with openings, a possible loss of connection between the brickwork and lintels. Whilst some of these issues could potentially be prevented through good construction practice, they are beyond the scope of this research. The tests have also highlighted the importance of the masonry possessing

a high ratio of brick to bond strength (f_{ut}/f_{mt}) in order to promote stepped failure over line failure and maintain the ability of vertical edges to provide a path for the horizontal load.

Part II

ANALYTICAL WORK

Chapter 4

ULTIMATE STRENGTH PREDICTION IN MORTAR-BONDED MASONRY WALLS

Abstract

Most state-of-the-art procedures for ultimate strength design of mortar-bonded, two-way walls are based on plastic analysis. The basis of these methods, however, assumes simultaneous attainment of moment capacities along the various cracks, which is known to be fundamentally flawed for unreinforced masonry due to its brittle nature. This chapter reviews the various available design methods and outlines the distinctions between them, particularly their approach to dealing with this conceptual flaw. Analytical expressions for calculating both the ultimate and residual moment capacities along the various types of crack lines are presented, which incorporate some improvements over previous models to enhance their versatility. These expressions were fed into the virtual work analysis to analyse the full-scale walls from tests reported in Chapter 2. Comparisons of the predicted and measured values of ultimate strength suggest that the diagonal cracks and vertical edge cracks in these walls did not achieve their moment capacities simultaneously. Furthermore, although the present AS 3700 code approach ignores any moment contributions from horizontal crack lines, as these are generally known to form early in the wall's response, the analyses indicate that inclusion of some residual moment capacity along these cracks helps to reduce the overall scatter in the predictions.

4.1 INTRODUCTION

Although computationally intensive analytical methodologies such as finite element analysis have been demonstrated to predict the out-of-plane strength of two-way spanning, mortar-bonded unreinforced masonry (URM) walls with good accuracy [Southcombe *et al.*, 1995; Ng, 1996; Lee *et al.*, 1996; Martini, 1998; Mathew *et al.*, 1999; Lourenço, 2000, 2002; Milani *et al.*, 2006; Cecchi *et al.*, 2007; Casolo and Milani, 2010], their reliance upon knowledge of precise values of material properties, high computational effort and high analytical skill of the user makes them unsuitable for everyday design use [Kappos *et al.*, 2002]. This creates a distinct need for *design* methodologies, which can accurately predict the ultimate strength, but are yet simple enough for code implementation and hand calculation.

The approach prescribed by the Australian masonry code AS 3700 [Standards Australia, 2001] for ultimate strength design of two-way walls is the so-called virtual work (VW) method, developed by Lawrence and Marshall [1996] [also reported in Lawrence and Marshall, 1998, 2000].¹ The method is a form of rigid plastic analysis, which assumes that at the point of ultimate strength the load resistance of the wall is obtained from contributions of moment capacities along vertical and diagonal crack lines. Comparisons of strength predictions with a large experimental data set have been shown to be largely favourable in the aforementioned sources, despite numerous shortcomings of the moment capacity expressions used within the method which are still currently prescribed in the code (refer to Appendix E.1). More recently, Willis [2004] [also reported in Willis *et al.*, 2004; Griffith *et al.*, 2005] developed alternative expressions for calculating the moment capacities which incorporate significant improvements over the code expressions, in that they are based on more rational mechanical models, account for the beneficial effects of vertical compression, and are dimensionally consistent. Furthermore, Willis demonstrated the expressions to perform favourably in predicting the ultimate load capacity when implemented into the VW approach.

The aim of this chapter is to examine the accuracy of the VW method by comparing its predictions of the ultimate load capacity to the experimental results reported in Chapter 2. Of particular interest is to find out how effectively the method can deal with the specific aspects of the tested walls, such as the presence of openings, axial loading and moment restraint along the vertical edges, and to suggest improvements and refinements to the method, as necessary.

This chapter is structured as follows: Section 4.2 describes the fundamental

¹The method was originally implemented in the 1998 version of the code and has been retained without modification in the subsequent 2001 and 2011 editions.

basis behind the plastic analysis approach and provides a discussion of the various subtleties between the different available methods. Section 4.3 provides analytical expressions for calculating the moment capacities of mortar-bonded URM with respect to the different types of bending. Section 4.4 describes a refined analysis for walls with openings. Section 4.5 compares analytical predictions to experimentally measured values of strength and provides a discussion of the results. A summary of the findings and recommendations is presented in Section 4.6. Additional information regarding various analytical models for calculation of moment capacities is also provided in Appendix E.

4.2 REVIEW OF PLASTIC ANALYSIS METHODS

4.2.1 Theoretical Basis

Most masonry codes today specify ultimate strength design of two-way spanning URM walls according to some form of rigid plastic analysis: including the Eurocode, former British code², Canadian code, as well as the Australian code.

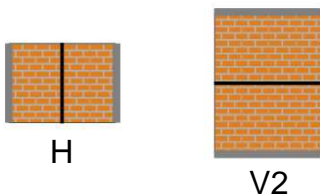
At the heart of these methods are two fundamental assumptions:

1. The first assumption is that at the point of ultimate strength, the wall's displacement profile exhibits a collapse mechanism—a series of flat plates with deformations concentrated in the form of rotations along crack lines. Because the most significant deformations of masonry panels in flexure occur along their crack lines, it is generally accepted that their collapse mechanisms can be generally defined by the overall crack patterns (refer to Figure 4.1).
2. The second assumption is that the moment capacities along the contributing cracks in the mechanism are all reached simultaneously. However, this assumption is well known to be theoretically flawed, since URM is a non-ductile material which cannot maintain its moment capacity at continued deformation. As such, the various design approaches have addressed this problem in different ways (as discussed further in Section 4.2.2).

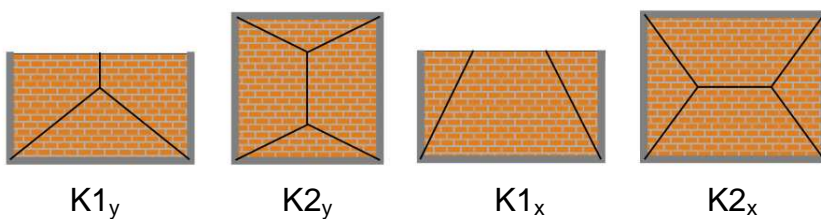
Any plastic analysis begins with the arbitrary selection a collapse mechanism. For the chosen mechanism, the lateral pressure resistance of the wall is evaluated from the principle of energy conservation, by equating the internal and external virtual work.

²Withdrawn on March 31st 2010 and now replaced by Eurocode 6.

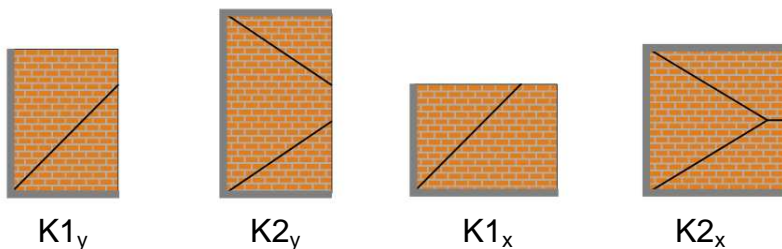
One-way spanning walls:



Two-way walls with both sides supported:



Two-way walls with a single side supported:



Two-way walls with an opening and both sides supported:

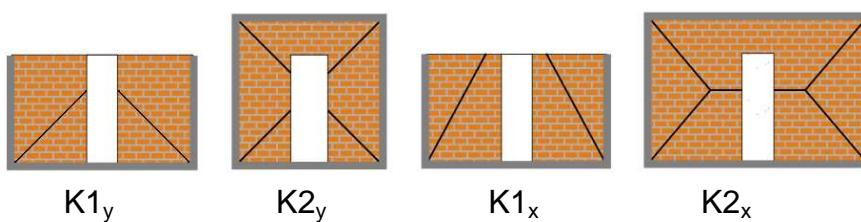


Figure 4.1: Failure mechanisms for various wall configurations as catered for by the AS 3700 VW method. Graphics from *Lawrence and Marshall [1996]* [as reproduced in *Lawrence and Page, 1999*]; however, labelling changed for consistency with Chapters 6 and 7 (used with permission from S. J. Lawrence.).

With loading due to a lateral pressure $q\langle x, y \rangle$, the total external virtual work E'_{tot} done on the wall is obtained by integrating the product of the applied pressure and the virtual displacement $u'\langle x, y \rangle$, along the face of the wall:

$$E'_{\text{tot}} = \int_Y \int_X q\langle x, y \rangle u'\langle x, y \rangle dx dy. \quad (4.1)$$

When the applied pressure is uniformly distributed, such that $q\langle x, y \rangle = q$, the above equation simplifies to

$$E'_{\text{tot}} = q V'_{\text{tot}}, \quad (4.2)$$

where V'_{tot} represents the total virtual displaced volume,

$$V'_{\text{tot}} = \int_Y \int_X u'\langle x, y \rangle dx dy. \quad (4.3)$$

Expressions for V' can easily be derived for various types of fundamental displaced shapes, which in turn can be used to construct different types of collapse mechanisms. This is done in Chapter 6 (refer to Figure 6.9 and Table 6.1).

The total internal virtual work is obtained by summing the energy contributions from the various cracks present in the mechanism. The energy of a single crack is a product of its moment M and virtual rotation θ' . Therefore, the total internal work along the mechanism is

$$U'_{\text{tot}} = \sum_{i=1}^n M_i \theta'_i, \quad (4.4)$$

where i is the crack index and n is the total number of cracks.

By applying the principle of energy conservation and equating the external and internal virtual work terms [Eqs. (4.2) and (4.4)], the pressure resistance of the wall becomes

$$q = \frac{U'_{\text{tot}}}{V'_{\text{tot}}} = \frac{\sum_{i=1}^n M_i \theta'_i}{V'_{\text{tot}}}, \quad (4.5)$$

where crack rotations (θ'_i) and displaced volume (V'_{tot}) are geometric properties dependent on the shape of the assumed collapse mechanism. By contrast, the moment contribution (M_i) along each crack is dependent on the geometric and material properties of the masonry, as well as vertical compression throughout the panel.

An inherent aspect of plastic analysis is that it requires an accurate assumed collapse mechanism to produce an accurate prediction of strength. Since conceptually there are an infinite number of possible collapse mechanism shapes that may be applied to any particular wall, the critical or 'correct' mechanism is the one that occurs under the smallest load—that is, it produces the minimum collapse

pressure based on Eq. (4.5). Because of this, the method is often termed *upper bound*, as any chosen mechanism can only provide an upper limit to the strength of the critical mechanism. Finding the critical solution not only requires for various different types of collapse mechanisms to be considered (for example refer to Section 6.2), but within each mechanism, the shape-defining variables such as the mechanism length and height dimensions and diagonal crack angles effectively become independent variables that need to be optimised in order to minimise the failure load.

4.2.2 Adaptations of the Method for Design

Numerous different adaptations of plastic theory have been developed for calculating the ultimate load capacity of two-way URM walls, several of which are used in design codes today. These include traditional yield line analysis [Johansen, 1962], the fracture line method [Sinha, 1978, 1980], the failure line method [Drysdale and Baker, 2003; Baker et al., 2005], and the virtual work method [Lawrence and Marshall, 1996, 1998, 2000]. The appeal of plastic analysis lies in its versatile applicability, in that it can easily deal with irregular wall configurations, walls with openings and different edge fixities.

The theoretical problem with the application of plastic theory, which assumes simultaneous attainment of moment capacities along the various cracks, to a brittle material such as URM is already well established [Baker, 1973; Haseltine et al., 1977; Lawrence, 1983; Baker et al., 1985; Haseltine and Tutt, 1986; Drysdale and Essawy, 1988; Lovegrove, 1988; Southcombe et al., 1995].³ This is particularly true in reference to the yield line method, which was the first application of plastic analysis to URM, and of the various methods makes the most unconservative set of assumptions; as such, it has been shown to overpredict wall strengths in many instances. The subsequent methodologies developed have addressed some of these conceptual issues and provided a more justifiable treatment of plastic analysis applied to URM. Therefore, the aim of this review is not to debate the validity of plastic analysis, but rather to provide an overview of the various methods and discuss their underlying assumptions with respect to further development. For a quantitative comparison between some of these methods, the reader is also referred to work by Maluf et al. [2008].

Generalisations

Each of the methods share the following features:

³Also see discussions between Lovegrove, Beal, and Lawrence [1989].

- The failure mechanisms implemented are based on typical two-way crack patterns shown by Figure 4.1. This general class of crack patterns, characterised by the propagation of diagonal crack lines from corners at which adjacent supported edges meet, has been observed throughout many experimental studies [*Baker, 1973; Anderson and Bright, 1976; West et al., 1977, 1979b,a; Hodgkinson et al., 1982a,b; Lawrence, 1983; Tapp, 1985; Drysdale and Essawy, 1988; Chong, 1993; Ng, 1996; Abrams et al., 1996; Griffith, 2000; Edgell and Kjær, 2000; Jaramillo, 2002; Korany, 2004; Edgell, 2005*] including the experimental work reported in Chapters 2 and 3.
- The length and height dimensions of the mechanism are assumed to take on the full length and height spans of the wall. This assumption appears to be reasonable for URM constructed with mortar based on both experimental evidence and analytical predictions, in that the longest possible mechanism span will generally lead to the lowest calculated load. However, as demonstrated through parametric studies reported in Section 6.7.1, this generalisation only remains valid as long as bond strength of the masonry significantly exceeds the vertical compression from the self-weight of the wall. For walls with very weak or zero bond cohesion, which obtain their strength primarily from self-weight effects, there exists a critical mechanism height at which the failure load becomes minimised. If the height of such a wall exceeds the critical height, then the mechanism will not utilise the full available span.

By contrast, the most significant distinctions between the methods lie in the following:

- Method of calculation of moment capacities along cracks;
- Selective inclusion of crack energies toward the internal work; and
- Treatment of the diagonal crack slope in the mechanism as either an independent variable or predefined.

Standard Yield Line Analysis

Yield line analysis, which was originally developed for design of reinforced concrete slabs by *Johansen [1962]*, was the first application of plastic analysis to ultimate strength design of two-way URM walls. The method was adopted in the 1978 version of the British code [*British Standards Institution, 2005*] and is still presently used by the Eurocode [*Comité Européen de Normalisation, 2005*]. The basic form of

the design equation in terms of the pressure capacity q_c is

$$q_c = \frac{\bar{M}_{vc}}{\beta L^2}, \quad (4.6)$$

where \bar{M}_{vc} is the moment capacity in vertical bending per unit length, L is the wall length, and β is a moment coefficient corresponding to the particular wall aspect ratio, orthogonal strength ratio and wall boundary condition. Eurocode 6 tabulates values of β for a range of wall configurations and edge fixities, including O-, U- and C-shaped walls, but not L-shaped (refer to Figure 1.2 for an explanation of the codes). Alternatively, these coefficients may also be calculated using closed-form expressions [e.g. *Golding, 1991*].

Yield line analysis makes the highest strength predictions of the various plastic analysis adaptations for design, as it assumes full moment capacities to be achieved along all cracks present in the mechanism. The effective moment capacity in vertical bending is specified as

$$\bar{M}_{vc} = (f_{mt} + \sigma_v) \bar{Z}, \quad (4.7)$$

where f_{mt} is the flexural tensile strength (determined from wallettes subjected to vertical bending), σ_v is the design vertical stress and \bar{Z} is the sectional modulus per unit length. By contrast, the capacity in horizontal bending is effectively treated as

$$\bar{M}_{hc} = f_h \bar{Z}, \quad (4.8)$$

where f_h is the equivalent flexural strength determined from wallettes subjected to horizontal bending, and hence intrinsically accounts for a combination of line and stepped failure (refer to Figure 4.4). Furthermore, the yield line approach implicitly assumes the diagonal moment capacity along an inclined crack with angle φ to be

$$\bar{M}_{dc} = \bar{M}_{vc} \cos^2 \varphi + \bar{M}_{hc} \sin^2 \varphi, \quad (4.9)$$

which simply resolves the capacities \bar{M}_{vc} and \bar{M}_{hc} along the diagonal axis and therefore effectively assumes that both are reached simultaneously. This treatment of diagonal bending appears to be a further unconservative aspect of the method, in light of various experimental evidence suggesting that the vertical and horizontal bending components in diagonal bending do not achieve their capacities simultaneously, but are rather governed by a biaxial failure criterion [*Baker, 1979; Sinha et al., 1997; Griffith et al., 2005*].

A feature of the yield line approach is that the diagonal crack angle φ is treated as an independent variable, which is implicitly optimised to minimise the failure load. This is in comparison to the Australian **VW** method, which assumes the

diagonal crack angle to be predefined along the natural slope of the masonry, on the basis of experimental observations and the reasoning that this is the natural plane of weakness for brickwork (as will be discussed later). While the treatment of φ as a variable is a conservative step in the yield line method, and will act to slightly counteract its set of other unconservative assumptions, it could be argued that for a material such as clay brick work it should not really be required since the cracks will generally form along the predefined line of weakness.

Fracture Line Method

The fracture line method is a modification of yield line analysis developed by *Sinha* [1978, 1980]. Even though the governing equations are derived using a moment equilibrium approach rather than the energy approach (as described in Section 4.2.1), the method is still based on the same concepts as standard yield line analysis, including moment contribution from all cracks, allowance for moment capacity orthotropy, and treatment of the diagonal crack slope as an independent variable. However, it also allows for independence between the developed internal moments in the vertical and horizontal directions, by making the approximation that these moments are distributed according to the stiffness orthotropy of the masonry k , defined in the method as the ratio of the Young's modulus of elasticity in the two directions:

$$k = E_x/E_y.$$

Hence, the method becomes equivalent to standard yield line analysis when $k = 1$ [*Hendry et al.*, 1997].

Failure Line Method

The Canadian code [*Canadian Standards Association*, 2004] uses a modified form of yield line analysis, referred to as the failure line method [*Drysdale and Baker*, 2003; *Baker et al.*, 2005]. The innovation of the method is that it omits internal work contributions along central vertical or horizontal cracks that form early. Assessment of whether or not an early crack forms is determined from comparing the cracking load obtained from a precursor elastic plate analysis, to the load calculated using standard yield line analysis assuming full crack contribution. If the elastic analysis predicts that cracking will occur at a load lower than the yield line method capacity, then a second plastic analysis is performed which omits the internal work contribution from the early crack. Otherwise, the yield line solution is adopted. Hence, the failure line method will always produce strength predictions that are either equal to or lower than standard yield line analysis. The Canadian

code implementation of this method only caters for three edge support shapes—O-, U- and C-shaped walls, with L-shaped walls omitted; and furthermore, for conservatism, it treats any supported edges as being simply supported regardless of the actual edge fixity.

It is also worth noting that similar methodology is currently being developed in Germany [Bakeer, 2011]. In the method described by Bakeer, the internal work contribution along the first crack is formulated in terms of a moment reduction factor, so that a portion of its moment capacity can still be included. This is to avoid underprediction of the strength for very long or very tall walls. Hence, the method becomes equivalent to standard yield line analysis (as per Eurocode 6) when this factor is set to 1 and the Canadian failure line method when it is set to 0.

Virtual Work Method

The virtual work (VW) method is an approach developed by Lawrence and Marshall [1996, 1998, 2000], which was adopted in the 1998 version of the Australian masonry code AS 3700 and retained in its more recent versions [Standards Australia, 2001]. The method differs from yield line analysis, in that: (i) it ignores the moment contribution of horizontal crack lines, (ii) assumes the slope of diagonal crack lines to follow a natural slope governed by the brick unit geometry, and (iii) is based on explicit calculation of the moment capacities in horizontal and diagonal bending using independent analytical expressions.

To calculate the design capacity of the wall, the code provides the formula

$$q = \frac{2a_f}{L_e^2} (k_h \bar{M}_h + k_d \bar{M}_d), \quad (4.10)$$

which is a more user-friendly but mathematically equivalent adaptation of Eq. (4.5). The term L_e is the wall's effective length, while a_f , k_h and k_d are coefficients based on the mechanism geometry. Expressions for these coefficients were derived by Lawrence and Marshall [1996] for the range of failure mechanisms shown by Figure 4.1, and are tabulated in AS 3700. Terms \bar{M}_h and \bar{M}_d represent the horizontal and diagonal bending moment capacities as a moment per unit length of crack. The expressions for these capacities prescribed by AS 3700 are included in Appendix E.1; however, these have numerous shortcomings as described therein. As such, alternate analytical expressions, based mainly on work by Willis [2004] and some modifications by the author, are recommended instead, as presented in Section 4.3.

The omission of horizontal crack contributions from the internal work is to account for the typical experimental observation that horizontal cracks form early

in the response and are therefore unlikely to contribute their full moment capacity at the point that the ultimate strength is reached [e.g. *Lawrence, 1983; Drysdale and Essawy, 1988*]. This measure, however, could result in underprediction of the wall strength in certain scenarios, in particular for walls with high L/H aspect ratio, since omitting the moment along horizontal cracks means that the calculated pressure capacity will become continually lower and approach zero as the length of the wall increases. Clearly, then, there must be some limiting value of wall length above which the load capacity becomes governed by one-way vertical bending response. A more realistic prediction of strength may for such cases could hence be achieved, for example, by introducing a design clause that specifies the pressure capacity as the larger of the two-way bending analysis [as per Eq. (4.10)], and an analysis treating the wall as one-way vertically spanning by ignoring any vertical supports. A further consideration is that since vertical compression will cause horizontal crack lines to provide some moment resistance following cracking, it may be reasonable to include this *residual* moment capacity in the analysis (such analyses are conducted in Section 4.5.2 with favourable results).

A feature of the *VW* approach is that it assumes the diagonal crack angle to inherently follow the natural diagonal slope of the masonry, i.e. one bed joint across, one perpend joint up, and so on (refer to Figure 4.8). Hence, for a given combination of wall dimensions and support arrangement, the collapse mechanism geometry becomes immediately defined from the start of the analysis (Figure 4.1). This allows for much simpler application of the method toward irregular walls such as those with openings, when compared to methods treating the angle as an independent variable, whose application to such scenarios can become quite complicated due to the need for optimisation [e.g. *Baker et al., 2005*]. Experimental studies [e.g. *Lawrence, 1983; Griffith, 2000*, as well the tests reported Chapters 2 and 3] have indeed shown the slope assumption to be reasonable for regular half-overlap clay brickwork walls, in which the natural diagonal slope defines the main line of weakness to diagonal crack formation. However, it may be prudent to treat this assumption with care when dealing with non half-overlapping brickwork or masonry where the tensile strength of the bricks units is low compared to that of the bond, and hence diagonal crack line failure passing through brick units becomes more likely.

Furthermore, there is an inherent difficulty with attempting to develop a rational approach that treats the angle as an independent variable, as it requires a diagonal bending model that can accurately describe the moment capacity as a function of the crack angle. Although some experimental work has been carried out in this area [*Gazzola et al., 1985*], the corresponding analytical models are not yet sufficiently

developed. For example, the approach implicitly used in yield line analysis [Eq. (4.9)], despite being formulated in terms of the crack slope, does not provide a representative model of the biaxial bending failure criterion since it assumes that the orthogonal capacities are reached simultaneously and is therefore likely to be highly unconservative. Alternatively, while the Willis diagonal bending model [refer to Eq. (4.32)] is also formulated in terms of the crack angle, it was developed based on tests where wallette specimens were subjected to a moment oriented along the natural diagonal slope [Griffith *et al.*, 2005]; and as such, it has not been validated for any other crack inclinations.

4.3 MOMENT CAPACITIES

This section presents analytical expressions for calculating the moment capacity of mortar-bonded URM with respect to vertical, horizontal and diagonal bending. These include, in part, expressions based on established bending theory, expressions based on work by Willis [2004] incorporating some modifications by the author, and original expressions by the author.

For each type of bending, two limit states are considered:

1. *Ultimate strength*, prior to which the masonry is assumed to be initially uncracked. At this state, the masonry derives its strength through a combination of material strength in addition to a contribution from vertical compression.
2. *Residual strength*, which assumes that the masonry is fully cracked and thus possesses zero bond strength. At this limit state, the masonry obtains its entire resistance from the acting vertical axial stress.⁴

It should be noted that while each of the presented analytical expressions account for the strengthening influence of vertical compression, it is assumed that the compressive strength of the masonry f_{mc} is large compared to both the flexural tensile strength f_{mt} and the axial stress σ_v (i.e. $f_{mc} \gg f_{mt} > \sigma_v$); and that as a result, the various sectional capacities are governed by the tensile, rather than compressive, modes of failure.

4.3.1 Basic Definitions

The notation used in reference to the geometry of half-overlap stretcher bonded masonry is illustrated by Figure 4.2. The length, height and width of the masonry

⁴Note that equations for the residual moment capacity in horizontal and diagonal bending are included for completeness, even though they are not utilised in the present chapter. The respective expressions are used in Chapter 6 as part of a virtual work analysis for cracked or dry stack masonry.

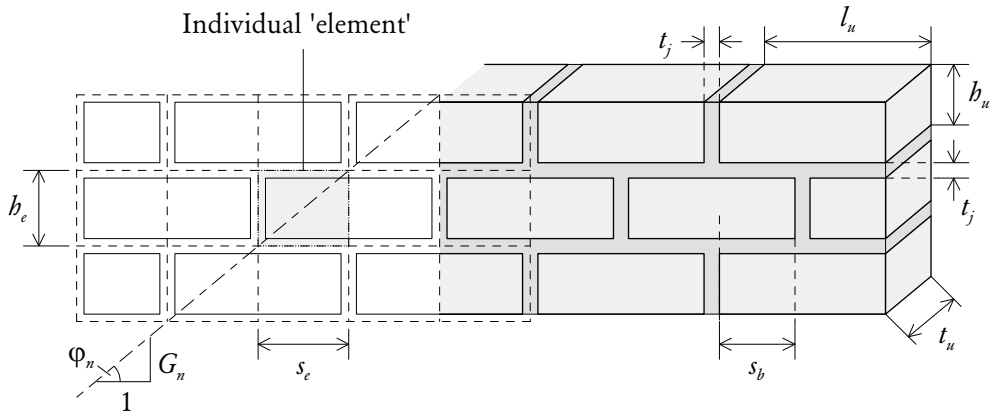


Figure 4.2: Notation relating to the basic geometric properties of half-overlap masonry.

unit are denoted by l_u , h_u and t_u , respectively. The mortar thickness is assumed to be equal for both bed joints and perpend joints and is denoted by t_j .

Let us define a basic 'element' of the masonry matrix as shown in Figure 4.2, whose length s_e and height h_e are, respectively:

$$s_e = (l_u + t_j) / 2, \quad (4.11)$$

and
$$h_e = h_u + t_j. \quad (4.12)$$

The natural diagonal slope of the masonry, G_n , and corresponding angle φ_n are defined by the slope that follows one bed joint across, one perpend joint up (and so on), which is equivalent to the slope of a single element:

$$G_n = \tan \varphi_n = \frac{h_e}{s_e} = \frac{2(h_u + t_j)}{l_u + t_j}. \quad (4.13)$$

As a matter of convenience, throughout this section the various moment capacities are generally provided in terms of the moment acting over a single element, denoted by m . To convert these expressions into a moment per unit length of crack format, denoted by \bar{M} , the following formulae may be used:

For vertical bending,
$$\bar{M}_v = \frac{1}{s_e} \cdot m_v; \quad (4.14)$$

for horizontal bending,
$$\bar{M}_h = \frac{1}{h_e} \cdot m_h; \quad (4.15)$$

and for diagonal bending,
$$\bar{M}_d = \frac{1}{\sqrt{s_e^2 + h_e^2}} \cdot m_d. \quad (4.16)$$

Any of the above \bar{M} formulations may be converted into an absolute moment along

a crack line, denoted by M , using the expression

$$M = \bar{M} \cdot l_C, \quad (4.17)$$

where l_C is the span of the crack, which may be oriented either horizontally, vertically or diagonally, depending on the type of bending.

4.3.2 Vertical Bending

Ultimate Strength

An unreinforced masonry section subjected to pure vertical bending develops flexural stresses normal to the bed joints. The section will begin to crack when the tensile stress reaches the flexural tensile strength of the masonry, f_{mt} . Based on simple elastic beam theory, the corresponding moment to cause cracking is

$$m_{v \text{ ult}} = (f_{mt} + \sigma_v) Z_{be}, \quad (4.18)$$

where σ_v is the acting vertical compression and Z_{be} is the elastic section modulus over the length of the element:

$$Z_{be} = \frac{s_e t_u^2}{6}. \quad (4.19)$$

While the Australian masonry code AS 3700 method ignores the contributions from vertical bending in the design of two-way walls, it prescribes a moment capacity equivalent to Eq. (4.18) for the design of vertically spanning walls. The code expression, which has been adapted for engineering design by incorporating characteristic values of material strength and capacity reduction factors, is included in Appendix E.1 [Eq. (E.1)]. It is worth noting that typical yield line analysis also uses this form of the vertical moment capacity equation for calculating the internal work contributions along horizontal crack lines in two-way wall collapse mechanisms [see Eq. (4.7)].

Residual Strength

Consider a cracked masonry section with thickness t_u , width s_e , and an acting axial load P , subjected to an increasing moment, as shown by Figure 4.3. At the resting state (Figure 4.3a), the stress along the section will be uniform and equal to

$$\sigma_v = \frac{P}{s_e t_u}.$$

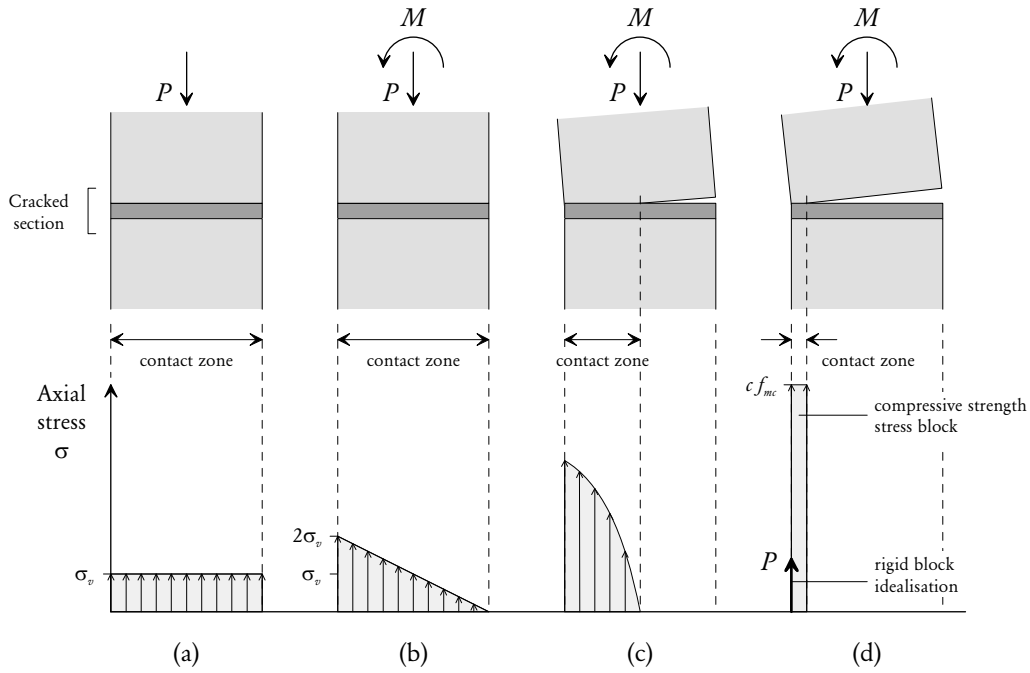


Figure 4.3: Normal stresses along a cracked section subjected to increasing rotation under vertical bending: (a) Resting state; (b) Imminent crack opening with linear elastic stress distribution [governed by Eq. (4.20)]; (c) Partially open crack; (d) Fully open crack with stress concentration at the material crushing limit [governed by Eq. (4.22)], and point load idealisation [governed by Eq. (4.21)].

As a moment is applied, the stress distribution will initially be linear elastic and continue to be so until the section reaches zero stress in the extreme tensile fibre (Figure 4.3b). This condition represents incipient opening of the crack. The corresponding moment at this state can be obtained directly from elastic theory by substituting $f_{mt} = 0$ into Eq. (4.18), producing

$$m_{v \text{ res}} = \sigma_v Z_{be}. \quad (4.20)$$

As the moment is increased further, the crack will continually open up, thus reducing the length of the contact zone across the section and shifting the compressive force resultant toward the extreme compressive fibre (Figure 4.3c). This will also cause the compressive stress to enter the nonlinear range of the material, as shown.

If the portions of the wall above and below the crack are assumed to act as rigid blocks, the maximum moment that can be reached occurs when the force resultant becomes concentrated as a point load at the extreme compressive fibre of the section (Figure 4.3d). The moment at this idealised state is

$$m_{v \text{ res}} = \sigma_v \frac{s_e t_u^2}{2}, \quad (4.21)$$

where σ_v is the equivalent axial compressive stress calculated as if it were uniformly distributed across the entire area of the section.⁵ This equation effectively provides an upper bound to the moment capacity that can be reached along a cracked section, since it assumes the idealisations of material rigidity, infinite compressive capacity (to avoid crushing) and a perfectly flat surface across the crack. Comparing Eqs. (4.21) and (4.20) shows that the moment capacity for the upper bound case of a concentrated compressive stress is three times greater than that of the linear elastic moment capacity at the incipient opening of the crack.

A more realistic estimation of the upper limit to the maximum developable moment can be obtained by accounting for the minimum bearing area necessary to transmit the compressive force across the crack. If we assume that the stress distribution at the material crushing limit can be approximated using a rectangular stress block of magnitude $c f_{mc}$ (Figure 4.3d), the corresponding moment capacity becomes

$$m_{v \text{ res}} = \sigma_v \frac{s_e t_u^2}{2} \left[1 - \frac{\sigma_v}{c f_{mc}} \right], \quad (4.22)$$

where f_{mc} is the crushing strength of the masonry and c is some factor (generally taken as 0.85 in reinforced concrete design). The square bracket term in the above equation effectively acts as a strength reduction factor relative to the moment capacity from idealised rigid block behaviour.

4.3.3 Horizontal Bending

Ultimate Strength

It is well established that horizontal bending generates cracks that can follow two distinct failure patterns: either stepped failure (Figure 4.4a), where the crack follows a toothed pattern alternating between across bed and perpend joints; or line failure (Figure 4.4b), where the crack cuts alternately through perpend joints and brick units. The critical mode of failure is dependent on the relative strength of the masonry with respect to these two modes, whereby the strength against stepped failure is governed by the torsional shear strength of the bed joint [Lawrence, 1975], while the strength against line failure is governed by the tensile rupture strength of the brick units.

The ultimate moment capacity with respect to both failure modes may be calculated either by using expressions provided in the Australian masonry code AS 3700 [Eqs. (E.2a) and (E.2b) in Appendix E.1], or more recent expressions

⁵In other words, $\sigma_v s_e t_u$ is the acting axial force and $t_u/2$ is the lever arm over which the force acts. The product of these is equivalent to Eq. (4.21).

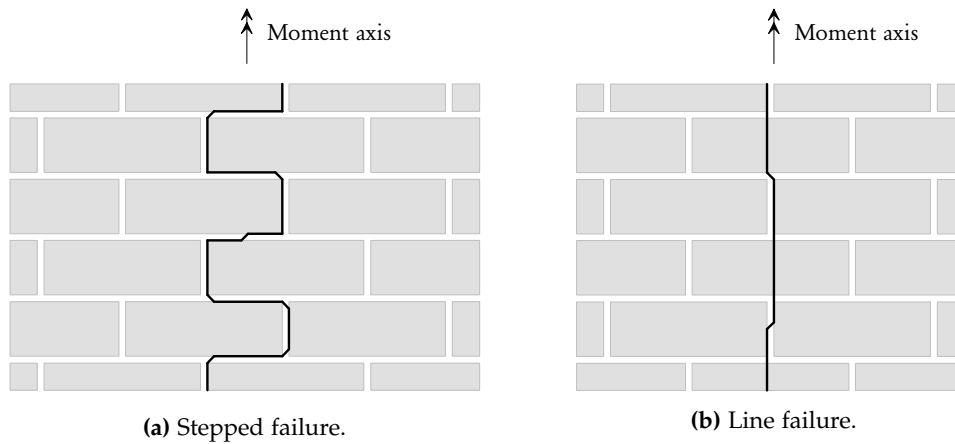


Figure 4.4: Failure modes in horizontal bending.

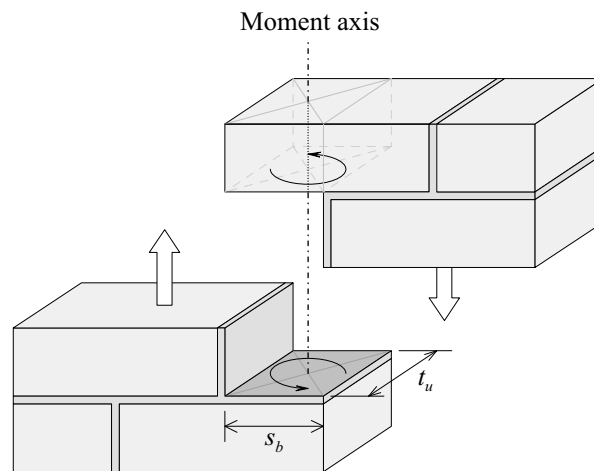


Figure 4.5: Torsion about the centroid of a bed joint.

developed by Willis [2004] [also reported in Willis *et al.*, 2004]. The expressions by Willis provide significant improvements over the code expressions and therefore the author considers them to be the current state-of-the-art models. A slight modification, however, is proposed to Willis' expression for stepped failure, as will be described.

STEPPED FAILURE In his doctoral work, Willis [2004] proposed an analytical equation for calculating the ultimate moment capacity with respect to stepped failure [Eq. (E.8) in Appendix E], which provided a significant improvement over the existing code expression [Eq. (E.2a)], in that it is founded on a rational mechanics-based model, has dimensional consistency, and accounts for the beneficial influence of vertical compression. For reasons that will be outlined, the author proposes a

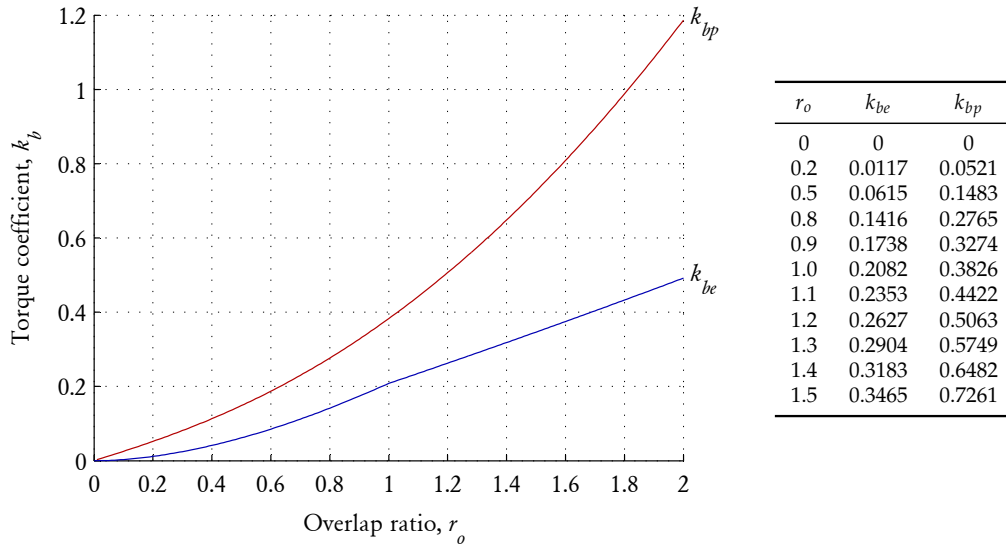


Figure 4.6: Bed joint torque coefficients for varying overlap.

slightly modified version of the expression developed by Willis, as follows:

$$m_{h \text{ ult step}} = k_{be} \tau_{um} t_u^3 \quad (4.23)$$

where τ_{um} is the ultimate shear stress of the masonry bond, and k_{be} is a torque coefficient based on elastic theory. Due to the well established experimental observation that perpend joints tend to crack early in the response [*Base and Baker, 1973; Lawrence, 1983; Gairns, 1983; Baker et al., 1985; Lawrence, 1995*], the equation omits any contribution from flexure along perpend joints and assumes that at the point of peak moment capacity, all resistance is obtained entirely from torsional resistance along the bed joint (refer to Figure 4.5). The fundamental model treats the bed joint as a rectangular section subjected to pure torsion, with failure occurring when the developed shear stress reaches the shear capacity of the bond. To estimate the ultimate shear capacity, Willis proposed the empirical Coulomb type expression

$$\tau_{um} = 1.6f_{mt} + 0.9\sigma_v, \quad (4.24)$$

where the σ_v coefficient, representing the coefficient of internal friction, was taken as 0.9 on the basis of values observed in numerous studies involving in-plane shear behaviour, and the f_{mt} coefficient of 1.6 was subsequently calibrated using data from flexural tests on small brickwork wallettes.

As mentioned, Eq. (4.23) represents a minor revision of the original equation proposed by Willis. While being based on the same fundamental model, the

improvement incorporated into the revised expression gives it more generic applicability. To explain this, let us first define s_b as the minimum bed joint overlap length between two successive courses as shown in Figure 4.2, which may be calculated as

$$s_b = (l_u - t_j)/2. \quad (4.25)$$

The rectangular bed joint section resisting torsion therefore has the dimensions $s_b \times t_u$ (Figure 4.5). Also define the overlap ratio, as the ratio of the overlap length and the brick unit width:

$$r_o = \frac{s_b}{t_u}. \quad (4.26)$$

Since, according to elastic theory [*Timoshenko and Goodier, 1934*], the location of the maximum shear stress along a rectangular section occurs at the midpoint of the longer side, Willis' original expression has the limitation in that it is only strictly valid for a section with good overlap ($r_o \geq 1$). The modified form of the expression [Eq. (4.23)] overcomes this and becomes applicable to any degree of bed joint overlap (i.e. $r_o \geq 0$), due to the method used to calculate the elastic torque coefficient k_{be} . The full procedure for calculating k_{be} as a function of r_o is described in Appendix E.2, or alternatively it may be obtained from Figure 4.6.

LINE FAILURE Willis [2004] proposed that the ultimate moment capacity against line failure can be calculated as

$$m_{h \text{ ult line}} = \frac{1}{2} (f_{ut} - \nu_u \sigma_v) \frac{h_u t_u^2}{6}, \quad (4.27)$$

where f_{ut} is the lateral modulus of rupture of the brick unit, ν_u is the Poisson's ratio of the brick units (typically taken as 0.2), and other variables as defined previously. This equation is based on simple elastic beam theory, with failure assumed to occur when the tensile stress reaches the modulus of rupture. The subtracted term $\nu_u \sigma_v$ in the equation accounts for the weakening influence of Poisson's effect, which causes vertical compression to induce additional lateral tensile stress within the brick units. The coefficient of 1/2 accounts for the fact that only half of the vertical line crack cuts through the available brick units (refer to Figure 4.4b), while the other half cuts through perpendicular joints whose contributions to the moment capacity are ignored, similarly to the previously discussed stepped failure model.

CRITICAL FAILURE MODE Figure 4.7 compares the failure mode expected to be dominant based on the predicted strengths for standard Australian brickwork ($230 \times 110 \times 76$ mm units with 10 mm joints). The plotted line represents equality between the moment capacities predicted using Eqs. (4.23) [with (4.24)] and (4.27).

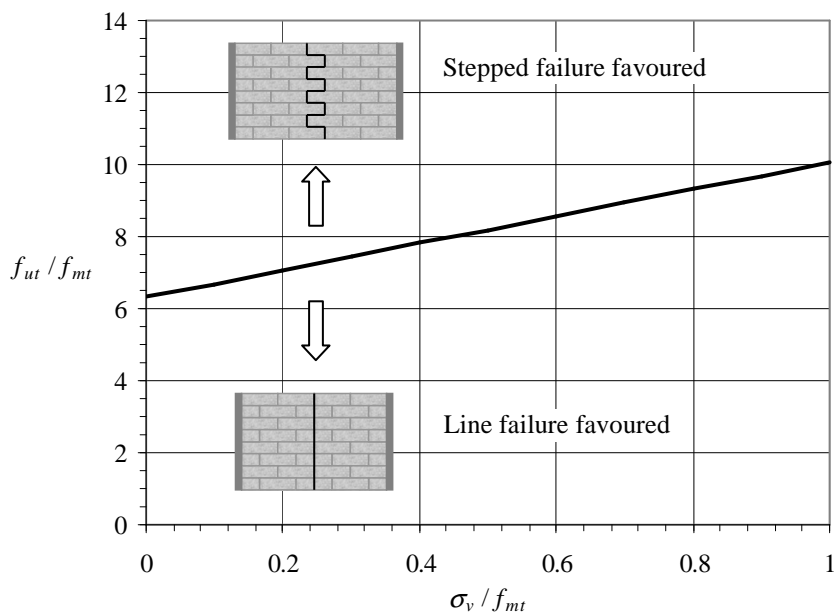


Figure 4.7: Predicted failure mode in horizontal bending for standard Australian brickwork.

It is seen that as the axial load σ_v is increased, the ratio f_{ut} / f_{mt} required for stepped failure to be favoured increases linearly. This trend is a combined effect of both the strengthening influence of σ_v on the resistance against stepped failure, and its weakening influence on the resistance against line failure.

According to the standard design procedure, including that prescribed by AS 3700, once the individual moment capacities for stepped and line failure are calculated independently, the governing moment capacity is taken as the one with the lower value:

$$m_{h \text{ ult gov}} = \text{lesser of } \begin{cases} m_{h \text{ ult step}} \\ m_{h \text{ ult line}} \end{cases} \quad (4.28)$$

However, as the material properties f_{mt} and f_{ut} which influence these moment capacities exhibit a large degree of variability, this treatment raises a conceptual problem when attempting to use a deterministic, rather than a probabilistic approach to calculating the critical moment capacity. This is because a crack will generally tend to follow weak links in the overall masonry matrix due to the variation of material properties throughout a panel, and therefore exhibit a mixture of the two failure modes. Since at a local level the crack effectively has the choice to cut across a brick unit in line failure, or along the bed joints in stepped failure, the option of having two parallel pathways means that the moment capacity of the mixed failure mode will always be lower than that of either mode considered individually.

These issues will not be dealt with in detail in the present section, as Chapter 5 is fully dedicated to investigating them through the development of probabilistic methodologies for estimating the resulting strength reduction, as well as the expected likelihood of each failure mode. It will be noted, however, that for typical levels of material strength variability, the adverse capacity reduction factor of 0.6 used for the design of walls in flexure according AS 3700 appears to be sufficient to cover these effects. As an estimate of the maximum possible strength reduction for a particular level of material strength variability, the reader is referred to Figure 5.9.

Residual Strength

Portions of a vertical crack that undergo stepped failure at the ultimate strength limit state are likely to possess some residual moment capacity due to frictional torsion across overlapping bed joints (Figure 4.5). This capacity may be calculated using the expression

$$m_{h\text{res}} = k_{bp} \tau_f t_u^3 \quad (4.29)$$

where τ_f is the frictional shear stress capacity of the bedded surface, k_{bp} is a plastic torque coefficient, and other variables as defined previously. The frictional shear stress capacity is taken as

$$\tau_f = \mu_m \sigma_v \quad (4.30)$$

where μ_m is the friction coefficient of the bedded surface and σ_v is the acting normal stress. The plastic torque coefficient k_{bp} for a bed joint section with the dimensions $s_b \times t_u$ can be calculated directly from the overlap ratio r_o [defined by Eq. (4.26)], as

$$k_{bp} = \frac{1}{12} \left[2r_o \sqrt{1 + r_o^2} + \ln \left(r_o + \sqrt{1 + r_o^2} \right) + r_o^3 \ln \left(r_o^{-1} + \sqrt{1 + r_o^{-2}} \right) \right]. \quad (4.31)$$

Full derivation of this equation is provided in Appendix E.3. The relationship between k_{bp} and r_o is also plotted in Figure 4.6.

The model is based on the following assumptions:

1. The cracked bed joint is assumed to exhibit full contact across the crack as well as a uniform normal stress, which results in a uniform frictional shear stress capacity along the surface.
2. To oppose the applied torsion, the section is assumed to develop a shear stress equal to its frictional shear capacity along its entire surface, regardless of its distance from the point of rotation. The shear stress distribution is therefore considered to be *plastic*.

3. The point of rotation is assumed to be positioned at the centroid of the rectangular section (as shown in Figure 4.5). This condition results in the shortest aggregate lever arm for the acting shear stresses, thus leading to the lowest possible value of torsion. This assumption is deemed conservative, since placing the pivot at any point other than the section centroid will result in increased torsion.

It is worth noting that the proposed model described here is very similar to a torsional friction model developed by *Orduña and Lourenço* [2005a], which also has the ability to deal with different (non centred) positions of the rotation point along the rectangular section.

Both equations (4.29) and (4.23), representing the residual and ultimate (stepped) moment capacities, have a very similar form—the difference being that the first is proportional to $k_{bp} \tau_f$ and the second to $k_{be} \tau_{um}$. Although it can be seen from Figure 4.6 that $k_{be} < k_{bp}$ for any value of overlap, this effect will generally be outweighed by the fact that $\tau_{um} \gg \tau_f$, due to the cohesion term $1.6f_{mt}$ in Eq. (4.24). The predicted moment capacity of an uncracked section will therefore exceed the predicted capacity after cracking, for realistic values of parameters.

It is important to note that only portions of the vertical crack which exhibit stepped failure (Figure 4.4a) are able to contribute to the residual moment capacity. By contrast, portions of the crack which undergo line failure (Figure 4.4b) provide no residual moment resistance. As mentioned earlier, Chapter 5 provides a developed probabilistic approach for estimating the expected likelihood of these failure modes, which can be used as an estimate of the proportion of the crack expected to undergo each type of failure. A potential application of this methodology is therefore to provide a reduction factor for the residual strength based on the approach presented herein. For an estimate of the proportion of stepped failure expected for standard Australian brickwork, the reader is referred to Figure 5.10.

4.3.4 Diagonal Bending

Ultimate Strength

The ultimate moment capacity along a diagonal crack line can be calculated using several alternative approaches: The first is a model developed by *Lawrence and Marshall* [1996] as part of the AS 3700 VW method, which is still currently in use and is reproduced in Appendix E.1.3. The second is a mechanics-based model developed more recently by *Willis* [2004] [also published in *Griffith et al.*, 2005], which provides numerous improvements over the code approach. The third model

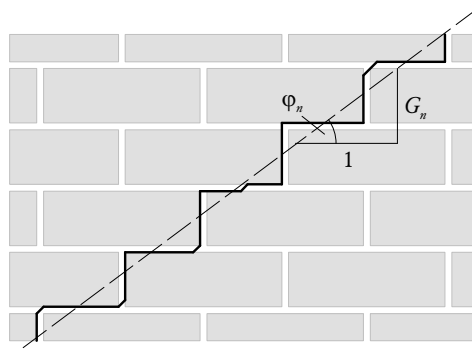


Figure 4.8: Diagonal stepped crack.

is a proposed approach that takes the fundamental concepts behind the Willis model and implements them with a more rational treatment of the biaxial failure criterion, by accounting for the inclination of the applied moments and the strength orthotropy of the masonry. The second and third models will now be described.

WILLIS MODEL Willis [2004] [as also reported in Griffith *et al.*, 2005] developed an analytical expression for predicting the ultimate moment capacity in diagonal bending on the basis that the crack follows the natural diagonal slope of the masonry (Figure 4.8). The model assumes that at the point of ultimate strength, the crack's moment resistance is obtained from combined flexure and torsion acting along the bed joints. By contrast, contributions from capacities along perpendicular joints are ignored due to the observation that they tend to crack early in the response. The model also applies reduction factors to the contributing bed joint flexural and torsional capacities to account for a mutually weakening interaction between these mechanisms—that is, a reduction in the effective torsional capacity due to the presence of normal stresses, and conversely, a reduction in the effective flexural capacity due to the acting shear stresses. Occurrence of such effects has been suggested on the basis of numerous studies [Baker, 1979; Sinha *et al.*, 1997; Hagsten and Nielsen, 2000].

A slightly reformulated but mathematically equivalent version of the equation proposed by Willis [2004] is

$$m_{d \text{ ult}} = m_{v \text{ ult}} \cos^3 \varphi + m_{h \text{ ult step}} \sin^3 \varphi, \quad (4.32)$$

where $m_{d \text{ ult}}$ is the ultimate diagonal moment capacity over a single element, $m_{v \text{ ult}}$ and $m_{h \text{ ult step}}$ are the respective moment capacities of the element with respect to vertical bending and horizontal bending by stepped failure [as given by Eqs. (4.18) and (4.23)], and φ is the angle of diagonal crack line. By separating the portions of

the trigonometric terms in Eq. (4.32) accounting for moment interaction from those acting to resolve the respective moments along the diagonal axis, and converting to a moment per length formulation [using Eqs. (4.14)–(4.16)], Willis' model can be presented in the more generalised form:⁶

$$\bar{M}_{d\text{ult}} = \bar{M}_{v\text{ult}} [\cos^{2n} \varphi \cdot \cos^2 \varphi + \eta \sin^{2n} \varphi \cdot \sin^2 \varphi], \quad (4.33)$$

where $\bar{M}_{d\text{ult}}$ and $\bar{M}_{v\text{ult}}$ are the respective moment capacities per unit length for diagonal and vertical bending, and η is the strength orthotropy ratio defined as $\bar{M}_{h\text{ult}}/\bar{M}_{v\text{ult}}$. This ratio may be calculated on the basis of Eqs. (4.18), (4.23) and (4.24) as

$$\eta = \left[\frac{1.6f_{mt} + 0.9\sigma_v}{f_{mt} + \sigma_v} \right] \frac{6k_{be}t_u}{h_e}. \quad (4.34)$$

The parameter n in Eq. (4.33) can be used to vary the degree of interaction between the flexural and torsional moments, as shown in Figure 4.9. Willis found that a linear interaction ($n = 1$) gave the most accurate predictions compared to the results from four individual tests on wallettes subjected to bending along the natural diagonal slope (Figure 4.8).

While the Willis model incorporates numerous advances over the current AS 3700 approach (included in Appendix E.1.3), its robustness could potentially be limited due to the fact that it ignores the ratio of the horizontal and vertical components of the applied moment and the strength orthotropy of the masonry, and implicitly assumes that the flexural and torsional capacities of the bed joint are reached simultaneously. Such an assumption is not theoretically justifiable and as a result, extension of the model to predicting the moment capacity along a generic crack angle becomes questionable, even though Eqs. (4.32) and (4.33) [also the original equation in *Willis, 2004*] are presented in terms of the crack angle φ . Nonetheless, it seems reasonable to presume that Willis' model should perform well when applied to cracks that follow the natural diagonal slope, since the interaction coefficients [the terms $\cos^{2n} \varphi$ and $\sin^{2n} \varphi$ in Eq. (4.33)] were effectively calibrated

⁶Note that the basic formula for resolving a combined vertical and horizontal bending moment onto an inclined axis can be written in the absolute moment form (M), as

$$M_d = M_v \cos \varphi + M_h \sin \varphi,$$

where M_d is the moment resultant, M_v is the vertical bending component (horizontal axis), M_h is the horizontal bending component (vertical axis) and φ is the angle of inclined axis with respect to the horizontal. Alternatively, in the moment per length (\bar{M}) form, this becomes

$$\bar{M}_d = \bar{M}_v \cos^2 \varphi + \bar{M}_h \sin^2 \varphi,$$

which is the form generally presented in the literature in relation to yield line analysis. It is obvious therefore that care needs to be exercised with regard to the exponents of the sine and cosine terms, depending on the type of formulation being used.

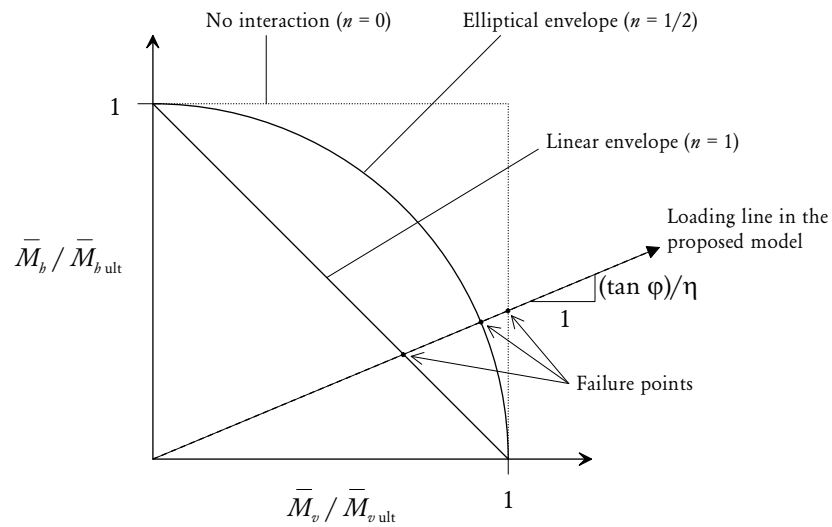


Figure 4.9: Biaxial bending failure criterion with various symmetric envelopes. Each axis plots the ratio of the developed moment to the moment capacity in the respective direction.

using tests on wallettes subjected to such a failure condition. Indeed, incorporation of the model as part of a AS 3700 type virtual work method, in which the diagonal crack slope is assumed to follow the natural slope of the masonry, has shown favourable predictions of strength in comparison to a data set of 64 full-scale walls [Griffith *et al.*, 2005].

DEVELOPED MODEL BASED ON BIAXIAL FAILURE CRITERION To overcome the aforementioned shortcomings of the Willis model, an alternative model based on a more rational treatment of the biaxial failure criterion has been developed. Its full derivation is presented in Appendix E.4.

The proposed model has a similar basis to the Willis model, in that the overall diagonal moment capacity is taken as the sum of the contributing flexural and torsional moments along the bed joints. However, the revised model uses a different implementation of the failure criterion which does not assume simultaneous attainment of the flexural and torsional capacities. Instead, consideration is given to the ratio of the developed flexural and torsional moments, by making the assumption that the ratio of these moments per unit length can be approximated by the inclination of the crack:

$$\frac{\bar{M}_h}{\bar{M}_v} \approx \tan \varphi. \quad (4.35)$$

This estimation of the loading line for a given crack inclination φ , as shown in Figure 4.9, allows for the failure point to be determined as the intersection of the loading line with the chosen failure envelope.

While it is possible for the model to utilise any failure criterion that is defined by a relationship between the ratios $\bar{M}_v/\bar{M}_{v\text{ult}}$ and $\bar{M}_h/\bar{M}_{h\text{ult}}$, the chosen form of the failure criterion is

$$\left(\frac{\bar{M}_v}{\bar{M}_{v\text{ult}}}\right)^{1/n} + \left(\frac{\bar{M}_h}{\bar{M}_{h\text{ult}}}\right)^{1/n} = 1, \quad \text{with } n > 0. \quad (4.36)$$

The effect of n on the resulting envelope is illustrated by Figure 4.9, where it is seen that as n is increased, the mutual weakening effect between flexure and torsion becomes more significant.

In summary, the implementation of the biaxial failure criterion in the proposed model achieves the following:

1. It makes a rational estimate of the ratio of the developed flexural and torsional moments along the crack, instead of making the assumption that their respective capacities are reached simultaneously.
2. It accounts for interaction between the two failure mechanisms (i.e. a mutually reducing effect).

By comparison, the Willis approach only achieves the second point above.

Implementation of the failure criterion defined by Eq. (4.36) into the proposed model results in the following general formula for the ultimate moment capacity along an inclined axis:

$$\bar{M}_{d\text{ult}} = \bar{M}_{v\text{ult}} \frac{(\cos \varphi)^3 + (\sin \varphi)^3}{\left[(\cos \varphi)^{1/n} + (\eta^{-1} \sin \varphi)^{1/n}\right]^n}, \quad (4.37)$$

where the orthogonal strength ratio η may be calculated with respect to the stepped failure mode using Eq. (4.34). Note, however, that as the crack approaches a vertical inclination ($\varphi \rightarrow \pi/2$), the crack becomes more likely to develop some proportion of line failure. Therefore, if the user intends to use this equation along a generic crack angle φ , it may be prudent to take the orthogonal ratio as the lesser of that for the stepped and line failure modes.

In order to determine an appropriate value of the interaction parameter n in the failure envelope defined by Eq. (4.36), a calibration process was undertaken to produce equality between capacities obtained using the proposed model [Eq. (4.37)] and the Willis model [Eq. (4.33)], using the test wallette properties originally used by Willis for the calibration of his equation. These comprised standard Australian brickwork ($230 \times 110 \times 76$ mm units with 10 mm mortar joints) with no applied

axial load ($\sigma_v = 0$), subjected to bending along the natural diagonal slope. Equality between the two models occurs at the value $n = 0.88$, which represents a failure envelope that lies in between linear and elliptical (Figure 4.9). It should be noted, however, that at this particular set of calibration conditions the capacity $\bar{M}_{d,ult}$ predicted using Eq. (4.37) is fairly insensitive to the chosen value of n . This is because at these conditions, the equivalent slope of the loading line in Figure 4.9 is quite low ($\tan \varphi/\eta = 0.717/2.86 = 0.25$), which causes failure to be governed primarily by the vertical bending capacity. This highlights the need for additional experimental data to allow calibration of the failure envelope for a wider range of crack angles.

Because the proposed model has been calibrated to give equal predictions to the Willis model for standard clay brick masonry with no axial stress and crack inclination at the natural diagonal slope, both models are equally valid and effectively interchangeable for the scope of application used in this chapter—that is, prediction of the ultimate strength of test walls from Chapter 2 using the AS 3700 type VW approach, which assumes diagonal cracks to follow the natural diagonal slope of the masonry. The author, however, considers the proposed model to be better suited to application beyond this scope, such as predicting the moment capacities along cracks that do not follow the natural slope, since it is based on a more rational treatment of the biaxial failure criterion. For example, it could be used as an alternative to the unconservative diagonal moment capacity model implicitly used in the yield line and failure line methods [Eq. (4.9)], which ignores interaction between the vertical and horizontal bending contributions and furthermore assumes that their capacities are reached simultaneously.

Residual Strength

The residual moment along a diagonal crack can be estimated using principles similar to those used for vertical bending. As shown by Figure 4.3(d) the maximum attainable moment occurs when the axial load is concentrated at the extreme compressive fibre of the section. If the portions of the masonry above and below the crack are assumed to act as rigid blocks, then the moment capacity at this state is equal to

$$m_{d, \text{res}} = \sigma_v \frac{s_e t_u^2}{2} \cos \varphi, \quad (4.38)$$

which is equivalent to the capacity for a horizontal crack under vertical bending [Eq. (4.21)], resolved onto the inclined axis of the crack by the $\cos \varphi$ term.

4.4 WALLS WITH OPENINGS

While the AS 3700 codified VW approach gives provisions for walls with openings, the treatment provided therein makes several conservative simplifying assumptions. One of these is that the area covered by the opening is subject to the same uniform pressure as the solid portions of the wall. Although this representation is reasonable when the wall is subjected to wind loading, it introduces some level of conservatism with respect to earthquake induced inertial loading, since the openings will generally have a lower mass density compared to the wall and therefore attract less load. For the purpose of force-based seismic design, this assumption seems quite acceptable since it errs on the side of safety. However, in order to assess the method's accuracy with respect to the walls with openings tested experimentally in Chapter 2, we need a refined approach, since the walls' openings were left unloaded in these tests.

The refined analysis performed for walls with openings is based on discretising the wall into individual elements and using only the solid portions of the wall for contributions to the internal and external work terms. Such an analysis may be easily performed using a spreadsheet. The general steps are as follows:

1. Discretise the wall into individual elements having the length s_e and h_e as given by Eqs. (4.11) and (4.12) and illustrated in Figure 4.2. It is convenient to treat this as the basic unit of discretisation, since it defines the diagonal crack slope based on the brick unit geometry.
2. Superimpose the assumed crack pattern (collapse mechanism) onto the wall. For each of the test walls analysed, the crack patterns used in the analysis were based on full utilisation of the wall length and height spans and closely resembled the experimentally observed crack patterns (see walls s3–s8 in Figure 2.23).
3. Generate a spatial representation of the vertical compressive stress (σ_v) distribution along the panel, and by doing so, calculate the compression acting within each element present. The model used for this purpose shall be described later in this section.
4. Calculate the moment capacity of each crack in the mechanism using the equations in Section 4.3 for the respective types of bending (vertical, horizontal or diagonal). The moment capacity along a single crack is then obtained as

$$M = n_e \cdot m,$$

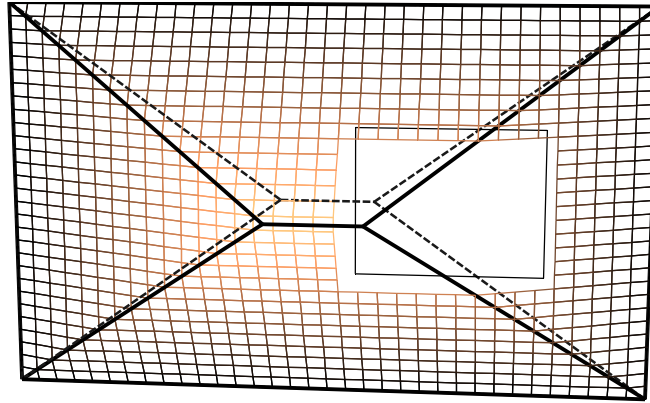


Figure 4.10: Displaced shape for walls s3–s5.

where n_e is the number of elements in the crack and m is the moment per a single element. The vertical stress used in the calculation of m for each crack can be taken as the average vertical stress of the participating elements in the crack, based on the stress profile obtained from step 3. Note that since the moment capacity in horizontal bending is taken as the minimum of the stepped and line failure modes, additional refinement may be introduced by calculating m for each element in the crack using its own value of σ_v , and summing these over the elements present to get the total moment along the crack.

5. Calculate the internal work for each crack by multiplying its moment capacity M by its virtual rotation θ' . (The reader is referred to Figure 6.9 for formulae to calculate the virtual rotations for the different types of cracks.) The total internal work along the mechanism U'_{tot} is then obtained by summing the individual crack energies [Eq. (4.4)].
6. To account for the external work, generate the displacement profile along the mechanism by calculating the displacement at the centroid of each element. The total virtual volume along the mechanism [refer to Eq. (4.3)] is obtained as

$$V'_{\text{tot}} = s_e h_e \sum u'_j,$$

where $s_e \times h_e$ represents the area of a single element and $\sum u'_j$ is the sum of all element displacements along the solid portions of the wall. An example of the calculated displacement profile is shown by Figure 4.10.

7. Finally calculate the wall's pressure capacity q using Eq. (4.5).

As described, step 3 involves the calculation of the spatial distribution of compressive stress (σ_v) within the wall, which is subsequently used to account for vertical stress effects in evaluation of moment capacities in step 4. In the analyses performed (reported in Section 4.5), the stress distribution throughout the wall was evaluated using a two-dimensional axial stress propagation model (Figure 4.11) in which the stresses in a particular course are calculated based on the stresses in the course directly above. Because this scheme computes the stresses in the wall course-by-course, from the top to the bottom of the wall, it is well suited to spreadsheet implementation. The model is based on the following rules:

- Noting that each full brick is comprised of a pair of elements as shown in Figure 4.11a, the stresses σ_{bl} and σ_{br} developed at the base of the brick are calculated from the stresses σ_{tl} and σ_{tr} applied at the top of the brick, by distributing them according to the dispersion coefficient c and adding the stress σ_w from self-weight. Hence, the stresses developed are as follows:

$$\text{for the left element,} \quad \sigma_{bl} = c \sigma_{te} + (1 - c) \sigma_{tr} + \sigma_w;$$

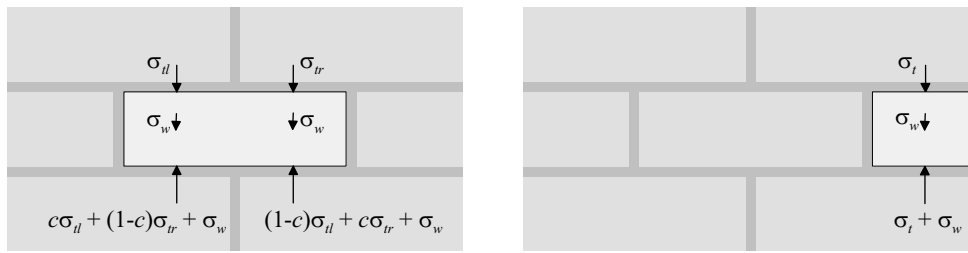
$$\text{and for the right element,} \quad \sigma_{br} = (1 - c) \sigma_{tl} + c \sigma_{tr} + \sigma_w.$$

Valid values of c range from 0.5 to 1.0, with 0.5 causing equal distribution of the stress at the top of the brick to each element below, and 1.0 generating a purely vertical flow of stress with no lateral dispersion. The analytical results reported in Section 4.5 used $c = 0.5$, however, it is noted that the value chosen had only a very minor (less than 1%) influence on the calculated wall strength for all cases considered.

- The stress applied at the base of a half-brick was simply calculated as stress applied at its top, in addition to self-weight (Figure 4.11b):

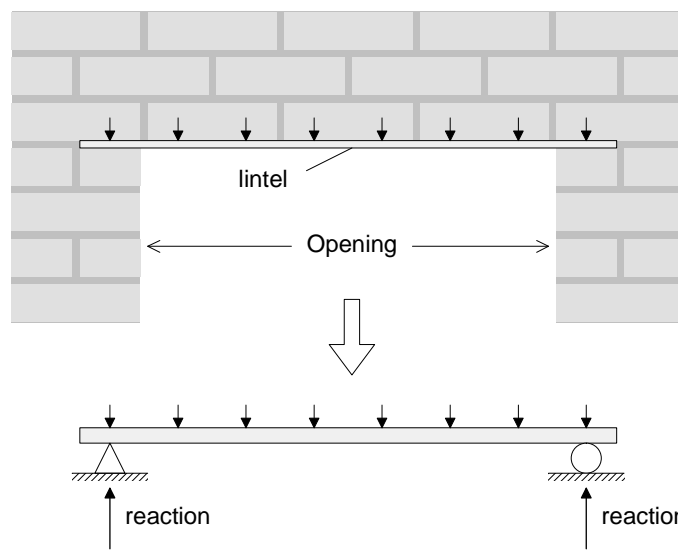
$$\sigma_b = \sigma_t + \sigma_w.$$

- The load reactions developed at the ends of the window lintels were calculated from the forces exerted by the acting elements by treating the lintel as a simply-supported beam (Figure 4.11c). The weight of the lintel itself was ignored from the calculations.
- In walls with precompression (walls s1, s3, s4 and s7), the applied stress was assumed to be uniformly distributed along the top edge; that is, the precise horizontal positioning of load bearing points in the experimental arrangement (Figure B.1 in Appendix B.1) was not accounted for.

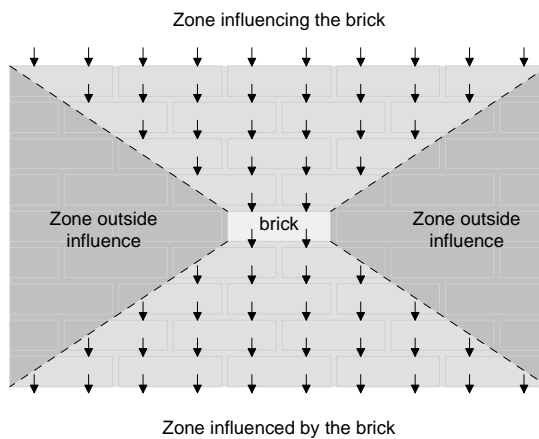


(a) Equilibrium for a full internal brick.

(b) Equilibrium for an external half brick.



(c) Treatment of lintel as a simply supported beam.



(d) Limitation of spatial flow of axial load information by the natural diagonal slope of the masonry.

Figure 4.11: Two dimensional axial stress propagation model.

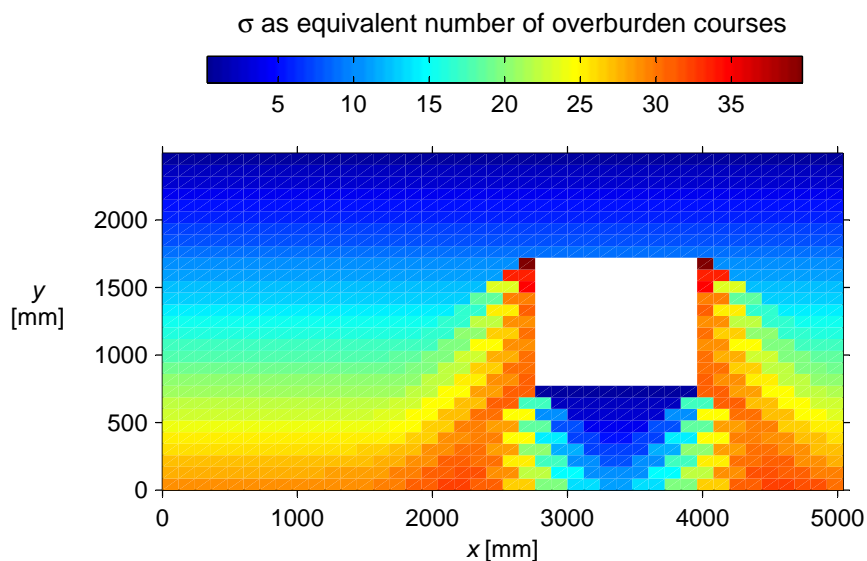


Figure 4.12: Calculated axial stress distribution for wall s5.

As seen from Figure 4.11d, the resulting dispersion of stress in the model is limited by the natural slope of the masonry. An example of the computed stress distribution is shown in Figure 4.12, for wall s5.

4.5 ANALYSIS RESULTS AND COMPARISON WITH EXPERIMENT

To examine the accuracy of the VW method, the measured values of the ultimate strength of the eight full-scale walls (as reported in Chapter 2) were compared to analytical predictions. Trialled within the VW method were two sets of moment capacity expressions for horizontal and diagonal bending: (i) the presently prescribed code expressions (provided in Appendix E.1), and (ii) expressions based on the work by Willis and incorporating some minor modifications by the author [Eqs. (4.23), (4.24) and (4.27) for horizontal bending, and Eq. (4.32) or alternatively Eq. (4.37) for diagonal bending]⁷.

Comparisons were made in two stages:

1. Firstly, by ignoring any moment contributions from vertical bending, as is done by the codified version of the approach in AS 3700 (Section 4.5.1);

⁷The precise results presented here are based on analyses that used the diagonal bending model by Willis [Eq. (4.32)]; however, replacing this with the revised model [Eq. (4.37)] provides wall strength predictions that are very close (within 0.5% for all walls), since the developed model was calibrated to the Willis model for standard Australian brickwork (refer to Appendix E.4.3).

2. And secondly, by including some contribution from vertical moment capacities along the horizontal cracks (Section 4.5.2).

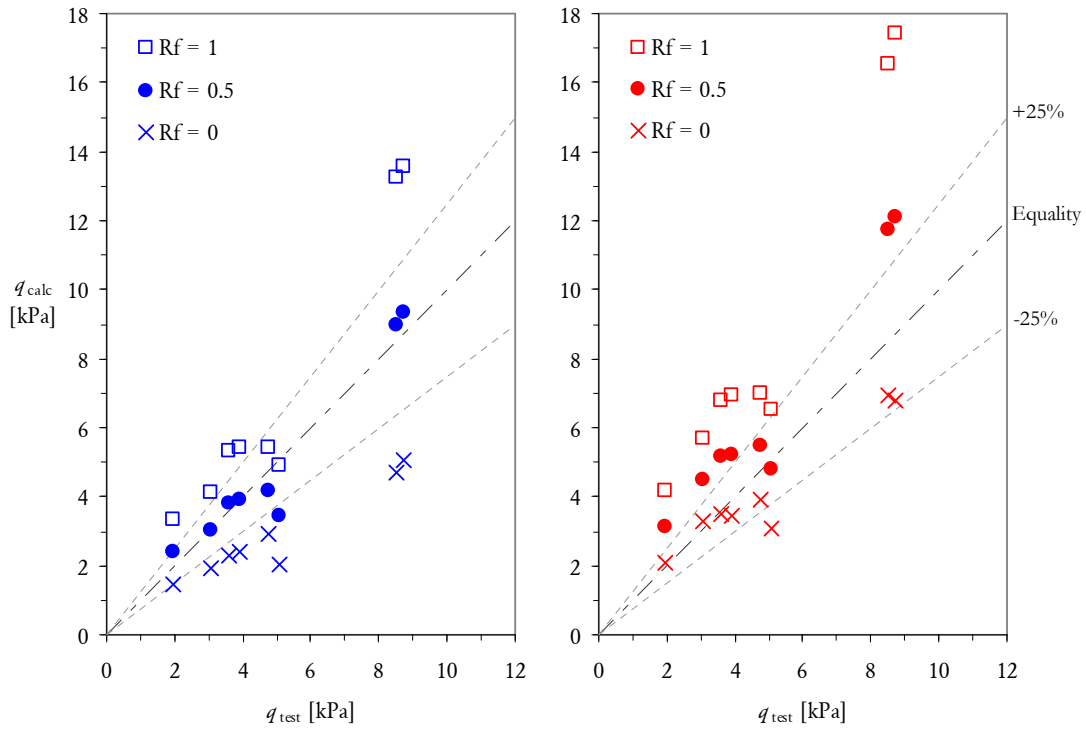
Details of various aspects of the wall configurations, which served as input values for the analyses, can be found in Section 2.3. Wall dimensions and values of precompression are summarised in Table 2.4. The analyses utilised mean values of the measured material properties, including f_{mt} and f_{ut} , as given in Tables 2.2 and 2.3. Note that for each wall its own specific value of f_{mt} was used. The collapse mechanisms applied to each wall were based on the general class of mechanisms illustrated in Figure 4.1. Analyses of walls with openings were performed according to the refined treatment described in Section 4.4.

4.5.1 Ignoring Vertical Bending

In addition to ignoring vertical moments present along horizontal cracks, the analyses conducted made the assumption that diagonal cracks develop their full moment capacities. Horizontal moments along the vertical edge cracks were treated as variable by means of the R_f factor, acting as a multiplier of their nominal moment capacities. In the AS 3700 approach, this factor provides scope to account for varied degree of rotational fixity along these edges. By contrast, internal vertical cracks (present only in wall s6) were assumed to provide their full moment capacity. Results of these analyses are summarised in Table 4.1 and also shown graphically in Figure 4.13.

From the results it is evident that regardless of which set of moment capacity expressions are used, assuming the vertical edge cracks to provide their full moment contribution ($R_f = 1$) leads to overprediction of the wall strength. The resulting strength overestimation is equal to 39% and 80%, on average, for the Willis-based and code expressions, respectively. Taking R_f as 1, however, makes the assumption that the capacities of cracks in diagonal and horizontal bending are reached simultaneously, which may not strictly be the case. In fact, observations of the sequence of crack formation and the cracking patterns at the conclusion of each test (refer to Section 2.5) suggested that the moment resistance along the diagonal cracks was reached before the horizontal bending moment capacity was reached along the vertical edges. Furthermore, cracking along the vertical edges of the walls did not appear to be fully developed in any of the specimens, even after the walls had reached their ultimate strength (refer to Figure 2.23).

To account for the fact that the full moment capacity along the vertical edges may not have been reached at the point of ultimate load capacity, the analyses were repeated, but this time assuming only a partial moment contribution along



(a) Willis-based moment expressions.

(b) Code moment expressions.

Figure 4.13: Comparison of measured and calculated values of strength for the eight test walls. The predictions assume no moment contribution from vertical bending.

Table 4.1: Summary of strength predictions using refined mechanisms and assuming zero moment contribution from vertical bending.

Wall	Measured Strength q_{test} [kPa]	Ratio of calculated to measured strength, q_{calc}/q_{test} , for:					
		Willis-based $M_{h,ult}$ and $M_{d,ult}$			Code based $M_{h,ult}$ and $M_{d,ult}$		
		$R_f = 1$	$R_f = 0.5$	$R_f = 0$	$R_f = 1$	$R_f = 0.5$	$R_f = 0$
s1	4.76	1.14	0.88	0.62	1.47	1.15	0.82
s2	3.04	1.35	0.99	0.64	1.88	1.48	1.09
s3	5.05	0.97	0.69	0.41	1.29	0.95	0.61
s4	3.91	1.38	0.99	0.61	1.78	1.33	0.89
s5	3.59	1.48	1.06	0.64	1.88	1.43	0.98
s6	1.97	1.69	1.22	0.75	2.13	1.60	1.06
s7	8.71	1.56	1.07	0.58	2.00	1.39	0.78
s8	8.52	1.56	1.05	0.55	1.94	1.38	0.81
Mean:		1.39	0.99	0.60	1.80	1.34	0.88
CoV:		0.17	0.16	0.16	0.16	0.15	0.18

the vertical edge cracks, through reduction of the R_f factor. It is seen from Table 4.1 that predictions using the Willis-based expressions provide good agreement with the experiment, in that the average ratio of the predicted and measured strength ($q_{\text{calc}}/q_{\text{test}}$) becomes approximately equal to unity, if the contributions of the vertical edges are taken as 50% of their ultimate moment capacity. Using the code expressions, the R_f factor would need to be reduced even further to 13% in order to achieve unity predictions. By contrast, if the vertical edges are effectively treated as simply supported by taking $R_f = 0$, analyses using both the Willis-based and code expressions underpredict the wall strength, on average, by 40% and 12% respectively. These results suggest that even though the vertical edge connections in the experimental arrangement were designed to behave as fully fixed by providing short return walls with rotational restraint, the vertical edge cracks formed along these edges are unlikely to have developed their full ultimate moment capacities at the same time as the walls achieved their ultimate load resistance.

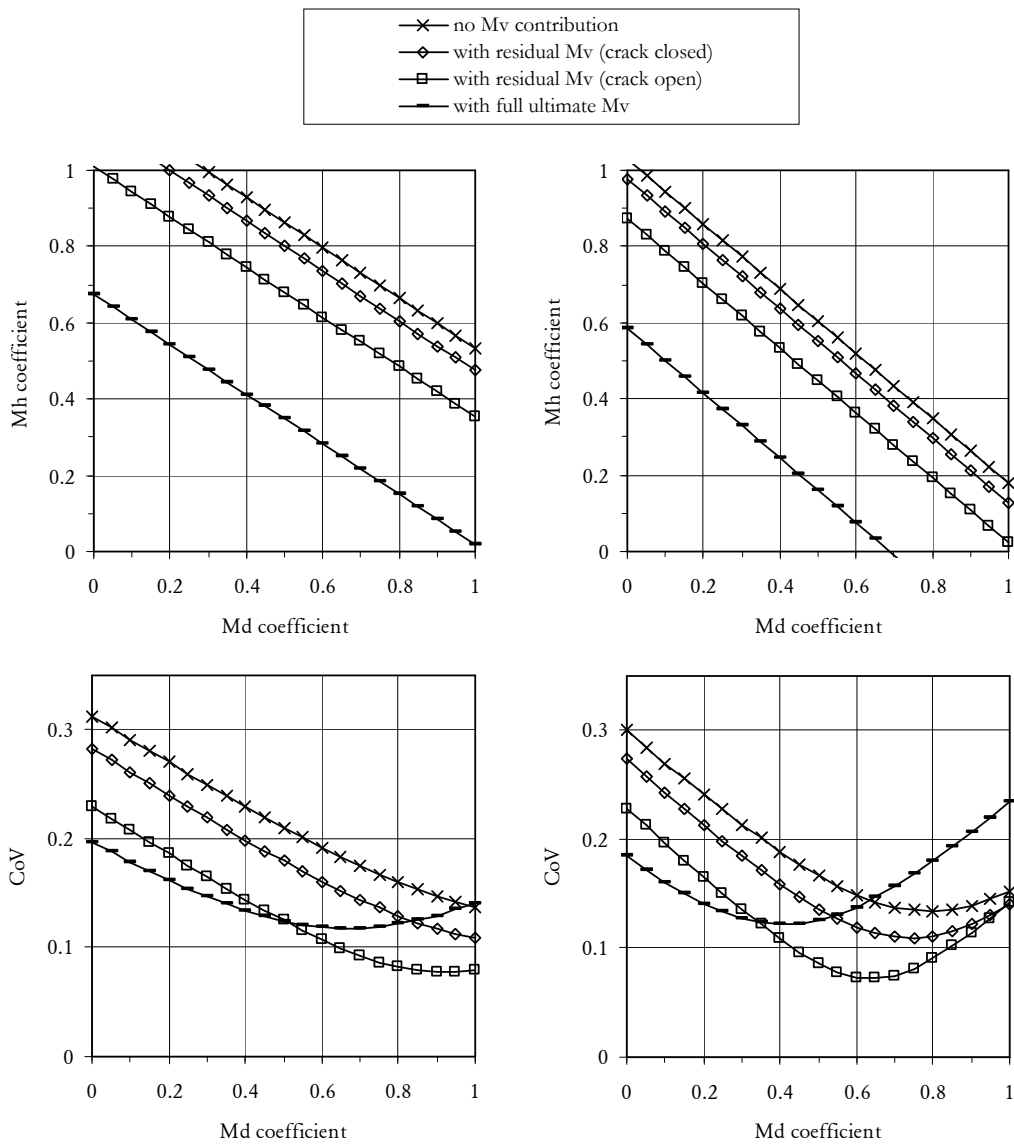
4.5.2 Inclusion of Residual Vertical Bending

It may seem that since the analyses in Section 4.5.1 have already established that strength overpredictions result when both the horizontal and diagonal moments are taken at their full capacities, there is no reason to include further internal work contribution from vertical bending. However, since we know that due to axial compression effects some albeit small residual moments must still be present along the horizontal cracks even after cracking, it could be argued that these should be included in the analysis in order to better represent actual behaviour.

Therefore, a second set of analyses was performed, which allowed for some degree of moment resistance along the horizontal cracks present. The various vertical bending moment capacities trialled as part of the VW approach included:

- Ultimate moment capacity [Eq. (4.18)];
- Residual moment capacity assuming the crack to be open together with idealised rigid rocking behaviour [Eq. (4.21)];
- Residual moment capacity at incipient opening of the crack with a linear elastic stress distribution [Eq. (4.20)]; and
- Zero moment contribution, for comparison.

An assumption of the analyses performed in Section 4.5.1 was that at the point of the wall's ultimate load resistance diagonal cracks within the mechanism exhibit their full moment capacities. However, there is no justifiable reason for making



(a) Willis-based moment expressions.

(b) Code moment expressions.

Figure 4.14: Calibration of moment capacity coefficients for horizontal and diagonal bending, so as to achieve average q_{calc}/q_{test} equal to unity for the eight walls tested. Results are shown for different types of assumed vertical moment capacity along horizontal cracks. The top graphs demonstrate the relationship between the horizontal and diagonal bending moment factors. The bottom graphs show the overall scatter in the predictions between the eight walls, by plotting the CoV of q_{calc}/q_{test} in terms of the assumed diagonal moment coefficient.

this assumption, other than the fact that the walls appeared to reach their ultimate strength close to when these cracks formed. In the opinion of the author, it is likely that at the point that the walls reached their ultimate strength both of these types of cracks exhibited only a limited proportion of their full moment capacities. As discussed in Sections 2.4 and 2.5, the observation of crack progression in conjunction with the measured load-displacement behaviour (Figures 2.11–2.13) suggested that some degree of moment redistribution occurred as the applied deformation was increased, with gradual transfer of the internal load resistance mechanisms from diagonal bending to horizontal bending. Hence, the peak load of the walls was most likely reached at some point during this moment redistribution process—that is, before the vertical cracks had yet reached their full moment capacity, but after the moment along diagonal crack lines had already begun to reduce.

To account for these effects in the analysis, reduction coefficients were implemented to both the ultimate diagonal and horizontal moment capacities M_d and M_h . A subsequent calibration process was undertaken to determine what proportion of the ultimate bending moment capacities in horizontal and diagonal bending was likely to contribute toward the ultimate strength of the test walls. This process involved assuming a particular value of the diagonal moment coefficient and varying the horizontal moment coefficient to achieve an average value of $q_{\text{calc}}/q_{\text{test}}$ for the eight walls equal to unity. Since this process ensures that the predictions are, on average, neither conservative nor unconservative, the only meaningful measure of prediction accuracy becomes the scatter in the predictions, which was quantified using the coefficient of variation (CoV) of $q_{\text{calc}}/q_{\text{test}}$ across the eight walls. Results of these analyses are provided in Figure 4.14 by graphing the relationship between the horizontal and diagonal moment coefficients and the resulting scatter in the predictions.

From the results, it is evident that prediction scatter becomes minimised when some quantity of residual moment capacity is assumed to be present along the horizontal crack lines. This is not surprising given that this representation provides a more accurate account of the internal resistance within the wall, compared to simply ignoring the vertical moment capacities as done by the codified AS 3700 approach. The graphs indicate that regardless of whether the VW analysis uses Willis-based or code expressions for M_h and M_d , the most favourable predictions occur when residual moment capacity based on rigid body rocking [Eq. (4.21)] is assumed to be active along the horizontal crack lines. Using the Willis-based moment equations (Figure 4.14a), the CoV becomes minimised at a value of 7.7%, when the diagonal and horizontal moment coefficients are set to 0.90 and 0.42, respectively. Values of these coefficients are comparable to those established to give

good predictions in Section 4.5.1 in the absence of vertical bending (1.0 and 0.5 respectively); however, the resulting prediction scatter becomes effectively halved (from $CoV = 16\%$) simply by accounting for residual vertical bending.

It is emphasised that the aim of this calibration study was not to derive values of moment factors that can be directly implemented into a generalised design procedure, but rather to establish likely values of the contributing moment capacities for this particular set of walls. These walls, in particular, had full moment restraint along their vertical edges and therefore different coefficients would be expected for similarly shaped walls, but with different rotational restraint. Derivation of such values for a generalised design procedure would furthermore require consideration of a much larger experimental data set.

Nonetheless, if we hope to implement moment capacity models such as those by Willis, which have been developed and calibrated based on uniaxial bending tests on small scale wallettes, into the plastic analysis approach for design of two-way walls, then application of such reduction factors for the purpose of design becomes conceptually justifiable on the following grounds:

- The various cracks present in the mechanism do not reach their ultimate capacities simultaneously, as already discussed.
- Due to the internal moment distribution developed throughout a wall as a result of two-way action, cracks generally form by propagating, rather than forming instantaneously along their entire length. Therefore, it is unlikely that even an individual crack could be able to reach its full moment capacity simultaneously, since some portions of the crack will already have failed, while others will not yet have achieved their capacity.
- Variability in material strength properties, including f_{mt} and f_{ut} , throughout the wall causes cracks to propagate along weak links within the masonry and therefore to exhibit a lower capacity than suggested by a deterministic analysis which uses mean values of these material properties. Such effects are investigated further in Chapter 5 with regard to horizontal bending.

4.6 CONCLUSIONS

A review of various plastic analysis techniques for ultimate strength design of two-way walls has been conducted. Of the methods available, the **VW** method used in AS 3700 is appealing because it is based on explicit calculation of moment capacities along the various types of crack lines. Significant advances have been

made recently in development of corresponding analytical models for predicting the moment capacities of URM in horizontal and diagonal bending. These models were fed into the VW method and analyses were conducted on the eight walls from tests reported in Chapter 2. Each of these walls had full moment connections along their vertical edges and thus required formation of vertical cracks to generate a failure mechanism. However, comparisons of the predicted values of strength with measured values indicate that it is unlikely that both the diagonal and vertical cracks achieved their full capacities simultaneously. Indeed, this conclusion was supported by the crack patterns observed during testing, as only a limited amount of cracking had been visible along the vertical edges even after the walls had been pushed beyond their ultimate strength. Furthermore, it was demonstrated that it may be worthwhile to include some residual capacity along horizontal crack lines in the mechanism—something not presently done by the codified version of the method—as this reduced the overall scatter in the predictions.

Nonetheless, it must be emphasised that these conclusions are based only on analytical predictions made for the eight walls reported in Chapter 2. A more comprehensive comparison study based on a much larger experimental data set is still needed in order to validate these findings, which can be a focus for future work. A summary of the existing experimental data that could be used for this purpose is presented in Table 2.1.

Chapter 5

PROBABILISTIC METHODOLOGY FOR HORIZONTAL BENDING

Abstract

Unreinforced masonry subjected to horizontal bending can undergo cracking by two distinct modes: either by stepped failure along the masonry bond, or line failure cutting directly through the brick units. Because of variability in the material properties, vertical cracks typically tend to develop a mixture of both failure modes. This chapter presents two stochastic analysis methodologies. The first deals with calculating the ultimate moment capacity in horizontal bending by accounting for the weakening effect associated with a combined mode of failure. Strength reduction factors are derived for the mean and characteristic strength, which may be applied toward both static and seismic design. The second methodology is for calculating the expected likelihood of each mode of failure, which has implications toward a wall's seismic resistance, since the two modes result in significantly different post-cracking behaviour. This approach may be used in the calculation of an effective residual moment capacity, as well as for assessing the integrity of supported vertical edges against various types of secondary failure in order to ensure that a panel can continue to respond in two-way bending after cracking.

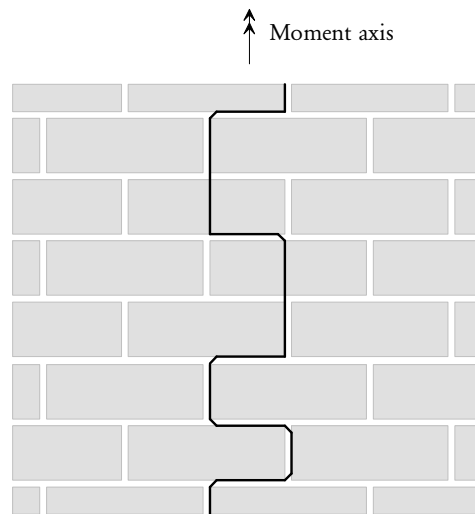


Figure 5.1: Mixed failure along a vertical crack in horizontal bending, consisting of both stepped and line failure.

5.1 INTRODUCTION

The material properties of unreinforced masonry (URM) exhibit a high degree of variability compared to other structural materials such as steel or concrete. This is due to factors such as variability in the manufacturing process, quality of on-site workmanship, environmental conditions during manufacture and construction, and random variation in the materials themselves [Lawrence and Lu, 1991]. Nonetheless, the current state-of-the-art probabilistic design procedures for masonry are still far less advanced than those for materials such as steel, concrete and wood [Schueremans and Gemert, 2006]. As noted by Stewart and Lawrence [2002], “a need clearly exists for developing a theoretical framework that can be used for the calculation of the reliability of masonry structures.”

Horizontal bending is an aspect of URM behaviour that warrants the attention of probabilistic techniques. As discussed in Section 4.3.3, vertical cracks can form by two distinct modes: (i) *stepped failure*, where the crack follows a stepped pattern along the bond of perpend and bed joints (see Figure 4.4a); and (ii) *line failure*, where the crack passes alternately through the brick units and perpend joints as a straight line (see Figure 4.4b). The tendency of either type of failure to be favoured depends on the relative strengths of the brick units and the masonry bond.

It has been demonstrated both in practice and experimentally, that vertical cracks rarely exhibit either of these failure modes exclusively; instead, they tend to develop a combination of the two modes (Figure 5.1), due to local variation in the material properties throughout the panel. Examples of this were evident in

the experimental study on full-scale walls, as demonstrated by the observed crack patterns (Section 2.5). Whilst major advances have been made in recent years in the analytical techniques for calculating the ultimate moment capacity with respect to both modes of failure [Willis *et al.*, 2004], little consideration has been given to the fact that these modes tend to occur in combination. This gives rise to several issues, which should be considered in the context of both static and seismic assessment.

ISSUES RELATING TO ULTIMATE MOMENT CAPACITY To obtain the design moment capacity according to the AS 3700 [Standards Australia, 2001] procedure, the designer must separately calculate the moment capacities for the stepped and line failure modes using characteristic material properties, and adopt the lower value.^{1,2} However, since crack formation is governed by weak link effects, the characteristic strength of the combined (stepped and line) failure mode will always be lower than the characteristic strength of either of the two failure modes considered separately (this is demonstrated later in this chapter). The same also holds for other statistical values, such as the mean and median strength. Hence, the currently-used design procedure has the potential to be unconservative. Whilst it can be reasoned that any reduction in ultimate strength arising from weak link effects is likely to be accounted for by the capacity reduction factor used in design,³ the issue should nonetheless be investigated using a probabilistic approach. These issues, concerning the ultimate strength limit state, have relevance to both static (e.g. wind) and seismic loading.

ISSUES RELATING TO WALL BEHAVIOUR AFTER CRACKING The type of failure developed along vertical cracks has significant influence on the post-cracking response of the wall, which is relevant to its seismic resistance. Because post-cracking resistance of stepped cracks is derived from friction, stepped cracks tend to possess residual strength with good energy dissipation characteristics. By contrast, line failure tends to be brittle with the resulting cracks having zero residual strength. Furthermore, if a large number of brick units along a panel's vertical edge support fail by line cracking, the support's capacity to provide a load path for the out-of-plane face load may become diminished. In extreme cases, it is even possible for the wall to separate from its vertical supports and revert to one-way vertical bending. Such failure occurred in several wall specimens from the quasistatic cyclic tests reported in Chapter 2 (refer to Figures 2.26 and 2.27);

¹Throughout this chapter, characteristic strength is defined as the strength below which 5% of the samples are expected to fail.

²The AS 3700 equations for horizontal bending are reproduced as Eqs. (E.2a) and (E.2b) in Appendix E.1

³AS 3700 prescribes a capacity reduction factor of 0.6 for design of URM walls in flexure.

which, in one case, led to the wall's post-cracking strength, displacement capacity and hysteretic damping capability, becoming considerably reduced (refer to Figure 2.20). Therefore, in the context of seismic assessment, which relies on the wall's ability to maintain good residual strength, it is of significant interest to develop an analytical tool that can quantify the influence of material variability on the wall's post-cracking behaviour.

The aforementioned issues justify development of probabilistic methodology for horizontal bending, which can have potential application to both static and seismic design of two-way panels. The main objectives of this chapter are twofold:

1. Investigate the weakening influence of the mixed mode of failure on the ultimate load capacity, and derive equivalent strength reduction factors for characteristic and mean strength. This approach is developed in Section 5.5.
2. Develop a method for calculating the expected likelihood of each individual failure mode, and in doing so, derive an effective strength reduction factor for residual strength. This is achieved in Section 5.6.

This chapter is structured as follows: Past research on the use of probabilistic methods applied to masonry is reviewed in Section 5.2. A study involving the characterisation of the variability aspects of the relevant material properties is presented in Section 5.3. The theoretical basis of the new methodology is discussed in Section 5.4. A developed stochastic approach for calculating the ultimate moment capacity is presented in Section 5.5. A developed approach for calculating the expected likelihood of each of the failure modes, which has influence on the residual strength of the masonry, is presented in Section 5.6. The predictions made by the proposed methodology are compared to the results of experimental work in Section 5.7. A study investigating the influence of various parameters using the new methodology is presented in Section 5.8. The conclusions and main outcomes are summarised in Section 5.9.

5.2 PREVIOUS USE OF PROBABILISTIC MODELS

Despite the highly variable nature of URM compared to other structural materials, development of probabilistic design methods has so far been limited [*Schueremans and Gemert, 2006*]. Furthermore, the majority of such work has focused primarily on compression loading, and only a small handful of studies have considered flexural strength [*Stewart and Lawrence, 2002*].

Most of the previous research involving out-of-plane bending of URM includes work by Lawrence. One set of such studies investigated the influence of material variability on the initial cracking strength of two-way panels [Lawrence and Cao, 1988; Lu and Lawrence, 1991]. These utilised Monte Carlo simulation whereby material properties were randomly assigned throughout the wall, followed by an elastic analysis to determine the load necessary to generate internal stresses which would cause the flexural capacity to become exceeded somewhere within the panel. This approach allowed the expected cracking load and its variability to be determined as a function of the variability in the material properties.

In another set of studies, Lawrence [1991] demonstrated the use of the Monte Carlo technique to predict the ultimate strength of vertically and horizontally spanning masonry panels. In the study involving vertical bending, Lawrence tested two hypotheses: (i) an averaging hypothesis, in which the strength of a course of units was taken as the average strength of the individual bonds along the course; and (ii) a weakest link hypothesis, in which the strength of a course was assumed to be governed by the weakest bond along the course. It was found that the averaging hypothesis tended to overestimate the panel strength and the weakest link hypothesis gave reasonably good correlation with experiment. The physical interpretation of this result is that failure in horizontal bending is initiated by the weakest joint within a masonry course and that once the weakest joint fails, the crack immediately propagates throughout the entire course. In the study involving horizontal bending, Lawrence conducted a Monte Carlo simulation utilising a finite element analysis to predict the cracking and ultimate strength. It was found that the analysis gave accurate although slightly conservative predictions of the ultimate strength and that the ultimate strength was highly dependent on the variability of the modulus of rupture of the brick units.

5.3 RANDOM VARIABILITY IN THE MATERIAL PROPERTIES

The methodology developed in this chapter is founded on representing key material properties as random variables, defined through a chosen probability distribution, mean value, and coefficient of variation (CoV)⁴. The two most influential material properties on the generated mode of failure are the flexural tensile strength of the masonry bond, f_{mt} , and the lateral modulus of rupture of the brick units, f_{ut} [refer to the governing equations, Eq. (5.1) and (5.2)]. This section reports a study aimed to establish typical levels of variability and suitable probability distributions to represent these properties. Although the Poisson's ratio of the brick units, ν_u ,

⁴Due to its dimensionless nature, the measure of the level of variability adopted throughout this chapter is the CoV, defined as the standard deviation divided by the mean.

is another material property influencing the moment capacity for line failure, its effect is expected to be minor since in most typical scenarios $f_{ut} \gg v_u \sigma_v$, where σ_v is the vertical compressive stress [refer to Eq. (5.2)]. Furthermore, due to a lack of available research on the topic, the variability effects of v_u will not be considered. The study conducted is based on the experimental work reported in Chapters 2 and 3. Relevant findings from available literature are also presented.

Three types of probability distribution were trialled for their suitability: normal, lognormal and Weibull. These were chosen for several reasons. The normal distribution, whilst being a good candidate for the subsequent development of an analytical approach due to its mathematical properties, has the inherent disadvantage that it can assume negative values and so may not be appropriate for representing f_{mt} and f_{ut} . The lognormal and Weibull distributions can only assume positive values making them potentially more appropriate for modelling these parameters; however, their mathematical form is more complex, thus making them more difficult to use in the subsequent development of an analytical approach.

The statistical test used throughout these studies for quantifying the goodness of fit between a hypothesized probability distribution and an empirical data set is the Kolmogorov-Smirnov (KS) test. The KS test uses the statistic D_n to measure the goodness of fit, which is taken as the maximum absolute difference between the empirical and hypothesized cumulative distribution functions (CDFs). A lower value indicates better fit. If D_n exceeds a cutoff value derived from a particular statistical significance level, then the hypothesized distribution is rejected as being the underlying distribution from which the empirical data set has been sampled. The KS test significance level used throughout this study is 5%.

5.3.1 Flexural Tensile Strength of Masonry f_{mt}

Results of Original Experimental Studies

During the course of the experimental work in Chapters 2 and 3, a large data set for f_{mt} was acquired through material testing, as reported in Appendix A.2. These included full-sized perforated brick specimens (from quasistatic tests) as well as half-sized solid brick specimens (from dynamic tests). In both types of brickwork, f_{mt} was quantified using the bond wrench method and typically 12 individual joints were tested for each batch of mortar.

For the full-scale walls s1–s8 (Chapter 2), approximately six batches of mortar were used in each panel's construction. Thus, pooling of the data for the constituent batches in each wall produced eight data sets, each consisting of approximately 70

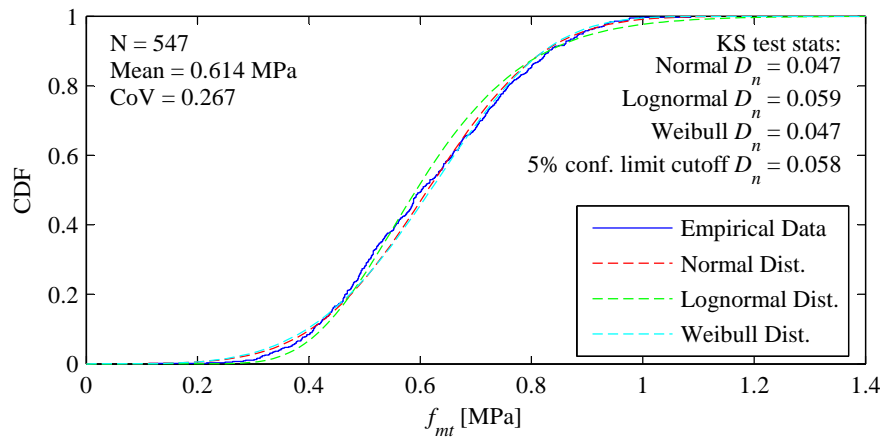


Figure 5.2: Distribution of f_{mt} in pooled data set for full-scale panels s1–s8.

individual data points. Note that although the Student’s t -test found a statistically significant difference between the distribution of data from individual batches and the pooled data sets for the parent wall in approximately 50% of cases (as reported in Appendix A), it is nonetheless deemed reasonable to pool the batch data belonging to each panel since this effectively reflects what occurs in practice. Furthermore, in typical ultimate strength design the engineer will generally use a single value of f_{mt} , as opposed to considering each constituent batch separately. The f_{mt} data sets based on the full-sized brickwork, which were used for subsequent distribution fitting, included a data set for each individual wall, in addition to a global pooled data set consisting of all individual joints tested across all walls.

In the shaketable test study (Chapter 3), the five half-scale walls D1–D5 were built using a combined total of four separate batches of mortar. Because of the shared use of these batches between the walls, and furthermore, since the batches all had a similar mean and CoV, it was deemed acceptable to pool all individual data points into a single global data set for the purpose of distribution fitting.

The hypothesized distributions (normal, lognormal and Weibull) were fitted to each empirical data set using its mean and CoV. Plots of the resulting CDFs are illustrated by Figures 5.2 and 5.3 for the pooled data sets for the full-scale panels and half-scale panels, respectively. Additional plots based on the data sets for the individual full-scale panels are included in Appendix F.1 (Figures F.1–F.8). The goodness of fit of the hypothesized distributions to each data set is summarised in Table 5.1, which provides the calculated KS test statistic D_n for each of the distributions, as well as the cutoff value at the 5% confidence limit. As D_n is smaller than the cutoff value in each case (except for one case where the result is very marginal), none of the distributions can be rejected as being the underlying

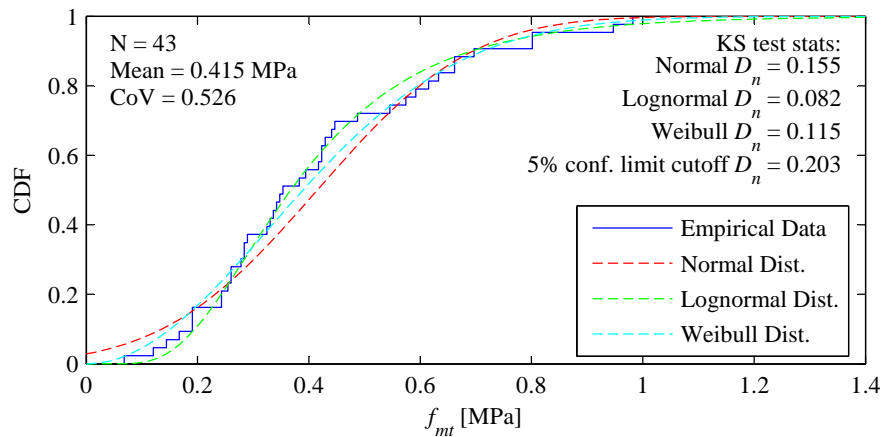


Figure 5.3: Distribution of f_{mt} in pooled data set for half-scale panels D1–D5.

Table 5.1: Kolmogorov-Smirnov test results for f_{mt} data (ordered by CoV).

Data Set	n	CoV	KS test statistic, D_n			
			Normal	Lognorm	Weibull	Cutoff
s8	59	0.19	0.077	0.093	0.068	0.174
s1	66	0.20	0.064	0.089	0.070	0.164
s4	82	0.21	0.065	0.078	0.083	0.148
s5	83	0.21	0.043	0.081	0.038	0.147
s6	74	0.22	0.098	0.061	0.121	0.155
s7	60	0.23	0.077	0.113	0.058	0.172
s2	66	0.27	0.145	0.094	0.157	0.164
s1–s8 pooled	547	0.27	0.047	0.059	0.047	0.058
s3	68	0.28	0.078	0.067	0.090	0.162
D1–D5 pooled	43	0.53	0.155	0.082	0.115	0.203

probability distribution of the empirical data sets at the 5% significance level. In other words, each type of probability distribution can be considered adequate for representing f_{mt} .

The results given in Table 5.1 also indicate only a minimal difference between the performance of the three distributions for the full-scale panels s1–s8, regardless of whether the data is considered individually for each panel or as a pooled data set. Interestingly, the normal distribution performs better than the lognormal distribution in five of the eight full-scale panels and also in the pooled set s1–s8. A similar trend is observed by comparing the normal and Weibull distributions, whereby the normal distribution appears to perform slightly better in the full-scale panels. However, in the pooled data set for half-scale panels D1–D5, the lognormal and Weibull distributions perform better than the normal distribution, which can also be seen from visual inspection of Figure 5.3. Notably this data set had by far the largest CoV of the data sets considered. In general, it can be seen from Table

5.1 that the normal and Weibull distributions performed better than the lognormal distribution in data sets with a small CoV and vice versa. Conversely, for data sets with a high CoV , the lognormal distribution performed better. The normal and Weibull distributions appear to perform equally well across all levels of variability.

Results of Studies by Other Researchers

Numerous experimental studies have been performed in the past to investigate variability in the material properties of URM. The flexural tensile strength of masonry, in particular, has received a significant amount of research attention.

For example, a study by *Lawrence* [1983] obtained a large amount of flexural tensile strength data from tests on vertically spanning beams. Several forms of probability distribution were tested to determine the underlying form of the data, including the normal, lognormal and Weibull distributions. The KS test at the 20% significance level was used to either accept or reject the distributions as providing adequate fit (a more stringent level than that used in the current study). It was found that all of the three types of distribution provided adequate fit to the f_{mt} data; however, the normal distribution typically gave the lowest test statistic and therefore provided the best fit. In the same study, tests were conducted to determine the shear strength of the masonry bond, τ_{um} . This property is perhaps of even greater significance to the current chapter than f_{mt} , since τ_{um} is directly related to the ultimate moment capacity for stepped failure [Eq. (4.23)]. All of the hypothesized probability distributions were found to provide acceptable fit to the τ_{um} data, with the normal distribution providing the best fit. It is worth mentioning that the study also conducted material tests to determine the flexural strength of horizontally spanning beams in bending. Again, the normal distribution was found to give the best fit to the strength, but all three types of distribution considered were deemed as acceptable.

Another study by *Heffler et al.* [2008] investigated spatial correlation of f_{mt} throughout entire masonry panels. The bond wrench method was used to determine the flexural tensile strength of all brick units within the panel and their underlying bond. Several types of probability distribution, including truncated normal, lognormal, Weibull, Gamma and Gumbel, were fitted to the data of four of the panels tested. The goodness of fit was measured using the KS test at the 5% significance level, which showed that the truncated normal distribution gave the best fit and was the only distribution that could not be rejected for any of the four panels. In addition, the Weibull distribution was shown to pass the test for one of the panels, but not for the other three.

A study by *Baker and Franken* [1976] on vertically spanning beams subjected to flexure also showed bond strengths to be adequately represented using the normal distribution. This study used the *KS* test at the 10% significance level.

Summary of Findings

On the basis of the original study performed herein and consideration of work by other researchers, the normal, lognormal and Weibull distributions are all deemed to adequately represent the flexural tensile strength of masonry when the degree of variability is within the range considered by these studies (i.e. *CoV* < 0.5). The normal distribution has been shown to provide the best fit by numerous studies, despite its simplicity and inclusion of negative values. It is the author's opinion, however, that caution should be exercised in using the normal distribution to represent f_{mt} at higher levels of variability, because a greater proportion of values are going to fall in the negative value range. In such a situation, the use of another distribution which can only assume positive values may be more appropriate.

A large body of experimental work exists in which f_{mt} was measured, either where the parameter formed the central focus of the research, or where it was determined as a byproduct of the test study in material testing. However, because such studies have most often been performed in laboratories with a certain degree of quality control, it is difficult to assess whether such studies reflect the extent of variability in masonry construction found in practice. A study which investigated the variability of f_{mt} in masonry in practice was conducted by *McNeilly et al.* [1996] who performed in-situ bond wrench tests on newly built brickwork panels at 19 different sites. In total, 25 sets of f_{mt} data were taken, each consisting of between 10 and 19 individual bond wrench tests. The mean tensile bond strength ranged between 0.22–0.85 MPa. The *CoV* ranged between 0.16–0.49, with an average of 0.30. By comparison, the *CoV* measured for walls s1–s8 in the present study ranged between 0.19–0.28, which falls in the lower end of the range observed in the in-situ tests; and the mean tensile bond strength ranged between 0.50–0.72 MPa (Table 2.3) which falls in the upper end of the range observed in the in-situ tests. Therefore, the mean tensile bond strength determined from the present laboratory study appears to be, on average, higher and less variable than from the in-situ data.

5.3.2 Lateral Modulus of Rupture of Brick Units f_{ut}

In the experimental study reported in Chapter 2, f_{ut} was determined using flexural tests on three brick long beams. A total of 12 specimens were tested using the full-sized perforated brick units used in panels s1–s8. Full details of the experimental

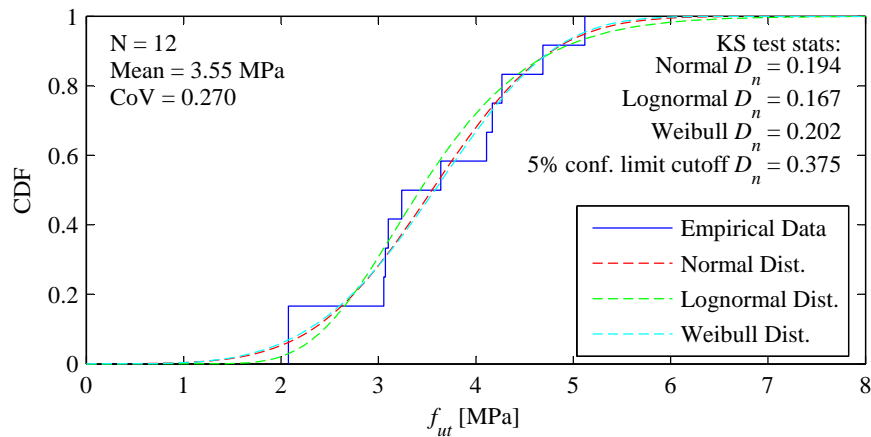


Figure 5.4: Distribution of f_{ut} for brick units used in full-scale panels s1–s8.

Table 5.2: Kolmogorov-Smirnov test results for f_{ut} data.

Data Set	n	CoV	KS test statistic, D_n			
			Normal	Lognorm	Weibull	Cutoff
s1-s8	12	0.27	0.194	0.167	0.202	0.375

method used are provided in Appendix A.3.

The hypothesized probability distributions (normal, lognormal and Weibull) were fitted to the f_{ut} data set using its mean and CoV. The resulting CDFs are shown by Figure 5.4, and the KS test statistics are given in Table 5.2. Based on the KS test, none of the hypothesized distributions can be rejected at the 5% significance level.

Lawrence [1983], who tested a total of 245 test specimens from 7 separate batches of brick units, also found that each of the three aforementioned distributions gave adequate representation of f_{ut} . Interestingly, in that study the Weibull distribution gave the best fit to the data which exhibited a slightly negative skew. The CoV of f_{ut} , measured by *Lawrence* through three-unit brick beam tests, ranged between 0.18 and 0.37. The average CoV was 0.26, which is very comparable to the value of 0.27 observed in the present study.

5.4 THEORETICAL BASIS

5.4.1 General Assumptions

The general assumptions made by the methods developed in this chapter are as follows:

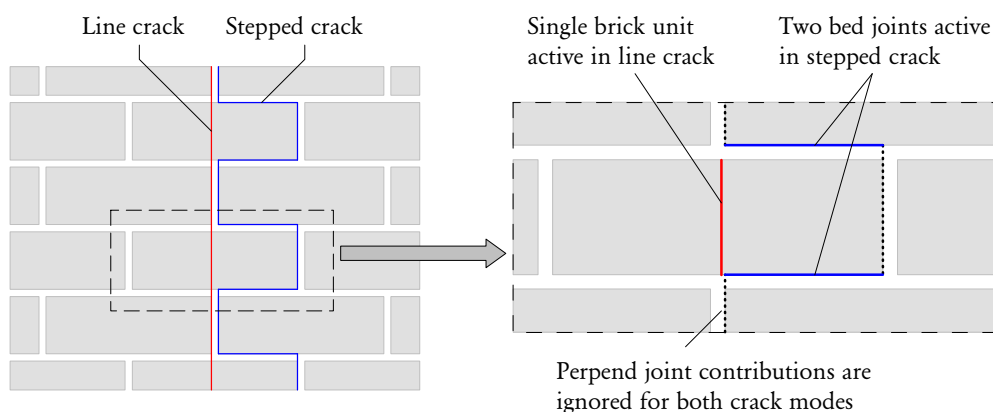


Figure 5.5: Basic masonry module consisting of two courses of bricks.

1. Weak link hypothesis is assumed to govern crack formation on a local level. Figure 5.5 shows a basic module of masonry over a height of two courses of bricks. The module will develop either stepped failure if two bed joints fail due to torsion, or line failure if a single brick fails due to flexural tension. The critical crack mode is taken as the one that has the lower moment capacity calculated using the fundamental equations presented in Section 5.4.2.
2. Material properties, including the flexural tensile strength (f_{mt}) and the lateral modulus of rupture of the brick units (f_{ut}), are treated as independent random variables. It is assumed that both properties can be represented using either the normal, lognormal or Weibull distributions. As reported in Section 5.3, this assumption is supported by statistical analyses on test data obtained from original experimental work as well as findings by other researchers. The choice of distribution for both these parameters will depend on purpose of the analysis, for reasons discussed later.
3. Because the influence of Poisson's effect on the line failure moment capacity is very small⁵, it is assumed that the variability in the Poisson's ratio of the brick units (ν_u) may be ignored and that it can be treated as a constant. Where allowances are made to treat ν_u as a random variable, it is assumed to follow the normal distribution.
4. All other parameters featuring in the governing equations (Section 5.4.2), including brick unit dimensions, mortar joint dimensions and vertical stress, are treated as constants.

⁵For example, if we assume typical values of material properties, such as $f_{ut} = 4$ MPa and $\nu_u = 0.2$; and a conservatively high value of axial stress $\sigma_v = 0.2$ MPa; then according to Eq. (5.2), the strength reduction due to Poisson effects on the line failure moment capacity is still only 1%.

5.4.2 Fundamental Equations

The governing equations providing the basis for the proposed methodology were introduced in Section 4.3.3 and are reproduced herein.

By generalising the f_{mt} and σ_v coefficients in Eq. (4.24) as r and μ , respectively, and substituting into Eq. (4.23), the ultimate moment capacity with respect to stepped failure over a single course of the masonry becomes

$$m_{\text{step}} = k_{be} (r f_{mt} + \mu \sigma_v) t_u^3, \quad (5.1)$$

where σ_v is the vertical compressive stress at the joint under consideration, t_u is the width of the masonry unit, k_{be} is the elastic torsion coefficient [calculated using Eqs. (E.9), (E.11) and (E.12) in Appendix E.2], and other parameters as defined previously. The coefficients r and μ have the empirically calibrated values $r = 1.6$ and $\mu = 0.9$, as per Eq. (4.24).

Reproducing Eq. (4.27), the ultimate moment capacity with respect to line failure over a single course of the masonry is

$$m_{\text{line}} = \frac{1}{2} (f_{ut} - \nu_u \sigma_v) \frac{h_u t_u^2}{6}, \quad (5.2)$$

where h_u is the height of the brick unit, and other parameters as defined previously. The factor of $1/2$ accounts for only one brick being involved in the crack for every two courses (see Figure 5.5).

Based on the weak link hypothesis (Assumption 1), the effective ultimate moment capacity for the mixed failure mode per a single course of the masonry, m_{mix} , is taken the minimum of the capacities for the two individual modes, such that

$$m_{\text{mix}} = \min(m_{\text{step}}, m_{\text{line}}). \quad (5.3)$$

Equations (5.1)–(5.3) provide the basis for the derivation of the methodologies proposed in this chapter.

Equations (5.1) and (5.2), which are based on work by Willis *et al.* [2004] [in addition to the modification implemented into Eq. (5.1), as described in Section 4.3.3], are considered to be the current state-of-the-art in analytical expressions for calculating the moment capacity of URM in horizontal bending. In validating the accuracy of the expressions, Willis calculated the total moment capacity of tested wallettes undergoing a mixed failure mode, by counting the number of cracked bed joints and brick units along the overall crack and summing their moment contributions. This approach was found to produce good correlation with the

experimentally measured moment capacities. However, because these calculations required prior knowledge of the proportion of the crack undergoing each failure mode, they could only be used as an a posteriori analysis. Nonetheless, the fact that the moment expressions were validated in such a way indicates that they provide a sound basis for the development of the a priori analysis techniques proposed in this chapter.

5.5 REDUCTION IN THE ULTIMATE STRENGTH

As outlined in Section 5.1, the AS 3700 procedure for calculating the characteristic ultimate strength in horizontal bending does not explicitly account for a strength reduction due to weak link effects. This section presents an analytical approach for predicting an effective ultimate moment capacity of the mixed failure mode and quantifying the expected strength reduction. The idea of the proposed method is to formulate the probability density function and cumulative distribution function curves of the effective moment capacity in terms of those of the individual failure modes, by applying the weak link hypothesis. From these curves, key statistical values can then be derived, including the mean and characteristic strengths, which enables the resulting reduction in strength to be quantified.

Further to the assumptions listed in Section 5.4, it is assumed that the ultimate moment capacity of both failure mechanisms is attained simultaneously. This assumption makes it possible to take the total moment capacity along a crack as the direct sum of the moment capacities for the two failure modes taking place at different regions along the crack. As mentioned in Section 5.4, *Willis et al.* [2004] showed such calculations to give good agreement with experimentally measured strength, thus, in essence supporting this assumption.

Because the characteristic ultimate strength (i.e. strength at which CDF is equal to 0.05) is of interest, only the lognormal and Weibull distributions are considered for representing tensile strengths f_{mt} and f_{ut} , as they only assume positive values and therefore provide more representative behaviour at the lower end tail. The normal distribution will not be considered.

5.5.1 Formulation

Before the governing equations for the method are presented, the symbolic notation used throughout this chapter will be defined: For a random variable X , its mean or expected value is denoted as either \hat{X} or $E\langle X \rangle$; its standard deviation as $S\langle X \rangle$; and its coefficient of variation as $C\langle X \rangle$. For a variable Y consisting of a random

component X and a constant component c , such that $Y = X + c$, the random part may be denoted as $X = \text{rand}(Y)$ and the constant part as $c = \text{const}(Y)$.

Non-dimensional Properties

For convenience, a non-dimensional formulation will be adopted, whereby the moment capacity in horizontal bending is normalised by the mean moment capacity in vertical bending to produce the orthogonal strength ratio:⁶

$$\eta = \frac{\bar{M}_h}{\bar{M}_v}. \quad (5.4)$$

It also becomes useful to normalise the mean lateral modulus of rupture \hat{f}_{ut} and vertical compressive stress σ_v by the mean flexural tensile strength \hat{f}_{mt} , to produce the non-dimensional quantities

$$F_{ut} = \frac{\hat{f}_{ut}}{\hat{f}_{mt}}, \quad (5.5)$$

and

$$\Sigma_v = \frac{\sigma_v}{\hat{f}_{mt}}. \quad (5.6)$$

Recognising that in the absence of vertical compressive stress, the mean vertical bending moment capacity per unit length of crack is

$$\bar{M}_v = \hat{f}_{mt} \frac{t_u^2}{6}, \quad (5.7)$$

and applying the conversion formula for horizontal bending Eq. (4.15), the orthogonal strength ratios for stepped failure and line failure become

$$\eta_{\text{step}} = k_{\text{step}} \left[r \frac{\hat{f}_{mt}}{\hat{f}_{mt}} + \mu \Sigma_v \right], \quad (5.8)$$

and

$$\eta_{\text{line}} = k_{\text{line}} \left[\frac{\hat{f}_{ut}}{\hat{f}_{mt}} - \nu_u \Sigma_v \right]. \quad (5.9)$$

⁶The definition of the orthogonal strength ratio is not always consistent throughout the literature and various design codes, which can sometimes lead to confusion. In some works, it is defined as \bar{M}_v/\bar{M}_h , whereas others define it as \bar{M}_h/\bar{M}_v . In this thesis, it is defined as the strength in horizontal bending divided by the strength in vertical bending (\bar{M}_h/\bar{M}_v) and hence its value will generally be greater than 1.

The terms k_{step} and k_{line} are constants dependent only on and containing all information regarding the geometry of the masonry constituents, calculated as

$$k_{\text{step}} = \frac{6 k_{be} t_u}{h_u + t_j}, \tag{5.10}$$

and

$$k_{\text{line}} = \frac{h_u}{2 (h_u + t_j)}. \tag{5.11}$$

Formulation of the PDFs and CDFs

The orthogonal strength ratios for stepped and line failure, given by Eqs. (5.8) and (5.9), both consist of a random part, proportional to the respective tensile strength term (f_{mt} or f_{ut}); plus a constant part, due to vertical compressive stress Σ_v .

The orthogonal ratio for stepped failure, η_{step} , consists of the random and constant parts

$$\eta_{\text{step}} = \underbrace{k_{\text{step}} r \frac{f_{mt}}{\widehat{f}_{mt}}}_{=\text{rand}(\eta_{\text{step}})} + \underbrace{k_{\text{step}} \mu \Sigma_v}_{=\text{const}(\eta_{\text{step}})}. \tag{5.12}$$

Since $\text{rand}(\eta_{\text{step}})$ is directly proportional to f_{mt} , both must have the same distribution and CoV. Therefore, $\text{rand}(\eta_{\text{step}})$ has the mean

$$\mathbb{E}\langle \text{rand}(\eta_{\text{step}}) \rangle = k_{\text{step}} r, \tag{5.13}$$

and CoV

$$\mathbb{C}\langle \text{rand}(\eta_{\text{step}}) \rangle = \mathbb{C}\langle f_{mt} \rangle. \tag{5.14}$$

Similarly, the orthogonal ratio for line failure, η_{line} , consists of the random and constant parts

$$\eta_{\text{line}} = \underbrace{k_{\text{line}} \frac{f_{ut}}{\widehat{f}_{mt}}}_{=\text{rand}(\eta_{\text{line}})} - \underbrace{k_{\text{line}} \nu_u \Sigma_v}_{=\text{const}(\eta_{\text{line}})}, \tag{5.15}$$

Since $\text{rand}(\eta_{\text{line}})$ is directly proportional to f_{ut} , both must have the same distribution and CoV. Therefore, $\text{rand}(\eta_{\text{line}})$ has the mean

$$\mathbb{E}\langle \text{rand}(\eta_{\text{line}}) \rangle = k_{\text{line}} F_{ut}, \tag{5.16}$$

and CoV

$$\mathbb{C}\langle \text{rand}(\eta_{\text{line}}) \rangle = \mathbb{C}\langle f_{ut} \rangle. \tag{5.17}$$

The probability density functions (PDFs) and cumulative distribution functions

(CDFs) of η_{step} and η_{line} can now be formulated. For η_{step} , the PDF at the value x is

$$p_{\eta_{\text{step}}}(x) = p_{\text{rand}(\eta_{\text{step}})}(x - \text{const}(\eta_{\text{step}})), \quad (5.18)$$

and the related CDF is

$$P_{\eta_{\text{step}}}(x) = P_{\text{rand}(\eta_{\text{step}})}(x - \text{const}(\eta_{\text{step}})). \quad (5.19)$$

The functions $p_{\text{rand}(\eta_{\text{step}})}(\dots)$ and $P_{\text{rand}(\eta_{\text{step}})}(\dots)$ are the PDF and CDF of the random component $\text{rand}(\eta_{\text{step}})$, which follow the same distribution (e.g. normal, lognormal or Weibull) as f_{mt} , and whose mean and CoV are given by Eqs. (5.13) and (5.14).

Similarly, the PDF of η_{line} at the value x is

$$p_{\eta_{\text{line}}}(x) = p_{\text{rand}(\eta_{\text{line}})}(x - \text{const}(\eta_{\text{line}})), \quad (5.20)$$

and the related CDF is

$$P_{\eta_{\text{line}}}(x) = P_{\text{rand}(\eta_{\text{line}})}(x - \text{const}(\eta_{\text{line}})). \quad (5.21)$$

The functions $p_{\text{rand}(\eta_{\text{line}})}(\dots)$ and $P_{\text{rand}(\eta_{\text{line}})}(\dots)$ are the PDF and CDF of the random component $\text{rand}(\eta_{\text{line}})$, which follow the same distribution as f_{ut} , and have a mean and CoV given by Eqs. (5.16) and (5.17).

Expressions for the PDF and CDF of the orthogonal strength ratio η_{mix} for the mixed mode of failure are obtained by applying the weak link hypothesis, as per Assumption 1 in Section 5.4. Equation (5.3) can be formulated in the orthogonal ratio form such that

$$\eta_{\text{mix}} = \min(\eta_{\text{step}}, \eta_{\text{line}}). \quad (5.22)$$

Since the weak link hypothesis defines η_{mix} as the minimum of pairs of independent random variables drawn from η_{step} and η_{line} , its PDF and CDF can be formulated as [e.g. *Simon, 2002*]

$$p_{\eta_{\text{mix}}}(x) = p_{\eta_{\text{step}}}(x) [1 - P_{\eta_{\text{line}}}(x)] + p_{\eta_{\text{line}}}(x) [1 - P_{\eta_{\text{step}}}(x)], \quad (5.23)$$

and

$$P_{\eta_{\text{mix}}}(x) = P_{\eta_{\text{step}}}(x) + P_{\eta_{\text{line}}}(x) - P_{\eta_{\text{step}}}(x) P_{\eta_{\text{line}}}(x). \quad (5.24)$$

It can be shown using Eq. (5.24) that for any arbitrary value of x , the value of the CDF for the mixed-mode capacity will always have a greater value than that of

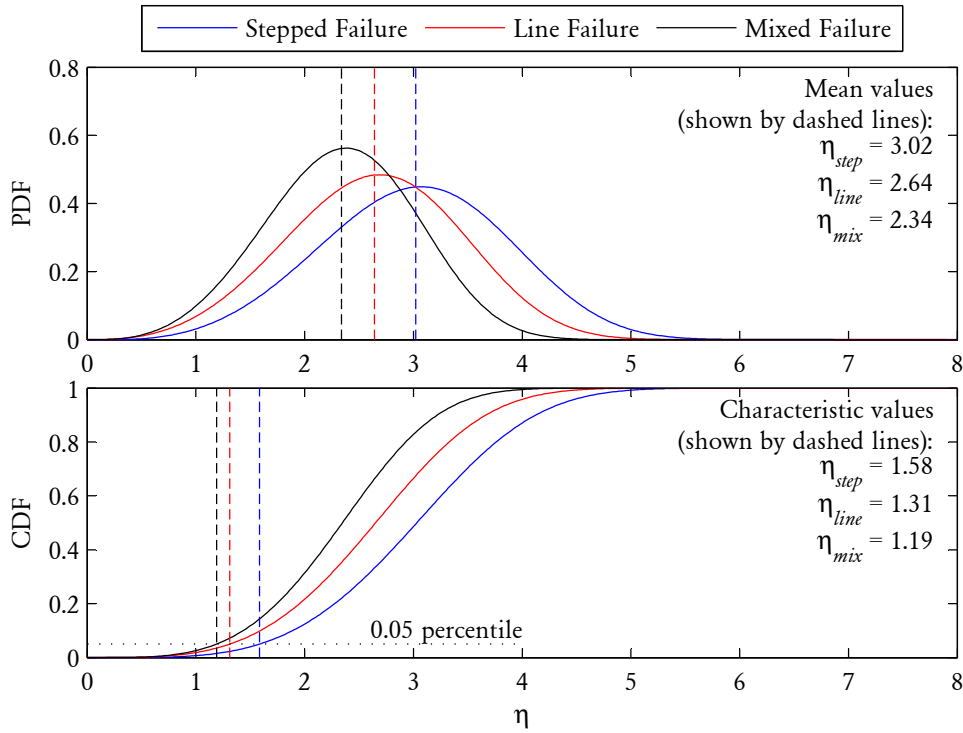


Figure 5.6: Example of the predicted distribution of orthogonal strength ratio for stepped, line and mixed mode failure. Standard clay brick masonry is considered with $F_{ut} = 6$, $\Sigma_v = 0.1$ and $C\langle f_{mt}, f_{ut} \rangle = 0.3$. The Weibull distribution is used to represent f_{mt} and f_{ut} .

either of the individual modes. Symbolically this means that

$$P_{\eta_{mix}}(x) > P_{\eta_{step}}(x), \quad \text{and} \quad P_{\eta_{mix}}(x) > P_{\eta_{line}}(x).$$

It follows that for any arbitrary value of y , where

$$y = P_{\eta_{step}}(x) = P_{\eta_{line}}(x) = P_{\eta_{mix}}(x),$$

the inequalities

$$P_{\eta_{mix}}^{-1}(y) < P_{\eta_{step}}^{-1}(y) \quad \text{and} \quad P_{\eta_{mix}}^{-1}(y) < P_{\eta_{line}}^{-1}(y)$$

must hold. This outcome demonstrates that at any given percentile (value of the CDF), the strength of the mixed failure mode will always be lesser than either of the strengths of the two pure failure modes. In other words, there is an always-weakening influence on the moment capacity as a result of weak link effects.

5.5.2 Mean and Characteristic Values of Strength

The proposed method is best suited for application using computer software where the PDFs and CDFs of the probability distributions of interest can be programmed in as functions. Figure 5.6 demonstrates an example of such an analysis graphically, showing the predicted PDFs and CDFs of the orthogonal strength ratios for the stepped, line and mixed failure modes and also indicating their respective mean and characteristic values. This example considers standard clay brick masonry, which for this example and others presented in this chapter will be defined as masonry consisting of bricks with dimensions $230 \times 110 \times 76$ mm and 10 mm thick mortar joints. It is assumed that this type of masonry has a Poisson's ratio $\nu_u = 0.2$, and coefficients $r = 1.6$ and $\mu = 0.9$, as per Eq. (4.24). In this example, the ratio of brick strength to bond strength is $F_{ut} = 6$ and the ratio of axial stress to bond strength is $\Sigma_v = 0.1$. The Weibull distribution is used to represent the tensile strengths f_{mt} and f_{ut} with the CoV taken as 0.3. The CDFs of the three modes demonstrate the weakening influence on the strength of the mixed failure mode.

For the purposes of design or analysis, it will typically be of interest to determine the mean and characteristic values for each of the parameters η_{step} , η_{line} and η_{mix} . The mean values of η_{step} and η_{line} can be obtained directly from Eqs. (5.8) and (5.9), by assigning mean values of the respective tensile strengths f_{mt} and f_{ut} . This gives

$$\mathbb{E}\langle\eta_{\text{step}}\rangle = k_{\text{step}}(r + \mu \Sigma_v), \quad (5.25)$$

and
$$\mathbb{E}\langle\eta_{\text{line}}\rangle = k_{\text{line}}(F_{ut} - \nu_u \Sigma_v). \quad (5.26)$$

The mean value of η_{mix} , however, needs to be calculated numerically, since its PDF and CDF will not generally follow any common distribution. This can be done by numerically integrating the first moment of the PDF. The characteristic values of η_{step} , η_{line} and η_{mix} are also easily obtained numerically, by employing root finding techniques to find the value of η at which the CDF equals 0.05.

5.5.3 Capacity Reduction Factors

Since the computation of the mean and characteristic values of effective strength requires the use of computer techniques, a more practical way to implement the proposed methodology is to derive strength reduction factors for the statistical values of interest, such as the mean, median and characteristic strengths. In general terms, let us define the strength reduction factor ϕ as the ratio of the effective moment capacity and the lesser of the moment capacities for stepped and line

failure. Therefore, for characteristic strength, the reduction factor becomes

$$\phi_{\text{char}} = \frac{\text{Char}\langle\eta_{\text{mix}}\rangle}{\min(\text{Char}\langle\eta_{\text{step}}\rangle, \text{Char}\langle\eta_{\text{line}}\rangle)}.$$

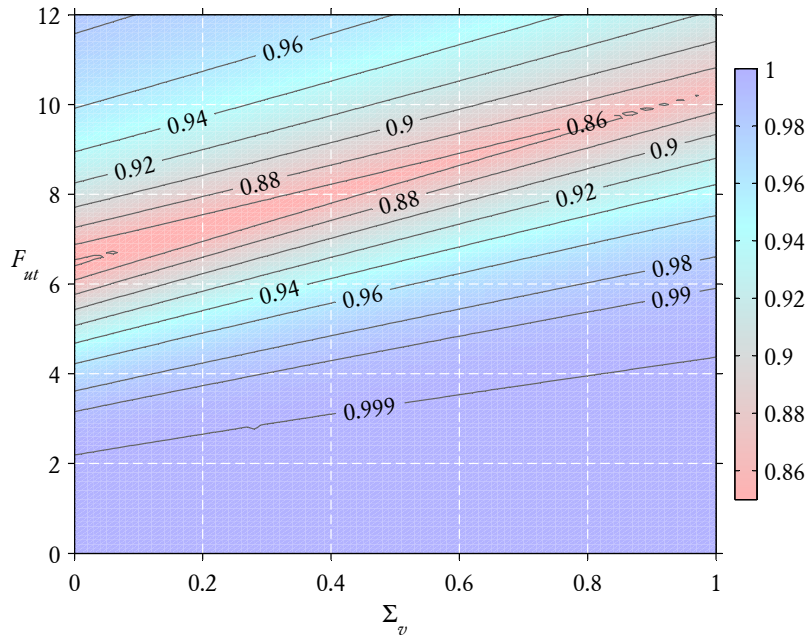
Similarly, for mean and median strength:

$$\phi_{\text{mean}} = \frac{\mathbb{E}\langle\eta_{\text{mix}}\rangle}{\min(\mathbb{E}\langle\eta_{\text{step}}\rangle, \mathbb{E}\langle\eta_{\text{line}}\rangle)}, \quad \phi_{\text{med}} = \frac{\text{Med}\langle\eta_{\text{mix}}\rangle}{\min(\text{Med}\langle\eta_{\text{step}}\rangle, \text{Med}\langle\eta_{\text{line}}\rangle)}.$$

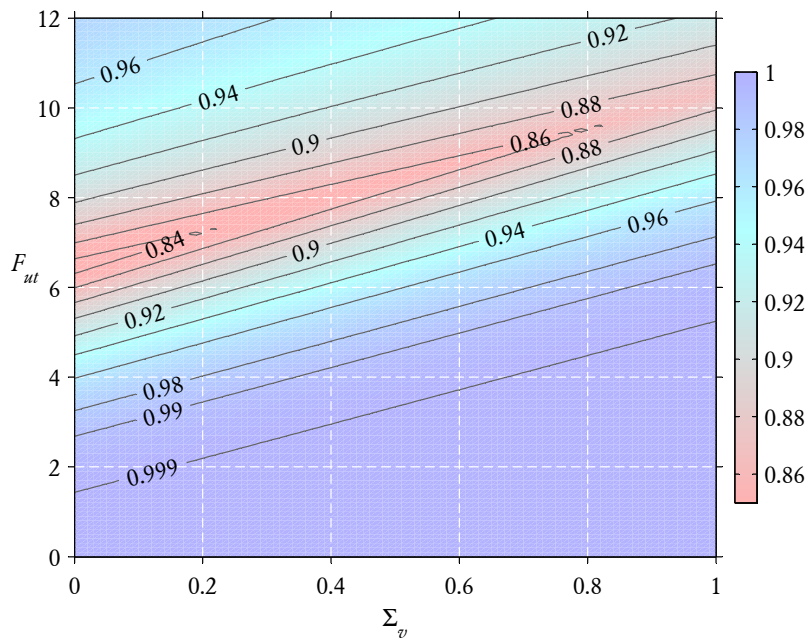
For instance, in the example shown by Figure 5.6, the mean strength reduction factor is $\phi_{\text{mean}} = 2.34/2.64 = 0.89$, and the characteristic strength reduction factor is $\phi_{\text{char}} = 1.19/1.31 = 0.91$. This indicates that mean strength undergoes an 11% reduction as a result of mixed failure, relative to the value that would be calculated if only the pure stepped and line modes were considered. Similarly, there is a 9% reduction in the characteristic strength compared to that which would be calculated using the current design philosophy.

To determine when the reduction in strength becomes most significant, strength reduction factors were computed for standard clay brick masonry for a range of F_{ut} and Σ_v values, as plotted in Figures 5.7 and 5.8 for the mean and characteristic strength, respectively. The CoV of f_{mt} and f_{ut} was taken as 0.3, which is considered to be a typical value, as reported in Section 5.3. Furthermore, 0.3 is the CoV value allowed by AS 3700 when calculating the characteristic values of these material properties from test results. These graphs may be directly used, in analysis or design, to account for the influence of weak link effects on the ultimate strength. To determine the effective moment capacity, one can simply calculate the moment capacities for stepped and line failure modes independently, using mean or characteristic values of f_{mt} and f_{ut} (i.e. according to the conventional AS 3700 method); and then multiply the lower of these values by the appropriate strength reduction factor (as determined from the graphs) for given F_{ut} and Σ_v .

Comparing Figures 5.7a and 5.7b, and Figures 5.8a and 5.7b, demonstrates the difference between the computed strength reduction when the lognormal and Weibull distributions are used to represent the material properties. It is seen from Figure 5.7 that the mean strength reduction factor is not overly sensitive to the type of probability distribution used. However, as seen from Figure 5.8, the characteristic strength reduction factor is quite sensitive to the chosen probability distribution; particularly, the reduction factors computed using the Weibull distribution are more adverse than those based on the lognormal distribution. This trend can be explained by the fact that the Weibull distribution has a fatter lower end tail than the lognormal distribution.

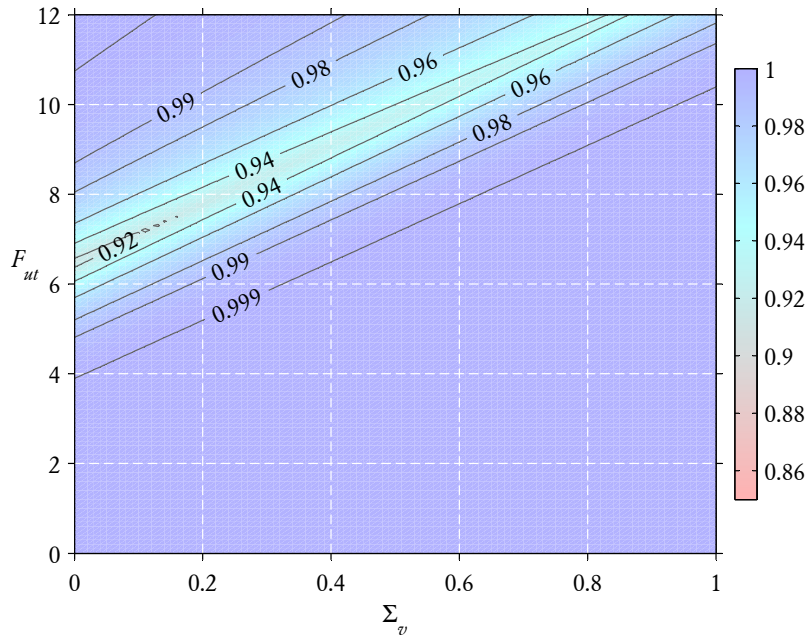


(a) Properties f_{mt} and f_{ut} following lognormal distribution with $\text{CoV} = 0.3$.

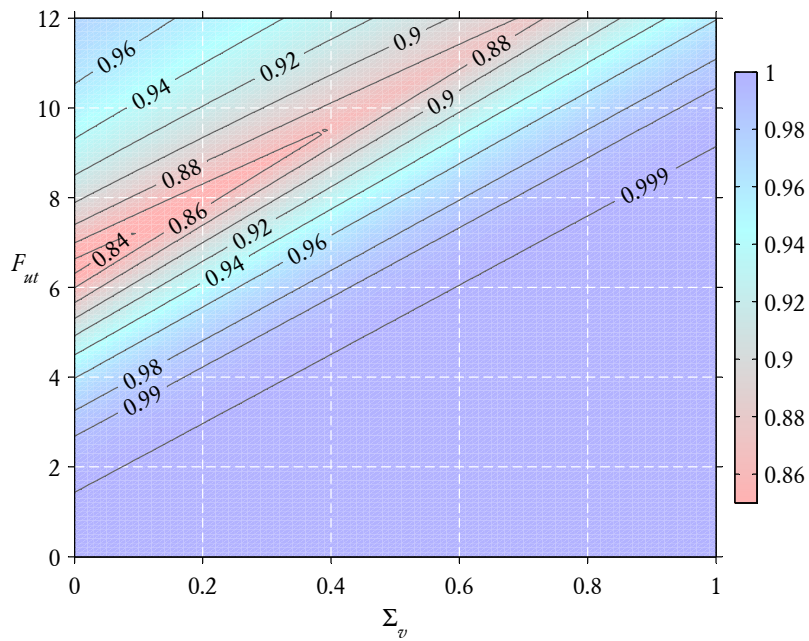


(b) Properties f_{mt} and f_{ut} following Weibull distribution with $\text{CoV} = 0.3$.

Figure 5.7: Mean strength reduction factor ϕ_{mean} for standard clay brick masonry.



(a) Properties f_{mt} and f_{ut} modelled by lognormal distribution with $CoV = 0.3$.



(b) Properties f_{mt} and f_{ut} modelled by Weibull distribution with $CoV = 0.3$.

Figure 5.8: Characteristic strength reduction factor ϕ_{char} for standard clay brick masonry.

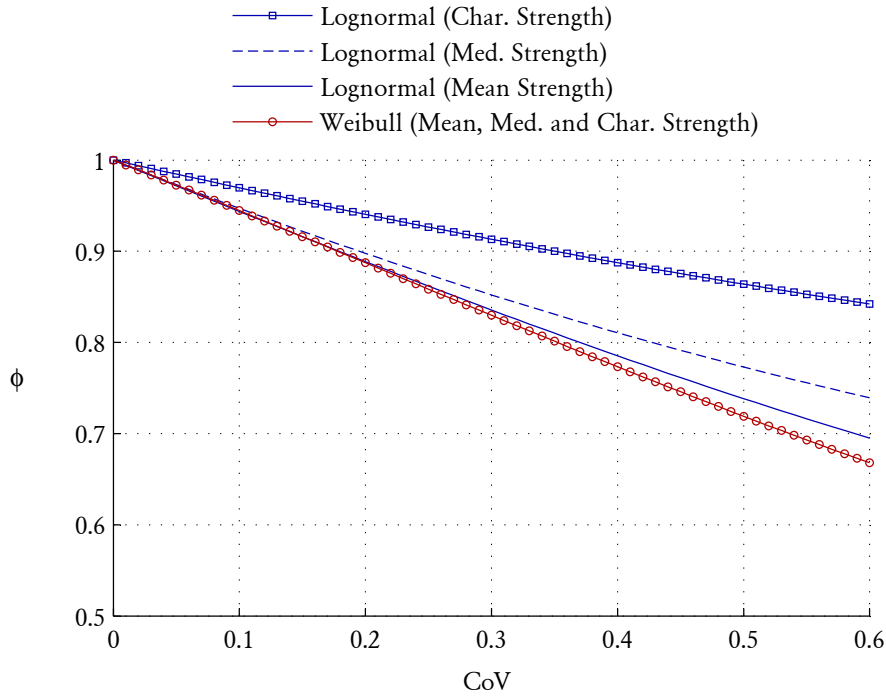


Figure 5.9: Capacity factors corresponding to the most adverse strength reduction possible at different levels of variability in the material properties.

Another notable observation from these graphs is that there are distinct regions in the $F_{ut}-\Sigma_v$ space where the strength reduction effects are most pronounced. These zones correspond to similar magnitudes of strength (mean or characteristic) for the stepped and line failure modes, thus causing the mixed failure mode to become dominant. Furthermore, the graphs demonstrate that the most adverse strength reduction occurs at zero axial stress ($\Sigma_v = 0$), at a value of approximately $F_{ut} = 6.5$ for this particular type of masonry. The critical value of F_{ut} associated with the greatest strength reduction can be calculated as

$$F_{ut} = r \frac{k_{\text{step}}}{k_{\text{line}}}. \quad (5.27)$$

It is worth noting that a ratio of the mean lateral modulus of rupture and bond strength of 6.5 is well within the typical range observed in practice; for example, as demonstrated by the results of material testing performed as part of the experimental work in Chapter 2 (details in Appendix A).

Recognising that the largest reduction in strength occurs when the means of the two moment capacities are equal and the constant offset in capacity due to axial stress is zero, we can determine the maximum possible reduction that can occur at different levels of material strength variability. Figure 5.9 plots the most

adverse reduction in the mean, median and characteristic strength which may occur at a particular CoV in the material properties, when represented using the lognormal or Weibull distributions.⁷ It is seen that the Weibull distribution predicts a greater reduction in strength than the lognormal distribution, particularly for the characteristic strength. This is consistent with the observations made previously through Figures 5.7 and 5.8.

Figure 5.9 also demonstrates that the reduction in strength that can occur at typical levels of material strength variability can be quite significant. For a CoV of 0.3, which was determined to be a typical level of variability through in-situ testing [McNeilly *et al.*, 1996, refer to Section 5.3.1], there is a potential 17% reduction in strength. The largest CoV observed in the study by McNeilly *et al.* was approximately 0.5, which corresponds to a potential strength reduction of 28%. However, whilst such a reduction in strength is considerable, it is nonetheless accounted for by the capacity reduction factor used in the AS 3700 design procedure for masonry in bending ($\phi = 0.6$). In the latter case, this still allows for a left over capacity reduction factor of $0.6/0.72 = 0.83$. It is therefore concluded that whilst the strength reduction effects could, under certain circumstances, be significant, the current AS 3700 procedure sufficiently accounts for them with the capacity reduction factor of 0.6.

5.6 EXPECTED LIKELIHOOD OF EACH FAILURE MODE

As discussed in Section 5.1, the type of failure mode developed along the vertical cracks in a wall can have a significant effect on its post-cracking behaviour and seismic resistance. This section presents an analytical technique for predicting the relative proportions of stepped and line failure expected to develop along a vertical crack.

The proposed method is based on the assumptions and underlying theory discussed in Section 5.4. Moreover, it assumes (as per Assumption 2 in Section 5.4) that the tensile strengths f_{mt} and f_{ut} follow the normal distribution, which allows for some useful simplifications in the derivation of the governing equations. Furthermore, since we are interested in the full range of values for these material properties, the fact that the normal distribution assumes negative values at the lower end tail is of little consequence. The normal distribution's suitability for representing these properties was scrutinised in Section 5.3, where it was shown

⁷Note that in the case of the Weibull distribution, these three factors coincide because of a special property of the distribution whereby the minimum of two Weibull distributed variables is also Weibull distributed.

that it can adequately represent them at the typical levels of variability, that is, for $\text{CoV} < 0.5$.

The proposed method also makes allowance to treat the Poisson's ratio of the brick units (ν_u) as a random variable, despite Assumption 3 in Section 5.4, which stated that its variability could be ignored. The parameter ν_u is assumed to be normally distributed.

5.6.1 Formulation

According to the weak link hypothesis (Assumption 1 in Section 5.4), a masonry section subjected to horizontal bending will undergo stepped failure in favour of line failure when

$$m_{\text{step}} < m_{\text{line}}. \quad (5.28)$$

Substituting in Eqs. (5.1) and (5.2), gives

$$r f_{mt} + \mu \sigma_v < G_h (f_{ut} - \nu_u \sigma_v), \quad (5.29)$$

where the term G_h contains all information regarding the geometric properties of the masonry, and is calculated as

$$G_h = \frac{k_{\text{line}}}{k_{\text{step}}} = \frac{h_u}{12 t_u k_{be}}. \quad (5.30)$$

Inequality (5.29) contains three randomly distributed variables: f_{mt} , f_{ut} and ν_u . By assuming that each of these is normally distributed and taking advantage of the normal distribution's properties,⁸ inequality (5.29) can be reduced into

$$0 < u, \quad (5.31)$$

where u is a normally distributed dummy variable with the mean

$$\mathbb{E}\langle u \rangle = G_h F_{ut} - r - \Sigma_v (G_h \mathbb{E}\langle \nu_u \rangle + \mu), \quad (5.32)$$

and variance

$$\mathbb{S}\langle u \rangle^2 = (G_h F_{ut} \mathbb{C}\langle f_{ut} \rangle)^2 + (r \mathbb{C}\langle f_{mt} \rangle)^2 + (\Sigma_v G_h \mathbb{E}\langle \nu_u \rangle \mathbb{C}\langle \nu_u \rangle)^2. \quad (5.33)$$

From this, the probability of stepped failure is determined by computing the

⁸In particular, the addition of normally distributed variables.

probability that u is greater than zero, such that

$$P_{\text{step}} = \Pr(u > 0) = \Phi_N\left(\frac{S\langle u \rangle}{E\langle u \rangle}\right), \quad (5.34)$$

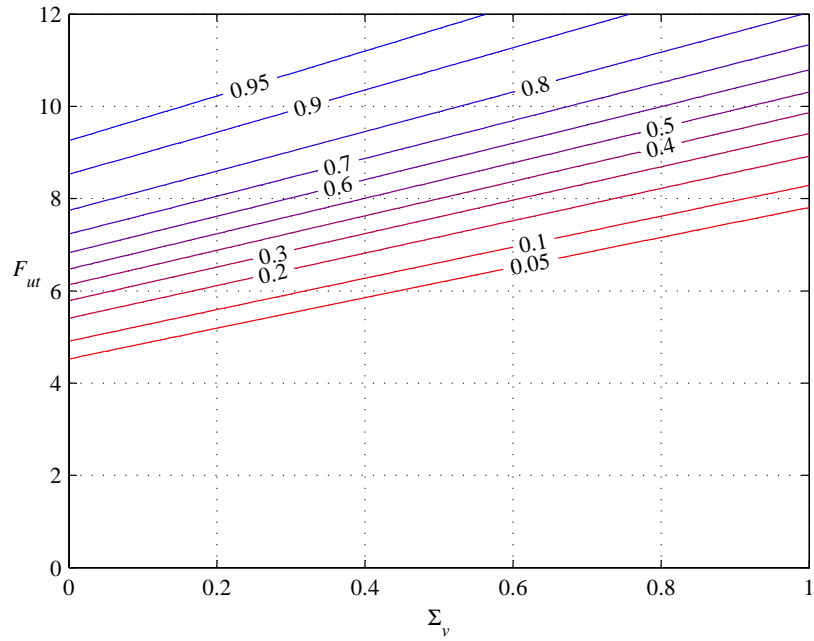
where $\Phi_N(\dots)$ is the standard normal cumulative distribution function. The parameter P_{step} can be interpreted as either the expected likelihood of stepped failure, or the proportion of the crack expected to undergo stepped failure. No closed-form solutions exist for computing the CDF of the normal distribution; however, it may be calculated using functions built into software such as EXCEL and MATLAB, or otherwise obtained from textbook probability tables.

5.6.2 Solution Process

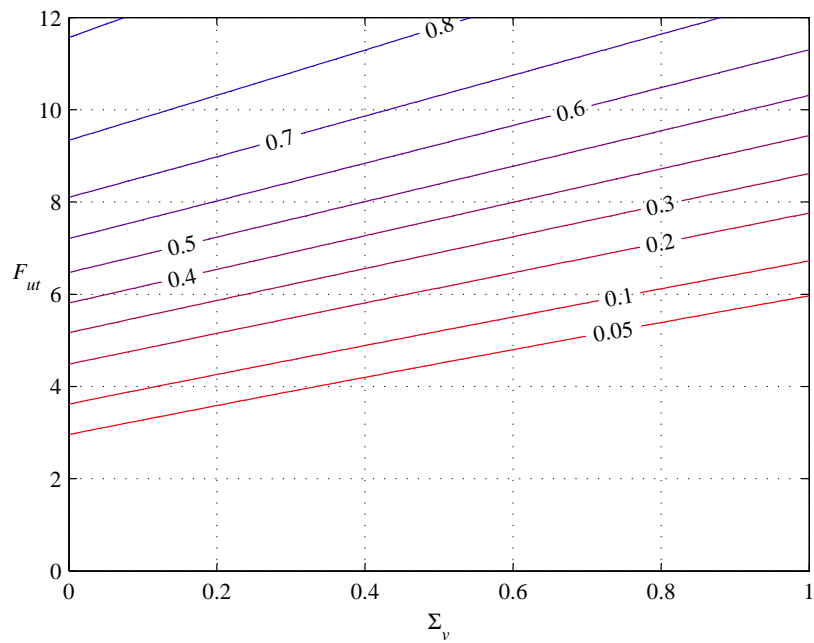
As shown by Figure 5.10, the proposed method is well suited to graphical application by plotting contour lines of the expected likelihood of stepped failure (P_{step}) versus the ratio of unit to bond strength (F_{ut}) and normalised axial stress (Σ_v). Such graphs may be generated for a particular combination of brick and mortar joint geometry; coefficients ν_u , r and μ ; and level of material variability. Once generated, a graph could be readily used in practice to assess the expected likelihood of each failure for a given masonry type.

The particular plots in Figure 5.10 correspond to standard clay brick masonry ($230 \times 110 \times 76$ mm units with 10 mm mortar joints). They demonstrate two general trends: Firstly, the likelihood of stepped failure increases with increasing ratio of brick to bond strength F_{ut} , due to the direct effect of the relative material strengths. Secondly, the likelihood of stepped failure reduces as the ratio of axial stress and bond strength Σ_v increases. This second trend is due to a combination of two factors: the axial compression's strengthening influence on the capacity against stepped failure, and its weakening influence on the capacity against line failure due to Poisson's effect.

The influence of material variability can be observed by comparing Figures 5.10a and 5.10b. It is seen that the median contour line at $P_{\text{step}} = 0.5$, which represents equal amount of stepped and line cracking, is unaffected by the CoV. However, for a larger value of the CoV, the other contour lines become more spread out around the median contour line; and hence, increasing the CoV effectively causes P_{step} to approach 0.5 at any particular value of F_{ut} and Σ_v . In other words, as the level of material variability increases, the masonry will tend toward developing more equal amounts of stepped and line failure. Note that since all material properties have been represented using the normal distribution, the median contour line may be



(a) CoV = 0.15



(b) CoV = 0.3

Figure 5.10: Probability of stepped failure for standard clay brick masonry.

calculated directly using Eq. (5.32), by assigning $\mathbb{E}\langle u \rangle = 0$.

5.6.3 Possible Applications

The proposed method for estimating the relative likelihood of stepped and line failure has numerous potential applications, some of which will now be briefly discussed.

Capacity Reduction Factor for Residual Strength

In his research, *Willis et al.* [2004] proposed an equation for calculating the residual moment capacity of brick masonry derived from frictional torsion along the bed joints [reproduced as Eq. (E.13) in Appendix E.3]. He was able to demonstrate good agreement between the predicted and experimentally measured moment capacity in small-sized wallettes failing by a combination of stepped and line failure. In these calculations, the total moment capacity of the crack was calculated by counting the number of bed joints active along the crack, and multiplying this number by the theoretical capacity of an individual bed joint.

Whilst the author has proposed an alternative and more robust expression for calculating the residual moment capacity [Eq. (4.29)], Willis' findings effectively indicate that a crack's residual moment capacity is proportional to the amount of stepped failure along the crack. The parameter P_{step} therefore has the potential to be used as a capacity reduction factor, which may be used to multiply the nominal residual moment capacity, to obtain the effective residual moment capacity. Using Eq. (4.29), the effective residual moment capacity, expressed as an orthogonal ratio, would therefore become

$$\eta_{\text{res}} = P_{\text{step}} k_{\text{res}} \mu \Sigma_v, \quad (5.35)$$

where k_{res} is the geometric parameter

$$k_{\text{res}} = \frac{6 k_{bp} t_u}{(h_u + t_j)}. \quad (5.36)$$

Note the similar form between k_{res} and k_{step} [Eq. (5.10)]; the only difference being that the former uses the plastic torsion coefficient k_{bp} , and the latter uses the elastic torsion coefficient k_{be} (refer to Figure 4.6). It is further worth noting that the frictional coefficient μ in Eq. (5.35) is for the post-cracked state only, and is distinct from that used in Eq. (5.1). On the basis of bed joint torsion tests by *Willis* [2004], which used solid clay pavers with a flat surface, and equating Eq. (4.29) to Eq. (E.13), the equivalent post-cracking friction coefficient is shown to be approximately

1.04. For typical clay brick units, however, which may be perforated or frogged, μ is likely to be even higher, due to interlock effects.

As a final comment, it will be noted that predicting the residual moment capacity of mixed-mode cracks may be further complicated by the fact that the pattern of the crack itself may have a significant influence on the local propagation of vertical compressive stress, which will in turn affect its frictional capacity. However, further research is required to investigate these effects, as they are beyond the scope of this thesis.

Assessment of Wall Separation Along Vertical Edges

Another potential application of the proposed method could be in the assessment of the vertical edges' capacity to provide a support reaction. In addition to line failure due to horizontal bending, there are also several other non-flexural failure modes which could cause separation between a wall and its vertical supports, thereby preventing the wall from undergoing two-way flexural response after crack formation (see for example, Figures 2.26 and 2.27). Such failure modes could include, for example:

- Tensile failure at the return wall,
- Shear failure at the main wall,
- Sliding due to insufficient friction,
- Or any combination of the above.

A wall's capacity against each of these secondary failure modes relies on good interlock between the units of successive courses, which would be weakened by the occurrence of line failure. The expected likelihood of stepped failure, P_{step} , could therefore potentially be utilised during an analytical check of the vertical edges' ability to withstand separation. Development of such methodology, however, is beyond the scope of this thesis.

5.7 COMPARISON WITH EXPERIMENT

5.7.1 Small-Sized Wallettes

Accuracy of the stochastic methodologies described in Sections 5.5 and 5.6 was examined through comparison with the results of horizontal bending tests on small-sized wallettes, as performed by Willis [2004] [also reported in Willis *et al.*, 2004]. It is

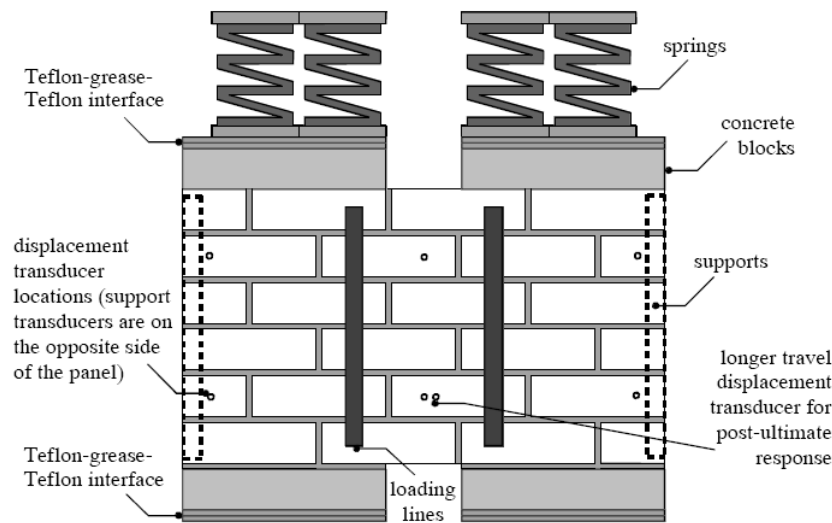
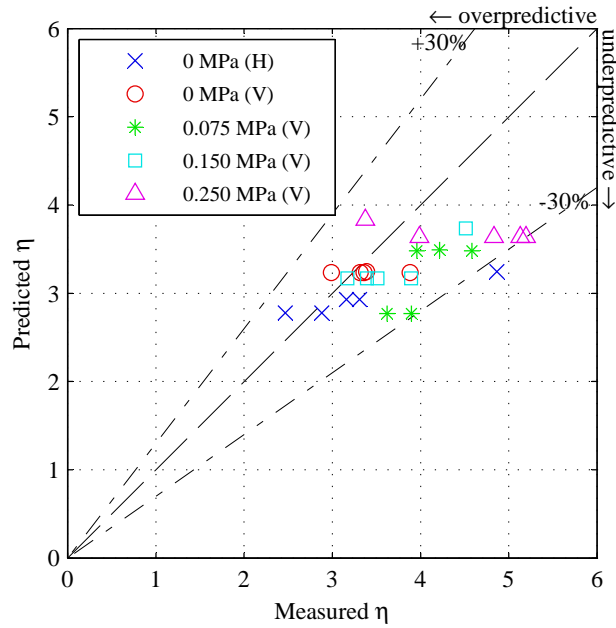


Figure 5.11: Horizontal bending test arrangement used by Willis [2004]. (Graphic used with permission from C. R. Willis.)

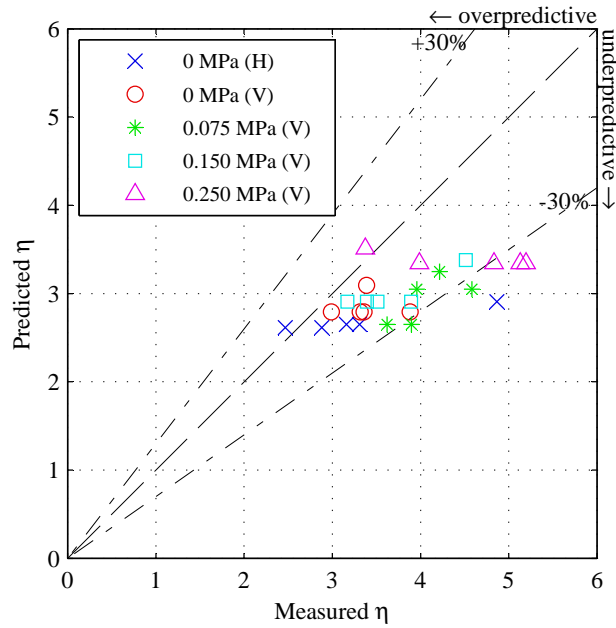
noted that these experiments were part of the data set that Willis used to develop the ultimate moment capacity expressions, Eqs. (5.1) and (5.2); particularly, to calibrate the empirical parameters r and μ in Eq. (5.1). As such, one would naturally expect the correlation between the measured and predicted moment capacity to be good. However, since the main purpose of the comparisons conducted here is to study the stochastic aspects of failure, which were not previously addressed by Willis, the author believes the use of this data set for comparative purposes to be valid.

The brickwork used in this study was constructed using extruded clay brick paving units with nominal dimensions of $230 \times 114 \times 65$ mm and 10 mm mortar joints. The test specimens were three-and-a-half bricks in length and six courses high, and were subjected to four-point bending, as shown in Figure 5.11. Fives sets of tests were conducted: In the first four sets, the walls were oriented vertically and were subjected to varied levels of axial compression using springs (Figure 5.11), including 0.075, 0.15 and 0.25 MPa, as well as a control set with no precompression. In the fifth set, the specimens were oriented horizontally and had no axial loading. Each set consisted of five repetitions, resulting in a total of 25 individual tests.

The methodology described in Section 5.5 was used to predict the ultimate moment capacity of the tested wallettes. Detailed analysis results are provided in Appendix F.2 (Table F.1). Figure 5.12 compares the computed strength (as orthogonal ratio) with the measured strength. Two cases are considered: Part (a) used conventional analysis, where the strength was taken as the minimum of the separately calculated stepped and line failure capacities. Part (b) used the developed approach, whereby the strength was taken as that of the mixed mode of



(a) Strength calculated as minimum of stepped and line failure (conventional approach).



(b) Strength calculated using the mixed failure mode (proposed approach).

Figure 5.12: Comparison of predicted and measured ultimate strength in small-sized wallettes.

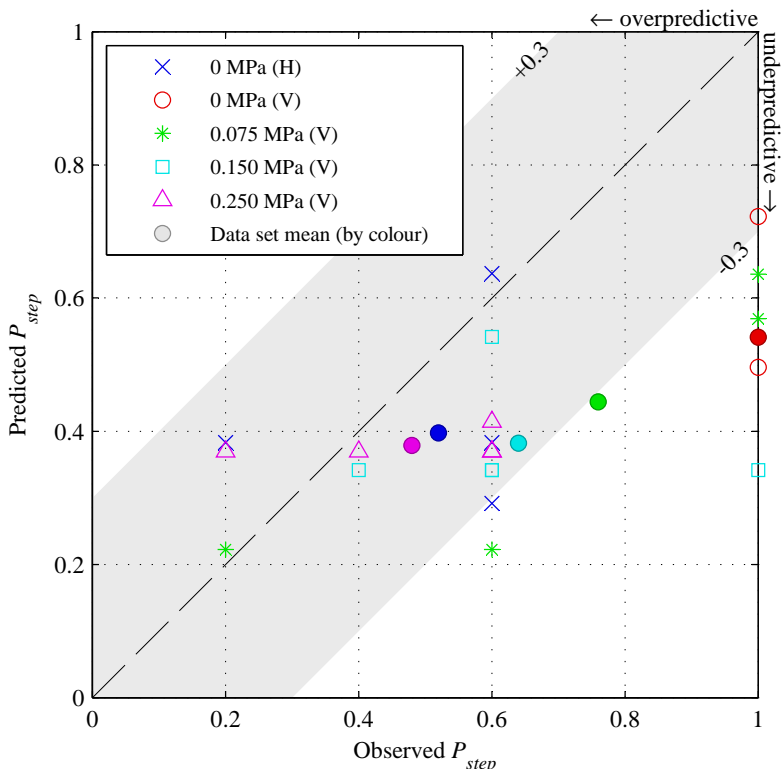


Figure 5.13: Comparison of predicted and observed proportion of stepped failure for small-sized wallettes.

failure, taking into account weak link effects. The average ratio of the predicted and measured strengths was 0.88 for the conventional approach and 0.80 for the stochastic approach. That the conventional approach is slightly more accurate in this case, is not surprising, given that this data set was used by Willis [2004] in calibration of the governing moment capacity expressions. In turn, the stochastic approach will always predict a lower capacity than the conventional approach, since it takes into account the weak link effects, and is equivalent to applying a strength reduction factor to the capacity obtained by the conventional approach (as discussed in Section 5.5.3).

The methodology described in Section 5.6 was used to determine the expected likelihood of stepped failure for the tested wallettes. The predictions are compared to the proportion of stepped failure observed experimentally in Figure 5.13 (full results provided by Table F.1 in Appendix F.2). The plot shows a large amount of scatter between the predicted and observed results, with the analysis, on average, underpredicting the proportion of stepped failure (or overpredicting the proportion of line failure) by -0.25 . Whilst these comparisons suggest the developed method to be conservative, it is not entirely clear why the method tends to overpredict the

Table 5.3: Comparison of predicted and observed proportion of stepped failure along vertical edges of full-scale panels.

Wall	σ_{vo} [MPa]	P_{step} observed			P_{step} calculated	Error (calc – obs)	
		Avg	L edge	R edge		L edge	R edge
s1	0.1	0.25	0.36	0.14	0.12	–0.24	–0.03
s2	0	0.49	0.43	0.56	0.53	+0.10	–0.03
s3	0.1	0.18	0.18	–	0.44	+0.26	–
s4	0.05	0.29	0.29	–	0.25	–0.04	–
s5	0	0.43	0.43	–	0.28	–0.15	–
s6	0	0.43	0.50	0.36	0.58	+0.08	+0.23
s7	0.1	0.11	0.07	0.14	0.15	+0.08	+0.01
s8	0	0.25	0.21	0.29	0.19	–0.03	–0.10
Mean:						+0.01	
Std:						0.14	

amount of line failure for this data set.

Another point of interest is that whilst both the experimental tests and developed approach indicate a positive correlation between the level of axial stress and the likelihood of line failure, sensitivity between P_{step} and σ_v appears to be higher in the experiment than in the analytical predictions. Possible reasons for this include that values of either the coefficient of friction, μ [which was taken as 0.9, as per Eq. (4.24)], or the Poisson's ratio of the masonry units ν_u (assumed as 0.2), may have been underestimated in the analysis. Underestimation of μ is also indicated by a comparison of the predicted and measured strengths (Figure 5.12), whereby the strength predictions for wallettes with an applied axial stress are, on average, more conservative than for wallettes without axial stress (also refer to Table F.1).

5.7.2 Full-Scale Panels

Accuracy of the developed method for predicting the relative likelihood of stepped and line failure (as described in Section 5.6) was also examined through comparisons to the observed cracking patterns in full-scale walls s1–s8 (Chapter 2).

The crack patterns used for the comparisons were those at the conclusion of the cyclic tests (see Figure 2.24). In walls s1–s2 and s6–s8, cracks along both vertical edges were considered; however, in walls s3–s5, only the edges of the longer subpanel were considered, as the edges of the shorter subpanels developed only partial cracking. The experimental value of P_{step} was determined along each vertical edge as the observed number of bed joints undergoing stepped failure, divided by the total number of potential bed joints that could have failed. The results are provided in Table 5.3 (columns 3–5) for the left and right edge of each panel, as well as the average value. As was the case for the small-sized wallettes

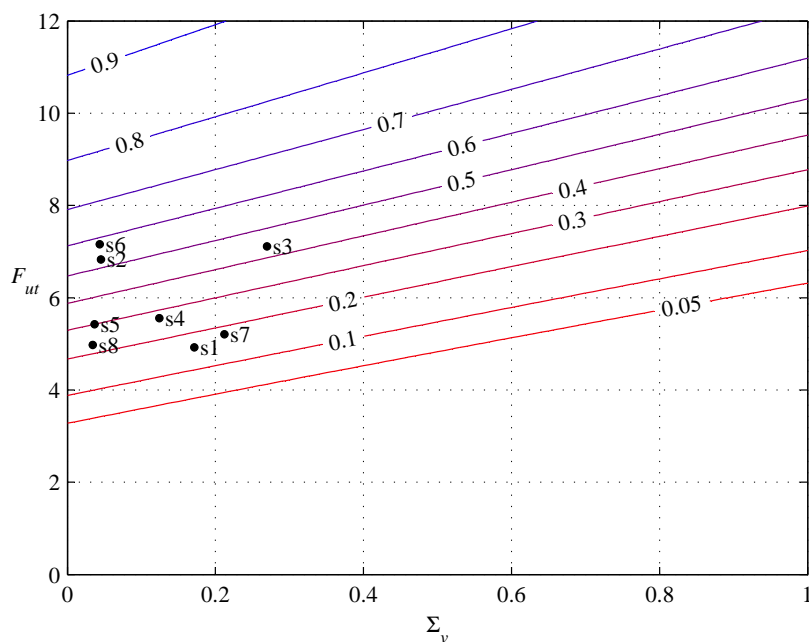


Figure 5.14: Predicted probability of stepped failure for walls s1–s8.

analysed in Section 5.7.1, there is a clear trend whereby the proportion of line failure increases with higher axial stress. For example, in the case of the long solid panels (s1, s2), panel s2 (with zero axial load) had 49% stepped failure, but panel s1 (with 0.1 MPa precompression) had only 25% stepped failure. The same trend is also evident for the long panels with an asymmetrically positioned window (s3–s5) and short panels with a centred window (s7, s8). It is noted, however, that the bond strength (f_{mt}) determined for each panel happened to be such that it may also have contributed to this trend. Full results are given in Appendix F.2 (Table F.2).

The expected proportion of stepped failure was determined using the method proposed in Section 5.6. Each wall was analysed using its own value of the mean bond strength (\hat{f}_{mt}) and corresponding coefficient of variation ($C\langle f_{mt} \rangle$), as determined from material tests (reported in Table A.2, Appendix A). The axial stress was taken as the average value along the vertical edge of the panel, accounting for both the applied axial loading and self-weight. Other input parameters included: $r = 1.6$, $\mu = 0.9$; whilst the Poisson’s ratio of the brick units was taken as $\nu_u = 0.2$, with $C\langle \nu_u \rangle = 0.2$. The predicted values of P_{step} are given in Table 5.3 (column 6). A detailed summary of the results and input parameters is provided in Appendix F.2 (Table F.2).

Figure 5.14 provides an illustrative example of the graphical method of solution proposed in Section 5.6.2. This graph uses a single value of the CoV, taken as $C\langle f_{mt} \rangle = 0.27$, based on the pooled bond strength data set (refer to Table 5.1). It is

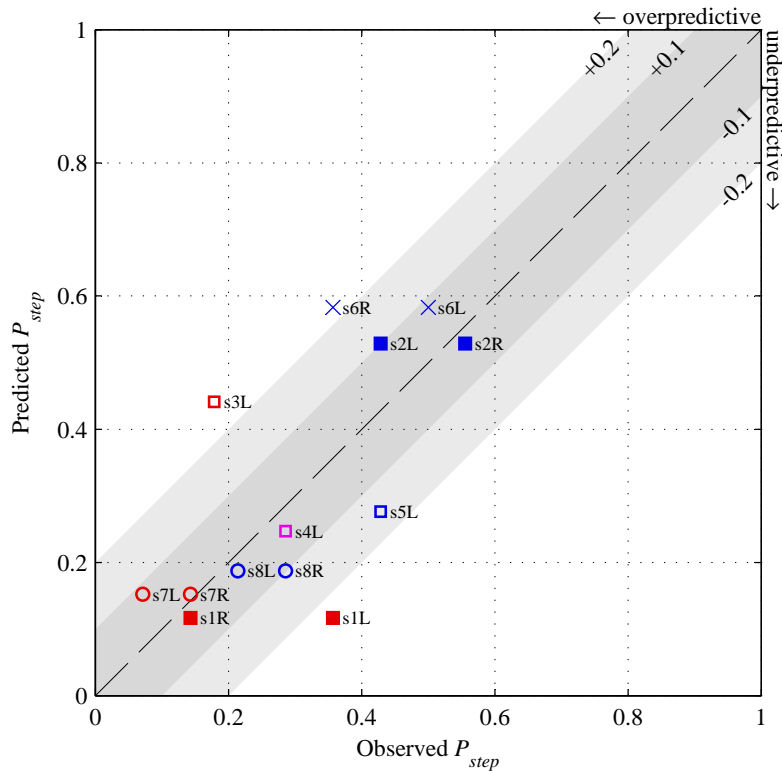


Figure 5.15: Comparison of predicted and observed proportion of stepped failure for full-scale test walls.

seen that this does not significantly alter the results compared to predictions based on panel-specific values of the CoV (in Table 5.3).

A comparison of the predicted and observed proportion of stepped failure is provided in Figure 5.15. The accuracy of the predictions is highly promising, and significantly better than for the small-sized wallettes (Section 5.7.1). The average error in P_{step} (taken as the calculated value minus the observed value) is $+0.01$, which is approximately neutral (Table 5.3). Furthermore, the results lie within the ± 0.1 band, in nine of the 13 cases considered. The only two panels where the method overpredicts P_{step} by more than 0.2, are walls s3 and s6, which incidentally had the lowest measured bond strength of the eight walls. By contrast, the only case where the method underpredicts P_{step} by more than 0.2, is wall s1, in which the measured bond strength was the highest.

5.8 PARAMETRIC STUDY

Several studies were conducted using the developed stochastic methodologies, to investigate the effects of various parameters on the expected ultimate and residual

strengths. The parameters considered include:

- Geometry of the masonry units, particularly the ratio of h_u/t_u ;
- Mean tensile strengths \hat{f}_{ut} and \hat{f}_{mt} , and their ratio (F_{ut}); and
- The amount of vertical compressive stress σ_v (or Σ_v).

To investigate the effect of these parameters, material variability was kept constant at $\text{CoV} = 0.3$ in the examples presented herein.

5.8.1 Influence of Brick Geometry on Likelihood of Stepped Failure

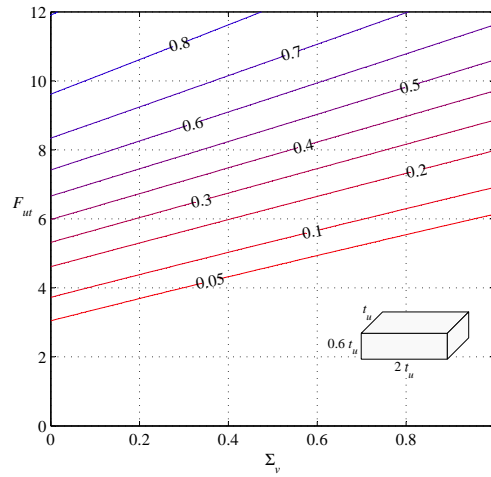
Figure 5.16 shows the effect of brick geometry on the likelihood of stepped failure, by varying the height of the brick unit. The ratio of the length and width of the unit is kept constant at $l_u/t_u = 2$. For simplicity, the mortar joint thickness has been ignored in this example ($t_j = 0$). The plots show that short units have a greater chance of undergoing line failure, while tall units are more likely to develop stepped failure. This is because whilst both types of units have the same capacity against stepped failure, a taller unit has a greater resistance against line failure, due to its larger sectional area.

5.8.2 Influence of Brick Geometry on Ultimate and Residual Strength

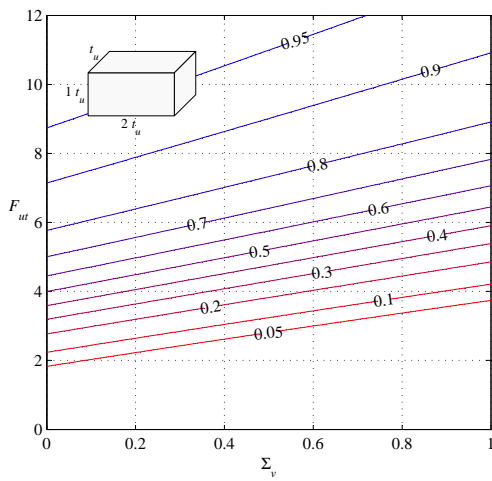
The influence of brick geometry on the ultimate strength (η_{mix}) and residual strength (η_{res}) of the masonry is shown by Figure 5.17. The ratio of axial stress to bond strength is kept constant at $\Sigma_v = 0.4$. Note that the residual strength was calculated using Eq. (5.35), which effectively factors the nominal strength (assuming a fully stepped crack) by the probability of stepped failure.

When the ratio of brick strength to bond strength is small (approx. $F_{ut} \lesssim 1.5$, for the tall unit), line failure will be the dominant mode. Consequently, within this range of F_{ut} , the ultimate strength is proportional to F_{ut} and approximately equal for all three unit geometries. At small F_{ut} , the residual strength is negligible, due to the very low probability of stepped failure.

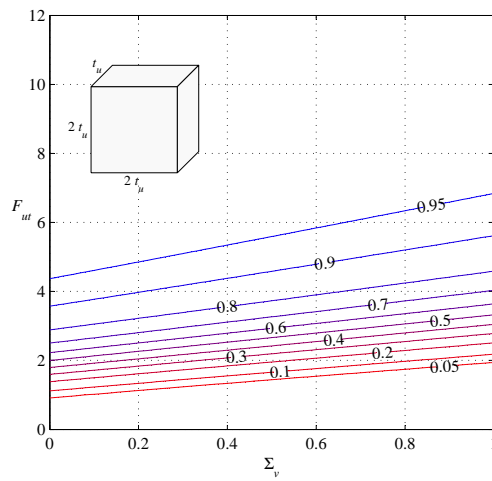
As the ratio of the brick strength to bond strength increases, the failure mode undergoes a transition from the line mode to the stepped mode (between approx. $1.5 \lesssim F_{ut} \lesssim 4$, for the tall unit). Within this range of F_{ut} , the ultimate moment capacity goes from being f_{ut} - to f_{mt} -proportional. The masonry also begins to develop residual strength, due to the increased likelihood of stepped failure. The



(a) Short unit, $t_u : l_u : h_u = 1 : 2 : 0.6$



(b) Intermediate unit, $t_u : l_u : h_u = 1 : 2 : 1$



(c) Tall unit, $t_u : l_u : h_u = 1 : 2 : 2$

Figure 5.16: Influence of brick shape on the probability of stepped failure ($CoV = 0.3$).

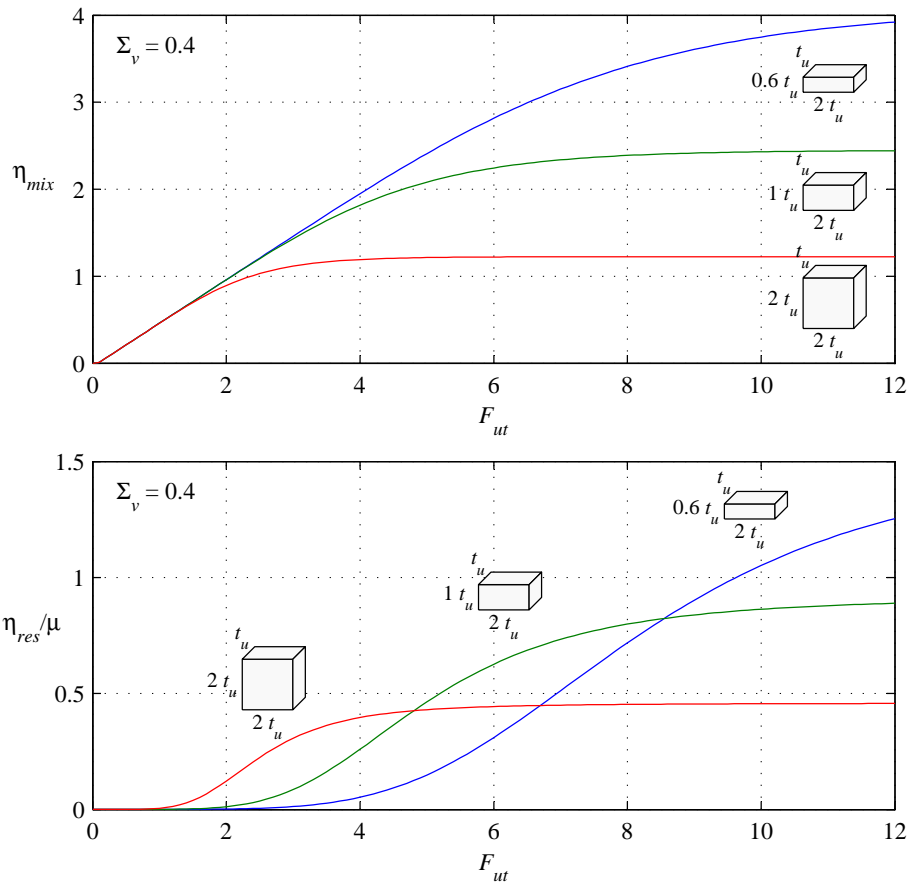


Figure 5.17: Influence of brick shape on ultimate and residual strength for $\Sigma_v = 0.4$, $CoV = 0.3$.

range of F_{ut} at which this transition occurs is dependent on the brick geometry and becomes higher as the h_u/t_u ratio reduces.

When the brick strength is sufficiently high relative to the bond strength (approx. $F_{ut} \gtrsim 4$, for the tall unit), stepped failure becomes the dominant mode. This causes the ultimate moment capacity to become f_{mt} -proportional. The residual strength also reaches its full potential, due to the absence of any strength reduction from line failure. In this range of F_{ut} , capacity for both the ultimate and residual strength is derived from torsional resistance along the bed joints. Since masonry built with short bricks has a greater number of bed joints over a given height of the crack compared to tall brick masonry, the ultimate and residual strength both increase as the units become shorter in height.

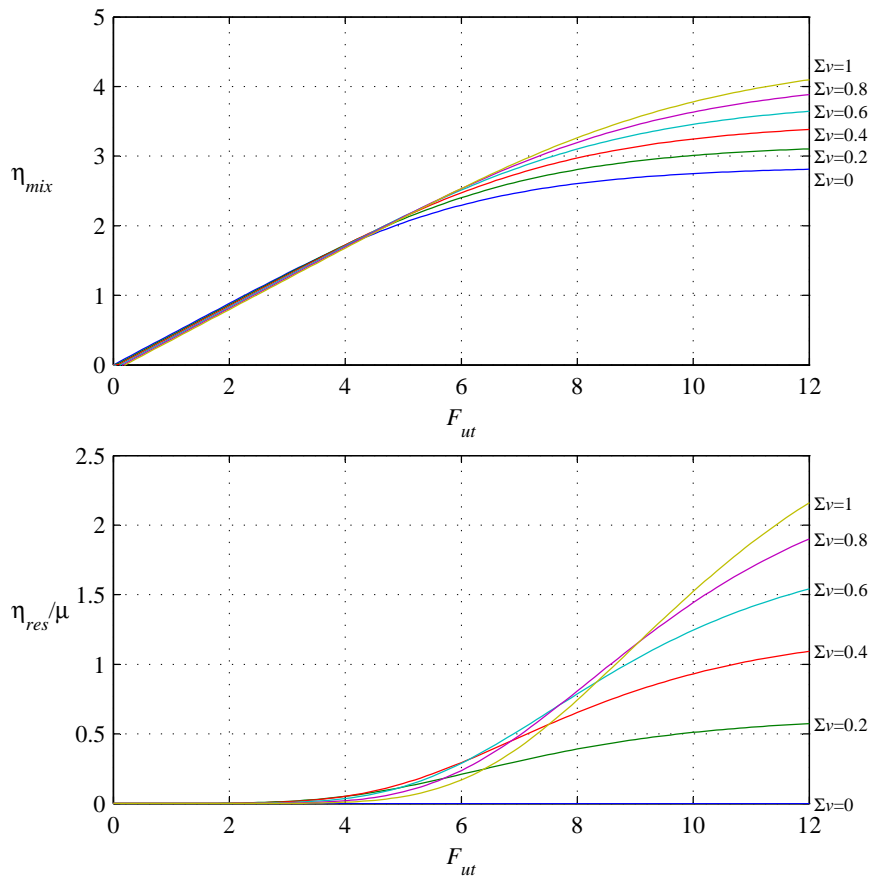


Figure 5.18: Influence of axial stress on ultimate and residual strength for standard clay brick masonry ($\text{CoV} = 0.3$).

5.8.3 Influence of Axial Stress on Ultimate and Residual Strength

The influence of axial stress (Σ_v) on the ultimate and residual strength is shown by Figure 5.18. The masonry constituent geometry in this example corresponds to standard clay brickwork.

When the ratio of the brick strength to bond strength is small (approx. $F_{ut} \lesssim 4$), ultimate strength (η_{mix}) is governed by line failure. It is seen that in this range of F_{ut} , an increase in the amount of axial stress acts to reduce the strength, due to Poisson's effect. At high brick to bond strength (approx. $F_{ut} \gtrsim 8$), stepped failure becomes dominant and the axial stress generates a positive effect on the ultimate strength, by enhancing the frictional moment resistance along the bed joint.

The effect of axial stress on the residual strength (η_{res}) is particularly interesting. In general terms, as the axial stress increases, the maximum potential residual strength due to friction (assuming full stepped failure) also increases proportionally. However, as Σ_v is varied, the F_{ut} transition zone between stepped and line failure

also shifts. Consequently, when F_{ut} is low, axial stress will have a detrimental effect on the residual strength, since it increases the amount of line failure. However, if F_{ut} becomes sufficiently high, then the amount of stepped failure increases and the masonry becomes able to exploit its full frictional capacity, thus making a higher axial stress more beneficial.

5.9 CONCLUSIONS

The main outcome of this chapter has been the development of a pair of stochastic methodologies for dealing with combined stepped and line failure in horizontal bending.

The first methodology is used to predict the expected reduction in the ultimate strength caused by weak link effects. Equivalent strength reduction factors have been derived for mean and characteristic ultimate strength, with the latter applicable toward design. The predictions indicate that for a typical level of variability in the material properties ($\text{CoV} = 0.3$), there can be a potential 17% reduction in strength; whilst for higher levels of material variability ($\text{CoV} = 0.5$), the strength reduction could be as high as 28%. However, although such a strength reduction is considerable, it appears to be sufficiently accounted for by the capacity reduction factor of 0.6, which is used in flexural design according to AS 3700. A potential use of the proposed method is to provide a basis for the development of a partial safety factor design procedure.

The second developed methodology is used to predict the relative likelihood of stepped failure versus line failure. The method has produced good correlation with experimentally observed crack patterns in full-scale panels. Since previous research [Willis, 2004] has demonstrated that the residual moment capacity in horizontal bending is effectively proportional to the amount of stepped failure along the crack, the proportion of stepped failure predicted using the proposed approach could be used as a strength reduction factor applicable to the post-cracking strength. Furthermore, the method could be used as the basis for the development of an assessment technique to check against other types of secondary failure along vertical cracks, in order to ensure that vertical edge separation does not occur in two-way walls.

Chapter 6

COLLAPSE LOAD PREDICTION IN DRY MASONRY WALLS

Abstract

This chapter describes an analytical procedure for predicting the static strength of unreinforced masonry walls using a collapse mechanism analysis. The proposed method treats the masonry as having zero cohesion (bond strength) and assumes that a wall's lateral load resistance is obtained entirely from rigid body restoration due to gravity and frictional sources. As such, the developed approach becomes potentially suitable for the assessment of existing unreinforced masonry buildings, where it can be particularly difficult to reliably quantify the tensile bond strength of the masonry. Considered are a set of standard mechanisms involving flexural deformation along the out-of-plane panel, as well as hybrid mechanisms incorporating combined flexural deformation along the out-of-plane panel with in-plane shear deformation in the connecting return walls. The accuracy of the analysis is assessed by comparisons with the results of tilting table experiments involving dry-stack masonry, which demonstrate that predictions made by the analysis are in good agreement with both the experimentally measured collapse loads and observed failure patterns. A significant aspect of the proposed method is that it is based entirely on principles of mechanics and does not rely upon any empirically calibrated parameters.

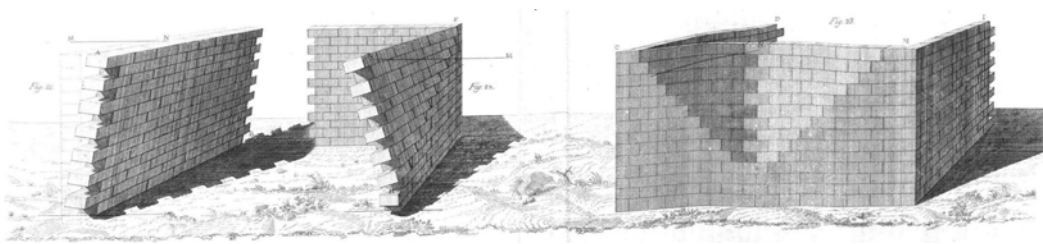


Figure 6.1: Rondelet's three mechanisms [Rondelet, 1802].

6.1 INTRODUCTION

Accurate calculation of a brick masonry wall's flexural strength can be obtained using sophisticated finite element analyses, which require accurate knowledge of the material properties as well as geometry and boundary conditions [e.g. Lourenço, 2002]. Finite element based limit analyses have also been shown to perform favourably in predicting wall failure mechanisms [Orduña and Lourenço, 2005a,b; Cecchi et al., 2007; Milani et al., 2007; Milani, 2008; Cecchi and Milani, 2008]. Nonetheless, there is also a parallel interest to develop more simplistic analytical procedures requiring a lesser computational effort, which may be implemented, for example, into large scale vulnerability assessment of historical structures. This has led to numerous works aimed at characterising possible types of out-of-plane collapse mechanisms and development of closed-form analytical expressions to evaluate their strength.

It could naturally be expected that with judicious choice of a collapse mechanism, a reasonably accurate prediction of the out-of-plane strength of a masonry wall could be made solely on the basis of its geometry and boundary conditions. This philosophy was used over two centuries ago by Rondelet [1802], who described three simple out-of-plane failure mechanisms for different wall support conditions and used stability principles to determine their capacities (Figure 6.1). Modern day research in this field began with work by Giuffrè [1990, 1993], who conducted post-earthquake inspections of historical buildings and identified several likely out-of-plane collapse mechanisms based primarily on rigid body overturning. Significant advancements to the analytical methodology were made by de Felice and Giannini [2001], by proposing a pair of collapse mechanisms incorporating combined out-of-plane failure of the façade walls with shear failure in the adjoining in-plane walls, and also accounting for friction along the in-plane shear cracks. D'Ayala and Speranza [1999, 2002, 2003] identified numerous additional out-of-plane failure mechanisms and made further refinements to the corresponding calculation techniques by allowing for additional frictional effects, the presence of overburden loads, and the ability of mechanisms to span over multiple storeys within the

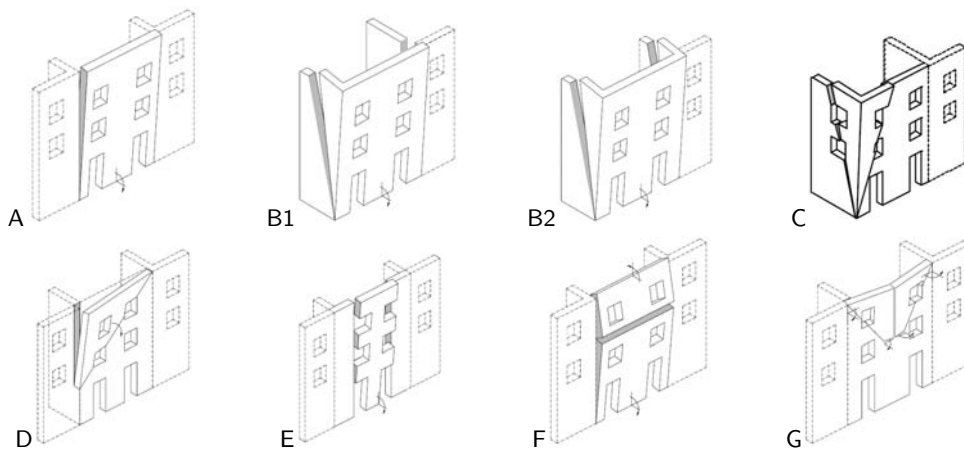


Figure 6.2: Mechanisms considered by *D'Ayala and Speranza* [2003]. (Graphics used with permission from EERI.)

building (Figure 6.2). Additional development of the analytical approach was performed by *Casapulla* [2008], who also reasoned that frictional contributions to the strength should be treated in terms of possible bounds rather than specific values.

In this chapter, the general analytical approach is further refined to account for: (i) horizontal bending due to torsional friction along bed joints, (ii) translational bed joint friction due to internal shear deformation of participating in-plane walls; and (iii) the potential strengthening or weakening influence that can result from a restrained/unrestrained overburden load and its eccentricity. Additional collapse mechanisms are also proposed on the basis of failure patterns observed in experimentally tested dry-stack masonry (DSM) walls [*Restrepo Vélez, 2004; Restrepo Vélez and Magenes, 2009*]. The analytical formulations are based on the virtual work approach, in which the external work done by the load on the wall is equated to the internal work done along deforming flexural cracks and, where the mechanism involves cracks in the return walls, also due to in-plane shear deformation. This conveniently leads to the calculation of the collapse load in terms of the load multiplier λ_o , defined as the ratio of the lateral load capacity to the weight of the panel [refer to Eq. (2.3)], which may also be interpreted as an equivalent lateral acceleration in units of g 's.

A key feature of the presented methodology is that, unlike the ultimate strength analysis presented in Chapter 4, it neglects any strength contribution from the tensile bond strength (f_{mt}), and thus effectively treats the wall as being already cracked. In turn, the analysis assumes that the wall derives its entire load resistance from gravity effects, including internal restoration moments and friction. Whilst this approach will generally predict lower (more conservative) load capacities, the

fact that it does not rely on the stress capacities of the masonry material for inputs makes it a suitable seismic assessment tool for existing unreinforced masonry (URM) buildings, where it can be particularly difficult to determine a reliable value of f_{mt} or to detect any preexisting cracking.

The chapter is structured as follows: The various collapse mechanisms considered are introduced in Section 6.2. Considerations relating to the wall boundary conditions are discussed in Section 6.3. The general analytical procedure for calculating the collapse load is described in Section 6.4, and derived analytical equations for the specific mechanisms are presented in Section 6.5. Analytical predictions are compared with experimental results in Section 6.6, and a set of parametric studies are undertaken in Section 6.7 to determine the sensitivity of the predictions to the choice of mechanism. The chapter concludes in Section 6.8 with a summary of the outcomes. Additional information related to the topics covered in this chapter is provided in Appendix G, including derivations and worked examples demonstrating the application of the method.

6.2 COLLAPSE MECHANISMS

The various mechanisms considered in this chapter are illustrated in Figure 6.3. All mechanisms assume that the wall's bottom edge in addition to at least one vertical edge are restrained from lateral movement—conditions sufficient to facilitate two-way bending. They include the pure out-of-plane mechanisms G, K1 and K2 (referred to as *standard* mechanisms); and the *hybrid* mechanisms J and B, combining flexural deformation along the out-of-plane panel with shear deformation in the adjacent in-plane return walls. The mechanisms can also be categorised as either type-1, in which the top edge of the wall is free to undergo lateral movement (including G, J, B and K1), or type-2, where the top edge of the wall is laterally restrained (only K2).¹ Furthermore, each of the mechanisms can assume one- or two-sided forms, based on the number of supported vertical edges.

6.2.1 Type G

Type G mechanisms (Figure 6.3) are a class of standard two-way mechanisms applicable to walls free along their top edge. In the present treatment, they are subcategorised into the complimentary forms G_x and G_y , corresponding to different length to height aspect ratios. The overall shapes of these mechanisms are characterised by a V-shape, formed by diagonal crack lines propagating downwards from

¹While type-2 versions of mechanisms G, J and B are also conceptually possible, they are not considered here, as such forms are generally not known to occur.

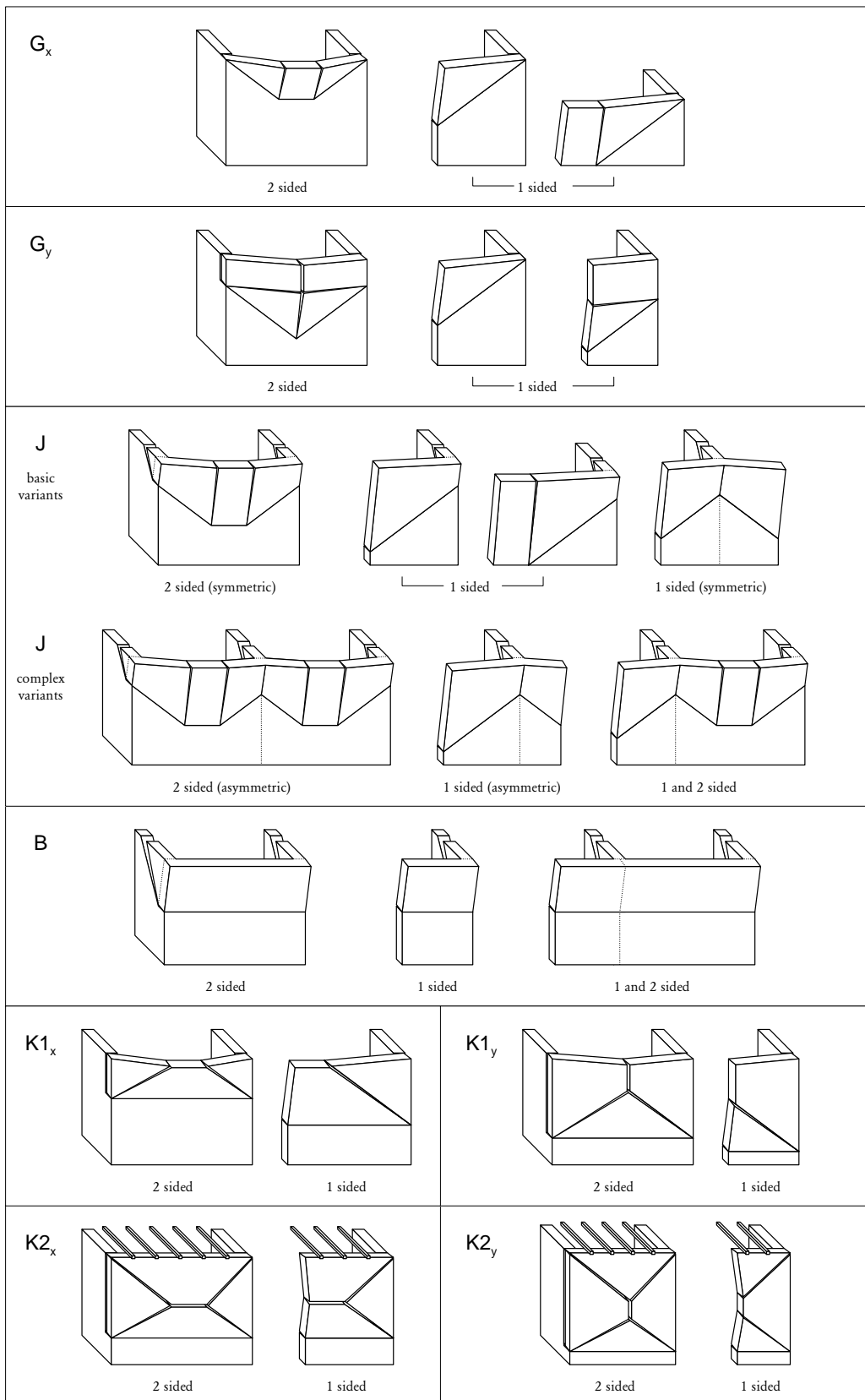


Figure 6.3: Collapse mechanisms.

laterally supported vertical edges. The mechanisms can be considered variations of Rondelet's second and third mechanisms (Figure 6.1), or D and G reported by *D'Ayala and Speranza* [2003] (Figure 6.2). Interestingly, type G mechanisms have been observed through several different experimental studies on DSM walls [*Ceradini, 1992; Giuffrè, 1993; Restrepo Vélez, 2004; Vaculik et al., 2004; Shi et al., 2008*]; however, they are generally not known to occur in mortar-bonded URM walls, which instead tend to undergo type K mechanisms (Section 6.2.3).

6.2.2 Hybrid Types J and B

Mechanisms J and B (Figure 6.3) are hybrid mechanisms applicable to two-way walls free along the top edge. In applying these mechanisms, it is assumed that the loading direction is outward from the supporting return walls, which enables the return walls to participate through in-plane shear deformation. Hence, a significant feature of these mechanisms is that, unlike the standard mechanisms, they do not necessarily need to be confined to a single out-of-plane wall, but rather have the ability to form chains spanning along multiple adjacent out-of-plane walls.

Mechanism J is a proposed mechanism which can be considered to be a hybrid variant of the standard mechanism G_x . Its one-sided form somewhat resembles a combination of *D'Ayala and Speranza's* D and B1, whilst its two-sided form is similar to a combination of G and B2 (Figure 6.2). This mechanism can be observed extensively in Restrepo Vélez's experimental study using DSM [*Restrepo Vélez, 2004*] and has been developed on this basis. It also appears to be present in DSM tests reported by *Shi et al.* [2008]. Mechanism B is a hybrid version of the typical one-way vertical bending mechanism for parapet walls (referred to throughout as V1), and is equivalent in shape to B1 and B2 by *D'Ayala and Speranza*. While it may appear that mechanism B is simply a particular case of J in which the length of the diagonal cracks approaches zero (or $a = 1$, refer to Figure 6.14), the difference in their treatment is the inclusion of additional internal work along the internal vertical cracks in J, which are absent from B. This means that mechanism B could become energetically more feasible than J in certain situations, particularly for walls with a high H/L aspect ratio.

The fundamental distinction between the treatment of hybrid mechanisms in this chapter and *D'Ayala and Speranza* [2003], is the resistance model used for the in-plane components. While both models allow the mobilised portion of the in-plane panel to adopt a triangular shape, the approach by *D'Ayala and Speranza* assumes that the mobilised panel undergoes rigid body overturning. This assumption, however, implies that the masonry has sufficient tensile strength to remain monolithic, which is inaccurate when dealing with DSM or masonry with

very poor bond strength. As a result, the *D'Ayala and Speranza* approach could potentially become unconservative when applied to this type of masonry, as the assumed rigid body restoring moment can constitute a significant proportion of the overall lateral load resistance. The proposed in-plane deformation model adopted throughout this chapter (described in Section 6.4.3) is fundamentally different: It treats the in-plane walls as having zero bond strength and assumes that internal resistance is obtained purely from frictional sources. Consequently, the mobilised panel not only slides with respect to the stationary part of the return wall, but it also undergoes internal shear deformation whereby adjacent courses of bricks slide relative to each other (refer to Figure 6.11). The latter condition is necessary in order to satisfy displacement compatibility between the in-plane and the out-of-plane panels within the overall mechanism.

6.2.3 Types K1 and K2

Type K mechanisms (Figure 6.3) are a general class of mechanisms characterised by diagonal crack lines propagating from corners at which orthogonal supported edges of the wall intersect. In the present treatment, they are divided into two subclasses: K1, in which the top edge is free; and K2, where the top edge is laterally restrained. Both subclasses are further subdivided into their complimentary forms, $K1_x/K1_y$ and $K2_x/K2_y$, depending on the length to height aspect ratio. Type K mechanisms represent the most common class of mechanisms associated with mortar-bonded URM walls possessing tensile bond strength, and have been observed throughout many experimental studies [*Baker, 1973; Anderson and Bright, 1976; West et al., 1977, 1979b,a; Hodgkinson et al., 1982a,b; Lawrence, 1983; Tapp, 1985; Drysdale and Essawy, 1988; Chong, 1993; Ng, 1996; Abrams et al., 1996; Griffith, 2000; Edgell and Kjær, 2000; Jaramillo, 2002; Korany, 2004; Edgell, 2005*] including the original experimental work reported in Chapters 2 and 3. As such, these mechanisms have been used as the basis of numerous methods for ultimate strength design of two-way walls (see Section 4.2), including the virtual work (VW) approach developed by *Lawrence and Marshall [1996]* and adopted in the Australian code AS 3700 [*Standards Australia, 2001*]; traditional yield line analysis [originally developed by *Johansen, 1962*]; as well as modified versions of yield line analysis [*Sinha, 1978; Baker et al., 2005*].

6.3 BOUNDARY CONDITIONS

The position of a wall within the overall building plays an important role with regard to its out-of-plane behaviour. In the analysis of a particular wall, the wall is treated in isolation from the surrounding structure, and the influence of the

structure gets replaced by a set of idealised boundary conditions acting upon the wall. This section provides a discussion of considerations relating to boundary conditions and the resulting implications toward the analysis, including: lateral restraint of the top edge (Section 6.3.1); loadbearing walls (Section 6.3.2); and vertical edge supports (Section 6.3.3).

6.3.1 Lateral Restraint Along the Top Edge

A particularly important consideration when undertaking an analysis is determining whether the top edge of the wall is laterally restrained or free to displace horizontally. As mentioned earlier, all of the mechanisms presented in Section 6.2 assume that the wall has translational restraint along the bottom edge and at least one vertical edge. The flowchart in Figure 6.4 can be subsequently used to establish whether the top edge of the wall is adequately restrained to allow the use of a type-2 mechanism, or whether a type-1 mechanism must be used instead whereby the top edge is treated as unrestrained. The latter option will generally yield lower (more conservative) capacities.

6.3.2 Overburden Loads

A wall is considered to be loadbearing if it acts as a gravity force path for an overburden load (OBL) due to a floor system or some other part of the overall structure. A feature of the analytical methodology presented in this chapter is that it allows for the presence of an OBL and accounts for the resulting effects on the wall's load capacity. The following considerations are taken into account:

- Enhancement in the wall's flexural resistance as a result of higher vertical compressive stress;
- Restraint of the OBL against horizontal movement;
- Adequacy of the shear connection between the OBL and the wall; and
- Eccentricity of the force transfer point between the OBL and the wall.

These will now be discussed in greater detail. Firstly however, some basic symbolic notation will be introduced, as it is referred to throughout the upcoming discussions.

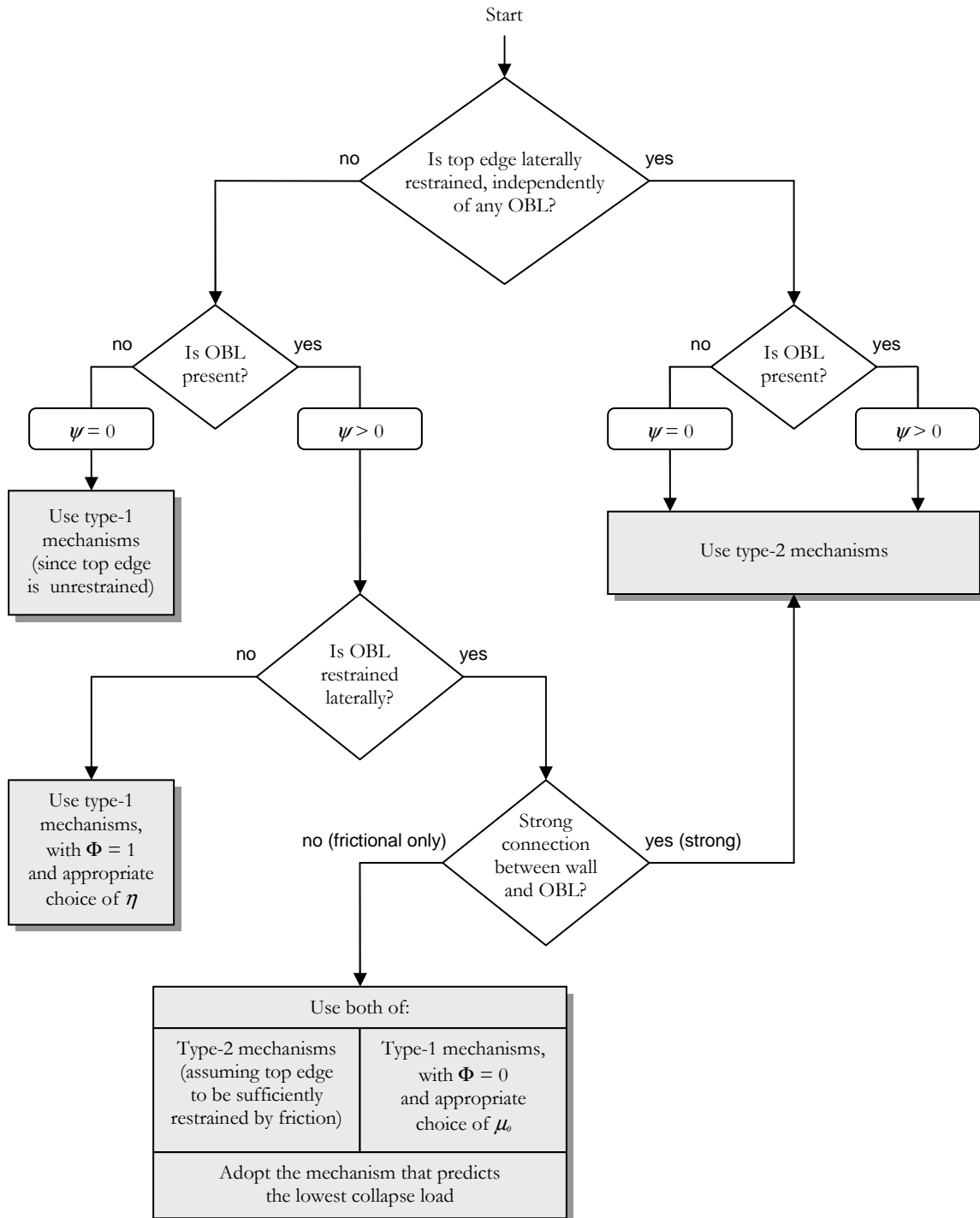


Figure 6.4: Flowchart for choosing an appropriate type of mechanism (type-1 or type-2), as well as parameters ψ and Φ , as necessary. In type-1 mechanisms, the top edge of the wall is able to displace horizontally (includes G, J, B and K1). In type-2 mechanisms, the top edge is restrained from lateral movement (includes K2).

A convenient way to express the magnitude of the OBL is in terms of the overburden weight ratio ψ , defined as

$$\psi = \frac{W_{vo}}{W_{tot}}, \quad (6.1)$$

where W_{vo} is the vertical force exerted by the OBL onto the wall, and W_{tot} is the weight of the wall over the mechanism's total height H_t .² The corresponding vertical compressive stress generated at the top of a wall is³

$$\sigma_{vo} = \frac{W_{vo}}{t_u L}, \quad (6.2)$$

where t_u is the thickness of the wall and L is the length over which W_{vo} acts. It may also be expressed in terms of ψ , as

$$\sigma_{vo} = \psi \gamma H_t, \quad (6.3)$$

where γ is the weight density of the masonry material.

Enhancement of Internal Flexural Resistance

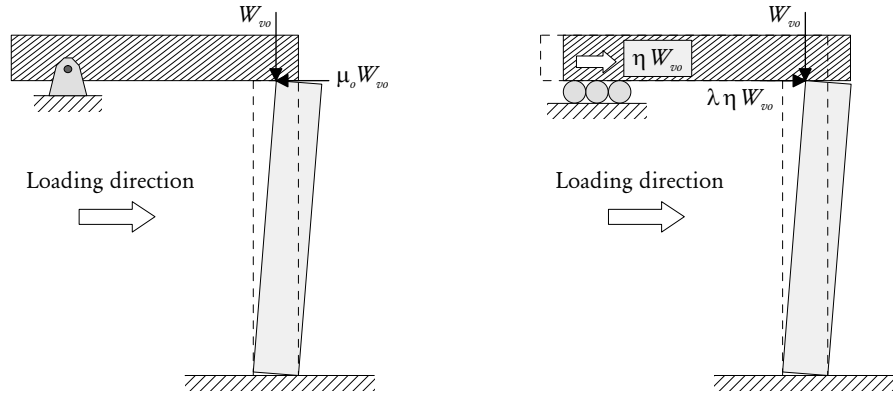
An important influence of an OBL is that it generates additional vertical compression throughout the wall, which enhances the wall's capacity to resist flexure. In the analysis procedure presented in this chapter, this effect is accounted for by the σ_{vo} term in the stress capacity function [Eq. (6.22)] which is subsequently used in calculating the internal moment capacities.

Restraint of the Overburden Load

When applying type-1 mechanisms to loadbearing walls, a particularly important consideration is establishing whether or not the OBL is restrained from displacement along the horizontal degree-of-freedom (DOF) (Figure 6.5). We define the OBL to be *restrained* when some part of the overall structure can provide a load path for the OBL's horizontal inertial load, and conversely, *unrestrained* when the only part of the structure able to provide a horizontal load path is the out-of-plane wall itself. A typical example of a restrained OBL is a stiff slab that rests upon the out-of-plane

²It should be noted that since the mechanism height H_t is treated as an independent variable in the analytical method presented in this chapter, ψ will not necessarily remain constant when considering a particular wall.

³Note that the axial stress σ_v refers to the equivalent stress generated at a particular height of the wall, by treating the compressive force as acting over the entire bedded area. It is not intended to account for stress concentrations across cracked sections.



(a) Overburden load restrained against lateral movement ($\Phi = 0$) with a frictional mode of connection between the wall and load. The resulting friction provides an additional restoration force to the wall.

(b) Overburden load unrestrained against lateral movement ($\Phi = 1$), thus exerting an additional overturning force on the wall. It is assumed that the connection between the load and wall is sufficient to avoid slip.

Figure 6.5: Additional horizontal loads imposed on a wall by either a restrained or unrestrained overburden load in type-1 mechanisms.

wall, but whose horizontal inertial load can be resisted by stiff in-plane shear walls. By contrast, a flexible floor diaphragm may act as an unrestrained OBL that can apply additional lateral load to an out-of-plane wall along its top edge.

The influence of the restraint is illustrated by Figure 6.5, which shows that when a type-1 mechanism is considered in conjunction with an acting OBL, an additional horizontal force becomes generated and transferred to the wall along its top edge. If the OBL is restrained and a frictional connection is present between the wall and OBL (Figure 6.5a), a frictional force equal to $\mu_o W_{vo}$ (where μ_o is the friction coefficient) becomes generated in opposition to the wall's motion, thereby enhancing its strength. By contrast, if the OBL is unrestrained (Figure 6.5b), then under inertial loading it will apply an additional overturning force onto the wall, thus reducing its load capacity. This additional load is equal to $\lambda \eta W_{vo}$, where λ is the lateral load multiplier; and η is defined to as the orthogonal factor of the OBL, which corresponds to the ratio

$$\eta = \frac{W_{ho}}{W_{vo}}, \quad (6.4)$$

where W_{ho} is the component of the OBL's weight free to impose a horizontal reaction onto the wall and W_{vo} is the acting vertical reaction. The factor η is introduced because in certain instances the weight components acting horizontally and vertically may not necessarily be equal. Nonetheless, its value may generally be determined directly from statics. As a further note, when dealing with an unrestrained OBL and type-1 mechanisms, the proposed approach assumes that

the connection between the wall and overburden load is sufficiently strong to accommodate full transfer of the overburden load's horizontal inertial force. Whilst this assumption is conservative with respect to calculating the wall's collapse load, it can be verified at the discretion of the user. For example, it can be easily shown that for a purely frictional connection with a friction coefficient μ_o , the load multiplier to cause slip along the joint is

$$\lambda = \mu_o / \eta. \quad (6.5)$$

To activate the effects associated with the OBL restraint in the analytical equations presented throughout this chapter, the binomial variable Φ is used, defined as the DOF factor of the OBL with respect to the horizontal direction of displacement. Its value is taken as

$$\Phi = \begin{cases} 0 & \text{for a restrained overburden load,} \\ 1 & \text{for an unrestrained overburden load.} \end{cases} \quad (6.6)$$

The flowchart provided in Figure 6.4 may also be used to determine its value.

Horizontal Strength of the Connection

In the case of a restrained OBL, the strength of the shear connection between the OBL and the wall can have a significant influence on the wall's response, because it influences whether the top edge of the wall is sufficiently restrained. We define the connection to be either *frictional* or *strong*. A frictional connection is one where load transfer relies purely on friction between the OBL and the wall, whereas a strong connection is one that is assumed to have sufficient capacity to accommodate any required load transfer. For instance, a strong connection may result from steel ties connecting the wall to an adjacent concrete slab.

As seen from the flowchart in Figure 6.4, if the OBL is restrained and a strong shear connection is provided, then the top edge of the wall can also be considered restrained and a type-2 mechanism may automatically be used. However, in the case of a frictional connection, the wall may respond either by a type-1 or type-2 mechanism, depending on whether the friction is sufficient to accommodate the required reaction at the top edge. The suggested approach in such a case is to consider both types of mechanisms individually, and adopt the one that predicts the lower collapse load. Alternatively, by making the conservative assumption the top and bottom edges each resist half of the lateral load in a type-2 mechanism,⁴

⁴This assumption is deemed conservative, because it may be demonstrated using statics that

it follows that friction should be sufficient to provide lateral restraint to the top edge when the available friction capacity ($\mu_o \psi W_{\text{tot}}$) exceeds the required reaction ($\frac{1}{2} \lambda_o W_{\text{tot}}$). This leads to the inequality expression

$$\lambda_o < 2\mu_o \psi, \quad (6.7)$$

which could be used to check whether the calculated collapse multiplier λ_o can be realised with the available friction. Therefore, a two tiered approach may also be implemented, in which a type-2 mechanism is first used, and if the calculated collapse multiplier satisfies the above inequality then the result is accepted; otherwise, a type-1 mechanism is used instead.

Eccentricity Effects

The position of the load transfer point between the OBL and the wall influences the wall's lateral load resistance and displacement capacities, since it affects the moment imposed on the wall. These effects were recognised in analytical load-displacement relationships derived by *Doherty* [2000] for vertically spanning one-way panels, where he considered the OBL to act at either the upward-deflecting rotational point at the top edge, or at the mid-thickness of the wall. The treatment used here is a more generalised one, in that the eccentricity is specified using the factor ϵ , defined such that the OBL acts at a distance ϵt_w measured from the upward-deflecting point along the wall's cross section (Figure 6.6). It is worth noting that the upward-deflecting point occurs on the windward side in type-1 mechanisms and on the leeward side in type-2 mechanism, as denoted by 'W' and 'L' in Figures 6.7 and 6.8.

A further consideration which has implications toward the cyclic behaviour of the wall, is the mode of connection between the OBL and the wall, particularly whether the load is transferred through a bearing (Figure 6.7) or across a horizontal surface such as a stiff slab (Figure 6.8). In the case of a bearing connection, the position of the load transfer point will remain fixed regardless of whether the displacement is positive or negative (Δ^+ and Δ^- as shown in Figure 6.7), and hence the eccentricity ϵ will alter depending on the displacement direction. Therefore, unless the bearing is positioned at the mid-thickness of the wall ($\epsilon = 1/2$), the wall's load-displacement behaviour will be asymmetric. In the case of a stiff slab, the load transfer point will shift when the wall transitions between the opposite displacement directions, such that it is always positioned at the upward-deflecting point ($\epsilon = 0$), and hence the wall's behaviour will be symmetric. It can further be

the lateral reaction along the top edge is always lower than along the bottom edge, at the point of incipient rocking for mechanism K2 (refer to Appendix H.1). Furthermore, the assumption neglects any additional force transfer across the supported vertical edges.

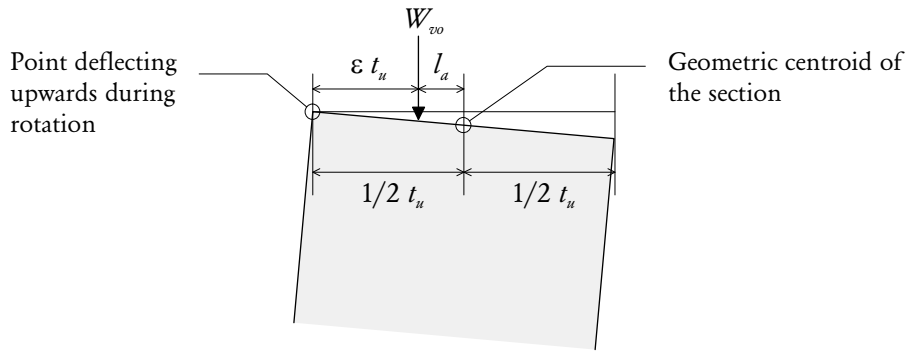


Figure 6.6: Overburden load eccentricity factor ϵ , defined such that the OBL acts at a distance ϵt_u measured from the upward-deflecting point along the wall's cross section.

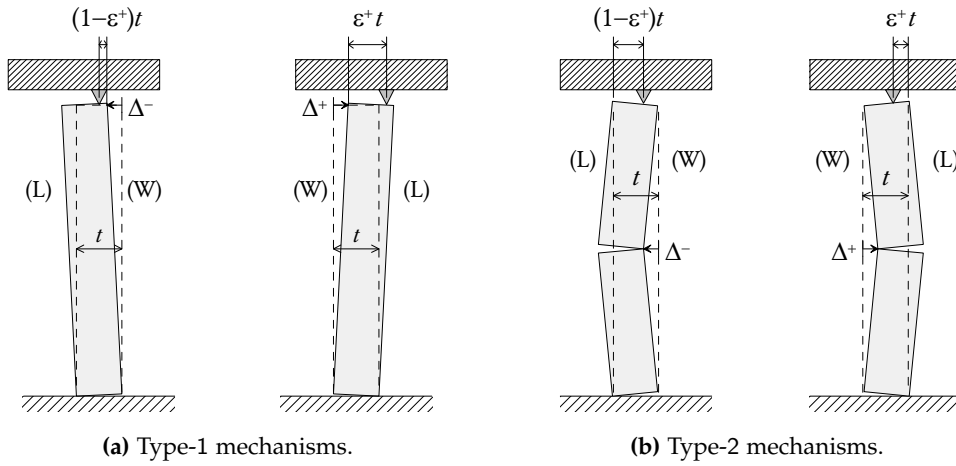


Figure 6.7: Eccentricities during reversed loading when force transfer occurs through a bearing. Asymmetric behaviour will result when $\epsilon \neq 1/2$.

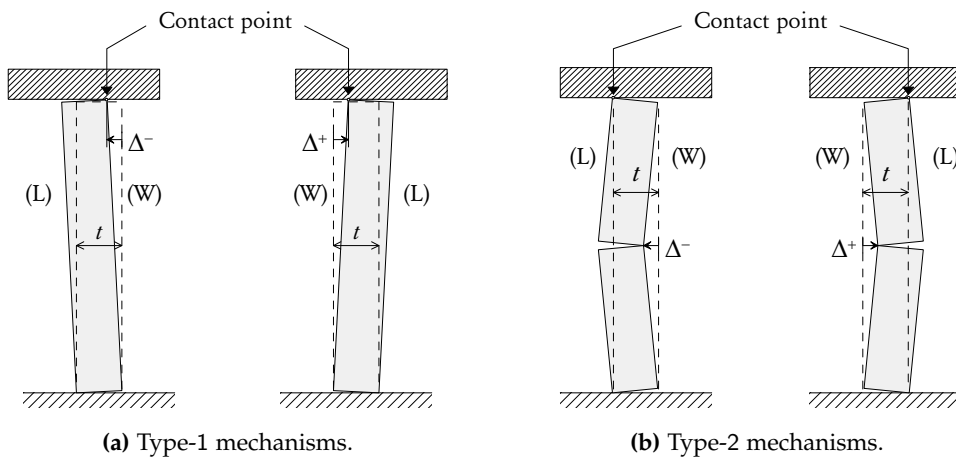


Figure 6.8: Eccentricities during reversed loading when force transfer occurs through a stiff horizontal surface such as a concrete slab. The load always acts at the upward-deflecting point of the wall section; therefore, $\epsilon = 0$ regardless of the loading direction.

demonstrated that the wall receives the maximum beneficial influence toward both its strength and displacement capacities when the OBL acts at the upward-deflecting point ($\epsilon = 0$), as this causes the OBL to impose the largest possible restoring moment onto the wall.⁵

6.3.3 Vertical Edge Restraint

The type of support condition present along the vertical edges of a wall can influence:

- The rotational restraint along the boundary; and
- The ability of the wall to undergo a hybrid mechanism.

The level of rotational restraint along a supported vertical edge affects the horizontal bending moment capacity that it can develop. From the collapse mechanisms defined in Section 6.2, this has relevance toward mechanism G_y and the full family of type K mechanisms ($K1_x$, $K1_y$, $K2_x$ and $K2_y$). In the methodology presented in this chapter, the rotational restraint is accounted for using the factor R_{vs} . This is equivalent to the R_{f1} and R_{f2} factors used in the AS 3700 virtual work procedure for ultimate strength design [developed by *Lawrence and Marshall, 1996*]. For consistency with AS 3700, it is recommended for R_{vs} to be taken as

$$R_{vs} = \begin{cases} 0 & \text{for no rotational restraint (simple support),} \\ 1 & \text{for full rotational restraint (fixed connection),} \\ \text{intermediate value} & \text{for partial rotational restraint.} \end{cases} \quad (6.8)$$

AS 3700, however, does not give any provisions regarding the types of support conditions that qualify for each of the above categories. The author recommends that full rotational restraint should only be assumed when the wall is continuous past the support, or when it is fully engaged into either an adjoining pier or a continuing return wall around a corner. For cases where the vertical edges are restrained only using wall ties (such as infill panels), it is prudent to assume zero rotational restraint. In cases where a wall has both vertical edges supported, but with different levels of rotational restraint, an average value may be used in the analysis.

The second consideration listed previously concerns whether or not the out-of-plane wall is able to form a hybrid mechanism J or B (Section 6.2.2). A conservative

⁵As demonstrated by analytical equations presented in Table 7.1.

approach recommended by the author is to always consider these mechanisms; however, the angle of the in-plane shear crack that can form may be limited in certain situations. For example, if the vertical edges of the out-of-plane wall are restrained using wall ties or engaged into a masonry pier, then the in-plane crack may only assume a vertical inclination ($\omega = 0$ in Figure 6.14). When the out-of-plane wall is engaged into adjoining return walls, it becomes possible for the in-plane shear crack to assume any diagonal inclination, assuming that the return wall is sufficiently long [within the limits of Eq. (6.33), as discussed in Section 6.4.3].

6.4 GENERAL METHOD FOR CALCULATING THE COLLAPSE LOAD

The methodology employed for calculating a wall's load capacity is based on the classical rigid plastic **VW** approach, which involves selecting an arbitrarily assumed collapse mechanism and calculating the corresponding kinematic collapse load. Due to the upper-bound nature of this method (as discussed in Section 4.2.1), the critical collapse mechanism is the one at which the collapse load is minimised. The process of solving for the collapse load therefore becomes an optimisation problem. An outline of the overall solution procedure is as follows:

1. Select the fundamental form of the collapse mechanism (for instance mechanism G_x), and express its geometry in terms of a series of independent variables such as its length and height dimensions.
2. Using the virtual work method, formulate a closed-form expression for the collapse load λ_o in terms of the relevant independent variables and constant properties for the particular masonry wall under consideration.
3. Define a set of constraints that govern the mechanism's geometry for the wall under consideration. This includes, for example, ensuring that the mechanism's length and height do not exceed the dimensions of the wall.
4. Perform an optimisation process to minimise λ_o for the selected mechanism, by varying the independent variables whilst satisfying the given set of geometric constraints.
5. Repeat steps 1 to 4 for each viable collapse mechanism; for example, after considering mechanism G_x analyse the wall with respect to the remaining type-1 mechanisms, G_y, J, B, \dots
6. Adopt the lowest calculated λ_o value together with the associated collapse mechanism as the overall critical solution.

This section provides the methodology used for calculating the collapse load λ_o for a particular chosen mechanism (Point 2 above), including: a discussion of the overall **VW** approach (Section 6.4.1); moment capacities of different types of cracks (Section 6.4.2); and shear capacity of in-plane walls involved in the hybrid mechanisms (Section 6.4.3).

6.4.1 Virtual Work Formulation

The load capacity of a wall with respect to a particular collapse mechanism is calculated using the **VW** approach, consisting of four basic steps:

1. Postulate a collapse mechanism,
2. Calculate the total internal work,
3. Calculate the total external work, and
4. Evaluate the collapse multiplier.

These steps will now be discussed in greater detail.

Postulate a Collapse Mechanism

Due to the inherent planes of weakness in an out-of-plane masonry wall, flexural (or rotational) cracks tend to be oriented either horizontally, vertically, or diagonally in accordance with the natural diagonal slope of the masonry, G_n , which may be determined directly from masonry unit geometry using Eq. (4.13) (refer to Figure 4.2). This reduces the number of viable collapse mechanisms to those that contain these three fundamental types of flexural cracks. With this in mind, several basic building blocks may be used to construct most typical mechanisms. Figure 6.9 shows the different types of blocks that may be used to compose the out-of-plane component of the mechanism along walls orthogonal to the loading direction. In the case of hybrid mechanisms, the block shown in Figure 6.10, which corresponds to a triangular-shaped deforming portion, may be used to account for the in-plane component (discussed in greater detail in Section 6.4.3). The various types of mechanisms considered in this chapter (Figure 6.3) are all composed using these fundamental blocks. For example, type G mechanisms consist of blocks shown in Figures 6.9a and 6.9d, whilst type K mechanisms consist of the blocks in Figures 6.9c and 6.9d. By contrast, hybrid mechanism J is composed of the blocks in Figures 6.9b, 6.9d and 6.10.

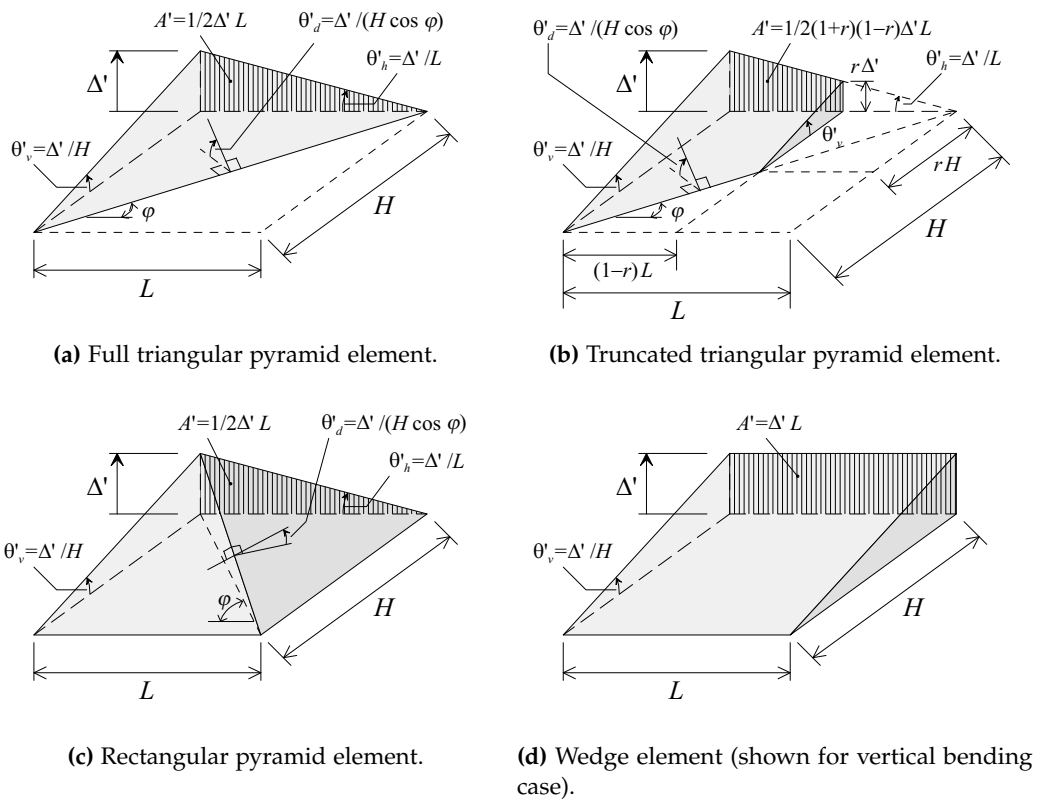


Figure 6.9: Fundamental blocks for constructing the out-of-plane component of a collapse mechanism.

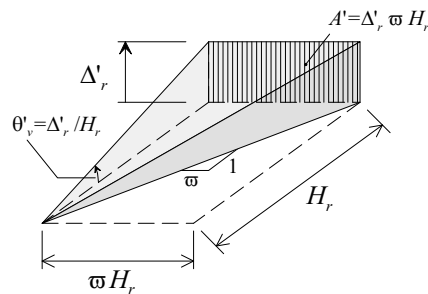


Figure 6.10: Block corresponding to a triangular-shaped, linearly deforming in-plane panel, as used in hybrid mechanisms J and B. For ease of visualisation, the displacement $d\Delta_r$ is illustrated as being orthogonal to the surface, even though it is actually in parallel.

Once a collapse mechanism has been postulated, the remaining steps in the λ_o calculation process will be to determine the associated internal and external work terms. These steps involve the consideration of certain properties which are directly proportional to the size of the applied displacement. Therefore, for brevity, it is convenient to denote the derivatives of these properties with respect to the displacement Δ using Lagrange's notation, so that for a generic property X , its corresponding virtual property X' is

$$X' \equiv \frac{dX}{d\Delta}. \quad (6.9)$$

This leads to the definition of the virtual displacement Δ' :

$$\Delta' \equiv \frac{d\Delta}{d\Delta} = 1, \quad (6.10)$$

as well as other virtual properties, including internal virtual work U' , external virtual work E' , virtual rotation θ' , virtual displaced volume V' , and virtual displaced area A' :

$$U' \equiv \frac{dU}{d\Delta}, \quad E' \equiv \frac{dE}{d\Delta}, \quad \theta' \equiv \frac{d\theta}{d\Delta}, \quad V' \equiv \frac{dV}{d\Delta}, \quad A' \equiv \frac{dA}{d\Delta}. \quad (6.11)$$

When considering a particular mechanism, it is essential that all of these virtual properties are formulated with respect to a reference virtual displacement Δ' at a particular location along the mechanism. In the treatment of each of the predefined mechanisms (G_x , G_y , J , B , ...) presented in this chapter, the reference displacement is taken at the position of the mechanism's largest displacement (refer to Figures 6.15–6.17).

Calculate Internal Work

The next step is to calculate the total internal work performed by the overall mechanism. The three sources of internal resistance that may be active in the mechanisms include: internal moments along flexural cracks in the out-of-plane component of the mechanism; internal resistance associated with shear deformation of the in-plane component in the hybrid mechanisms; and in the case of type-1 mechanisms, possible friction between the top edge of the wall and a restrained OBL.

For flexural cracks, the internal crack energy U'_C is calculated as the product of the crack's virtual rotation θ' and its moment capacity M :

$$dU_C = d\theta M, \quad \text{or} \quad U'_C = \theta' M. \quad (6.12)$$

The virtual rotations of cracks present in the various types of mechanism building blocks are shown in Figures 6.9 and 6.10.⁶ Analytical expressions for calculating the moment capacities for each type of bending and crack orientation are presented in Section 6.4.2.

The internal energy U'_r performed by an in-plane panel undergoing shear deformation (in hybrid mechanisms J and B) is the product of the shear displacement and the corresponding frictional force resistance, in addition to a contribution from vertical bending along the boundary between the in-plane and out-of-plane components. The analytical expression for calculating the resulting internal virtual work is presented as Eq. (6.36) in Section 6.4.3.

The energy performed due to frictional sliding between a free top edge (in type-1 mechanisms) and a restrained OBL is the product of the virtual displacement along the top of the wall and the acting frictional force. The expression used to calculate the corresponding internal virtual work U'_O is

$$U'_O = (1 - \Phi) \mu_o \sigma_{vo} t_u A', \quad (6.13)$$

where Φ is the DOF factor for the OBL as defined in Section 6.3.2; μ_o is the friction coefficient between the wall and the OBL; σ_{vo} is the acting vertical stress; t_u is the thickness of the wall; and A' is the virtual displaced area along the wall's top edge, which is determined by integrating the virtual displacement along the length of the wall. The derivation of Eq. (6.13), along with expressions for A' for the various mechanisms considered are provided in Appendix G.2.9. Expressions used to calculate A' for the various building blocks are given in Figures 6.9 and 6.10.

Thus, the total internal work of the overall mechanism is the sum of the work done by all participating flexural cracks, in-plane panels, and contributions from any restrained OBLs; and is calculated according to the formula

$$U'_{\text{tot}} = \sum U'_C + \sum U'_r + \sum U'_O. \quad (6.14)$$

Calculate External Work

The external work performed by the acting lateral load on the wall is the product of the lateral pressure and the virtual displacement, integrated along the surface of the wall. This can be formulated as

$$E' = \int_Y \int_X q \langle x, y \rangle u' \langle x, y \rangle dx dy, \quad (6.15)$$

⁶These rotations are based on small angles, at which $d\theta \approx \tan d\theta$.

Table 6.1: Expressions for calculating the virtual displaced volumes (V') for different types of block elements. Note that for each block type, L , H and Δ' are defined in the respective diagrams.

Block Type	Diagram	$V' = \dots$
Full triangular pyramid	Figure 6.9a	$\frac{1}{6}\Delta' LH$
Truncated triangular pyramid	Figure 6.9b	$\frac{1}{6}\Delta' \frac{H^2(1-r^3)}{G_n}$, where $G_n = \tan \varphi$
Rectangular pyramid	Figure 6.9c	$\frac{1}{3}\Delta' LH$
Wedge	Figure 6.9d	$\frac{1}{2}\Delta' LH$
In-plane shear triangular pyramid	Figure 6.10	$\frac{1}{3}\Delta'_r H_r^2 \omega$

where E' is the external virtual work; $q\langle x, y \rangle$ is the lateral pressure and $u'\langle x, y \rangle$ is the virtual displacement acting at the point defined by the coordinates x and y ; and L and H are the length and height of the wall.

The two major sources of external loads considered include: (i) the wall's self-weight; and (ii) in type-1 mechanisms, the lateral component of a possible unrestrained overburden load along the top edge of the wall. Other mass concentrations that may be present, such as lintels or other fittings, could also be accounted for with this approach; however, they were not a feature of any of the walls considered in this chapter. As a result, the total external work is

$$E'_{\text{tot}} = \sum E'_W + \sum E'_O, \quad (6.16)$$

where $\sum E'_W$ is the sum of contributions from the wall's self-weight and $\sum E'_O$ is the sum of contributions from an unrestrained OBL.

For seismic lateral loading, which is weight-proportional in nature, the acting lateral force is equal to the component's weight times the load multiplier λ . The lateral pressure from the wall's self-weight therefore becomes

$$q = \lambda \gamma t_u,$$

where γ is the weight density of the masonry and t_u is the thickness of the wall. The external work due to the wall's self-weight may be formulated as

$$\sum E'_W = \lambda \gamma t_u \sum V', \quad (6.17)$$

where $\sum V'$ is the sum of the virtual displaced volumes of all individual blocks comprising the mechanism. Expressions for calculating volumes of the different displaced shapes in Figures 6.9 and 6.10, are listed in Table 6.1.

The sum of external work contributions from all unrestrained OBLs is

$$\sum E'_O = \Phi \lambda \eta t_u \sum \sigma_{vo} A', \quad (6.18)$$

with parameters Φ and η having been defined in Section 6.3.2. Derivations of this formula and expressions for A' for the various mechanisms are presented in Appendix G.2.9.

Evaluate the Collapse Multiplier

An expression for the collapse load multiplier λ_o is obtained by applying the principle of energy conservation and equating the total internal work to the total external work, such that

$$dU_{\text{tot}} = dE_{\text{tot}}, \quad \text{or} \quad U'_{\text{tot}} = E'_{\text{tot}}. \quad (6.19)$$

Substituting in Eqs. (6.14) and (6.16), together with Eqs. (6.17) and (6.18) and rearranging in terms of λ , yields

$$\lambda_o = \frac{\sum U'_C + \sum U'_r + \sum U'_O}{\gamma t_u \sum V' + \Phi \eta t_u \sum \sigma_{vo} A'}. \quad (6.20)$$

6.4.2 Moment Capacities of Flexural Cracks

The moment capacity of a masonry crack with respect to any mode of bending (vertical, horizontal and diagonal) can be expressed in the general form

$$M = f\langle \dots \rangle l_C \bar{Z}, \quad (6.21)$$

where M is the moment capacity of the crack, $f\langle \dots \rangle$ is a stress capacity function, l_C is the span (length or height) of the crack, and \bar{Z} is the moment modulus per unit span of the crack, for the particular type of bending. It is convenient to express the moment capacity in the above form, because it separates the moment moduli which remain constant, from the stress capacity and crack span terms which are dependent on the dimensions of the overall mechanism and the location of the crack.

Since masonry without bond strength attains its flexural strength entirely from vertical compression acting throughout the panel, the stress capacity becomes equivalent to the vertical compressive stress σ_v . For a solid wall (without openings) this may be defined as³

$$f\langle d \rangle \equiv \sigma_v = \sigma_{vo} + \gamma d, \quad (6.22)$$

where d is the vertical distance measured from the top edge of the wall to the centroid of the crack under consideration, γ is the unit weight of the masonry, and σ_{v0} is the precompression stress applied at the top of the wall. If the distance d is equal to the total mechanism height H_t times some coefficient c , then by incorporating Eq. (6.3), $f\langle \cdot \cdot \cdot \rangle$ can also be rewritten in terms of the overburden weight ratio ψ , as

$$f\langle cH_t \rangle = \gamma H_t (\psi + c). \quad (6.23)$$

For walls with openings, it is recommended that a more refined approach be used to calculate the compressive stress distribution throughout the wall, as presented previously in Section 4.4.

The moment capacities for the different types of bending, which are used for subsequent analyses of DSM walls, will now be presented in the same form as Eq. (6.21), together with their corresponding moment moduli (\bar{Z}). The expressions are based on models already discussed in Section 4.3. Symbols l_u , t_u , h_u and t_j featuring in the upcoming expressions are defined by Figure 4.2. Note that while it is assumed that the DSM possesses zero tensile bond strength, the provided expressions do allow for the possibility of the masonry being built with mortar joints for the purpose of calculating various related geometric properties. However, for DSM where mortar joints are absent, the joint thickness is simply taken as $t_j = 0$.

Vertical Bending Along Internal Cracks

The moment resistance along any horizontal crack undergoing vertical bending is based on the restoring moment opposing rigid body rotation about the extreme compressive fibre of the section (refer to Figure 4.3d). The corresponding moment capacity obtained by Eq. (4.21) may be formulated as

$$M_v = f\langle d \rangle L \bar{Z}_v, \quad (6.24)$$

where L is the length of the crack, and \bar{Z}_v is the vertical bending moment modulus per unit length, given by

$$\bar{Z}_v = t_u^2 / 2. \quad (6.25)$$

This moment capacity is applicable to all horizontal flexural cracks within the mechanism.

Vertical Bending Along the Top Edge in Presence of an OBL

Although the top edge of a wall is not a true masonry ‘crack’, it may nonetheless act as a hinge with the ability to provide an internal work contribution when it undergoes rotation about the horizontal axis and is subjected to an overburden load. This concept is applicable regardless of whether the top edge is restrained or free to undergo lateral movement (i.e. both type-1 and type-2 mechanisms, as discussed in Section 6.3.1). An OBL will provide rotational restraint to the top edge when its vertical force resultant acts at an offset relative to the centre of the wall’s cross section. The moment capacity of the hinge may be calculated as

$$M_{vo} = R_{ts}M_v, \quad (6.26)$$

where R_{ts} is defined an effective rotational restraint factor along the top edge, and M_v is the nominal vertical bending moment capacity [given by Eq. (6.24)]. The effective restraint factor is calculated from the OBL eccentricity ϵ (defined in Figure 6.6) as

$$R_{ts} = 1 - 2\epsilon. \quad (6.27)$$

Derivation of this equation is presented in Appendix G.2.10. It follows that when the load acts upon the upward-deflecting point along the section ($\epsilon = 0$), as for the case of a slab connection (Figure 6.8), the load applies a full restoring moment to the wall, and hence R_{ts} achieves a value of 1. If the load acts at the centre of the wall’s thickness ($\epsilon = 1/2$), then the load provides no net moment, and R_{ts} becomes zero. If the load acts at the downward-deflecting point across the wall’s cross section ($\epsilon = 1$), then R_{ts} becomes -1 , and the hinge provides a negative internal work contribution; or in other words, the load exerts an overturning moment onto the wall.

Furthermore, as the top edge requires that $d = 0$ in Eq. (6.22), the moment capacity simplifies to

$$M_{vo} = R_{ts}f\langle 0 \rangle L\bar{Z}_v. \quad (6.28)$$

This moment capacity is applicable to any part of the top edge belonging to a sub-plate which undergoes some component of rotation about the horizontal axis.

Diagonal Bending

Similarly to vertical bending, the resistance to diagonal bending is based on rigid body rotation about the extreme compressive fibre of the section. The corresponding

moment capacity is given by Eq. (4.38), which may be formulated as

$$M_d = f\langle d \rangle L_d \bar{Z}_v \cos \varphi \quad \text{or} \quad M_d = f\langle d \rangle \frac{H_d}{G_n} \bar{Z}_v \cos \varphi, \quad (6.29)$$

where L_d is the horizontal projection of the diagonal crack and H_d is its vertical projection. This equation is applicable to all flexural diagonal cracks along the out-of-plane component of the mechanism.

Horizontal Bending

The moment resistance along any flexural vertical cracks that undergo horizontal bending is assumed to be obtained from rotational friction along the participating bed joints. The corresponding moment capacity, as given by Eq. (4.29), can be formulated as

$$M_h = f\langle d \rangle H \bar{Z}_h, \quad (6.30)$$

where H is the crack height and \bar{Z}_h is the moment horizontal bending modulus per unit height of crack. This modulus is obtained as

$$\bar{Z}_h = \frac{\mu_m k_{bp} t_u^3}{h_u + t_j}, \quad (6.31)$$

where μ_m is the coefficient of friction along the bed joint interface; and k_{bp} is the plastic torque coefficient which, for a rectangular overlapping section as illustrated by Figure 4.5, may be obtained either using Eq. (4.31) or from Figure 4.6. The resulting moment capacity is applicable to all flexural vertical cracks within the mechanism, except in the special case where the vertical crack acts as the boundary between the out-of-plane panel and sliding in-plane panel in hybrid mechanisms J and B.

6.4.3 Frictional Shear Deformation Model for In-Plane Panels

Hybrid mechanisms J and B (Section 6.2.2) incorporate a frictional shear deformation model for calculating the internal resistance of the participating in-plane walls. As illustrated by Figure 6.11, it is assumed that the mobilised in-plane panel has a triangular shape, whereby the angle of the shear crack with respect to the vertical is treated as a variable and denoted by ω . The geometries of mechanisms J and B require that in order to satisfy displacement compatibility between the in-plane panel and the adjacent out-of-plane panel, the in-plane panel must undergo shear deformation with a linear profile along its height.

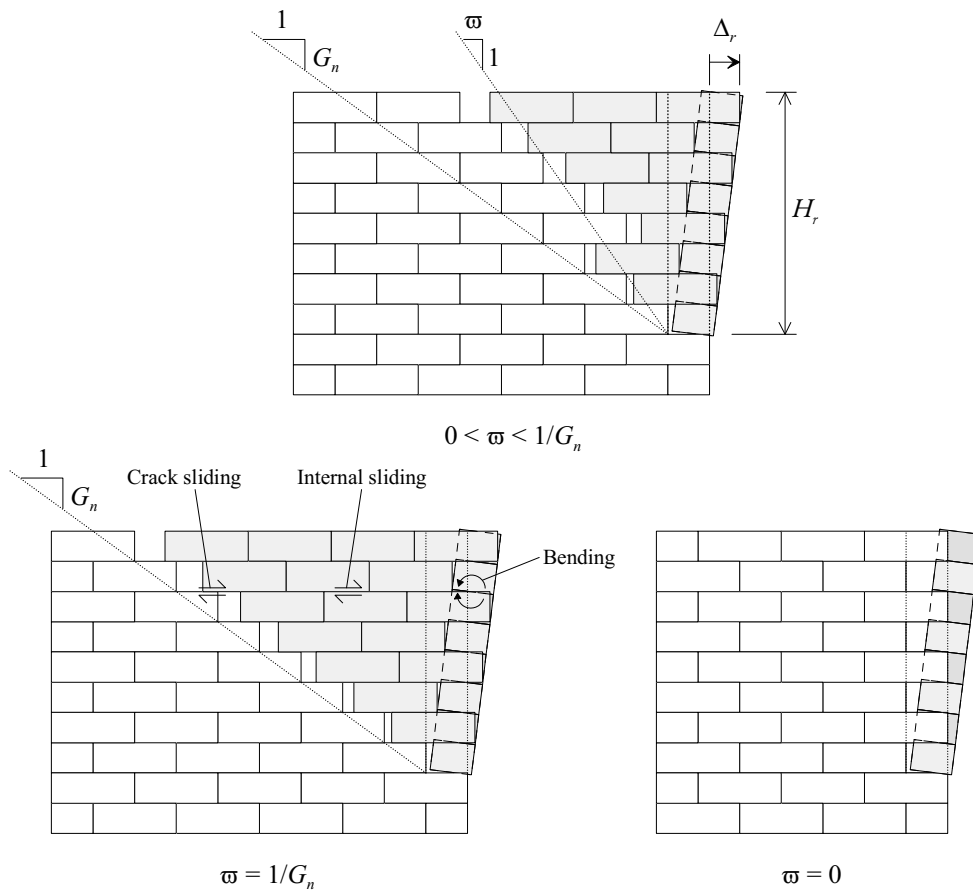


Figure 6.11: In-plane panel undergoing frictional shear deformation.

The total internal resistance of the in-plane panel is obtained from three sources:

1. Frictional resistance within the panel due its internal shear deformation;
2. Frictional resistance due to sliding between the panel and the stationary portion of the return wall along the diagonal crack; and
3. Vertical bending at the interface between the sliding in-plane panel and the adjacent out-of-plane panel, which must occur since the masonry units within the out-of-plane wall become rotated relative to the units within the in-plane wall.

Contributions from Frictional Shear Resistance

For a triangular in-plane panel subjected to a virtual displacement $d\Delta_r$ at its top edge (Figure 6.11), the increment of internal work dU_{fs} performed by the two

sources of translational friction (Points 1 and 2 listed above) is calculated from the expression

$$dU_{fs} = \frac{1}{2} d\Delta_r \mu_m t_u H_r \left(\frac{1}{G_n} + \varpi \right) f \left\langle \frac{1}{3} H_r \right\rangle, \quad (6.32)$$

which is derived in Appendix G.1. The variables include: H_r , the height of the panel; μ_m , the coefficient of friction along the bed joints; and others as defined previously. The geometric limits of ϖ are governed by

$$0 \leq \varpi \leq 1/G_n. \quad (6.33)$$

The case where $\varpi = 0$ corresponds to the in-plane crack being oriented vertically, whilst $\varpi = 1/G_n$ corresponds to the crack following the natural diagonal slope of the masonry, which is the upper limit at which Eq. (6.32) remains valid.

It is assumed here that the return wall has sufficient length to accommodate the full length of the diagonal in-plane crack (i.e., that the crack terminates at the top edge of the return wall). Whilst it is possible that an in-plane crack may terminate at an in-plane wall's free vertical edge in cases where the in-plane wall is short, such cases are not considered here. Similar equations may nonetheless be derived for such scenarios.

Contribution from Vertical Bending at the Interface

An additional component of internal work is generated from vertical bending along the vertical crack forming the boundary between the in-plane and out-of-plane panels (Point 3 stated above). The moment capacity M_{vy} of the crack may be calculated from Eq. (6.24), together with an equivalent length of $L = H_r/G_n$, and a depth of $d = \frac{1}{2}H_r$ below the top of the wall. This gives

$$M_{vy} = f \left\langle \frac{1}{2} H_r \right\rangle \frac{H_r}{G_n} \bar{Z}_v. \quad (6.34)$$

As shown by Figure 6.10, the crack's effective increment of rotation about the horizontal axis is

$$d\theta_v = d\Delta_r / H_r,$$

hence the crack provides an increment of internal work equal to

$$dU_{vy} = d\theta_v M_{vy} = d\Delta_r \frac{\bar{Z}_v}{G_n} f \left\langle \frac{1}{2} H_r \right\rangle. \quad (6.35)$$

Total Internal Work

The overall increment of internal work dU_r for an in-plane panel involved in the mechanism is the sum of the contributions from frictional shear resistance and vertical bending at the interface, or

$$dU_r = dU_{fs} + dU_{vy}.$$

Substituting in Eqs. (6.32) and (6.35) and dividing by the increment of displacement $d\Delta_r$ at the top edge of the in-plane panel, results in

$$\frac{dU_r}{d\Delta_r} = \frac{1}{2} \mu_m t_u H_r \left(\frac{1}{G_n} + \varpi \right) f\langle \frac{1}{3} H_r \rangle + \frac{\bar{Z}_v}{G_n} f\langle \frac{1}{2} H_r \rangle.$$

However, since all virtual work expressions must be formulated with respect to the mechanism's reference displacement Δ' (as discussed in Section 6.4.1), in order to obtain the internal virtual energy U'_r of the in-plane panel, it is necessary to multiply the above derivative by $d\Delta_r/d\Delta$ according to the formula

$$\frac{dU_r}{d\Delta} = \frac{d\Delta_r}{d\Delta} \frac{dU_r}{d\Delta_r}, \quad \text{or} \quad U'_r = \Delta'_r \frac{dU_r}{d\Delta_r}.$$

This results in the expression

$$\begin{aligned} U'_r &= \Delta'_r \left[\frac{1}{2} \mu_m t_u H_r \left(\frac{1}{G_n} + \varpi \right) f\langle \frac{1}{3} H_r \rangle + \frac{\bar{Z}_v}{G_n} f\langle \frac{1}{2} H_r \rangle \right] \\ &\equiv \mathbf{U}'_r \langle \Delta'_r, H_r, \varpi \rangle. \end{aligned} \quad (6.36)$$

Variables in this equation which are dependent on the mechanism geometry include Δ'_r , H_r and ϖ , with all other properties being constant for a particular masonry type. Therefore, this equation will be abbreviated using the function notation $\mathbf{U}'_r \langle \Delta'_r, H_r, \varpi \rangle$.

6.5 FORMULATIONS FOR TYPE G, J, B, K1 AND K2 MECHANISMS

This section presents closed-form virtual work expressions for calculating the collapse multiplier λ_o with respect to the mechanisms considered in Section 6.2, including hybrid mechanisms J and B, and standard mechanisms G, K1 and K2. For each mechanism, expressions are provided for the total internal work, U'_{tot} ; and for the total external work premultiplied by the reciprocal of the load multiplier,

$\lambda^{-1}E'_{\text{tot}}$. This allows for the collapse multiplier to be calculated as

$$\lambda_o = \frac{U'_{\text{tot}}}{\lambda^{-1}E'_{\text{tot}}}. \quad (6.37)$$

Derivations of the presented analytical expressions are included in Appendix G.2.

The presented formulations specifically assume that a wall is solid; that is, it contains no openings. Analysis of a wall with openings can be performed from first principles using the refined VW treatment covered in Section 4.4.

6.5.1 General Concepts

The following general concepts and calculations are applicable toward all of the mechanisms considered.

Individual Out-of-Plane Walls

The first step in conducting an analysis is to identify individual out-of-plane panels within the overall masonry specimen. Figure 6.12 shows examples of several different wall configurations where an out-of-plane façade wall is supported by in-plane return walls at one or multiple locations. As shown, an individual out-of-plane wall is defined as having the dimensions L_w and H_w , which are measured as the spans between either a free edge and a support, or between two supports. For a particular out-of-plane wall, the number of supported vertical and horizontal edges are denoted by n_{vs} and n_{hs} , respectively.

Out-of-Plane and In-Plane Mechanism Modules

The treatment herein is based on the concept that an overall collapse mechanism is comprised of a series of *out-of-plane modules* and *in-plane modules*. Out-of-plane modules feature in all mechanisms, whilst in-plane modules are relevant to only the hybrid mechanisms. As demonstrated by each of the cases in Figure 6.12, an out-of-plane wall will accommodate either a single out-of-plane module when only one of its vertical edges are supported, or two modules when both of its vertical edges are supported. The length and height dimensions of an individual out-of-plane module are denoted by L_e and H_t , respectively.

Each of the mechanisms considered treat the height of the mechanism, H_t , as an independent variable which may assume values within the range

$$0 < H_t \leq H_w. \quad (6.38)$$

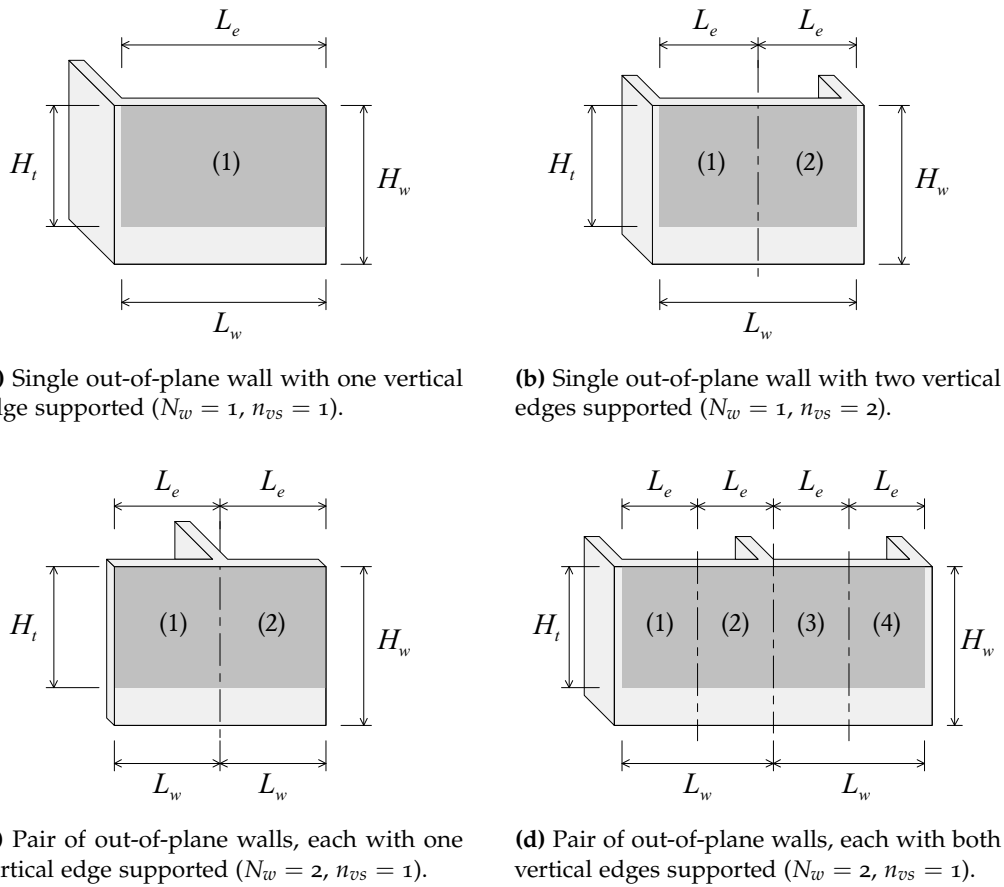


Figure 6.12: Subdivision of various types of wall configurations into individual out-of-plane mechanism modules.

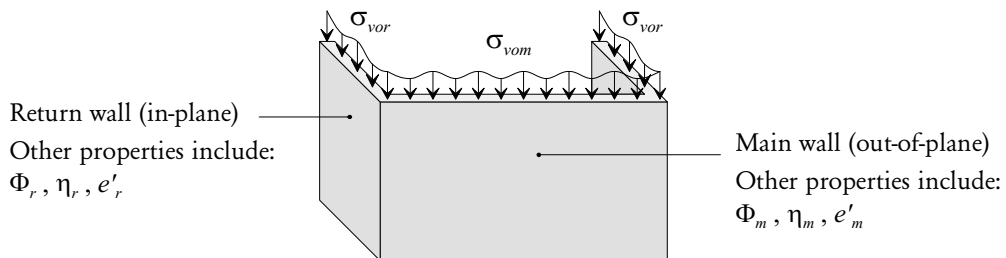


Figure 6.13: Properties that may have different values for the participating out-of-plane and in-plane walls, as denoted by the subscripts m and r , respectively.

Minimisation of λ_o generally tends to occur when $H_t < H_w$, or in other words, when the mechanism does not utilise the full available height of the wall. In addition, it is useful to define the effective height of the mechanism H_e , as

$$H_e = H_t/n_{hs}, \quad (6.39)$$

which is equal to the full height of the mechanism when the top edge is free, and half of the mechanism's total height when both horizontal edges are supported. Or alternatively, it may be taken as

$$H_e = \begin{cases} H_t, & \text{for type-1 mechanisms (G, J, B and K1),} \\ \frac{1}{2}H_t, & \text{for type-2 mechanisms (K2).} \end{cases} \quad (6.40)$$

The allowable limits on the length of the out-of-plane component of the mechanism depend on whether the mechanism under consideration is standard or hybrid. In the standard mechanisms, the length span is allowed to assume values anywhere within the geometric limits of the out-of-plane wall, whereas in the hybrid mechanisms it must span the full length of the wall. Therefore, the out-of-plane module length L_e is constrained by

$$0 < L_e \leq L_w/n_{vs} \quad \text{in standard mechanisms (G, K1 and K2),} \quad (6.41)$$

$$\text{and} \quad L_e = L_w/n_{vs} \quad \text{in hybrid mechanisms (J and B).} \quad (6.42)$$

As will be shown later, however, minimisation of λ_o generally occurs when the mechanism utilises the maximum available length of the wall.

Note that in the treatment of hybrid mechanisms, it is possible for certain properties to adopt different values along the out-of-plane and in-plane walls/modules. This is catered for in the analysis. Such properties are denoted using the subscripts m and r , respectively, as illustrated in Figure 6.13.

Mechanism Aspect Ratios

Based on the effective mechanism dimensions L_e and H_e , it is useful to calculate a pair of aspect ratios. These include the effective aspect ratio:

$$\beta = \frac{L_e}{H_e}; \quad (6.43)$$

and the normalised effective aspect ratio:

$$\alpha = G_n \frac{L_e}{H_e} = G_n \beta. \quad (6.44)$$

The parameter α has special significance to the pure out-of-plane mechanisms G, K1 and K2, as the condition $\alpha = 1$ represents the limiting case between each complimentary pair of mechanisms G_x/G_y , $K1_x/K1_y$, and $K2_x/K2_y$.⁷

6.5.2 Hybrid Types J and B

Presented here is a simplified treatment for mechanisms J and B, which makes the simplifying assumption that all participating out-of-plane modules and in-plane modules are equivalent. Consequently, this treatment is only applicable to specimens in which all out-of-plane walls share the following properties:

- Length span L_w ;
- Overburden load properties, including σ_{vom} , Φ_m and η_m ; and
- Number of vertical supports (i.e., all walls must be either 1- or 2-sided, but not a mixture of both).

Similarly, the OBL characteristics (σ_{vor} , Φ_r and η_r) for all in-plane walls must also be identical. Examples of allowable configurations include the four cases shown in Figure 6.12.

For configurations that fail to satisfy any of the above conditions, it becomes necessary to use a more generalised approach that allows each wall to have unique values of the aforementioned properties and in which the virtual work equations are formulated in terms of independent shape variables for each participating wall. This refined procedure is presented in Appendix G.3 and is applicable to any arbitrary configuration where the out-of-plane walls are connected in series and separated by in-plane return walls (refer to Figure G.13). The generalised method, however, is considerably more involved than the simplified analysis presented here.

A further consideration is that the simplified approach is only guaranteed to find optimal solutions for configurations that are symmetric with respect to every out-of-plane and in-plane wall present, or in other words, when a line of symmetry exists between each possible pair of out-of-plane and in-plane modules in the mechanism. Whilst the simplified approach may nonetheless be applied

⁷This is equivalent to the so-called *slope factor* used in the AS 3700 virtual work method, also denoted by α .

to forms that fail to meet this condition of symmetry (as long as they satisfy the aforementioned dot points), the solutions found will generally be sub-optimal, due to an insufficient number of independent variables to describe the optimal mechanism state. Therefore, from the configurations shown in Figures 6.12, the simplified procedure will only reach optimal states for configurations (a), (b) and (c), but not (d).⁸ A practical example of this is demonstrated in Section 6.6.1 for a pair of test specimens having the geometry shown in Figure 6.12d (walls R20 and R21). It is noted, however, that in that case, the refined solution gives only a minor (approximately 1%) reduction in the computed collapse load relative to the simplified analysis. Figure 6.3 illustrates all of the basic variants of mechanism J for which the simplified approach will find optimal solutions, as well as examples of complex variants that require the general approach.

Common Calculations

When analysing a wall specimen using the simplified treatment presented here, the first step is to establish the number of out-of-plane and in-plane modules participating in the overall mechanism. The number of in-plane modules, N_r , is simply taken as the number of in-plane return walls present. In the simplified approach presented here, the number of out-of-plane modules, N_m , may be calculated as

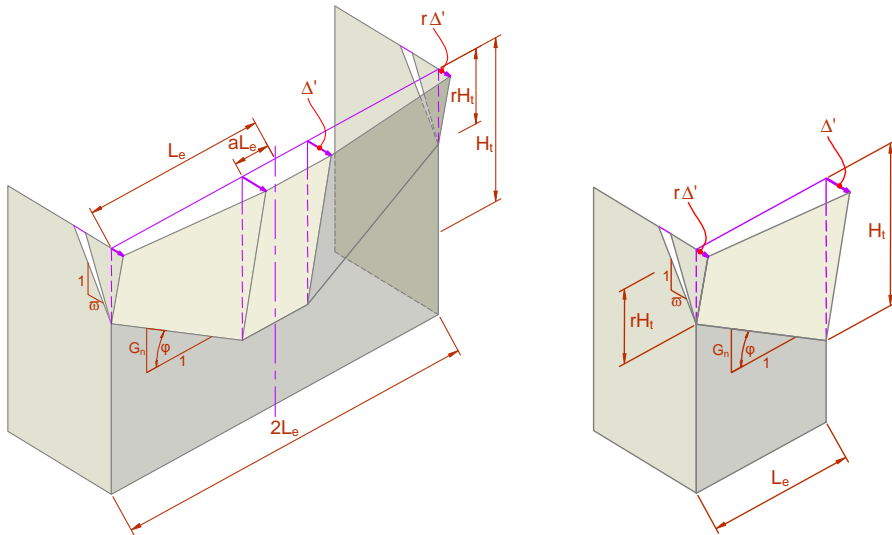
$$N_m = N_w \cdot n_{vs}, \quad (6.45)$$

where N_w is the number of out-of-plane walls, and n_{vs} is the number of vertical supports per wall. For example, the specimen shown in Figure 6.12d consists of three return walls ($\therefore N_r = 3$) and two out-of-plane walls ($\therefore N_w = 2$) both of which have two vertical supports ($\therefore n_{vs} = 2$), so the resulting number of out-of-plane modules [from Eq. (6.45)] is $N_m = 2 \times 2 = 4$. It should be noted that the simplified treatment requires all walls present within the specimen to participate in the overall mechanism. By contrast, the generalised approach (detailed in Appendix G.3) allows for selective participation of the various walls present, which may lead to lower values of the calculated collapse multiplier for configurations that do not satisfy the aforementioned symmetry condition.

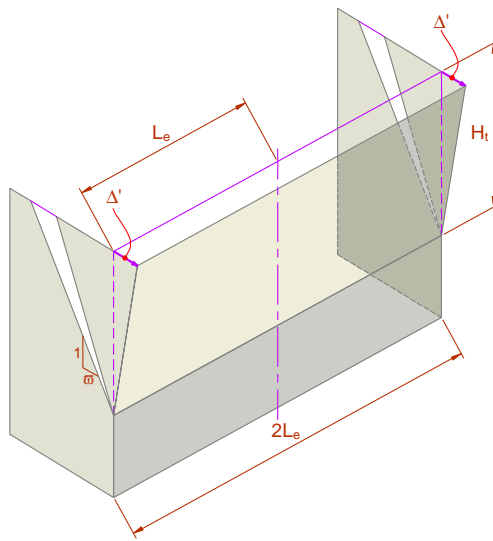
The geometries and deflected shapes of mechanisms J and B are shown in Figure 6.14.⁹ The common independent variables for both mechanisms include: the

⁸Since (in Figure 6.12d) out-of-plane modules 1 and 4 are not equivalent to modules 2 and 3. Similarly, the central return wall is not equivalent to either of the external ones.

⁹Figures 6.14, 6.15, 6.16 and 6.17 all illustrate the mechanisms as they appear when the wall has two-sided vertical supports and therefore two out-of-plane modules. In each scenario shown, the deflected shape is mirrored by the vertical line of symmetry at the mid-length of the wall. The



(a) Mechanism J: general form (left); with $n_{os} = 1$ and $a = 0$ (right).



(b) Mechanism B.

Figure 6.14: Type J and B hybrid mechanisms.

total height H_t ; and slope of the in-plane shear crack, ϖ . As per Eq. (6.42), both mechanisms must span the full length of the wall, thereby making the out-of-plane module length L_e predetermined, as ¹⁰

$$L_e = L_w/n_{vs}. \quad \text{rep. (6.42)}$$

Common auxiliary variables include: effective height H_e , which from Eq. (6.40) is equal to the total height for both these mechanisms; and the aspect ratios β and α calculated from Eqs. (6.43) and (6.44). The common optimisation constraints include restrictions on the mechanism's total height and in-plane crack slope, which must adhere to

$$0 < H_t \leq H_w, \quad \text{rep. (6.38)}$$

and
$$0 \leq \varpi \leq 1/G_n. \quad \text{rep. (6.33)}$$

It should be noted that the in-plane model also assumes the return walls to have sufficient length to accommodate any length of the diagonal in-plane crack within the above limit, as discussed in Section 6.4.3.

Mechanism J

For this mechanism, an additional independent variable is the shape parameter a . Additional dependent variables include the shape parameter r :

$$r = 1 - \alpha(1 - a); \quad (6.46)$$

work contribution factor ζ_{hi} for the vertical crack undergoing horizontal bending:¹¹

$$\zeta_{hi} = \begin{cases} a, & \text{if one vertical edge is supported, i.e. } n_{vs} = 1, \\ 1, & \text{if two vertical edges are supported, i.e. } n_{vs} = 2; \end{cases} \quad (6.47)$$

case where the wall has only one vertical support can be visualised by considering only one of the out-of-plane modules present on either side of the line of symmetry.

¹⁰Although mechanism B is effectively a hybrid version of the one-way vertical bending mechanism for a parapet wall, in the provided approach the effective mechanism length L_e still considers the number of vertical supports. This is done for consistency with the formulations used for the other mechanisms.

¹¹A more in-depth discussion of the reasoning behind implementation of the factor ζ_{hi} is provided in Appendix G.2.1. The factor effectively accounts for a reduction in the crack's rotation when it is parallel to an unrestrained vertical edge, as shown by Figure G.3. It also ensures continuity in the calculated collapse load λ_o in transitioning between the complimentary pair of mechanisms G_x and G_y.

and if an OBL is present on either the out-of-plane or in-plane walls, the virtual energy quantities e'_m and e'_r :

$$e'_m = \frac{1}{2}(1 + a + r - ar) L_e t_u \sigma_{vom}, \quad (6.48)$$

and
$$e'_r = r^2 \omega H_t t_u \sigma_{vor}. \quad (6.49)$$

The total internal work for a total of N_m out-of-plane modules and N_r in-plane modules is calculated as

$$\begin{aligned} U'_{\text{tot}} = N_m [& \bar{Z}_v \beta (f \langle \frac{1}{2}(1 + a + r - ar) H_t \rangle + R_{ts} f \langle 0 \rangle) \\ & + \zeta_{hi} \bar{Z}_h G_n f \langle \frac{1}{2} H_t \rangle + (1 - \Phi_m) \mu_o e'_m] \\ & + N_r [\mathbf{U}'_r \langle r, r H_t, \omega \rangle + (1 - \Phi_r) \mu_o e'_r], \end{aligned} \quad (6.50)$$

whilst the total external work premultiplied by λ^{-1} is

$$\begin{aligned} \lambda^{-1} E'_{\text{tot}} = N_m [& \gamma t_u H_t^2 \left(\frac{1}{2} a \beta + \frac{1}{6} \frac{1-r^3}{G_n} \right) + \Phi_m \eta_m e'_m] \\ & + N_r [\gamma t_u H_t^2 \left(\frac{1}{3} r^3 \omega \right) + \Phi_r \eta_r e'_r]. \end{aligned} \quad (6.51)$$

Additional optimisation constraints include restrictions on the shape parameters a and r , which must satisfy

$$0 \leq a \leq 1, \quad (6.52)$$

and
$$0 \leq r \leq 1. \quad (6.53)$$

Mechanism B

Additional dependent variables include the OBL virtual energy quantities e'_m and e'_r :

$$e'_m = L_e t_u \sigma_{vom}, \quad (6.54)$$

and
$$e'_r = \omega H_t t_u \sigma_{vor}. \quad (6.55)$$

The total internal work for a total of N_m out-of-plane modules and N_r in-plane modules is

$$\begin{aligned} U'_{\text{tot}} = N_m [& \bar{Z}_v \beta (f \langle H_t \rangle + R_{ts} f \langle 0 \rangle) + (1 - \Phi_m) \mu_o e'_m] \\ & + N_r [\mathbf{U}'_r \langle 1, H_t, \omega \rangle + (1 - \Phi_r) \mu_o e'_r], \end{aligned} \quad (6.56)$$

and the total external work premultiplied by λ^{-1} is

$$\begin{aligned} \lambda^{-1} E'_{\text{tot}} = N_m [& \gamma t_u H_t^2 \left(\frac{1}{2} \beta \right) + \Phi_m \eta_m e'_m] \\ & + N_r [\gamma t_u H_t^2 \left(\frac{1}{3} \omega \right) + \Phi_r \eta_r e'_r]. \end{aligned} \quad (6.57)$$

6.5.3 Standard Types G, K1 and K2

The standard mechanisms G, K1 and K2 are applicable to individual out-of-plane walls. Therefore, when applying them to specimens consisting of multiple out-of-plane walls (e.g. Figure 6.12d), each wall present may be treated independently (unlike for the hybrid mechanisms). For such specimens, the wall with the longest span will generally have the lowest associated collapse multiplier.

Common Calculations

The geometries and deflected shapes of the mechanisms are shown in Figure 6.15 for type G mechanisms G_x and G_y , Figure 6.16 for type K1 mechanisms $K1_x$ and $K1_y$, and Figure 6.17 for type K2 mechanisms $K2_x$ and $K2_y$.⁹ For each of the mechanisms, the independent variables include the effective length L_e and total height H_t . Common auxiliary dependent variables include: effective height H_e , obtained from Eq. (6.40) based on the type of mechanism; and aspect ratios β and α [from Eqs. (6.43) and (6.44)]. In addition, it is necessary to calculate either

$$a = 1 - \frac{1}{\alpha} \quad \text{for x-forms (G}_x, K1_x \text{ and K2}_x), \quad (6.58)$$

or
$$r = 1 - \alpha \quad \text{for y-forms (G}_y, K1_y \text{ and K2}_y). \quad (6.59)$$

Common geometric constraints include the mechanism length and height restrictions

$$0 < H_t \leq H_w, \quad \text{rep. (6.38)}$$

and
$$0 < L_e \leq L_w / n_{vs}. \quad (6.60)$$

In addition, α must satisfy

$$\alpha \geq 1 \quad \text{for x-forms (G}_x, K1_x \text{ and K2}_x), \quad (6.61)$$

and
$$\alpha \leq 1 \quad \text{for y-forms (G}_y, K1_y \text{ and K2}_y). \quad (6.62)$$

Mechanism G_x

Additional dependent variables include the work contribution factor ζ_{hi} for the vertical crack undergoing horizontal bending:¹¹

$$\zeta_{hi} = \begin{cases} a, & \text{if one vertical edge is supported, i.e. } n_{vs} = 1, \\ 1, & \text{if two vertical edges are supported, i.e. } n_{vs} = 2; \end{cases} \quad (6.63)$$

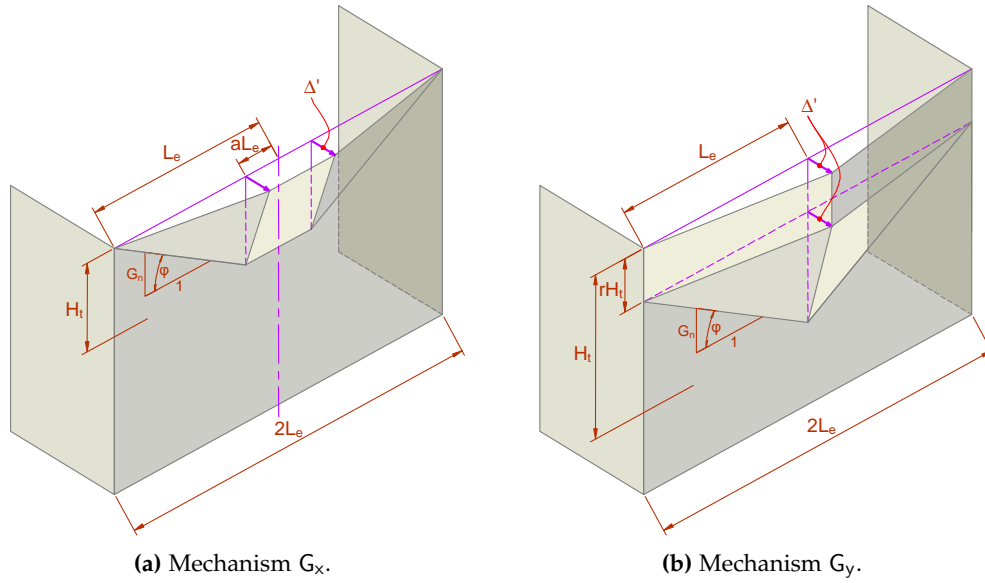


Figure 6.15: Type G mechanisms.

and if an OBL is present on the out-of-plane wall, then the energy quantity e'_m :

$$e'_m = \frac{1}{2} (1 + a) L_e t_u \sigma_{vom}. \quad (6.64)$$

The total internal work for a single out-of-plane module is

$$U'_{\text{tot}} = \bar{Z}_v \beta \left[f \left\langle \frac{1}{2} (1 + a) H_t \right\rangle + R_{ts} f \langle 0 \rangle \right] + \zeta_{hi} \bar{Z}_h G_n f \left\langle \frac{1}{2} H_t \right\rangle + (1 - \Phi_m) \mu_o e'_m, \quad (6.65)$$

whilst the total external work premultiplied by λ^{-1} is

$$\lambda^{-1} E'_{\text{tot}} = \gamma t_u L_e H_t \left(\frac{1}{6} + \frac{1}{3} a \right) + \Phi_m \eta_m e'_m. \quad (6.66)$$

Mechanism G_y

Additional dependent variables include the work contribution factor ζ_{vi} for the internal horizontal crack:¹²

$$\zeta_{vi} = r; \quad (6.67)$$

the corresponding work contribution factor ζ_{vo} for the top edge hinge:

$$\zeta_{vo} = 1 - \zeta_{vi}; \quad (6.68)$$

¹²The reasoning behind implementing the work contribution factors ζ_{vi} and ζ_{vo} is explained in Appendix G.2.4. As shown by Figure G.7, the factors effectively account for a reduction or enhancement in the crack rotations, due to the top edge being unrestrained.

work contribution factor ζ_{hi} for the central vertical crack in horizontal bending:

$$\zeta_{hi} = \begin{cases} 0, & \text{if one vertical edge is supported, i.e. } n_{vs} = 1, \\ 1, & \text{if two vertical edges are supported, i.e. } n_{vs} = 2; \end{cases} \quad (6.69)$$

and if an OBL is present on the out-of-plane wall, the virtual energy e'_m :

$$e'_m = \frac{1}{2} L_e t_u \sigma_{vom}. \quad (6.70)$$

The total internal work for a single out-of-plane module is

$$\begin{aligned} U'_{\text{tot}} = & \frac{\bar{Z}_v}{G_n} [\zeta_{vi} f \langle r H_t \rangle + f \langle \frac{1}{2} (1+r) H_t \rangle + R_{ts} \zeta_{vo} f \langle 0 \rangle] \\ & + \frac{\bar{Z}_h}{\beta} [\zeta_{hi} f \langle \frac{1}{2} H_t \rangle + R_{vs} r f \langle \frac{1}{2} r H_t \rangle] + (1 - \Phi_m) \mu_o e'_m, \end{aligned} \quad (6.71)$$

and the total external work premultiplied by λ^{-1} is

$$\lambda^{-1} E'_{\text{tot}} = \gamma t_u L_e H_t \left(\frac{1}{6} + \frac{1}{3} r \right) + \Phi_m \eta_m e'_m. \quad (6.72)$$

Mechanism K1_x

If an OBL is present on the out-of-plane wall, then an additional dependent variable is the energy quantity e'_m :

$$e'_m = \frac{1}{2} (1+a) L_e t_u \sigma_{vom}. \quad (6.73)$$

The total internal work for a single out-of-plane module is

$$\begin{aligned} U'_{\text{tot}} = & \bar{Z}_v \beta [f \langle H_t \rangle + R_{ts} a f \langle 0 \rangle + (1-a) f \langle \frac{1}{2} H_t \rangle] \\ & + R_{vs} \bar{Z}_h G_n f \langle \frac{1}{2} H_t \rangle + (1 - \Phi_m) \mu_o e'_m, \end{aligned} \quad (6.74)$$

whilst the corresponding total external work premultiplied by λ^{-1} is

$$\lambda^{-1} E'_{\text{tot}} = \gamma t_u L_e H_t \left(\frac{1}{3} + \frac{1}{6} a \right) + \Phi_m \eta_m e'_m. \quad (6.75)$$

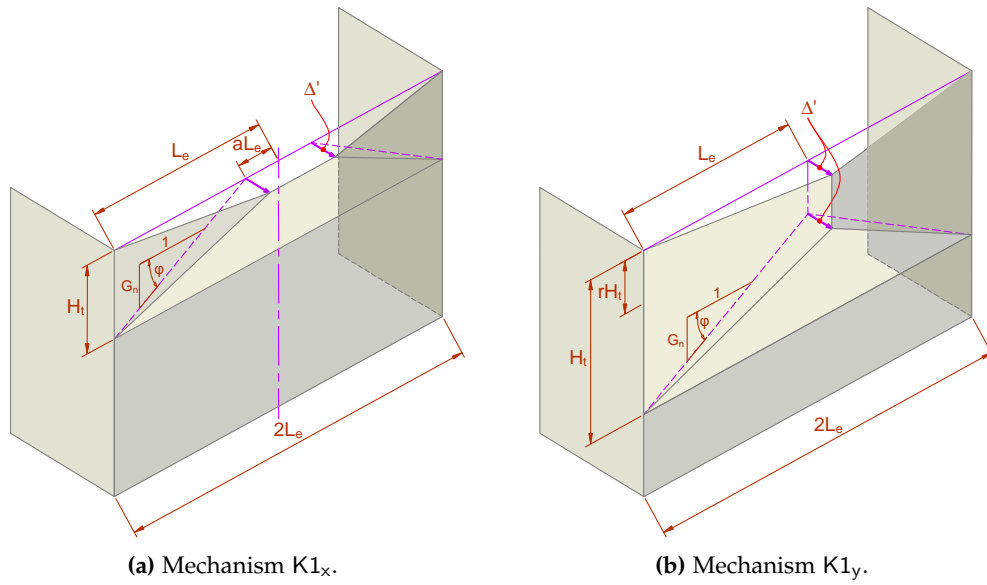


Figure 6.16: Type K1 mechanisms.

Mechanism K1_y

Additional dependent variables include the work contribution factor ζ_{hi} for the internal vertical crack:

$$\zeta_{hi} = \begin{cases} 0, & \text{if one vertical edge is supported, i.e. } n_{vs} = 1, \\ 1, & \text{if two vertical edges are supported, i.e. } n_{vs} = 2; \end{cases} \quad (6.76)$$

and if an OBL is present on the out-of-plane wall, the energy quantity e'_m :

$$e'_m = \frac{1}{2} L_e t_u \sigma_{vom}. \quad (6.77)$$

The total internal work for a single out-of-plane module is

$$U'_{tot} = 2 \frac{\bar{Z}_v}{G_n} f \left\langle \left(\frac{3}{4} + \frac{1}{4} r \right) H_t \right\rangle + \frac{\bar{Z}_h}{\beta} [R_{vs} f \langle \frac{1}{2} H_t \rangle + \zeta_{hi} r f \langle \frac{1}{2} r H_t \rangle] + (1 - \Phi_m) \mu_o e'_m, \quad (6.78)$$

whilst the corresponding total external work premultiplied by λ^{-1} is

$$\lambda^{-1} E'_{tot} = \gamma t_u L_e H_t \left(\frac{1}{3} + \frac{1}{6} r \right) + \Phi_m \eta_m e'_m. \quad (6.79)$$

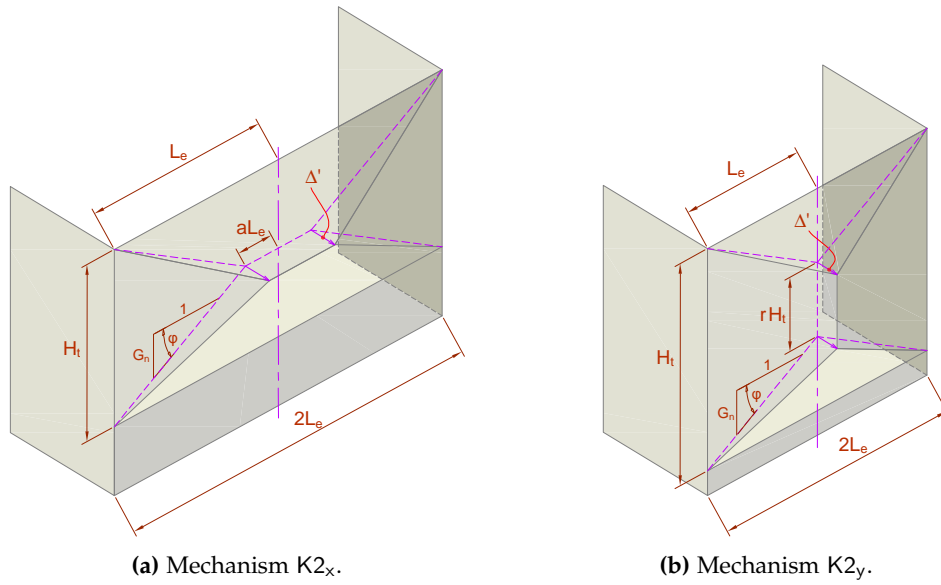


Figure 6.17: Type K2 mechanisms.

Mechanism K2_x

The total internal work for a single out-of-plane module is

$$U'_{\text{tot}} = \bar{Z}_v \beta \left[f\langle H_t \rangle + R_{ts} f\langle 0 \rangle + 2f\langle \frac{1}{2} H_t \rangle \right] + 2R_{vs} \bar{Z}_h G_n f\langle \frac{1}{2} H_t \rangle, \quad (6.80)$$

whilst the corresponding total external work premultiplied by λ^{-1} is

$$\lambda^{-1} E'_{\text{tot}} = \gamma t_u L_e H_t \left(\frac{1}{3} + \frac{1}{6} a \right). \quad (6.81)$$

Mechanism K2_y

An additional dependent variable is the work contribution factor ζ_{hi} for the internal vertical crack, taken as

$$\zeta_{hi} = \begin{cases} 0, & \text{if one vertical edge is supported, i.e. } n_{vs} = 1, \\ 1, & \text{if two vertical edges are supported, i.e. } n_{vs} = 2. \end{cases} \quad (6.82)$$

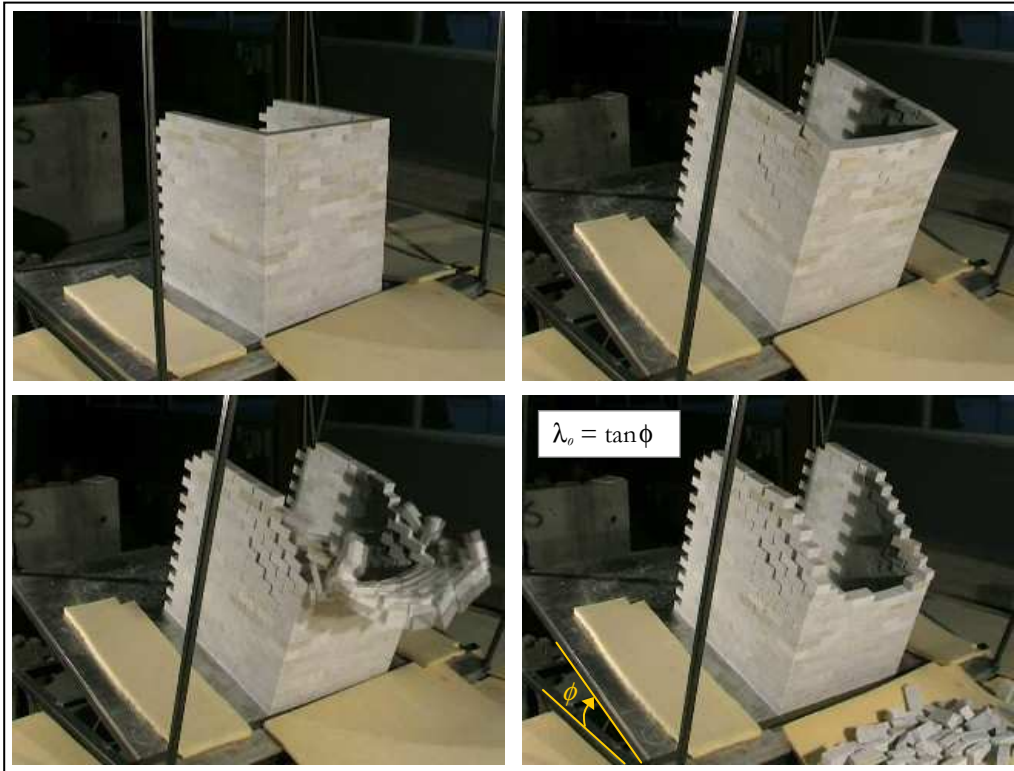


Figure 6.18: Tilting table tests on dry-stack masonry walls by *Restrepo Vélez and Magenes [2009]*. The shown test corresponds to wall r9. (Graphics used with permission from IUSS Press.)

The total internal work for a single out-of-plane module is

$$U'_{\text{tot}} = \frac{\bar{Z}_v}{G_n} [f\langle H_t \rangle + R_{ts}f\langle 0 \rangle + 2f\langle \frac{1}{2}H_t \rangle] + 2\frac{\bar{Z}_h}{\beta} (R_{vs} + \zeta_{hi}r) f\langle \frac{1}{2}H_t \rangle, \quad (6.83)$$

whilst the corresponding total external work premultiplied by λ^{-1} is

$$\lambda^{-1}E'_{\text{tot}} = \gamma t_u L_e H_t \left(\frac{1}{3} + \frac{1}{6}r \right). \quad (6.84)$$

6.6 COMPARISON OF PREDICTIONS WITH EXPERIMENTAL RESULTS

To validate the accuracy of the proposed methodology, its predictions were compared to the results of experimental tests conducted at the University of Pavia by *Restrepo Vélez [2004]* [also reported in *Restrepo Vélez and Magenes, 2009*]. These tests considered a set of 1:5 scale, stone brick dry-stack masonry (DSM) walls, loaded up to collapse using a tilting table arrangement (Figure 6.18). Because of the inertial

Table 6.2: Material properties of the dry-stack masonry in tests by *Restrepo Vélez* [2004].

Parameter	Mean value	Units
Brick length, l_u	79.8	mm
Brick height, h_u	28.2	mm
Brick thickness, t_u	39.7	mm
Joint thickness, t_j	0	mm
Friction coefficient of the masonry, μ_m	0.71	-
Unit weight of the masonry, γ	26.8×10^{-6}	N/mm ³

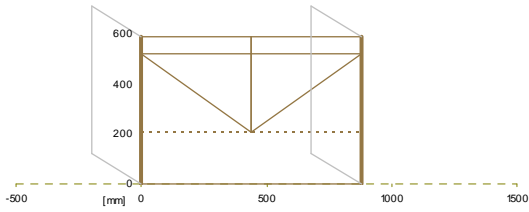
Table 6.3: Wall definition input parameters used in the analysis of walls tested by *Restrepo Vélez* [2004].

Wall	$\frac{L_w}{l_u}$	$\frac{H_w}{h_u}$	N_w	n_{vs}	N_r	R_{vs}	$\frac{\sigma_{vom}}{\gamma h_u}$	ϵ	Φ_m	η_m	$\frac{\sigma_{vor}}{\gamma h_u}$	Φ_r	η_r
R1, R2, R3	11	21	1	2	2	1	0	-	-	-	0	-	-
R5	8	21	1	2	2	1	0	-	-	-	0	-	-
R6	13	21	1	2	2	1	0	-	-	-	0	-	-
R7	8	21	1	2	2	1	0	-	-	-	0	-	-
R8, R9	6	21	1	2	2	1	0	-	-	-	0	-	-
R10	12	21	1	2	2	1	0	-	-	-	0	-	-
R11	12	21	1	1	1	1	0	-	-	-	0	-	-
R12	8	21	1	1	1	1	0	-	-	-	0	-	-
R13	6	21	1	1	1	1	0	-	-	-	0	-	-
R14, R17	3	21	2	1	1	1	0	-	-	-	0	-	-
R15, R18	4	21	2	1	1	1	0	-	-	-	0	-	-
R16, R19	6	21	2	1	1	1	0	-	-	-	0	-	-
R20, R21	7	21	2	2	3	1	0	-	-	-	0	-	-
R23, R24	14	21	1	2	2	1	0	-	-	-	0	-	-
R34, R35	10	21	1	2	2	1	5.50	0.5	1	1.3	0	-	-
R36	10	21	1	2	2	1	0	-	-	-	5.16	1	1
R37	8	21	1	1	1	1	0	-	-	-	5.16	1	1
R38	8	21	1	1	1	1	6.02	0.5	1	1.3	0	-	-
R41	10	21	1	2	2	1	5.50	0.5	0	-	0	-	-

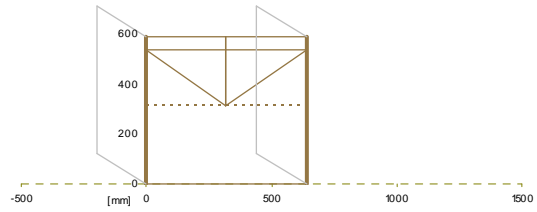
nature of loading, the test arrangement allowed the collapse multiplier (λ_o) to be easily measured as the tangent of the table's angle of tilt at the point of failure. The material properties and geometric configurations of the walls (which served as input parameters for the analyses) are given in Tables 6.2 and 6.3. The various specimen configurations tested are illustrated in Tables 6.4 and 6.5. All walls were free to displace along their top edge (with the exception of wall R41, as described later). Where vertical edge support was provided to the out-of-plane panels, it was done so by means of return walls.

The equations for calculating λ_o , as they are presented in Section 6.5, were coded into an EXCEL spreadsheet, and the built-in optimisation tool SOLVER was used to perform the minimisation process. Results of the analyses are provided in Tables 6.4 and 6.5, respectively, for walls with and without overburden loads. The critical mechanism for each wall, as revealed by the analysis, is shown in Figure 6.19. Table 6.6 compares the predictions made using the proposed method with other methods, based on calculations made by *Restrepo Vélez* [2004] in his thesis;

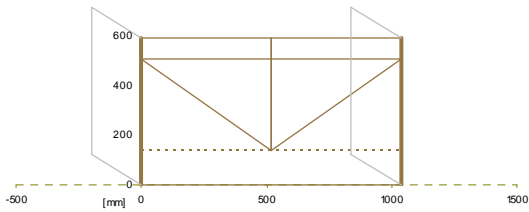
Walls R1, R2 and R3: Mech. G_y , $\lambda_o = 0.244$



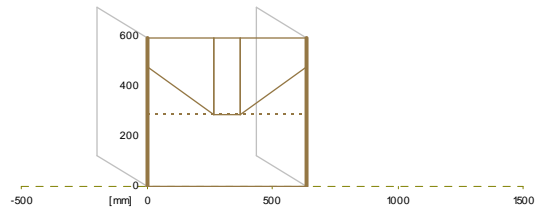
Wall R5: Mech. G_y , $\lambda_o = 0.336$



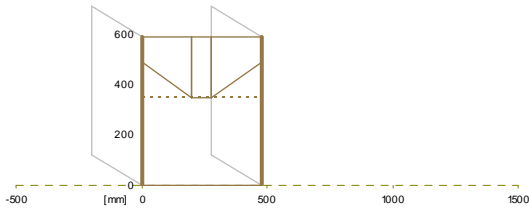
Wall R6: Mech. G_y , $\lambda_o = 0.207$



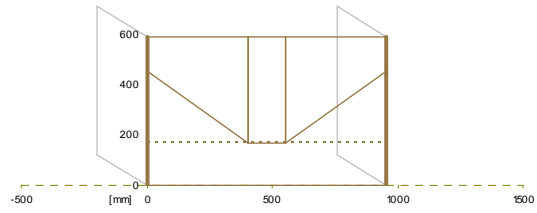
Wall R7: Mech. J , $\lambda_o = 0.273$



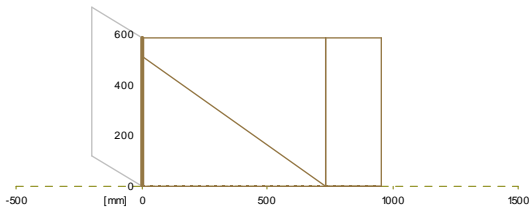
Walls R8 and R9: Mech. J , $\lambda_o = 0.352$



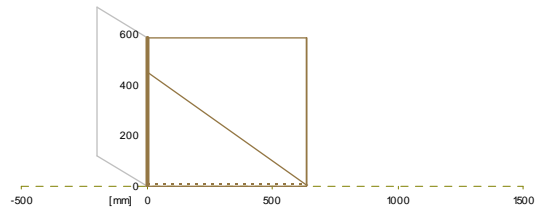
Wall R10: Mech. J , $\lambda_o = 0.190$



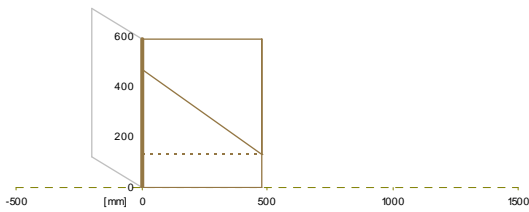
Wall R11: Mech. J , $\lambda_o = 0.092$



Wall R12: Mech. J , $\lambda_o = 0.112$



Wall R13: Mech. J , $\lambda_o = 0.145$



Walls R14 and R17: Mech. J , $\lambda_o = 0.226$

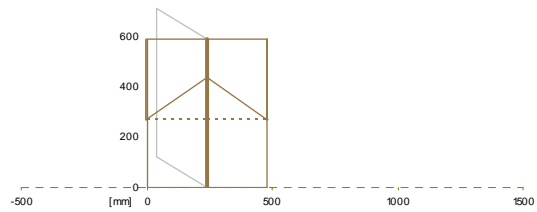
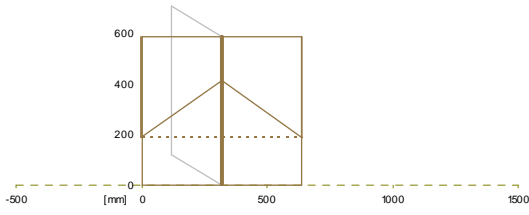
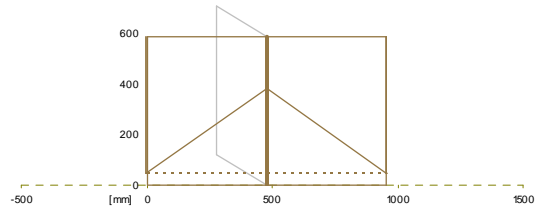


Figure 6.19: Critical mechanism shapes for each wall as revealed by the analysis.

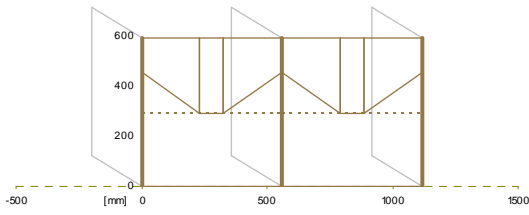
Walls R15 and R18: Mech. J, $\lambda_o = 0.179$



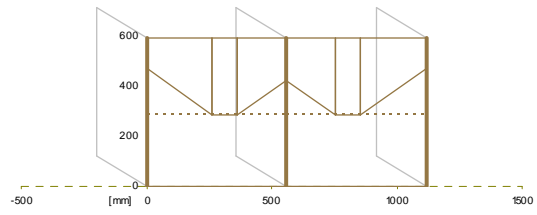
Walls R16 and R19: Mech. J, $\lambda_o = 0.128$



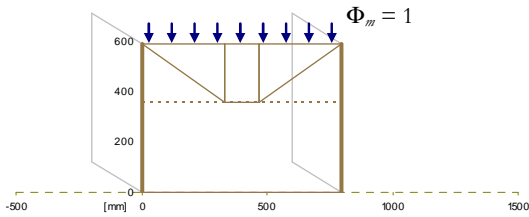
Walls R20 and R21: Mech. J (simple), $\lambda_o = 0.289$



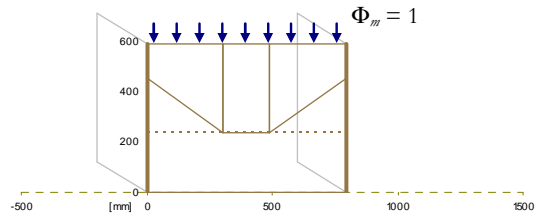
Walls R20 and R21: Mech. J (general), $\lambda_o = 0.284$



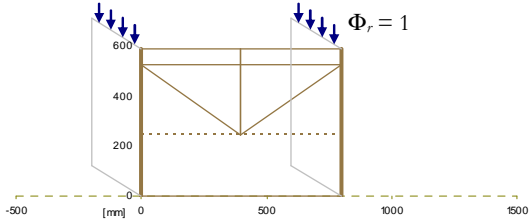
Wall R34: Mech. G_x , $\lambda_o = 0.189$



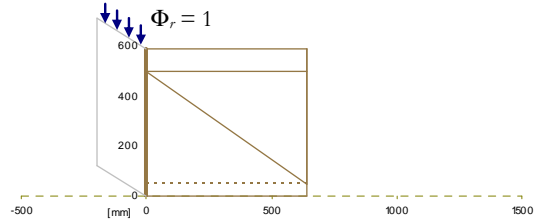
Wall R35: Mech. J, $\lambda_o = 0.143$



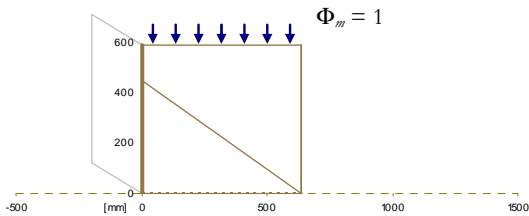
Wall R36: Mech. G_y , $\lambda_o = 0.268$



Wall R37: Mech. G_y , $\lambda_o = 0.122$



Wall R38: Mech. J, $\lambda_o = 0.075$



Wall R41: Mech. J, $\lambda_o = 0.316$

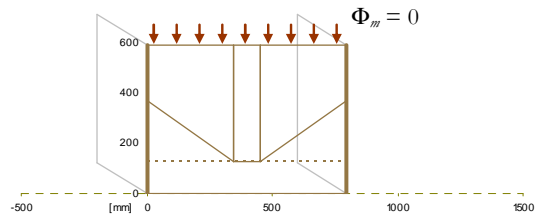


Figure 6.19: (cont'd).

including methods by *de Felice* [1999], *Picchi* [2002], *de Riggi* [1999], *Casapulla* [1999], as well as Restrepo Vélez's own predictions. The results will now be discussed with respect to each type of configuration tested.

6.6.1 Walls Without Axial Loading

The predicted values of strength for walls without axial loading are presented in Table 6.4, with comparison to the experimentally measured values. All walls except R1–R5 were loaded in the outward direction (away from the return walls).

WALLS R1–R4, R6 Each of these five walls consisted of a single out-of-plane panel having two-sided support. Loading was administered in the inward direction (toward the return walls). As such, hybrid mechanisms J and B became inapplicable and only the standard mechanisms of type G and K1 were considered. For every wall, G_y was shown to be the critical mechanism, giving extremely good predictions with an average accuracy ratio (defined as the calculated λ_o divided by the measured λ_o) of 1.00.

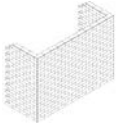
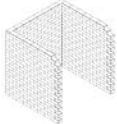
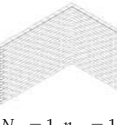
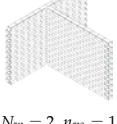
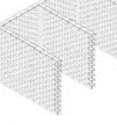
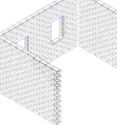
WALLS R7–R10 These walls had the same configuration as R1–R6; however, they were loaded in the outward direction, and hence hybrid mechanisms became applicable. For each wall, hybrid mechanism J was shown to be critical. The predictions were very accurate, with an average accuracy ratio of 0.95.

WALLS R11–R13 Each of these walls consisted of a single out-of-plane panel with one vertical edge supported and the other edge free. Mechanism J was shown to be critical for each wall. The average accuracy ratio was 0.87, meaning that the calculations slightly underestimated the walls' strength.

WALLS R14–R19 These specimens consisted of a pair of out-of-plane panels sharing a common return wall, whilst the outside vertical edge of each panel remained free. Walls R14–R16 had identical overall dimensions as walls R15–R17, but a slightly different mode of connection between the out-of-plane wall and the return walls. Mechanism J was shown by the analysis to be critical for each wall, with an average accuracy ratio of 0.91.

WALLS R20 AND R21 These specimens comprised of a pair of connected out-of-plane walls having both vertical edges supported and sharing a common internal return wall. While both specimens had identical dimensions, a slightly different

Table 6.4: Collapse loads calculated using the proposed method for non-loadbearing walls tested by *Restrepo Vélez and Magenes [2009]*. (Graphics used with permission from IUSS Press.)

Configuration	Wall	Test λ_0	Calculated λ_0 (Critical mechanism indicated in bold)							Ratio λ_0 calc/test
			G_x	G_y	J	B	$K1_x$	$K1_y$	var	
 $N_w = 1, n_{vs} = 2,$ $N_r = 2$	R1	0.254	0.257	0.244	‡	‡	0.325*	0.323	0.96	
	R2	0.226	0.257	0.244			0.325*	0.323	1.08	
	R3	0.244	0.257	0.244			0.325*	0.323	1.00	
	R5	0.349	0.353	0.336			0.447*	0.444	0.96	
	R6	0.208	0.217	0.207			0.275*	0.273	0.99	
 $N_w = 1, n_{vs} = 2,$ $N_r = 2$	R7	0.291	0.353	0.336	0.273	0.442	0.447*	0.444	0.94	
	R8	0.362	0.470	0.447	0.352	0.489	0.596*	0.591	0.97	
	R9	0.352	0.470	0.447	0.352	0.489	0.596*	0.591	1.00	
	R10	0.213	0.235	0.224	0.190	0.380	0.298*	0.296	0.89	
 $N_w = 1, n_{vs} = 1,$ $N_r = 1$	R11	0.097	0.094	0.101*†	0.092	0.265	0.152	0.170*†	0.94	
	R12	0.129	0.132*	0.122	0.112	0.333	0.223*	0.221	0.87	
	R13	0.181	0.176*	0.163	0.145	0.380	0.298*	0.294	0.80	
 $N_w = 2, n_{vs} = 1,$ $N_r = 1$	R14	0.251	0.352*	0.326	0.226	0.380	0.596*	0.589	0.90	
	R15	0.199	0.264*	0.245	0.179	0.333	0.447*	0.441	0.90	
	R16	0.139	0.176*	0.163	0.128	0.265	0.298*	0.294	0.92	
	R17	0.207	0.352*	0.326	0.226	0.380	0.596*	0.589	1.09	
	R18	0.230	0.264*	0.245	0.179	0.333	0.447*	0.441	0.78	
	R19	0.151	0.176*	0.163	0.128	0.265	0.298*	0.294	0.85	
 $N_w = 2, n_{vs} = 2,$ $N_r = 3$	R20	0.285	0.403	0.384	0.289	0.418	0.511*	0.507	0.284	1.00
	R21	0.244	0.403	0.384	0.289	0.418	0.511*	0.507	0.284	1.16
 $N_w = 1, n_{vs} = 2,$ $N_r = 2$	R23	0.144	0.202	0.192	0.165	0.358	0.255*	0.253	0.138	0.96
	R24	0.156	0.202	0.192	0.165	0.358	0.255*	0.253	0.136	0.87
Loading direction in the diagrams: ↙									Mean:	0.95
									CoV:	0.10
									Min:	0.78
									Max:	1.16

* λ_0 was minimised at $\alpha = 1$; i.e. the limiting case between complimentary mechanisms G_x/G_y or $K1_x/K1_y$.
 †The mechanism was unable to utilise the full wall length, due to the wall's aspect ratio and constraint on α .
 ‡Hybrid mechanisms not applicable, since test walls were loaded in the direction toward the return walls.
 ||Unique mechanism variant. Description provided in the text.

method of connection had been used between the façade wall and the central return wall. Mechanism J was found to be critical in the case of each wall; however, two different approaches were undertaken: The first (given in column J in Table 6.4) used the simplified treatment for mechanism J, outlined in Section 6.5.2, whereby all participating in-plane and out-of-plane modules are assumed to be equivalent. The second approach (in column 'var') used the generalised treatment for mechanism J (described in Appendix G.3), which allowed for non-equivalence between participating modules. Since this specimen configuration failed to satisfy the requirements of symmetry (as discussed in Section 6.5.2), the generalised approach was applied, which yielded a slightly lower collapse load than the simplified approach. However, in the case of these particular specimens, this difference was very minor (approximately 1%). The average accuracy ratio for these walls was 1.08, meaning that the analysis slightly overpredicted the walls' measured strength.

WALLS R23 AND R24 Each of these specimens comprised an out-of-plane wall with two-sided support and containing a pair of window openings, which were slightly differently positioned in the two specimens. The failure patterns observed in the tests strongly resembled mechanism J. The analysis results reported for mechanisms G_x , G_y , J, B, $K1_x$ and $K1_y$ in Table 6.4 were based on the standard analysis, which ignored the openings and treated the walls as if they were solid. The results reported in column labelled 'var' were obtained from a refined analysis that accounted for the presence of the openings, but only considered the precise failure pattern observed in the tests, which was not subject to any further λ_o minimisation process. These analyses were based on the procedure described in Section 4.4, performed by discretising the wall into individual elements and using only the solid portions of the wall to provide contributions to the internal and external work terms. They also utilised the refined approach to calculating the axial stress distribution throughout the wall, as described therein (refer to Figures 4.11 and 4.12), which was used in the subsequent calculation of the crack energies. The collapse multiplier was then evaluated using Eq. (6.20). As indicated by Table 6.4, the refined analyses taking into account the openings provided the critical solutions (despite not undergoing optimisation), with an average accuracy ratio of 0.91. By contrast, mechanism J gave the lowest predictions for the analyses that ignored the openings; however, it still slightly overpredicted the strength of both specimens. This outcome indicates that it may be unconservative to ignore the presence of openings in the analysis. However, it is noted that such an analysis requires significant additional effort to perform, as it is generally necessary to set up an individual spreadsheet for each unique failure pattern.

GENERAL REMARKS

- The proposed method performed with very good accuracy for the 22 walls without precompression, giving an average accuracy ratio of 0.95 and coefficient of variation (CoV) of 0.10. Importantly, the method did not perform poorly for any particular configuration.
- Furthermore, comparison to predictions made using other methods, as provided by Restrepo Vélez in his thesis (Table 6.6), demonstrates the proposed method to not only be the most accurate overall, but also the only method that did not, on average, overpredict the walls' strength.
- The analysis showed mechanism G_y to be critical for all specimens loaded in the inward direction (toward the return walls), and mechanism J for all walls loaded in the outward direction.
- Comparison of the predicted failure shapes (Figure 6.19) with the observed failure patterns [provided in *Restrepo Vélez and Magenes, 2009*] shows that for every wall, the analysis had managed to capture the actual collapse mechanism reasonably well.
- For almost every wall analysed, all non-critical mechanisms produced strength predictions that were unconservative. This highlights the importance of considering all possible mechanisms during the analysis in the search for the critical one.
- The strength predictions obtained from mechanism B were highly unconservative for every wall considered and, on average, approximately twice as high as the predictions from mechanism J. This illustrates that mechanism J is a fundamentally more energetically feasible failure shape compared to B. This outcome is somewhat surprising, given that mechanism B has already attracted considerable attention in previous published literature [e.g. mechanisms B1 and B2 by *D'Ayala and Speranza, 2003*], whereas mechanism J has been overlooked.
- That the proposed approach performed with such good accuracy may also be somewhat surprising in light of issues highlighted by *Casapulla [2008]*, who argued that it is unlikely for the full capacity of frictional torsion to be realised due to dilatancy of the masonry during deformation, and therefore inclusion of full friction along cracks in horizontal bending could prove to be unconservative. Whilst the author recognises these points to be entirely valid, the analysis results indicate that while consideration of only the standard

type G mechanisms with full friction indeed results in strength overprediction for all walls loaded in the outward direction (refer to walls R7–R24 in Table 6.4), mechanism J appears to have offset any such effects by allowing for hybrid action and thus causing a reduction in the predicted collapse load. Furthermore, it can be demonstrated that for this particular experimental data set, type G mechanisms with zero friction would still overpredict the strength of the one-sided walls, while becoming underpredictive for the two-sided walls; and thus, neglecting friction would not provide any real improvement in the prediction accuracy.

- Type K1 mechanisms produced strength predictions that were, on average, approximately 50% higher than those from type G mechanisms, thus showing type G mechanisms to be more favoured in DSM. The relative favourability of these mechanisms is investigated further in Section 6.7.2.

6.6.2 Loadbearing Walls

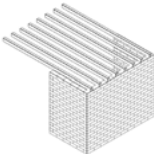
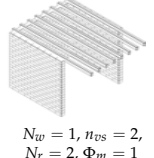
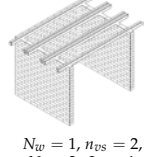
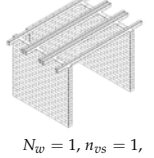
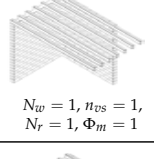
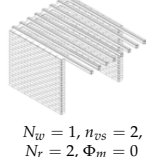

The applicability of the proposed method to loadbearing walls was assessed using test results for six such walls tested by Restrepo Vélez, with the experimental and analytical results provided in Table 6.5. In the test arrangement, the OBL was administered using a series of joists resting upon the top of the specimens and acting at the mid-thickness of the wall ($\epsilon = 1/2$), which meant that the R_{ts} factor in the analysis was taken as 0 [from Eq. (6.27)]. The joists were unrestrained in five of the specimens (R34–R38), thus enabling them to apply an additional lateral load to the wall; whilst in the last specimen (R41), they were restrained. All specimens except for R34 were loaded in the outward direction (away from the return walls).

WALL R34 This wall had two-sided support, and the OBL acted upon the out-of-plane panel. Loading was applied in the inward direction, meaning that only type G and K1 mechanisms were applicable. The critical mechanism was G_x .

WALLS R35 AND R38 These walls had two-sided and one-sided support respectively, with the OBL applied onto the main out-of-plane panel. Wall R35 had the same configuration as R34, except that it was loaded in the outward direction. Mechanism J was found to be critical in both walls.

WALLS R36 AND R37 These walls had two-sided and one-sided support respectively, and the OBL was applied onto the in-plane return walls. Despite being loaded in the outward direction, the analysis revealed the standard mechanism

Table 6.5: Collapse loads calculated using the proposed method for loadbearing walls tested by *Restrepo Vélez and Magenes [2009]*. (Graphics used with permission from IUSS Press.)

Configuration	Wall	Test λ_o	Calculated λ_o (Critical mechanism indicated in bold)								Ratio λ_o calc/test
			G_x	G_y	J	B	$K1_x$	$K1_y$	$K2_x$	$K2_y$	
 $N_w = 1, n_{vs} = 2,$ $N_r = 2, \Phi_m = 1$	R34	0.217	0.189	0.195*	‡	‡	0.291	0.306*	¶	¶	0.87
 $N_w = 1, n_{vs} = 2,$ $N_r = 2, \Phi_m = 1$	R35	0.168	0.189	0.195*	0.143	0.195	0.291	0.306*	¶	¶	0.85
 $N_w = 1, n_{vs} = 2,$ $N_r = 2, \Phi_r = 1$	R36	0.320	0.282	0.268	0.281	0.546	0.357*	0.355	¶	¶	0.84
 $N_w = 1, n_{vs} = 1,$ $N_r = 1, \Phi_r = 1$	R37	0.126	0.132*	0.122	0.131	0.471	0.223*	0.221	¶	¶	0.97
 $N_w = 1, n_{vs} = 1,$ $N_r = 1, \Phi_m = 1$	R38	0.055	0.094*	0.094*	0.075	0.159	0.191	0.197*	¶	¶	1.37
 $N_w = 1, n_{vs} = 2,$ $N_r = 2, \Phi_m = 0$	R41 [§]	0.423	0.604	0.466	0.316	0.450	0.635*	0.523	0.723*	0.708	0.75
Loading direction in the diagrams: 									Mean:	0.94	
									CoV:	0.24	
									Min:	0.75	
									Max:	1.37	

* λ_o was minimised at $\alpha = 1$; i.e. the limiting case between complimentary mechanisms G_x/G_y or $K1_x/K1_y$.

‡Hybrid mechanisms not applicable, since test walls were loaded in the direction toward the return walls.

§Overburden load was restrained; however, the friction coefficient along the vertical edge was taken as $\mu_o = 0$.

¶Type-2 mechanisms not applicable, as top edge was free to move horizontally.

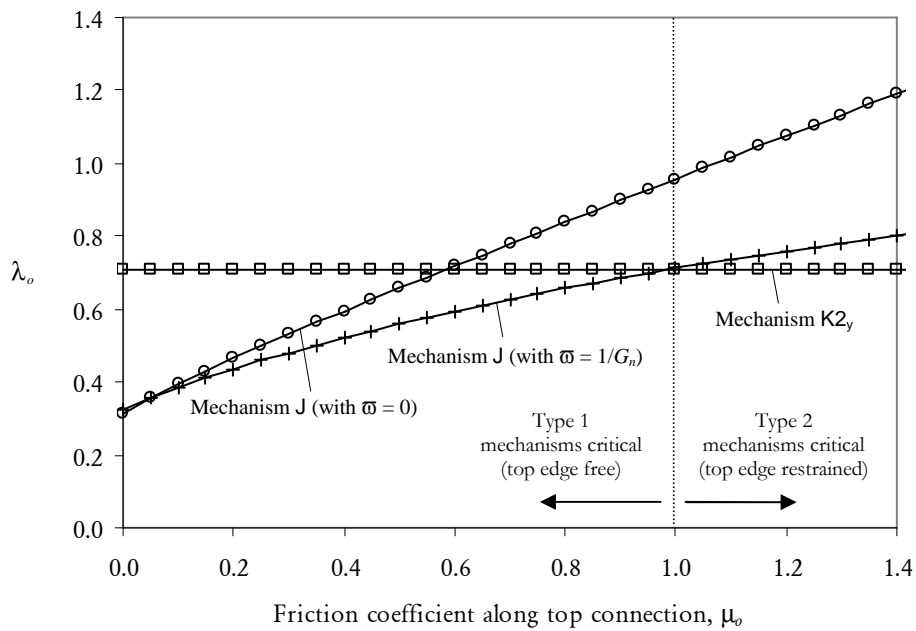


Figure 6.20: Influence of the coefficient of friction μ_0 on the critical mechanism and collapse multiplier for wall R41.

G_y to be favoured over J for both these walls, albeit only slightly. This outcome is a consequence of the additional internal work cost required to mobilise the in-plane panels within mechanism J, which made the pure out-of-plane mechanism G_y energetically more feasible. Inspection of the photographed failure patterns [provided in Restrepo Vélez, 2004] confirms that the in-plane panels were not active in the mechanism. This result is interesting when compared to both the predicted and observed response for walls R35 and R38, where the OBL acted upon the out-of-plane panels, and which instead underwent the hybrid mechanism J.

WALL R41 The out-of-plane wall in this specimen had two-sided support and was subjected to an OBL which was restrained against horizontal movement. A frictional connection was present between the wall and OBL; however, the value of the friction coefficient μ_0 was not reported and needed to be assumed in the analysis. Considered in the analysis were all type-1 mechanisms as well as the type-2 mechanisms K2 $_x$ and K2 $_y$. It was found that the critical mechanism was dependent on the assumed value of μ_0 , as demonstrated by Figure 6.20. Mechanism J was found to be critical when the assumed value of μ_0 was less than approximately 1.0, which is considered to be within the realistic range of values. As seen from Figure 6.20, within this range, the calculated collapse multiplier was quite sensitive to the value of μ_0 . When μ_0 was increased beyond 1.0, the connection became sufficiently

Table 6.6: Comparison of collapse loads predicted using different methods. Results for all third party methods are based on calculations by *Restrepo Véllez [2004]* with the corresponding mechanism shapes referred to using the naming convention by *D'Ayala and Speranza [2003]* as indicated in Figure 6.2. Only the results for the critical mechanism are provided for each wall.

Wall	Test λ_0	Proposed method			de Felice			D'Ayala and Speranza			Picchi, de Ruggi, Casapulla			Restrepo Véllez		
		Mech	Calc λ_0	Ratio	Mech	Calc λ_0	Ratio	Mech	Calc λ_0	Ratio	Mech	Calc λ_0	Ratio	Mech	Calc λ_0	Ratio
R1	0.254	G _y	0.244	0.96	-	-	-	G	0.222	0.87	G	0.334	1.31	G	0.235	0.93
R2	0.226	G _y	0.244	1.08	-	-	-	G	0.222	0.98	G	0.334	1.48	G	0.235	1.04
R3	0.244	G _y	0.244	1.00	-	-	-	G	0.147	0.60	G	0.334	1.37	G	0.242	0.99
R5	0.349	G _y	0.336	0.96	-	-	-	G	0.187	0.54	G	0.459	1.32	G	0.333	0.95
R6	0.208	G _y	0.207	0.99	-	-	-	G	0.279	1.34	G	0.283	1.36	G	0.183	0.88
R7	0.291	J	0.273	0.94	-	-	-	A	0.438	1.51	-	-	-	A	0.294	1.01
R8	0.362	J	0.352	0.97	B2	0.421	1.16	A	0.506	1.40	-	-	-	A	0.361	1.00
R9	0.352	J	0.352	1.00	B2	0.421	1.20	A	0.545	1.55	-	-	-	A	0.403	1.14
R10	0.213	J	0.190	0.89	A	0.337	1.58	A	0.356	1.67	-	-	-	A	0.215	1.01
R11	0.097	J	0.092	0.94	D	0.100	1.03	-	-	-	-	-	-	A	0.098	1.01
R12	0.129	J	0.112	0.87	D	0.124	0.96	-	-	-	-	-	-	D	0.132	1.02
R13	0.181	J	0.145	0.80	D	0.141	0.78	-	-	-	-	-	-	D	0.176	0.97
R14	0.251	J	0.226	0.90	A	0.331	1.32	A	0.351	1.40	-	-	-	A	0.280	1.12
R15	0.199	J	0.179	0.90	A	0.303	1.52	A	0.317	1.59	-	-	-	A	0.234	1.18
R16	0.139	J	0.128	0.92	A	0.244	1.76	A	0.253	1.82	-	-	-	A	0.183	1.32
R17	0.207	J	0.226	1.09	A	0.317	1.53	A	0.334	1.61	-	-	-	A	0.235	1.23
R18	0.230	J	0.179	0.78	A	0.287	1.25	A	0.302	1.31	-	-	-	A	0.233	1.01
R19	0.151	J	0.128	0.85	A	0.293	1.94	A	0.302	2.00	-	-	-	A	0.179	1.19
R20	0.285	J var	0.284	1.00	A	0.317	1.11	A	0.334	1.17	-	-	-	A	0.263	0.92
R21	0.244	J var	0.284	1.16	A	0.309	1.27	A	0.326	1.34	-	-	-	A	0.256	1.05
R23	0.144	J var	0.138	0.96	A	0.094	0.65	-	-	-	-	-	-	G	0.231	1.60
R24	0.156	J var	0.136	0.87	A	0.094	0.60	-	-	-	-	-	-	G	0.182	1.17
R34	0.217	G _x	0.189	0.87	-	-	-	G	0.137	0.63	-	-	-	G	0.229	1.06
R35	0.168	J	0.143	0.85	-	-	-	A	0.689	4.10	-	-	-	A	0.173	1.03
R36	0.320	G _y	0.268	0.84	-	-	-	G	0.669	2.09	G	0.283	0.88	G	0.348	1.09
R37	0.126	G _y	0.122	0.97	D	0.132	1.05	-	-	-	D	0.184	1.46	D	0.132	1.05
R38	0.055	J	0.075	1.37	-	-	-	-	-	-	-	-	-	D	0.085	1.55
R41	0.423	J	0.316	0.75	-	-	-	F	0.291	0.69	-	-	-	A	0.471	1.11
<i>n:</i>				28			18		21			10			28	
Mean:		All walls		0.95			1.23		1.44			1.34			1.09	
Cov:				0.13			0.29		0.53			0.13			0.15	
Min:				0.75			0.60		0.54			0.88			0.88	
Max:				1.37			1.94		4.10			1.48			1.60	
<i>n:</i>		Walls without axial loading (R1-R24)		22			17		17			8			22	
Mean:				0.95			1.24		1.34			1.38			1.08	
Cov:				0.10			0.30		0.50			0.04			0.15	
Min:				0.78			0.60		0.54			1.31			0.88	
Max:				1.16			1.94		2.00			1.48			1.60	
<i>n:</i>		Loadbearing walls (R34-R41)		6			1		4			2			6	
Mean:				0.94			1.05		1.88			1.17			1.15	
Cov:				0.24			-		0.87			0.35			0.17	
Min:				0.75			1.05		0.63			0.88			1.03	
Max:				1.37			1.05		4.10			1.46			1.55	

strong that the type K2 mechanisms became favoured. In the type-1 mechanism analyses, whose results are presented in Table 6.5, the connection was assumed to be perfectly smooth ($\mu_o = 0$), which resulted in underprediction of the wall's capacity by 25%. By varying the friction coefficient, it was found that the predicted strength equalled the measured strength at $\mu_o = 0.17$, which is considered to be well within the range of values typically prescribed by design codes. Nonetheless, because of a lack of data for walls with such restraint conditions in the available experimental work, it is difficult to validate the accuracy of the proposed method. Hence, it is recommended that inclusion of a frictional resistance along the top edge be treated with caution, as it could result in unconservative values of strength.

GENERAL REMARKS

- For five of the six walls, the proposed method produced strength predictions that were within the mildly conservative range (accuracy ratio between 0.75–0.97). The strength of only one of the walls (R38) was overestimated (accuracy ratio of 1.37).
- The proposed method produced, on average, the most accurate predictions of the methods considered in Table 6.6. It was also the only method whose predictions were, on average, conservative (average accuracy ratio of 0.94).

6.7 SENSITIVITY OF PREDICTIONS TO THE CHOICE OF MECHANISM

This section presents a set of parametric studies investigating the sensitivity of the calculated collapse multiplier (using the governing equations presented in Section 6.5) to the choice of mechanism and independent geometric variables, in particular, the mechanism length L_e and height H_t . The aim of this study was to gain an insight into the relationship between λ_o and the mechanism dimensions, and also to identify general trends relating to the optimisation process.

The internal work equations for each of the predefined mechanisms (given in Section 6.5) have been formulated in terms of the stress capacity function $f\langle \cdot \cdot \cdot \rangle$, whose meaning is defined according to the fundamental form of the moment capacity expression [Eq. (6.21)] in combination with the derived moment moduli \bar{Z}_v and \bar{Z}_h . In the parametric studies undertaken, two different forms of the stress capacity function were considered:

1. The first is a self-weight (or height) proportional form, where σ_{vo} in Eq. (6.22) is taken as zero, resulting in

$$f\langle d \rangle = \gamma d. \quad (6.85)$$

This is representative of either DSM or mortar-bonded URM with negligible bond cohesion, in both cases without precompression.

2. The second is a constant form,

$$f\langle \dots \rangle = \text{constant}, \quad (6.86)$$

which when dealing with DSM makes the effective assumption that the acting precompression is much larger than the compressive stress from self-weight ($\sigma_{vo} \gg \gamma H_t$). The resulting algebraic form is also analogous to mortar-bonded masonry if the bond cohesion f_{mt} far exceeds the self-weight stress ($f_{mt} \gg \gamma H_t$). This follows from inspection of analytical expressions for the ultimate moment capacities of mortar-bonded masonry in vertical, horizontal and diagonal bending [see Eqs. (4.18), (4.23)–(4.27) and (4.32)], since each has the same general form as Eq. (6.21) but with varied moduli \bar{Z} and a stress capacity function in the form

$$f\langle \dots \rangle = a f_{mt} + b \sigma_v, \quad (6.87)$$

where a and b are some constants. Therefore, by treating the stress capacity function as constant, it is possible to gain a qualitative insight into the trends that might be expected for URM with strong bond cohesion.¹³

The case study analysed was a single out-of-plane wall with two-sided support, based on walls R7–R10 tested by Restrepo Vélez [2004] (refer to Table 6.4) and having the same material properties (Table 6.2). Two parametric studies were conducted for each type of stress capacity function: Firstly, the mechanism length was fixed such that $L_e/l_u = 6$ bricks, and H_t was varied from 0 to ∞ . Secondly, the mechanism height was fixed at $H_t/h_u = 12$ courses and L_e varied from 0 to ∞ . The fixed dimensions were chosen to achieve realistic slenderness ratios, with $L_e/t_u = 12.1$ and $H_t/t_u = 8.5$, respectively in the two studies. Analyses were performed with each of the predefined type-1 mechanisms presented in Section 6.5, including G, J, B and K1. For the standard mechanisms G and K1, at each set of chosen values of L_e

¹³The resulting trends in the expected behaviour for mortar-bonded URM should be treated as indicative only, as several simplifying assumptions are made. These include: (i) The moment moduli used in the calculations correspond to those for masonry without cohesion, as presented in Section 6.4.2; (ii) Capacities from vertical, diagonal and horizontal crack lines are all assumed to contribute and thus achieve their capacities simultaneously. By contrast, in the usual ultimate strength calculation for uncracked URM walls in two-way bending, capacities along horizontal cracks are typically ignored as they form early in the response; (iii) Calculations for the hybrid mechanisms use the original shear deformation model, which is based on frictional shear deformation of the in-plane panel (Section 6.4.3). By implementing a constant stress capacity function within the corresponding internal work equation, it is effectively assumed that a Mohr-Coulomb type failure criterion ($\tau = c + \mu\sigma_v$) governs, in which the cohesion term c becomes dominant.

and H_t , the collapse multiplier was evaluated directly. For the hybrid mechanisms J and B, the remaining independent variables ϖ and a (a only in J) were optimised to minimise the collapse multiplier. The results are plotted over the full domains of λ_o and α in Figure 6.21, for a weight-proportional stress capacity function [Eq. (6.85)]; and Figure 6.22, for a constant stress capacity function [Eq. (6.86)].¹⁴ It is worth noting that for the standard mechanisms, $\alpha = 1$ defines the boundary between each complimentary pair of x and y forms.

To illustrate the strengthening benefit obtained from two-way response due to the presence of vertical edge support, the graphs also show the strength based on the simple rocking mechanism for a parapet wall (mechanism V1). The equation used to calculate λ_o for this mechanism is

$$\lambda_o = \frac{t_u}{\gamma H_t^2} f(H_t). \quad (6.88)$$

As seen from the provided graphs, all curves converge with mechanism V1 as $\alpha \rightarrow \infty$, indicating that all mechanisms approach simple vertical one-way bending for walls with large L_w/H_w aspect ratios.

6.7.1 Influence of the Mechanism Dimensions

General trends relating to the influence of mechanism dimensions L_e and H_t on the calculated collapse load λ_o will now be discussed with reference to Figures 6.21 and 6.22.

Mechanism Height

Perhaps the most important trend demonstrated is the existence of a critical mechanism height at which λ_o becomes minimised for masonry with zero bond strength (Figure 6.21a). This trend is evident for each two-way mechanism and can be rationalised as follows: As the height H_t and slenderness ratio H_t/t_u is reduced, the mechanism becomes increasingly stable with respect to overturning, and therefore $\lambda_o \rightarrow \infty$ as $H_t \rightarrow 0$. In standard mechanisms, as H_t becomes increasingly large, the height-proportional stress capacity function [Eq. (6.85)] causes the internal work to increase proportionally to H_t^2 , whereas the external work only increases in proportion to H_t . This results in $\lambda_o \propto H_t$ at large H_t , and hence $\lambda_o \rightarrow \infty$ as $H_t \rightarrow \infty$. In hybrid mechanisms, the frictional in-plane component becomes dominant over the flexural out-of-plane component as the L_e/H_t aspect ratio becomes small, causing

¹⁴An arbitrary value of $f(\dots) = 0.01$ MPa was used in the case of the constant stress capacity function.

the value of the collapse multiplier to approach the coefficient of friction (in this case $\mu_m = 0.71$). Consequently, $\lambda_o \rightarrow \mu_m$ as $\alpha \rightarrow 0$, which may be due to either $H_t \rightarrow \infty$ or $L_e \rightarrow 0$.¹⁵ Therefore, between the limits of $H_t = 0$ and $H_t = \infty$ (at which $\lambda_o = \infty$) a critical height must exist at which λ_o reaches a minimum value, in both the standard and hybrid mechanisms.

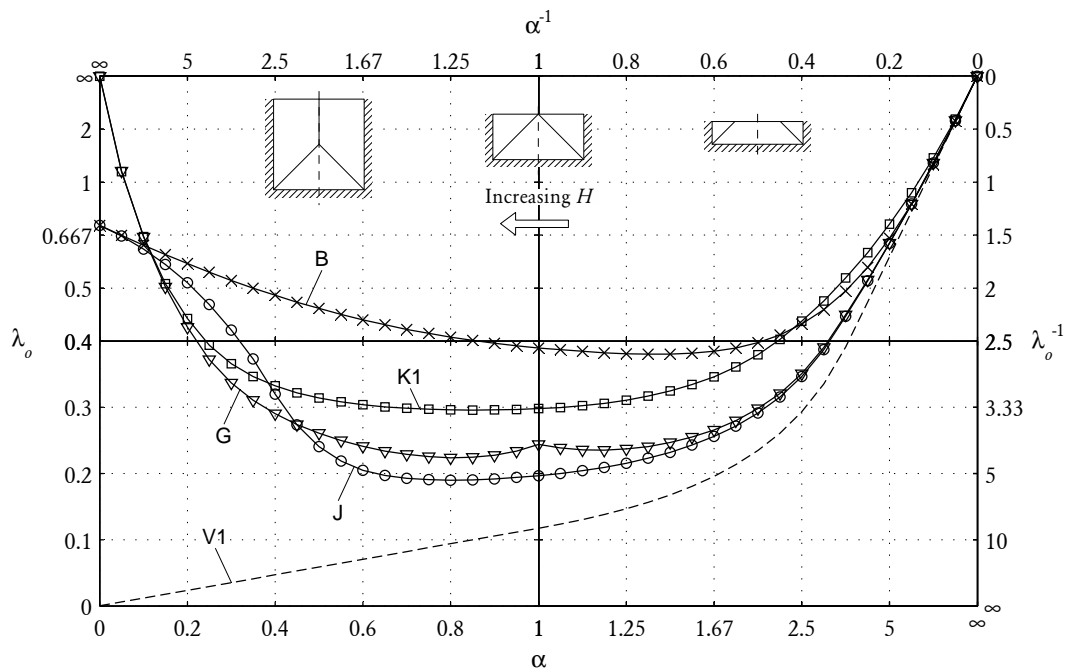
It should also be emphasised that Figures 6.21 and 6.22 demonstrate the direct influence of mechanism dimensions L_e and H_t , and not the wall dimensions L_w and H_w . Since H_t is an independent variable that may assume any value within the physical height limit of the wall (H_w), it follows that if the H_w is larger than the critical mechanism height, then the mechanism will adopt the critical height, and any additional increase in H_w will have no further influence on λ_o . Indeed, this was demonstrated by both the experimentally observed failure patterns for DSM (for example, as shown in Figure 6.18) and the critical mechanism shapes revealed by the analysis (Figure 6.19), which in most cases exhibited only partial utilisation of the wall's total height.

It is evident that as the mechanism height is varied (Figures 6.21a and 6.22a) a slope discontinuity occurs across $\alpha = 1$ for the standard type G mechanisms. As seen, this can create local minima within the sub-domains $0 < \alpha \leq 1$ (mechanism G_y) and $1 \leq \alpha < \infty$ (mechanism G_x), regardless of the stress capacity function used. This highlights the importance of considering each complimentary form of the mechanism separately during the optimisation process, to avoid the minimisation algorithm from potentially getting trapped at these local minima.

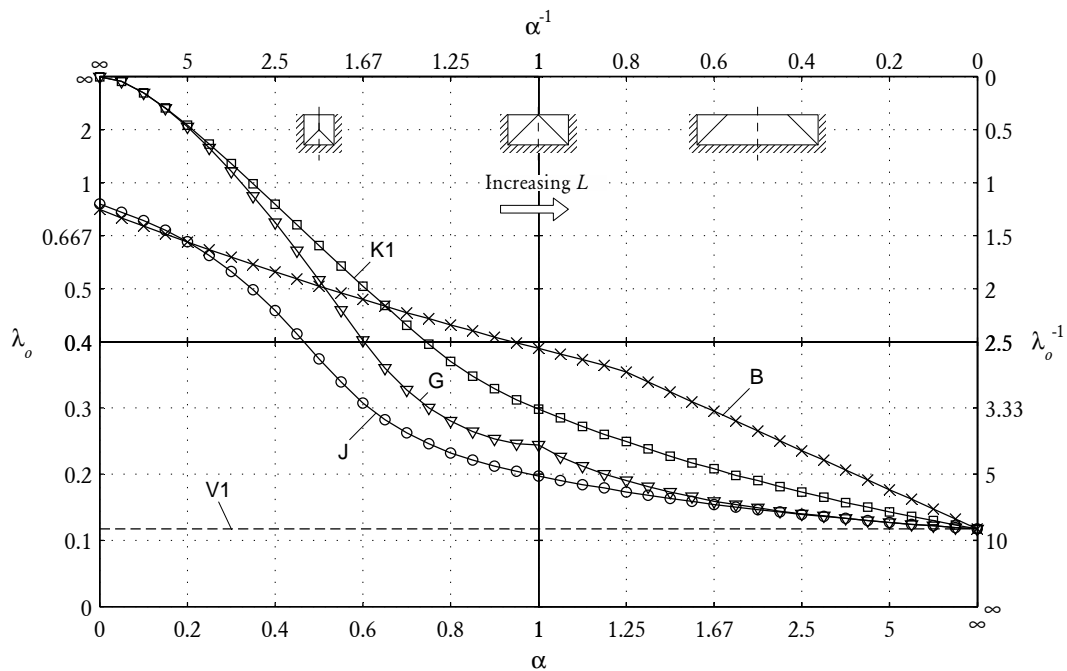
For mortar-bonded URM walls with strong bond cohesion (Figure 6.22a), the general trend demonstrated for mechanisms B and K1 is that λ_o reduces with increasing H_t . This trend also applies to the standard type G mechanism, except for a very minor local minimum for mechanism G_x at approximately $\alpha \approx 1.05$. This indicates that for this types of masonry, the mechanism will generally tend to utilise the full height of the wall.¹⁶ Indeed, this has been observed through a large number of experimental studies, including those mentioned in Section 6.2.3 and the original tests reported in Chapters 2 and 3.

¹⁵Note that in the case of $L_e \rightarrow 0$ for constant H_t (Figure 6.21b), λ_o approaches a value slightly higher than the coefficient of friction, due to the additional resistance from the vertical crack in horizontal bending as well as vertical bending along the vertical edge boundary crack.

¹⁶Whilst this trend is valid within the practical range of wall aspect ratios, as long as the influence of self-weight remains small (due to the assumption that $f_{mt} \gg \gamma H_t$); it should be treated with caution for walls with a large height, where the self-weight may become significant. Nonetheless, if the user is willing to ignore the influence of wall self-weight in calculating the ultimate load capacity, then the demonstrated parametric trends will still hold.

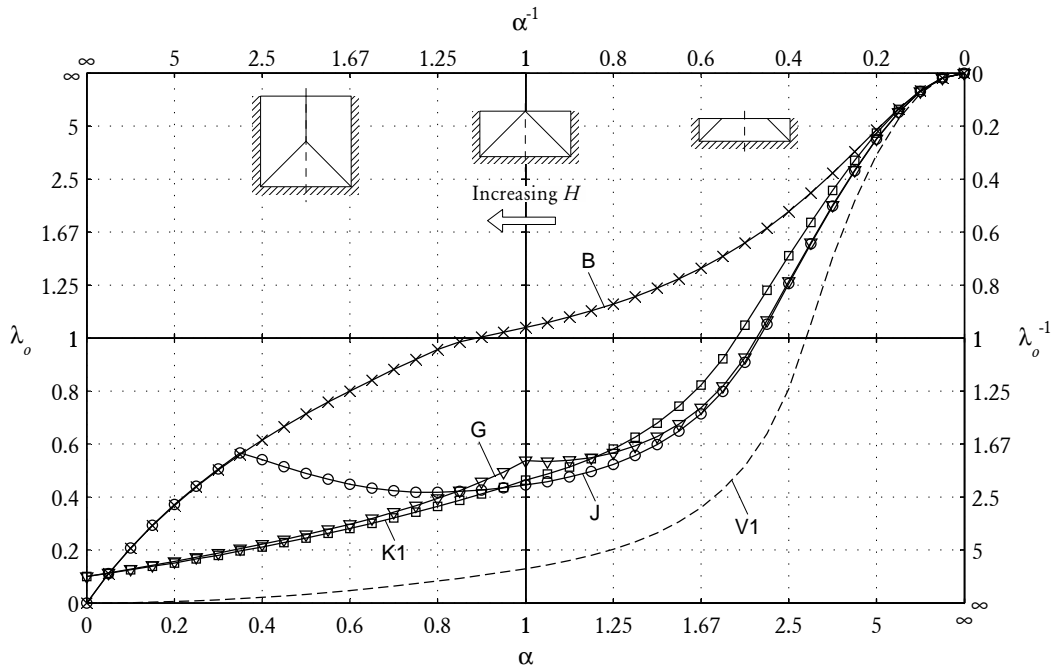


(a) Varied H_t (for fixed $L_e/l_u = 6$ bricks, $L_e/t_u = 12.1$).

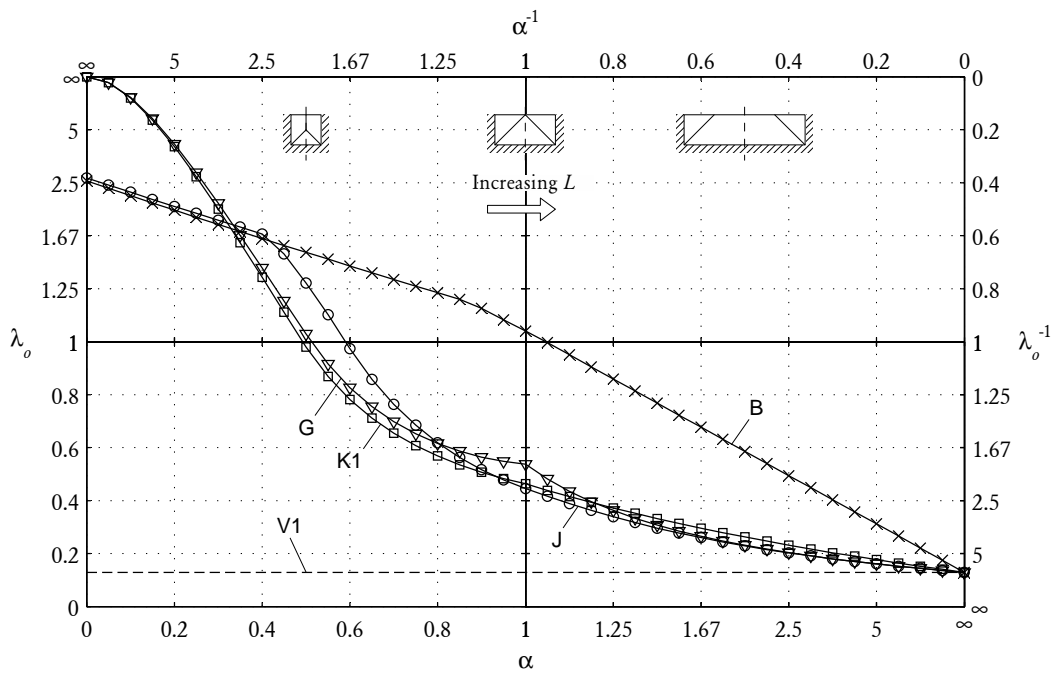


(b) Varied L_e (for fixed $H_t/h_u = 12$ courses, $H_t/t_u = 8.5$).

Figure 6.21: Parametric study implementing a weight-proportional stress capacity function. This is representative of non-loadbearing DSM or mortar-bonded URM with very weak bond cohesion.



(a) Varied H_t (for fixed $L_e/l_u = 6$ bricks, $L_e/t_u = 12.1$).



(b) Varied L_e (for fixed $H_t/h_u = 12$ courses, $H_t/t_u = 8.5$).

Figure 6.22: Parametric study implementing a constant stress capacity function. This is analogous to mortar-bonded URM with strong bond cohesion.

Mechanism Length

The influence of mechanism length (L_e) on the calculated collapse multiplier is much more direct than the effect of the mechanism height, in that regardless of the stress capacity function or type of mechanism used, λ_o always reduces as L_e is increased (Figures 6.21b and 6.22b). This is because with increasing L_e , the associated external work term for each mechanism increases at a greater rate than the internal work term, due to a larger proportion of the mechanism exhibiting vertical bending. The resulting trend implies that each type of mechanism will generally utilise the full available length of the wall. Nonetheless, when using the proposed optimisation approach (described in Section 6.5), it is recommended that L_e should be treated as an independent variable, as instances may arise where it may not be possible for a mechanism to span the full length of the wall due to constraints on α [as per Eqs. (6.61) and (6.62)] (for example, wall R11 in conjunction with mechanism G_y , as shown in Table 6.4).

6.7.2 Critical Mechanism

It is extremely difficult to make generalised predictions regarding the expected critical mechanism, as this depends on a variety of aspects of the wall's configuration, including:

- Length and height dimensions of the wall, and the resulting aspect ratio;
- Boundary conditions, in particular whether the wall is one- or two-sided (n_{vs}), the degree of rotational restraint along the supported vertical edges (R_{vs} factor), and the degree of effective rotational restraint along a top edge resulting from a potentially eccentric OBL (R_{ts} factor);
- Material characteristics, including the coefficient of friction μ_m and the nature of the stress capacity function $f\langle \dots \rangle$.

The influence of some of these properties on the relative favourability of the various mechanisms will now be discussed with reference to Figures 6.21 and 6.22, which, it should be recalled, are based on the particular case study of a two-sided wall with full moment connections along the vertical edges. The focus of these discussions is to identify: (i) the critical mechanism overall; and (ii) the relative dominance of the standard mechanisms G and K1, which becomes relevant when in-plane failure is preventable. Despite the best efforts of the author to explain the trends observed in these figures, it is nonetheless recommended that the explanations are treated as

indicative only—the safest and most prudent approach is for the user to always analyse a wall with respect to each of the mechanisms and adopt the critical one.

Masonry with Weak or Zero Bond Cohesion

For DSM or URM with very weak bond cohesion, hybrid mechanism J is shown to be critical overall across the full domain of L_w/H_w wall aspect ratios (Figure 6.21).¹⁷ The only exception is for walls with a very short length, where mechanism B becomes critical (Figure 6.21b). However, even in that instance both hybrid mechanisms still provide very similar predictions.

Comparison of the relative favourability of type G and K1 mechanisms on the basis of Figure 6.21 shows G to be dominant over K1, regardless of the wall aspect ratio L_w/H_w . The reason for this can be explained by performing an energy comparison for the two mechanisms using their respective internal and external work expressions (provided in Section 6.5.3). The fundamental difference between these two mechanisms is that G uses the triangular-based element (Figure 6.9a) and K1 uses the rectangular-based element (Figure 6.9c). For a weight-proportional stress capacity function together with the parameters $R_{vs} = 1$ and $n_{vs} = 2$, it may be demonstrated that while mechanism K1 has a larger external work compared to mechanism G (due to the different associated elements), it also has a disproportionately higher internal work term, due to vertical bending along the bottom edge crack. This causes mechanism G to be more favourable in this instance. However, it should be noted that for different values of the other input parameters this trend may not necessarily hold. For example, if the vertical edges of the wall were to have no rotational restraint ($R_{vs} = 0$), then mechanism K1 would not incur any internal work from horizontal bending along the vertical edge crack, thus making it energetically more feasible.

Masonry with Strong Bond Cohesion

For masonry with high bond strength, the wall's L_w/H_w aspect ratio influences which mechanism becomes dominant. From Figure 6.22, it is seen that for walls with a high aspect ratio (at $\alpha > 0.95$) mechanism J is the most critical overall, whereas for walls with a low aspect ratio (at $\alpha < 0.95$) mechanism K1_y becomes critical. However, it should be noted that mechanisms G, J and K1 all provide similar strength for $\alpha > 0.7$.

¹⁷Although Figure 6.21a shows mechanism J to be non-critical when $\alpha < 0.45$, if the wall's effective aspect ratio satisfies $\alpha < 0.8$, then the global minimum λ_o will apply, which corresponds to mechanism J.

Comparison of the relative favourability of type G and K1 mechanisms on the basis of Figure 6.22 again demonstrates a dependence on the wall's L_w/H_w aspect ratio. Mechanism K1 is slightly favoured for walls with low aspect ratio ($\alpha < 1.2$), whereas G is slightly favoured for walls with a high aspect ratio ($\alpha > 1.2$). It is also evident that the difference between the two mechanisms is minor in this instance when compared to the results of analyses using a weight-proportional stress capacity function (Figure 6.21), where mechanism G was shown to be significantly more favoured. Furthermore, it should be noted that in the studies conducted, the wall was assumed to have full rotational restraint along the vertical edges ($R_{vs} = 1$). However, if the wall was to have simply supported vertical edges instead, then mechanism K1 would become more favoured due to a reduction in the internal work from horizontal bending along these edges.

General Remarks

The parametric study undertaken indicates that in two-way walls with a free top edge, type G mechanisms are expected to be generally favoured for masonry with low or zero bond strength, whereas type K1 mechanisms are expected to be more favoured for masonry with high bond strength. Indeed, this is consistent with failure patterns observed throughout many experimental studies, as discussed previously in Section 6.2. However, the results have also shown that in certain instances, type G mechanisms are expected to become critical for masonry with strong bond cohesion, particularly for walls that have a high L_w/H_w aspect ratio. This is in contrast to the fact that type G mechanisms are not considered by any presently-used ultimate strength design procedures, including the Australian masonry code method, which only considers type K mechanisms (refer to Figure 4.1).

Finally, it will be noted that while the trends observed have been based on the particular case study where the mechanism slenderness ratios were fixed at $L_e/t_u = 12.1$ and $H_t/t_u = 8.5$ (Figures 6.21 and 6.22), they are also generally consistent with the results of a second case study with fixed slenderness ratios of $L_e/t_u = 6.0$ and $H_t/t_u = 14.9$. Graphical results of this second study are provided in Appendix G.5 (Figures G.19 and G.20).

6.8 CONCLUSIONS

This chapter has described an analytical procedure for calculating the collapse load multiplier (λ_o) in walls without any bond strength (or DSM), based on a virtual work

approach. The numerous refinements that have been made over previous methods [e.g. *D'Ayala and Speranza, 2003*] are: (i) inclusion of a horizontal bending moment capacity due to rotational friction along bed joints; (ii) development of a frictional shear deformation model for participating in-plane walls; (iii) a detailed account of the various possible effects due to overburden loads; and (iv) development of several additional collapse mechanisms.

Generic expressions were presented for calculating the moment capacities of DSM along horizontal, vertical and diagonal crack lines. Together with the new in-plane shear deformation model, these expressions were implemented in a set of derived closed-form analytical expressions for calculating λ_o for a range of collapse mechanisms. Accuracy of the developed technique was verified using experimental results for a set of 28 dry-stack masonry walls tested by *Restrepo Vélez [2004]*. The resulting comparisons were highly favourable, with predictions of the collapse load being, on average, slightly conservative and within 5% of the experimental values, whilst exhibiting a coefficient of variation of only 13%. The critical mechanism predicted by the analysis also closely resembled the observed failure pattern in the majority of the walls.

It has been demonstrated that since the VW method gives an upper-bound estimate of the critical collapse load, to find the critical solution for a particular wall, it is prudent to consider all possible mechanisms and perform a λ_o minimisation process within each mechanism by treating its dimensions as independent variables. Whilst it is impractical to perform all of the necessary calculations by hand, the method is nonetheless simple enough to be implemented using software such as EXCEL, where the minimisation process can be performed using the built-in optimisation package SOLVER. Finally, that the proposed method is based entirely on mechanics principles and does not rely on any empirically calibrated parameters, is considered to be another valuable aspect as a static analysis tool for seismic assessment.

Chapter 7

LOAD-DISPLACEMENT MODELLING

Abstract

This chapter presents a nonlinear inelastic load-displacement model for representing the behaviour of two-way walls subjected to out-of-plane loading. The model treats the walls as having zero tensile bond strength, akin to the treatment used in Chapter 6. Associated analytical expressions for calculating both the load and displacement capacities, which feed into the model, have also been derived for type K mechanisms using principles of statics and virtual work. Comparison of the model's predicted response to experimentally observed behaviour is quite favourable, in that it appears to provide a reasonable yet conservative estimate of the wall strength. Implementation of the model is also demonstrated as part of a displacement-based (DB) assessment approach using the substitute structure method. Influence of various aspects of the wall's configuration, such as vertical edge fixity, overburden loads, and different edge support shapes, on the predicted seismic performance is demonstrated through a set of examples. It is anticipated that an extensive set of parametric time-history analysis studies using the proposed model is the next necessary step toward developing a reliable DB assessment technique for two-way walls.

7.1 INTRODUCTION

An essential ingredient of displacement-based (DB) seismic analysis is an analytical model to define the structure's load-displacement capacity, sometimes referred to as a pushover or capacity curve. It is well established through both experiment and theory that vertically spanning unreinforced masonry (URM) walls tend to behave as rocking blocks when subjected to lateral loads (Figure 7.1), which has led to the subsequent development of a DB methodology for such walls [Doherty *et al.*, 2002]. By contrast, the load-displacement behaviour of two-way URM walls has gone largely unstudied, and as such, no analytical models exist for representing their behaviour. It is believed that the experimental studies performed as part of the present research in Chapters 2 and 3 now provide a basis for the development of such a model.

In Chapter 6, a force-based (FB) analytical approach was developed for calculating the load capacity of masonry walls with respect to various types of two-way mechanisms, by treating the wall as being cracked and having zero bond strength. In the present chapter, this procedure is further extended to modelling of the wall's load-displacement behaviour up to the point of collapse. The methodology presented focuses primarily on type K collapse mechanisms (refer to Figure 6.3 and discussions in Section 6.2.3), as these are the failure patterns most commonly associated with mortar-bonded URM and are used in the AS 3700 [Standards Australia, 2001] procedure for ultimate strength design. Nonetheless, the basic concepts and procedures used to derive the load-displacement relationships could also be applied to other types of mechanisms, such as the type G, J or B mechanisms dealt with in Chapter 6. The relationships derived are based on static equilibrium of the sub-plates comprising the mechanisms, with frictional modes of resistance also being taken into account, thus resulting in overall hysteretic response that is nonlinear and inelastic. Various considerations discussed in Section 6.3.2 relating to overburden loads (OBLs) are also considered in the derived relationships, including the OBL's restraint and eccentricity.

The layout of the chapter is as follows: The proposed load-displacement model, including the analytical equations used to calculate the various input properties, is presented in Section 7.2. Validation of the model with experimental data is performed in Section 7.3. The developed model is implemented into a prototype DB design procedure by means of the substitute structure approach in Section 7.4. Several examples illustrating application of this method are presented in Section 7.5. Conclusions and main outcomes of the chapter are summarised in Section 7.6.

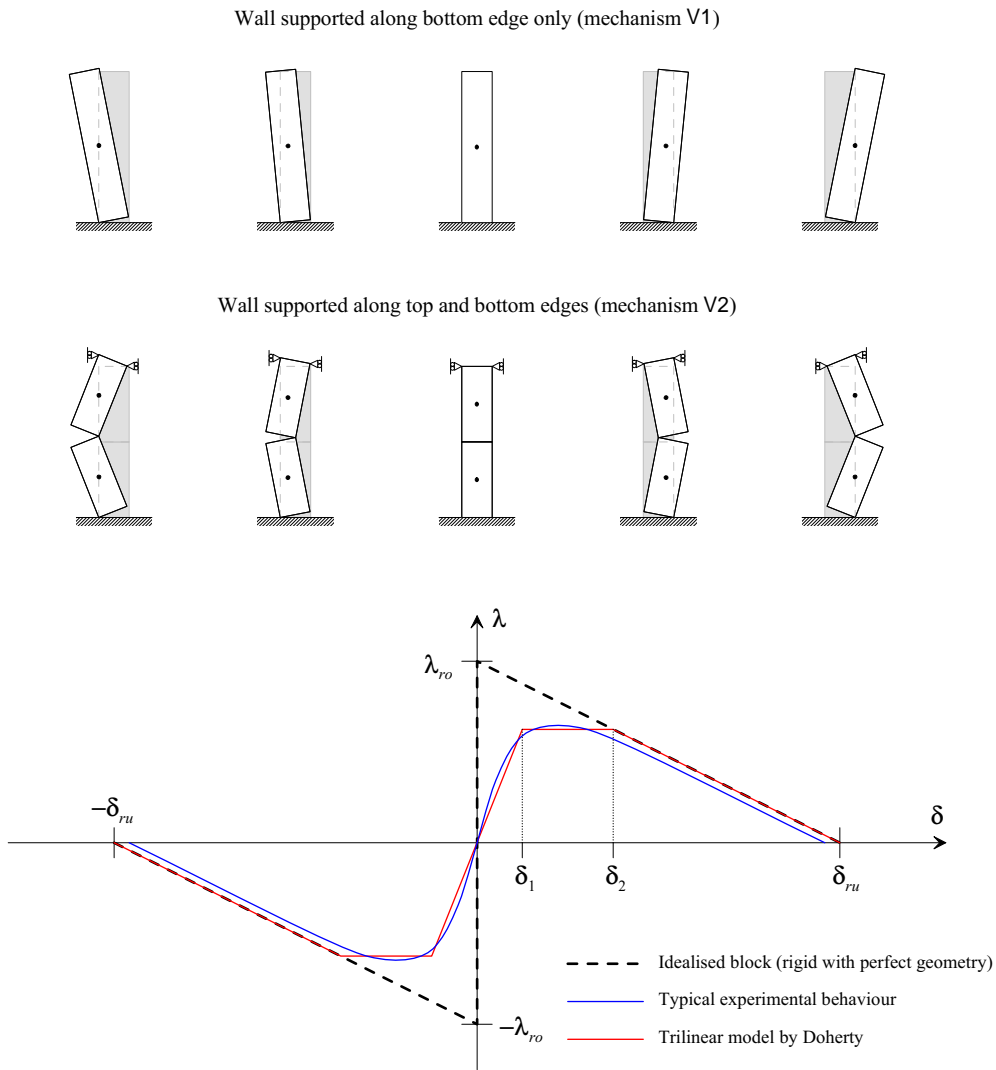


Figure 7.1: Rocking behaviour of vertically spanning walls.

7.2 LOAD-DISPLACEMENT CAPACITY MODEL

The proposed load-displacement model considers the wall to have zero tensile strength, akin to the treatment used for analytical prediction of the load capacity in Chapter 6. This is because in the response range of interest (i.e. large displacements), the wall will have formed a collapse mechanism and will therefore be already cracked. The fundamental assumption made by the developed approach is that at any point in the wall’s response, its total lateral load resistance is comprised of several sources of resistance acting independently of one another. By separately defining the hysteresis rules for each of these components in terms of a common

reference displacement, δ , the wall's overall response may then be obtained by superimposing the individual load contributions. For a wall with zero bond strength, the total lateral load resistance $\lambda\langle\delta\rangle$ may come from three possible sources:

$$\lambda\langle\delta\rangle = \lambda_r\langle\delta\rangle + \lambda_h\langle\delta\rangle + \lambda_s\langle\delta\rangle, \quad (7.1)$$

where $\lambda_r\langle\delta\rangle$ is resistance from rigid body rocking, $\lambda_h\langle\delta\rangle$ is frictional resistance from horizontal bending, and $\lambda_s\langle\delta\rangle$ is a possible additional contribution from frictional sliding between the top edge of the wall and an OBL. The proposed load-displacement representations for these components are shown by Figure 7.2. The following sections will describe the individual components in more detail.

Since the methodology presented here is effectively an extension of the FB analysis described in Chapter 6, various concepts and considerations described therein are also applicable. In particular, the model has the ability to deal with the following aspects related to a wall's boundary conditions, which were discussed in greater detail in Section 6.3:

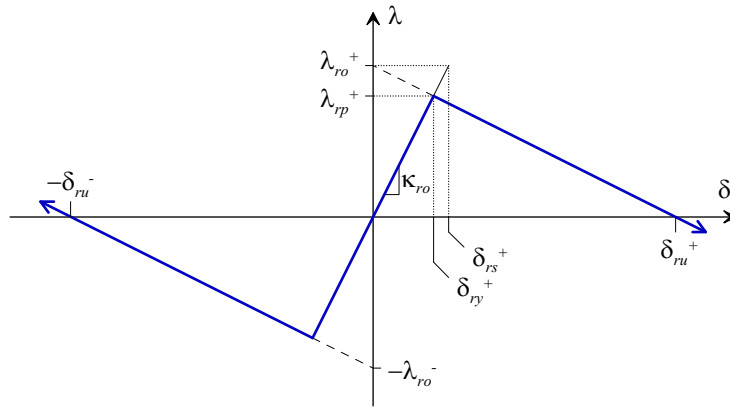
- Treatment of any OBLs present as either restrained or unrestrained;
- OBL eccentricity;
- Rotational fixity along supported vertical edges.

Furthermore, as the analytical equations presented here focus specifically at type K mechanisms, the mechanism specific calculations presented in Section 6.5 are also relevant. Definitions of the variables used throughout the analytical expressions presented are as given in Chapter 6.

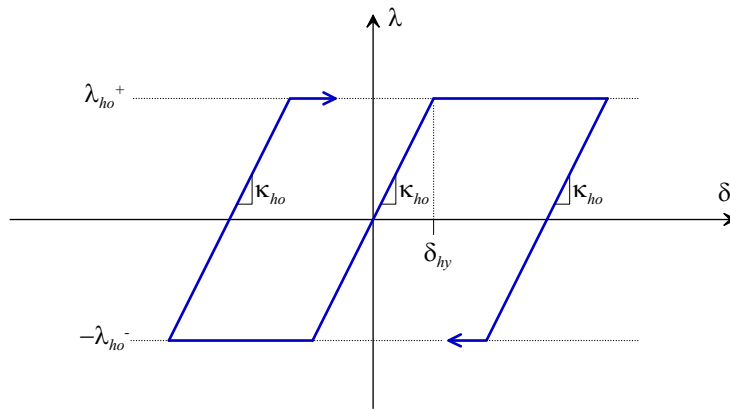
For convenience and consistency with other parts of this thesis, the developed load-displacement relationships are presented in the non-dimensional λ - δ format, where λ is the load multiplier, defined as the ratio of the lateral load to the self-weight of the wall [Eq. (2.3)]; and δ is the wall's lateral displacement normalised by its thickness [Eq. (2.2)]. Note that unless stated otherwise, displacement δ refers to the maximum surface displacement along the mechanism, as illustrated in Figures 6.16 and 6.17 (indicated by the symbol Δ').

7.2.1 Rocking Component (r)

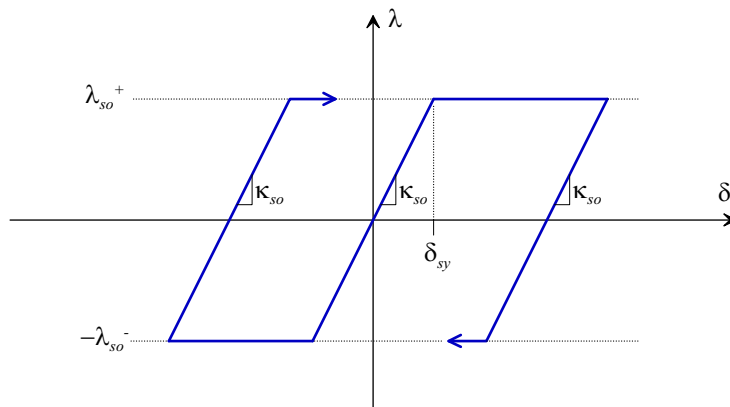
It is well established [e.g. *Ewing and Kariotis, 1981; Doherty et al., 2002; Derakhshan et al., 2011*] that vertically spanning walls undergo rocking behaviour when subjected to large out-of-plane deformations (Figure 7.1). Since two-way walls also



(a) Rocking component $\lambda_r(\delta)$, modelled using elastic bilinear-softening rule.



(b) Inelastic component due to horizontal bending friction, $\lambda_h(\delta)$, modelled using elastoplastic rule.



(c) Inelastic component due to overburden load sliding friction, $\lambda_s(\delta)$, modelled using elastoplastic rule.

Figure 7.2: Hysteresis rules proposed for representing various components of the wall's load resistance.

exhibit some degree of vertical bending, it follows that at larger deformations some component of their response must also include rocking type behaviour. Modelling this requires consideration of two types of rocking block systems: idealised rigid blocks, defined as being non-deformable with a perfectly rectangular cross sectional geometry; and in the realistic case, semi-rigid blocks that are deformable and have imperfect (non-flat) contact surface along cracked sections. While real masonry walls are semi-rigid, calculating the parameters that define their rocking load-displacement capacity inherently relies upon the idealisation of rigid behaviour.

Rigid Block System Idealisation

The elastic load-displacement response of an idealised rigid block system under rocking is shown by the dashed line in Figure 7.1. Initiation of motion from the resting position requires application of the overturning force, λ_{ro} , in order to overcome the initial restoring moment from self-weight. For a fixed pivot location, an increase in the displacement causes a linear reduction in the resisting moment, accompanied by a linear reduction in the restoring force. Eventually the system reaches its instability displacement, δ_{ru} , at which it becomes balanced and provides zero restoration force. If the system is allowed to displace beyond this point, then it enters the unstable range where it requires application of an external restoring force in order to avoid collapse. For a system with a known shape and spatial mass distribution, the response-defining load and displacement capacities λ_{ro} and δ_{ru} may be easily calculated from statics. When a displacement is applied in the opposite displacement direction, the pivot locations switch to the opposite side of the block, thus generating a discontinuity in the load-displacement curve across $\delta = 0$. Rocking behaviour is naturally elastic, due to conversion of applied external energy or the kinetic energy into potential energy manifested through vertical uplift of the block's mass, as illustrated by the wall diagrams in Figure 7.1. This causes the loading and unloading paths along the load-displacement capacity curve to coincide.¹

Presented in Table 7.1 are a set of λ - δ relationships that define the idealised rigid block rocking behaviour for the different forms of the type K mechanisms (Figure 6.3). These mechanisms are divided into the complimentary forms $K1_x/K1_y$,

¹Note that in the context described, rocking is considered to be *elastic* in terms of its load-displacement behaviour under quasistatic loading conditions. During dynamic motion, a rocking block undergoes energy losses associated with the change of rotation axis at the point of impact [see e.g. *Housner, 1963; Hogan, 1989*]. Whilst impact damping is not explicitly considered in the methodology described in this chapter, its influence could be accounted for by the choice of the nominal viscous damping, ζ_{nom} , used in a dynamic analysis (refer to Section 7.4.2).

Table 7-1: Equations defining the idealised rigid block load-displacement relationship for the rocking component of response.

Mech.	λ - δ relationship for $\delta > 0$	Ultimate overturning load λ_{ro}	Instability displacement δ_{ru}
K1 _x	$\lambda = \frac{t_u}{H_t} \cdot \frac{\left[\frac{3}{2} - \frac{1}{2}a + 2\psi(1 - a\epsilon) \right] - \delta \left[\frac{2}{3} + \frac{1}{3}a + \psi(1 + a) \right]}{\frac{2}{3} + \frac{1}{3}a + \Phi\eta\psi(1 + a)} \quad (7.2)$	$\lambda_{ro} = \frac{t_u}{H_t} \cdot \frac{\frac{3}{2} - \frac{1}{2}a + 2\psi(1 - a\epsilon)}{\frac{2}{3} + \frac{1}{3}a + \Phi\eta\psi(1 + a)} \quad (7.3)$	$\delta_{ru} = \frac{\frac{3}{2} - \frac{1}{2}a + 2\psi(1 - a\epsilon)}{\frac{2}{3} + \frac{1}{3}a + \psi(1 + a)} \quad (7.4)$
K1 _y	$\lambda = \frac{t_u}{H_t} \cdot \frac{\left[\frac{3}{2} + \frac{1}{2}r + 2\psi \right] - \delta \left[\frac{2}{3} + \frac{1}{3}r + \psi \right]}{\alpha \left(\frac{2}{3} + \frac{1}{3}r + \Phi\eta\psi \right)} \quad (7.5)$	$\lambda_{ro} = \frac{t_u}{H_t} \cdot \frac{\frac{3}{2} + \frac{1}{2}r + 2\psi}{\alpha \left(\frac{2}{3} + \frac{1}{3}r + \Phi\eta\psi \right)} \quad (7.6)$	$\delta_{ru} = \frac{\frac{3}{2} + \frac{1}{2}r + 2\psi}{\frac{2}{3} + \frac{1}{3}r + \psi} \quad (7.7)$
K2 _x	$\lambda = \frac{t_u}{H_t} \cdot \frac{4[1 + \psi(2 - \epsilon)] - \delta[2(1 + a)(1 + 2\psi)]}{\frac{2}{3} + \frac{1}{3}a} \quad (7.8)$	$\lambda_{ro} = \frac{t_u}{H_t} \cdot \frac{4[1 + \psi(2 - \epsilon)]}{\frac{2}{3} + \frac{1}{3}a} \quad (7.9)$	$\delta_{ru} = \frac{2[1 + \psi(2 - \epsilon)]}{(1 + a)(1 + 2\psi)} \quad (7.10)$
K2 _y	$\lambda = \frac{t_u}{H_t} \cdot \frac{4[1 + \psi(2 - \epsilon)] - \delta[2(1 + 2\psi)]}{\alpha \left(\frac{2}{3} + \frac{1}{3}r \right)} \quad (7.11)$	$\lambda_{ro} = \frac{t_u}{H_t} \cdot \frac{4[1 + \psi(2 - \epsilon)]}{\alpha \left(\frac{2}{3} + \frac{1}{3}r \right)} \quad (7.12)$	$\delta_{ru} = \frac{2[1 + \psi(2 - \epsilon)]}{1 + 2\psi} \quad (7.13)$
V1	$\lambda = \frac{t_u}{H_t} \cdot \frac{[1 + 2\psi(1 - \epsilon)] - \delta[1 + 2\psi]}{1 + 2\Phi\eta\psi} \quad (7.14)$	$\lambda_{ro} = \frac{t_u}{H_t} \cdot \frac{1 + 2\psi(1 - \epsilon)}{1 + 2\Phi\eta\psi} \quad (7.15)$	$\delta_{ru} = \frac{1 + 2\psi(1 - \epsilon)}{1 + 2\psi} \quad (7.16)$
V2	$\lambda = \frac{t_u}{H_t} \cdot [4[1 + \psi(2 - \epsilon)] - \delta[4(1 + 2\psi)]] \quad (7.17)$	$\lambda_{ro} = \frac{t_u}{H_t} \cdot [4[1 + \psi(2 - \epsilon)]] \quad (7.18)$	$\delta_{ru} = \frac{1 + \psi(2 - \epsilon)}{1 + 2\psi} \quad (7.19)$

which occur when the wall is unrestrained along the top edge (Figure 6.16); and forms $K2_x/K2_y$, applicable to walls whose top edge is restrained (Figure 6.17). The tabulated equations were derived from principles of statics, by discretising the wall into vertical strips, and integrating the increment of moment for each strip along the length of the wall to ensure that moment equilibrium is satisfied for the overall mechanism. For full derivation details the reader is referred to Appendix H.1. The main assumptions made in the derivation of these equations are as follows:

1. The wall is subjected to a lateral load distributed according to its mass.
2. Stresses across horizontal and diagonal cracks are concentrated at the extreme compressive fibre of the section. This is based directly on the assumption of idealised rigid block behaviour.
3. As mentioned, within the derivation process the wall is discretised into a series of vertical strips. It is then assumed that both the lateral and vertical inertia-based external forces applied onto each strip are transmitted to the supported horizontal (top or bottom) edges of the wall within the strip itself. In other words, there is no net flow of these forces between adjacent strips.

The second column of Table 7.1 provides relationships between the load resistance λ and the normalised displacement δ , in the positive displacement direction ($\delta > 0$). The third and fourth columns of the table provide the rocking overturning load λ_{ro} and the rocking instability displacement δ_{ru} , based on the λ - δ relationships in the second column. Using these capacities, the idealised rigid body rocking relationships (in the second column) can be expressed over the entire δ domain in the alternate form

$$\lambda_r\langle\delta\rangle = \begin{cases} \lambda_{ro}^+ (1 - \delta/\delta_{ru}^+) & \text{for } \delta > 0, \\ 0 & \text{for } \delta = 0, \\ \lambda_{ro}^- (-1 - \delta/\delta_{ru}^-) & \text{for } \delta < 0. \end{cases} \quad (7.20)$$

Properties superscripted with '+' or '-' denote the respective capacities in the positive and negative directions, as defined in Figure 7.2a. This allows for the possibility of asymmetric behaviour, which will occur when an OBL acts at different eccentricities in the two directions, as illustrated through Figure 6.7 and discussed in Section 6.3.2.

Table 7.1 also provides λ - δ capacity relationships for the one-way vertical bending mechanisms V1 and V2, where V1 represents a parapet wall supported along only its bottom edge and V2 represents a wall supported along both its bottom

and top edges (see Figure 7.1). These expressions were obtained by assigning $a = 1$ to the corresponding equations for two-way mechanisms $K1_x$ and $K2_x$, since these mechanisms will approach $V1$ and $V2$, respectively, when the horizontal span becomes sufficiently long. The resulting capacity expressions are similar to those presented by *Doherty et al.* [2002], with the additional features of allowing for control over the OBL eccentricity and restraint.

An important feature of the idealised rocking relationships in Table 7.1 is that the expressions for the overturning load λ_{ro} become identical to collapse load multiplier expressions derived in Chapter 6 based on the energy approach, when, in the latter, only cracks undergoing vertical and diagonal bending are included in contributing toward the internal work [i.e. inclusion of only the \bar{Z}_v terms in the respective equations (6.74), (6.78), (6.80) and (6.83), and exclusion of the frictional sources of resistance]. This results from the fact that both sets of analytical expressions are based on the same fundamental assumptions listed previously. In other words, the force-based methodology presented in Chapter 6 can be considered to be a particular case of the load-displacement model described in the present chapter, when the displacement approaches zero.

Real Block Systems

Real masonry walls differ from idealised rigid blocks in that they are deformable, possess geometric imperfections (a non-flat contact surface along cracked sections), and have a finite material compressive strength. The problem of the discontinuity in the λ - δ capacity curve across $\delta = 0$ (as is the case for idealised rigid systems) becomes avoided, since the curve must exhibit an effective linear elastic zone in the small displacement range (blue line in Figure 7.1), due to the deformability of the material and gradual shift of the compressive force resultant toward the extreme compressive fibre of the section with increasing rotation (refer to Figure 4.3d). This, however, also means that a real system cannot reach the full overturning force (λ_{ro}) and instability displacement (δ_{ru}) capacities of the idealised rigid system. Instead, the λ - δ capacity curve of the real system effectively becomes bounded by the response curve predicted using rigid body theory, as has been demonstrated through both static and dynamic experimental tests on vertically spanning walls [e.g. *Griffith et al.*, 2004; *Derakhshan et al.*, 2009].

As an analytical representation of the load-displacement behaviour of non-idealised vertically spanning walls, *Doherty et al.* [2002] proposed a trilinear elastic model (Figure 7.1) comprising of three zones: (i) initial linear elastic region, (ii) constant strength plateau, and (iii) softening branch for the equivalent rigid system. This model can be defined by four input parameters, including the overturning

Table 7.2: Empirically derived zone limiting displacements δ_1 and δ_2 for the trilinear λ - δ relationship by *Doherty et al.* [2002]. The yield displacement δ_y used in the various component hysteresis rules is taken as the average of these two values.

State of degradation at the cracked joint	δ_1	δ_2	δ_y
New	0.06	0.28	0.17
Moderate	0.13	0.40	0.27
Severe	0.20	0.50	0.35

force λ_{ro} , instability displacement δ_{ru} , and the zone limiting displacements δ_1 and δ_2 . However, while λ_{ro} and δ_{ru} can be easily calculated from statics, there are no rational means for determining displacements δ_1 and δ_2 . Instead, Doherty quantified these values empirically and presented them for three different damage states (Table 7.2). Further work on the trilinear form of the model has been carried out by *Derakhshan et al.* [2009], who proposed additional empirically derived relationships for quantifying the limiting displacement δ_2 as a function of the overburden weight ratio ψ , as well the wall slenderness ratio (t_u/H_t).

The approach proposed here to model the wall's rocking component of response is based on an elastic bilinear-softening rule, as shown by Figure 7.2a. The form of the model is slightly simpler than the trilinear representation by *Doherty et al.* [2002], in order to allow for easier merging of the rocking component with the inelastic components at a later stage (as outlined in Section 7.2.4). The model can be defined by three parameters: the rocking load and displacement capacities λ_{ro} and δ_{ru} provided in Table 7.1; in addition to either the initial stiffness κ_{ro} or yield displacement δ_{ry} (see Figure 7.2a). Unfortunately, predicting the initial stiffness of a wall after it is damaged is quite difficult, as it depends on a variety of factors including the effective material stiffness and the state of degradation in the vicinity of the cracked section. Therefore, it is proposed that the yield displacement δ_{ry} in the bilinear rule can be estimated using Doherty's empirical approach, by taking the average value of the zone limiting displacements δ_1 and δ_2 which define the trilinear model. These averaged values, denoted by δ_y , are provided in Table 7.2.

A further consideration when dealing with real wall systems is that due to the crushing strength of the material, compressive force transfer between adjacent blocks cannot occur across a point, as assumed in the rigid body idealisation, but requires a finite bearing area (refer to Figure 4.3d). Such effects have been considered in various modelling approaches for vertically spanning walls, for example that by *Derakhshan et al.* [2011]. This consequently acts to limit the internal lever arm that can be developed to resist the applied moment and means that the load and displacement capacities (λ_{ro} and δ_{ru}) in the real system become reduced relative to the idealised rigid system. In the analysis, this can effectively be taken

into account through a reduction of these capacities. For example, by adopting a rectangular stress block approach, it can be seen from Eq. (4.22) that the effective lever arm reduction factor is equivalent to

$$\phi_r = 1 - \frac{\sigma_v}{c f_{mc}}, \quad (7.21)$$

where σ_v is the average compressive stress along the section, f_{mc} is the crushing strength of the masonry (or the mortar, whichever is weaker) and c is the compressive strength factor (generally taken as 0.85 in reinforced concrete design). The factor ϕ_r can be subsequently used to reduce the nominal capacities λ_{ro} and δ_{ru} calculated using the equations in Table 7.1.

7.2.2 Horizontal Bending Frictional Component (h)

Unlike vertically spanning walls, whose response is nonlinear but elastic, the response of two-way walls contains some component of inelastic hysteresis behaviour due to the activation of frictional sources of internal resistance after cracking. This has been demonstrated through the presence of hysteresis loops in the observed load-displacement behaviour for walls tested both in the quasistatic cyclic tests and shaketable tests (Chapters 2 and 3). The primary source of this inelastic behaviour is believed to be residual horizontal bending, which generates rotational friction across the cracked bed joints present along vertical cracks.

As already discussed in Section 7.2.1, the load capacity of the rocking response component is equivalent to inclusion of only the vertical and diagonal crack lines in the energy-based load capacity calculation procedure in Chapter 6. It is therefore proposed that the resistance contribution from horizontal bending can be accounted for within the overall load-displacement model in terms of an inelastic component, whose load capacity λ_{ho} can be predicted by the approach in Chapter 6 by including only the \bar{Z}_h terms in the respective internal work equations [Eqs. (6.74), (6.78), (6.80) and (6.83) for the type K mechanisms]. The resulting λ_{ho} expressions for the various forms of type K mechanisms are provided in Table 7.3 (second column).

In the proposed approach, the load-displacement hysteresis for this component of response is modelled using the elastoplastic rule (Figure 7.2b). Due to the lack of a more sophisticated model for predicting the initial loading stiffness of a cracked masonry wall, as discussed in Section 7.2.1, it is suggested that the elastoplastic yield displacement δ_{hy} (see Figure 7.2b) could be estimated using the same simplified procedure used to estimate the yield displacement of the rocking response component, that is, according to the empirically derived δ_y limits by [Doherty *et al.*, 2002], as presented in Table 7.2.

Table 7.3: Equations for load capacities of the inelastic (frictional) components.

Mech.	Load capacity of horizontal bending rotational friction, λ_{ho}	Load capacity of OBL sliding friction, λ_{so}
K1 _x	$\lambda_{ho} = \frac{\bar{Z}_h G_n}{t_u L_e} \cdot \frac{R_{vs} (1 + 2\psi)}{\frac{2}{3} + \frac{1}{3}a + \Phi\eta\psi (1 + a)} \quad (7.22)$	$\lambda_{so} = (1 - \Phi) \frac{\mu_o \psi (1 + a)}{\frac{2}{3} + \frac{1}{3}a} \quad (7.23)$
K1 _y	$\lambda_{ho} = \frac{\bar{Z}_h G_n}{t_u L_e} \cdot \frac{R_{vs} (1 + 2\psi) + \zeta_{hi} r (r + 2\psi)}{\alpha \left(\frac{2}{3} + \frac{1}{3}r + \Phi\eta\psi \right)} \quad (7.24)$	$\lambda_{so} = (1 - \Phi) \frac{\mu_o \psi}{\frac{2}{3} + \frac{1}{3}r} \quad (7.25)$
K2 _x	$\lambda_{ho} = \frac{\bar{Z}_h G_n}{t_u L_e} \cdot \frac{2R_{vs} (1 + 2\psi)}{\frac{2}{3} + \frac{1}{3}a} \quad (7.26)$	—
K2 _y	$\lambda_{ho} = \frac{\bar{Z}_h G_n}{t_u L_e} \cdot \frac{2 (R_{vs} + \zeta_{hi} r) (1 + 2\psi)}{\alpha \left(\frac{2}{3} + \frac{1}{3}r \right)} \quad (7.27)$	—
V1	—	$\lambda_{so} = (1 - \Phi) (2\mu_o \psi) \quad (7.28)$
V2	—	—

While the overall proposed approach used to model the inelastic component of internal frictional resistance appears to be conservative based on comparison with the cyclic load-displacement curves observed through testing (refer to Section 7.3.1), it does make several simplifications of actual wall behaviour:

Firstly, friction along interlocking vertical crack lines is unlikely to be purely rotational as assumed by the model, but is expected to also have a translational component. This can be particularly true for vertical edge cracks when the direction of loading is away from the connecting return walls, in which case the main face of the wall may experience sliding away from the return walls along these boundaries. Such behaviour was observed in some of the walls tested as part of the quasistatic cyclic experimental study, especially once they underwent a sufficient number of repeated cycles at large deformations (refer to Figures 2.26–2.28). Nonetheless, a translational mode of frictional slip along these cracks is likely to be associated

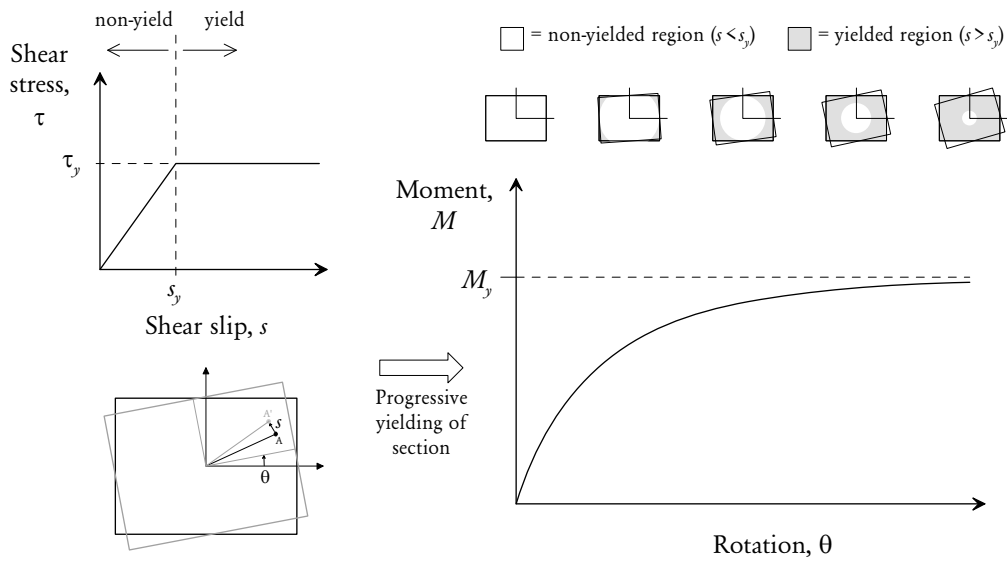


Figure 7.3: Curvilinear asymptotic $M-\theta$ behaviour of frictional torsion along a rectangular section, resulting from using an elastoplastic constitutive $\tau-s$ relationship for friction along the cracked interface.

with a higher load resistance than the rotational representation used, and on this basis, the model is expected to be conservative. Furthermore, comparisons of the predicted inelastic resistance with the cyclic load-displacement curves (refer to Section 7.3.1) suggest that the model underpredicts the inelastic load capacity.

Secondly, if we were to make the seemingly reasonable assumption of defining friction across the cracked bed-joint interface using an elastoplastic relationship between shear stress and shear slip ($\tau-s$), then the resulting moment versus rotation behaviour of the joints will become curvilinear, since a section subjected to increasing rotation would yield gradually rather than simultaneously (Figure 7.3). This would also cause the corresponding inelastic resistance component of the wall’s load-displacement behaviour to be curvilinear and asymptotic toward the maximum attainable strength λ_{ho} , and not strictly elastoplastic as assumed in the proposed modelling approach (Figure 7.2b). Nonetheless, the simplifying assumption of an elastoplastic representation for the load-displacement response seems a reasonable one, as long as an appropriate or conservative estimate of the equivalent yield displacement can be made.

Finally, the suggested approach for estimating the yield displacement δ_{hy} using the limits derived by Doherty (Table 7.2) is also very simplistic and does not properly account for the influence of the wall’s various physical properties. For example, consider two walls with identical L and H dimensions but varying thickness. If we assume frictional resistance across the cracked joint to have an

elastoplastic constitutive τ - s relationship (Figure 7.3), then the thicker wall would be expected to achieve yield² at a smaller crack rotation and therefore have a smaller yield displacement than the thinner wall. This is the opposite effect to that resulting from the simplified approach based on Doherty's yield displacement limits, which suggests that yield occurs at a constant value of δ and therefore at a larger displacement (Δ) for a thick wall compared to a thin one. As a second example, consider two walls with equal thickness and L/H aspect ratio, but different L and H spans. Since both walls would be expected to have the same yield rotation due to identical thickness, the longer wall should have a larger yield displacement than the shorter wall. The simplified approach, however, predicts both walls to have the same yield displacement. While the use of Doherty's displacement limits is expected to be conservative for most typical wall configurations (i.e. they will overestimate the yield displacement), these examples demonstrate the need for development of a more rational mechanics-based approach for predicting the initial loading stiffness and yield displacement of cracked walls.

As a final remark, it should be noted that for design or assessment purposes, it may be warranted to apply a capacity reduction factor to the nominal capacity λ_{ho} calculated using the equations in Table 7.3. This is to account for issues such as:

- The torsional friction mode of resistance not reaching its full capacity due to dilation effects, as described by *Casapulla* [2008]; and
- In the case of walls built with mortar, the cracks will generally exhibit a mixture of stepped and line failure, and only the stepped portions of the crack can contribute to the residual moment capacity. These effects were dealt with in Chapter 5, where a probabilistic methodology was developed for estimating the expected likelihood of stepped failure. It is suggested that the resulting parameter could be used as a capacity reduction factor for this purpose.

7.2.3 Overburden Load Frictional Sliding Component (s)

As discussed in Section 6.3.2, it is possible for a wall to benefit from an additional source of resistance due to friction between the wall and an OBL. In order for this resistance to be activated, a frictional connection must be present between the wall and OBL, and the OBL itself must be restrained against lateral movement

²Note that in this context, 'yield' can be interpreted as the instance at which yield slip is achieved at a particular percentile of the cracked interface (or by some other similar definition), since as noted by the previous point, the M - θ curve based on an elastoplastic τ - s relationship can merely asymptote toward the maximum attainable moment and never actually reach it (Figure 7.3).

(hence $\Phi = 0$; see Figure 6.5a). Nonetheless, the frictional connection must be sufficiently weak to enable the top edge to undergo lateral displacement (i.e. a type-1 mechanism). Establishing whether a wall with a frictional top connection will undergo a type-1 mechanism (in which the top edge is effectively unrestrained) or type-2 mechanism (where the top edge is restrained against movement) can be aided by the flowchart in Figure 6.4 together with the concepts provided in the accompanying discussions in Section 6.3.2.

While the boundary conditions necessary to generate these effects were not present in any of the walls tested as part of the experimental studies in Chapters 2 and 3, allowing for them was catered for in the analytical approach for calculating the collapse load multiplier, as described in Chapter 6. Therefore, for completeness and consistency, allowance for these effects is also made in the proposed load-displacement model through the λ_s term in Eq. 7.1. It is emphasised, however, that inclusion of this source of resistance should be treated with caution due to uncertainties regarding the choice of an appropriate value of the friction coefficient μ_o , as well as the need to ensure that frictional contact between the wall and OBL exists for a sufficient range of wall deformation.

Due to the frictional nature of this resistance component, it is suggested that it may be modelled using an elastoplastic hysteresis rule (Figure 7.2c). Two alternative but equivalent approaches may be used to calculate the component's load capacity λ_{s0} :

1. Either the energy approach described in Chapter 6, which will provide the corresponding load resistance contribution when only the μ_o -based terms are included (i.e. the \bar{Z}_v and \bar{Z}_h terms omitted) in the respective internal work equations [Eqs. (6.74), (6.78), (6.80) and (6.83) for the type K mechanisms];
2. Or the statics-based approach used to derive capacity expressions for the rocking response component, as per the derivations presented in Appendix H.1.

It can be easily demonstrated that both approaches produce equal values of load capacity. The resulting analytical expressions to calculate λ_{s0} for mechanisms K1_x, K1_y and V1 are provided in the third column of Table 7.3.

As already discussed in Sections 7.2.1 and 7.2.2, in the absence of a more rational analytical model for predicting the initial loading stiffness, it is suggested that Doherty's empirically derived δ_y limits (Table 7.2) can be used to estimate the equivalent yield displacement δ_{sy} in the corresponding elastoplastic rule (Figure 7.2c). Note, however, that there is no justifiable reason for the use of these limits for this particular purpose, except that they are likely to be conservative.

7.2.4 Complete Model

As per Eq. (7.1), the complete hysteresis model is obtained by superimposing the load contributions from the elastic rocking component, modelled by the bilinear softening rule (Figure 7.2a); and the two inelastic frictional components, modelled by elastoplastic rules (Figures 7.2b and 7.2c). The general shape of the overall hysteresis model is shown by Figure 7.4.

Merged Frictional Component (f)

At this point, it becomes convenient to reduce the complexity of the overall model by merging of the two inelastic components (h and s) into a single elastoplastic component (f) that accounts for all frictional sources present. The primary reason for this is to reduce the total number of parameters required to define the overall model and also enable ductility to be defined with respect to a single yield displacement.³

The effective yield displacement of the merged frictional rule can be calculated as the weighted average of the yield displacements for the individual components, using their respective force capacities as weighting factors:

$$\delta_{fy} = \frac{\sum \lambda_o \delta_y}{\sum \lambda_o} = \frac{\lambda_{ho} \delta_{hy} + \lambda_{so} \delta_{sy}}{\lambda_{ho} + \lambda_{so}}. \quad (7.29)$$

This calculation ensures that the total energy dissipated by the merged rule is equivalent to the energy dissipated by each of the inelastic components considered separately.

The force capacity of the combined frictional component hence becomes

$$\lambda_{fo} = \lambda_{ho} + \lambda_{so}. \quad (7.30)$$

Capacity Envelope

The capacity envelope of the overall model is obtained by superimposing the respective envelopes of the rocking and frictional components, as demonstrated in Figure 7.4. If we assume a single yield displacement δ_y for both components, as shown in the figure, then a bilinear envelope will be formed, whose segments are

³This condition is already ensured if one follows the simplified treatment suggested in Sections 7.2.1–7.2.3, whereby the yield displacement for each rule is taken according to Doherty's empirical δ_y limits given in Table 7.2.

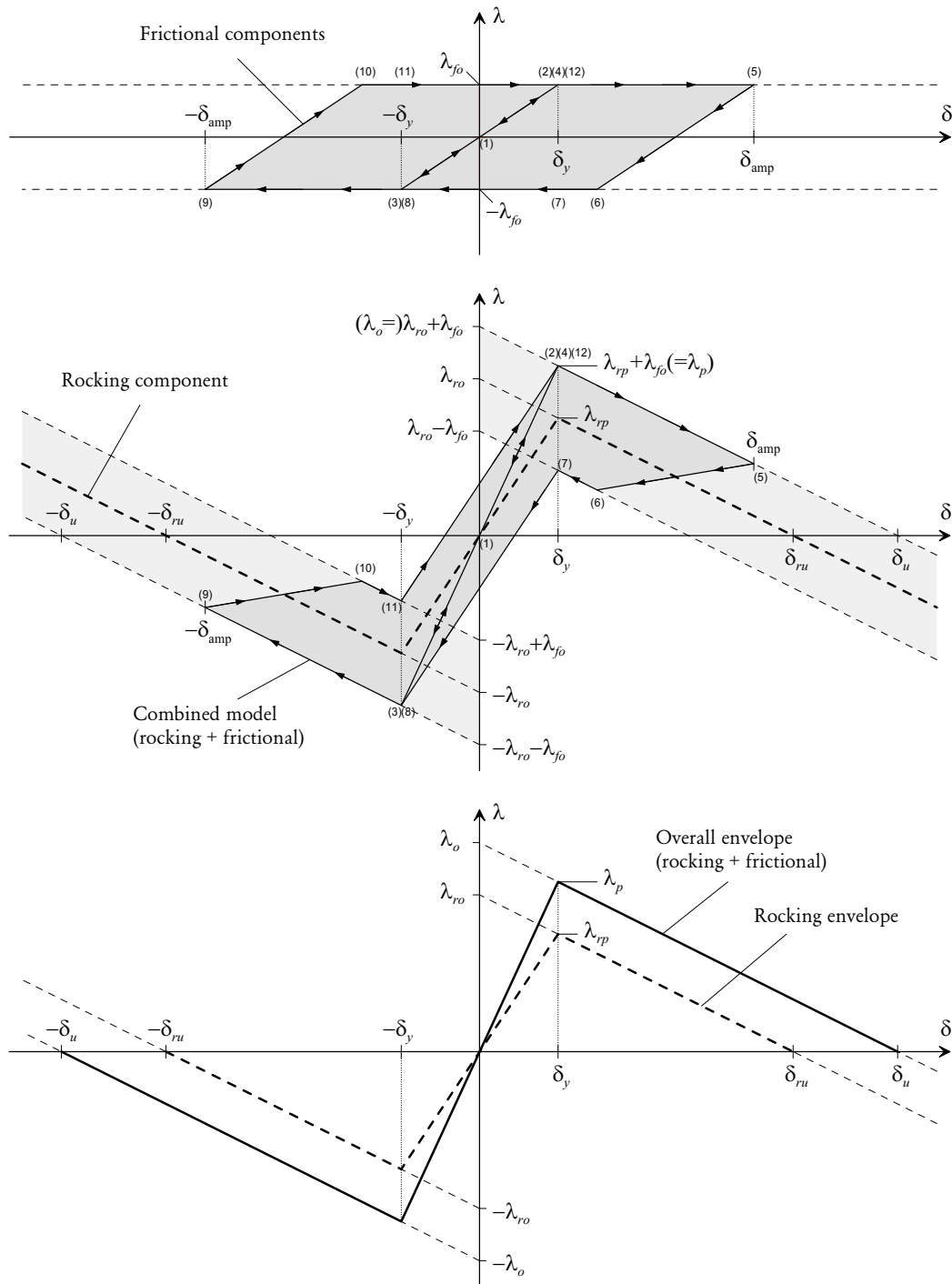


Figure 7.4: Complete load-displacement model obtained by superposition of the rocking and frictional components. In the representation shown, the yield displacements of the rocking and frictional components are assumed to be equal ($\delta_y = \delta_{ry} = \delta_{fy}$). Initiating from the resting position (1), response will remain linear elastic as long as the displacement does not venture beyond $\pm \delta_y$, i.e. remains inside the yield limits (2) and (3). Points (4)–(12) demonstrate a closed loop generated for a cycle with displacement amplitude $\pm \delta_{amp}$.

calculated according to the formulae

$$\lambda\langle\delta\rangle = \begin{cases} \lambda_p (\delta/\delta_y) & \text{for } \delta \leq \delta_y \text{ (ascending branch),} \\ \lambda_{ro} (1 - \delta/\delta_{ru}) + \lambda_{fo} & \text{for } \delta > \delta_y \text{ (softening branch).} \end{cases} \quad (7.31)$$

When the yield displacements of the components do not coincide, the envelope will have additional segments with progressive softening. In such an instance, a refined process can be employed to determine the points connecting the envelope line segments.

It can also be seen from Figure 7.4 and Eq. (7.31) that due to the inclusion of the frictional component, the combined envelope will have an overall instability displacement δ_u which is greater than that of the rocking component ($\delta_u > \delta_{ru}$). Whether or not one is willing to treat this increased displacement capacity as a reliable measure of the maximum displacement capacity of the wall depends on the judgement of the analyst, as it is difficult to say if these frictional components can be trusted to provide a continuous load resistance equal to their capacity at large displacements. Certainly at the current stage of research there is still a lack of experimental data to be able to make this assumption with confidence. A more conservative approach might be to treat the rocking instability displacement δ_{ru} as the maximum usable wall displacement capacity.

Peak Force Resistance

As already stated, the collapse load multiplier λ_o (dealt with in Chapter 6) is equivalent to summing the nominal capacities of the three components:

$$\lambda_o = \lambda_{ro} + \lambda_{ho} + \lambda_{so}, \quad (7.32)$$

where λ_{ro} , λ_{ho} and λ_{so} are determined according to expressions provided in Tables 7.1 and 7.3. However, it is obvious from both Figures 7.2a and 7.4 that because the proposed model treats the λ - δ behaviour of the rocking component as having an initial linear elastic zone, the peak attainable load in the overall model will always be lower than λ_o .

The peak force, λ_{rp} , of the bilinear rocking component (Figure 7.2a), occurring at the yield point, is

$$\lambda_{rp} = \lambda_{ro} (1 - \delta_{ry}/\delta_{ru}). \quad (7.33)$$

Therefore, the peak load in the overall capacity envelope (Figure 7.4) becomes

$$\lambda_p = \lambda_{rp} + \lambda_{fo}. \quad (7.34)$$

Note that this assumes that the individual components have an equal yield displacement, or at least that $\delta_{hy} \leq \delta_{ry}$ and $\delta_{sy} \leq \delta_{ry}$. Otherwise, the overall peak load capacity λ_p can be determined by considering the various cases possible.

7.3 MODEL VALIDATION USING EXPERIMENTAL DATA

To verify the accuracy of the proposed load-displacement model (described in Section 7.2), the predicted theoretical response was compared to measured behaviour of two-way walls tested experimentally. Three separate test data sets were considered: (i) the eight full-scale walls from quasistatic cyclic tests in Chapter 2, (ii) the five half-scale walls from the shaketable tests in Chapter 3, and (iii) three small-scale dry-stack masonry (DSM) walls tested by the author in a previous study [Vaculik *et al.*, 2003]. All of these walls underwent type K mechanism response during testing.

For each wall considered, the rocking load and displacement capacities λ_{ro} and δ_{ru} , and the horizontal bending load capacity λ_{ho} , were calculated based on the respective type K mechanisms using the formulae in Tables 7.1 and 7.3. None of the walls were provided with a frictional top edge connection, and hence the s-component described in Section 7.2.3 was not applicable. Detailed summaries of the analyses performed on each set of walls are presented throughout Tables 7.4, 7.5 and 7.6, including the computed capacities as well as various input properties and parameters calculated at intermediate steps during the analyses. Graphical comparisons between the predicted model response and experimental behaviour are provided by Figures 7.5, 7.6 and 7.7.

The key aspects of the analyses conducted are as follows:

- For each solid wall (i.e. without any openings), the length and height spans of the mechanism were taken according to the full dimensions of the wall. Therefore, the mechanism type (K1_x, K1_y, K2_x or K2_y) was immediately defined from the start of each analysis.
- Since the equations in Tables 7.1 and 7.3 are only strictly applicable to solid walls, two different approaches were used to analyse walls with openings: The first approach ignored the presence of any openings and treated the wall as being entirely solid. The second approach treated the wall as having a free vertical edge at the boundary between the wall and opening. In the latter treatment, only the longer side of the wall was analysed since this results in the more conservative (lower) capacities. Illustrations of the respective mechanisms used are also shown in Figures 7.5, 7.6 and 7.7. In

both treatments, the mechanism utilised the full available length and height of the wall.

Comparisons of the model and experimental behaviour will now be discussed for each set of walls.

7.3.1 Full-Scale Mortar-Bonded URM Walls s1–s8

This data set comprised the eight full-scale walls subjected to cyclic loading using airbags, as reported in Chapter 2. As discussed in Section 2.4.2, a notable aspect of the measured load-displacement behaviour of these walls (Figures 2.14–2.21) was the positive stiffness (slope) of the loading branches irrespective of the cyclic displacement amplitude or the degradation state of the wall. This was attributed to internal arching within the wall, which constitutes an additional source of resistance that is not accounted for in the proposed load-displacement model. Because of this behaviour, the walls did not possess a distinct value of residual strength that could be used for direct comparison to the values of strength predicted by the model. It therefore becomes more convenient to compare the observed and predicted response graphically.

Table 7.4 summarises the analysis results, while Figure 7.5 provides a graphical comparison of the predicted model response and experimental behaviour. On the basis of these results, the following conclusions can be made:

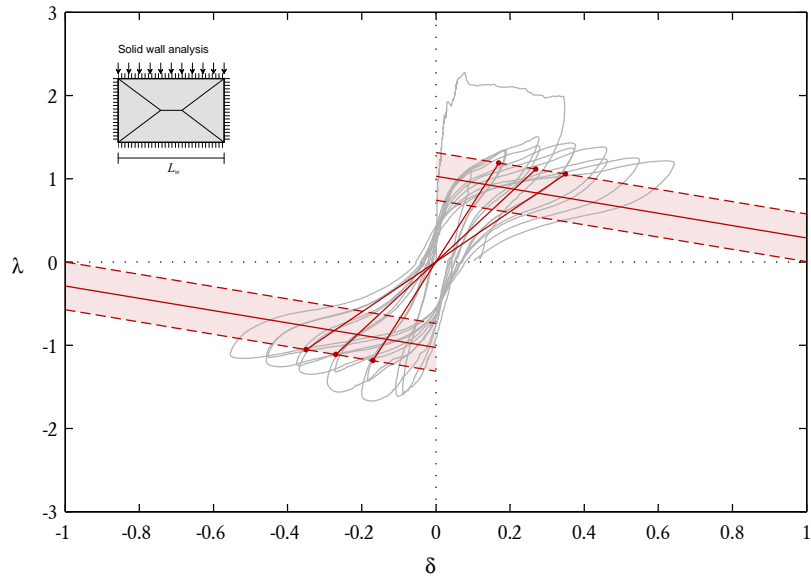
1. The model provides a conservative representation of each wall's F - Δ capacity envelope over the full range of displacement considered. It is worth emphasising that the analytically computed capacities presented are unfactored, in that they do not account for any of the additional capacity reduction effects that were discussed in Sections 7.2.1 and 7.2.2. Such factorisation would result in even further conservatism of the results. The discrepancy between the analytical model and experimental behaviour is believed to be primarily due to the presence of arching effects within the test walls.
2. The model appears to underpredict the inelastic capacity of the walls, as can be seen by comparing the hysteresis loops within the experimental response to the upper and lower bounds of the model ($\lambda_r \pm \lambda_{ho}$, shown using dashed lines in Figure 7.5). This is also likely to be due to arching effects, which induce additional compressive stresses throughout the wall and therefore generate a greater capacity to resist friction. Furthermore, the walls are also likely to experience additional frictional resistance from bed joint torsion along diagonal crack lines, particularly at small rotations before the cracks

Table 7.4: Details of analyses performed on quasistatic test walls s1–s8 (from Chapter 2).

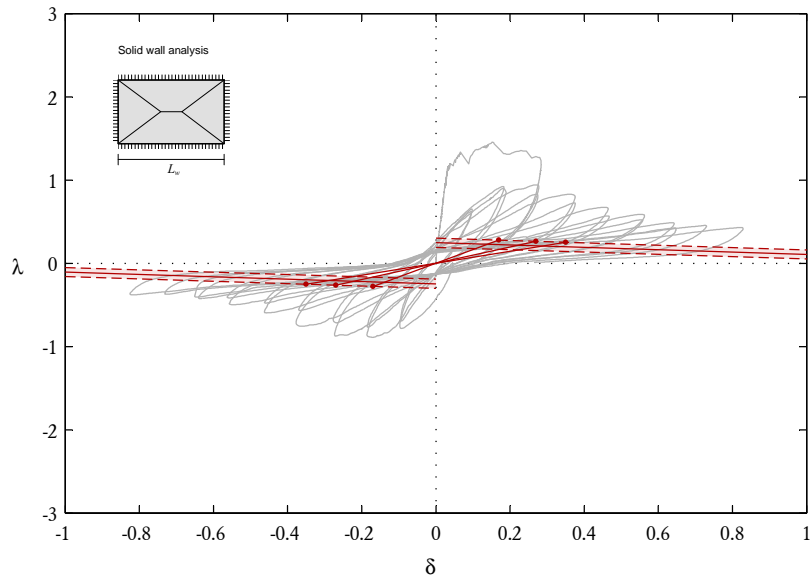
Wall	Treatment*	Input parameters				Intermediate variables							Calculated capacities					
		L_t [mm]	H_t [mm]	σ_{vo} [MPa]	ϵ	R_{os}	L_e [mm]	H_e [mm]	β	α	a	r	ψ	ζ_{hi}	Mech.	δ_{ru}	λ_{ro}	λ_{ho}
s1, s3	solid	4080	2494	0.1	0.5	1	2040	1247	1.64	1.17	0.15	-	2.11	-	K2 _x	1.39	1.03	0.29
s3	longer side	2220	2494	0.1	0.5	1	2220	1247	1.78	1.28	0.22	-	2.11	-	K2 _x	1.31	0.99	0.25
s4	solid	4080	2494	0.05	0.5	1	2040	1247	1.64	1.17	0.15	-	1.06	-	K2 _x	1.45	0.64	0.17
s4	longer side	2220	2494	0.05	0.5	1	2220	1247	1.78	1.28	0.22	-	1.06	-	K2 _x	1.37	0.62	0.15
s2, s5	solid	4080	2494	0	-	1	2040	1247	1.64	1.17	0.15	-	0	-	K2 _x	1.74	0.25	0.05
s5	longer side	2220	2494	0	-	1	2220	1247	1.78	1.28	0.22	-	0	-	K2 _x	1.64	0.24	0.05
s6	solid	4080	2494	0	-	1	2040	2494	0.82	0.59	-	0.41	0	1	K1 _y	2.12	0.16	0.05
s6	longer side	2220	2494	0	-	1	2220	2494	0.89	0.64	-	0.36	0	0	K1 _y	2.14	0.15	0.04
s7	solid	2520	2494	0.1	0.5	1	1260	1247	1.01	0.72	-	0.28	2.11	1	K2 _y	1.60	1.34	0.77
s7	longer side	660	2494	0.1	0.5	1	660	1247	0.53	0.38	-	0.62	2.11	0	K2 _y	1.60	2.22	1.91
s8	solid	2520	2494	0	-	1	1260	1247	1.01	0.72	-	0.28	0	1	K2 _y	2.00	0.32	0.15
s8	longer side	660	2494	0	-	1	660	1247	0.53	0.38	-	0.62	0	0	K2 _y	2.00	0.53	0.37

*Input constants*Unit geometry: $t_u = 230$ mm, $t_u = 110$ mm, $h_u = 76$ mm, $t_j = 10$ mmMaterial properties: $\gamma = 19 \times 10^{-6}$ N/mm³, $\mu_m = 1.037$ *Dependent constants*Natural diagonal slope: $G_n = 0.7167$ Bed joint overlap: $s_b = 110$ mm; Overlap ratio: $r_o = 1$; Plastic torque coefficient: $k_{bp} = 0.3826$ Moment moduli: $Z_o = 6050$ mm², $Z_h = 6140$ mm²

*Refers to the treatment used for walls with openings: In the 'solid' treatment any openings present were entirely ignored. In the 'longer side' treatment, the wall was treated as if it had a free vertical edge at the boundary of the opening.

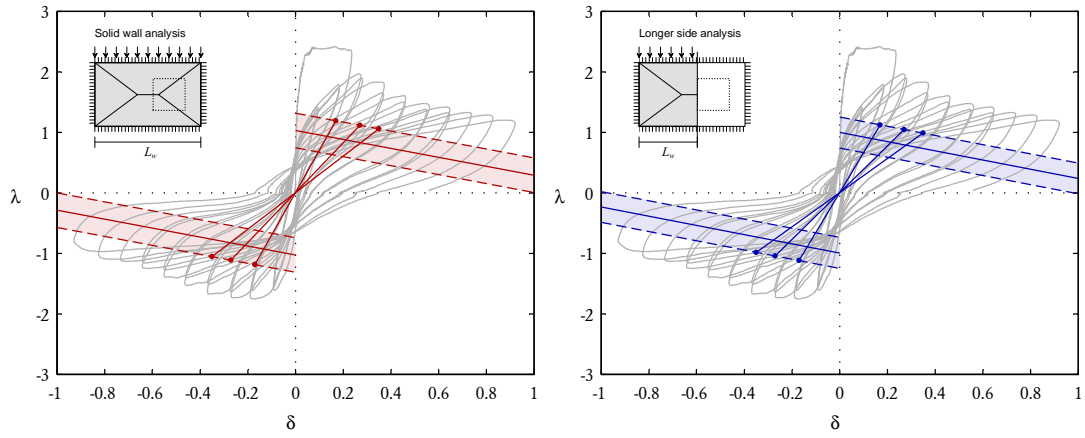


(a) Wall s1

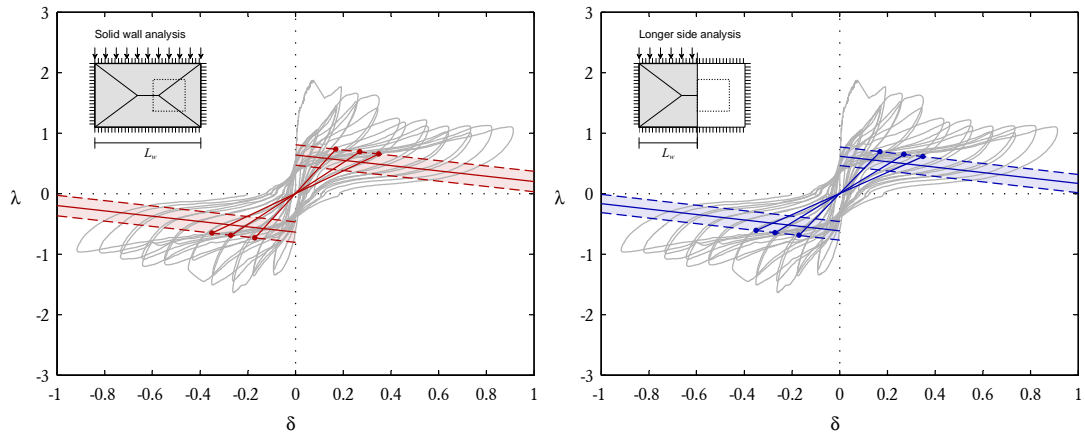


(b) Wall s2

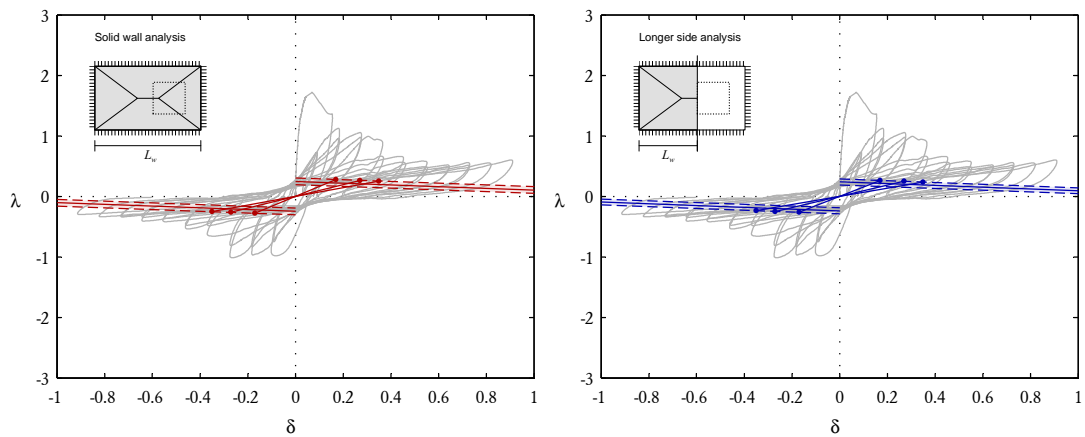
Figure 7.5: Comparison of theoretical behaviour and experimental response for quasistatic cyclic test walls s1–s8. The predicted rigid body rocking component (λ_r) is indicated by a coloured (red or blue) solid line (—). Response inclusive of the additional inelastic contribution from horizontal bending ($\lambda_r \pm \lambda_{h0}$) is shown by dashed lines (---) for the forward and reverse loading directions. The resulting bounded area (shaded) represents the energy dissipated under reversed cyclic loading. Initial loading branches based on Doherty’s empirical δ_y limits are also shown for the three different damage states (Table 7.2).



(c) Wall s3

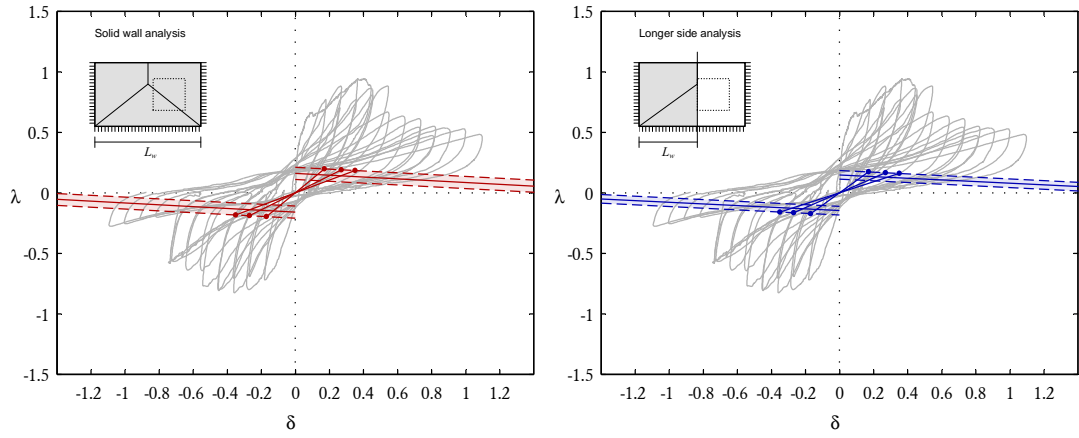


(d) Wall s4

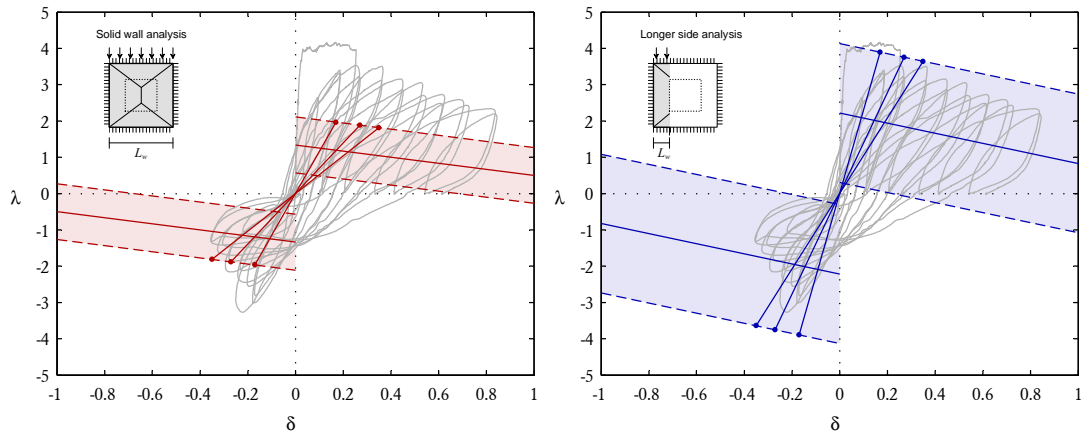


(e) Wall s5

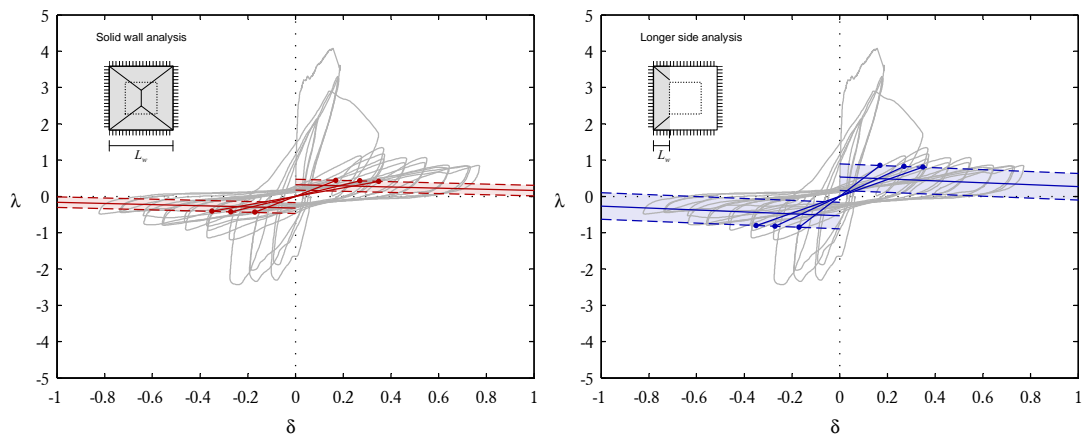
Figure 7.5: (cont'd).



(f) Wall s6



(g) Wall s7



(h) Wall s8

Figure 7.5: (cont'd).

become fully opened. This type of resistance is not accounted for in the model, which instead assumes diagonal cracks to undergo purely elastic rocking behaviour.

3. Differences between capacities predicted for walls with openings using the two alternative approaches (solid wall analysis and longer edge analysis) are relatively minor for walls s3, s4, s5 and s6, but somewhat more pronounced in walls s7 and s8. This relates to the value of the effective mechanism length (L_e) used in the respective analyses (refer to Table 7.4). It is suggested that an alternative and possibly more accurate approach to the analysis of walls with openings would be to use the refined virtual work treatment described in Section 4.4 to calculate the load capacities λ_{ro} and λ_{ho} , while still using the rigid body rocking relationships in Table 7.1 to determine the rocking instability displacement δ_{ru} .
4. Finally, for this set of walls the initial loading branches obtained using Doherty's empirical δ_y limits appear to be conservative, in that the approach underpredicts the loading stiffness of the walls.

7.3.2 Half-Scale Mortar-Bonded URM Walls D1–D5

This data set included the five half-scale walls tested by shaketable, as reported in Chapter 3. The corresponding analytical results are summarised in Table 7.5, while Figure 7.6 compares the model's theoretical response to the experimental behaviour graphically. The experimental response plotted by each graph represents the load and displacement coordinates for the largest amplitude cycles occurring within individual test runs performed on each wall (refer to Figure 3.17 and Section 3.4.3).

It is difficult to draw conclusions from these comparisons because of the relatively small wall deformations achieved in the tests. As discussed in Chapter 3, this was due to the limitation of the experimental setup, in particular the inability of the shaketable to generate stronger motions. It could be concluded, however, that in the range of wall deformations produced, the model appears to provide a conservative lower bound estimate of the experimental response.

7.3.3 Small-Scale DSM Walls F8–F10

This set of data comprised three reduced-scale DSM walls tested by the author in a previous study [Vaculik *et al.*, 2003] (some detail also reported in Vaculik *et al.*, 2004). The brick units used to build these walls were obtained by cutting standard brick paving units lengthwise using a circular saw. This cutting process introduced

Table 7.5: Details of analyses performed on dynamic test walls D1–D5 (from Chapter 3).

Wall	Treatment*	Input parameters				Intermediate variables							Calculated capacities					
		L_t [mm]	H_j [mm]	σ_{70} [MPa]	ϵ	R_{us}	L_e [mm]	H_e [mm]	β	α	a	r	ψ	ζ_{hi}	Mech.	δ_{ru}	λ_{ro}	λ_{ho}
D1, D3	solid	1840	1232	0.1	0.5	1	920	616	1.49	1.14	0.13	-	3.83	-	K2 _x	1.38	1.55	0.27
D3	longer side	949	1232	0.1	0.5	1	949	616	1.54	1.18	0.15	-	3.83	-	K2 _x	1.35	1.53	0.26
D4	solid	1840	1232	0.05	0.5	1	920	616	1.49	1.14	0.13	-	1.92	-	K2 _x	1.43	0.89	0.15
D4	longer side	949	1232	0.05	0.5	1	949	616	1.54	1.18	0.15	-	1.92	-	K2 _x	1.39	0.88	0.15
D2, D5	solid	1840	1232	0	-	1	920	616	1.49	1.14	0.13	-	0	-	K2 _x	1.78	0.23	0.03
D5	longer side	949	1232	0	-	1	949	616	1.54	1.18	0.15	-	0	-	K2 _x	1.74	0.23	0.03

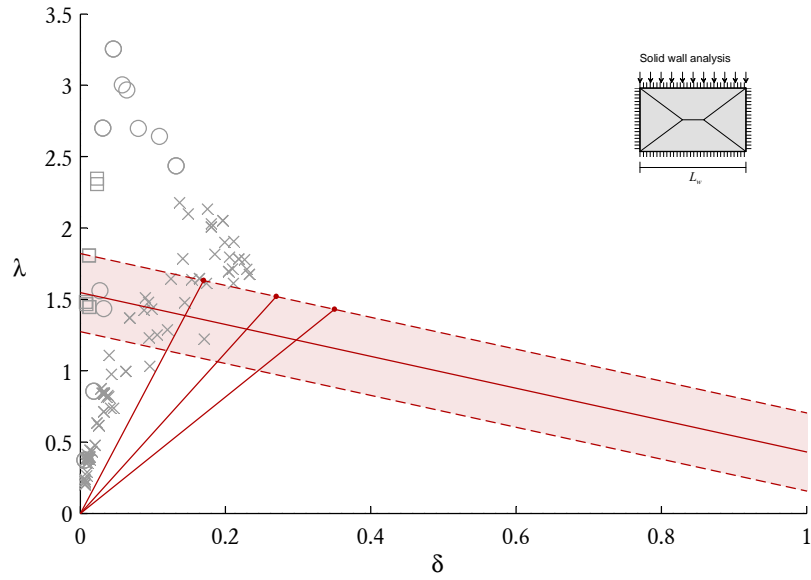
Input constants

Unit geometry: $l_u = 110$ mm, $t_u = 50$ mm, $h_u = 39$ mm, $t_j = 5$ mm
 Material properties: $\gamma = 21.17 \times 10^{-6}$ N/mm³, $\mu_m = 0.576$

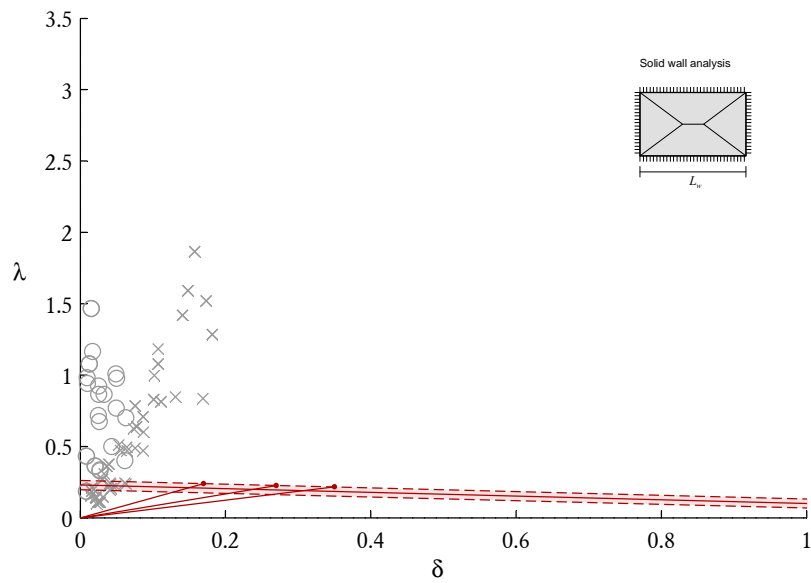
Dependent constants

Natural diagonal slope: $G_H = 0.7652$
 Bed joint overlap: $s_b = 52.5$ mm; Overlap ratio: $r_o = 1.05$; Plastic torque coefficient: $k_{bp} = 0.4118$
 Moment moduli: $Z_v = 1250$ mm²; $Z_h = 674$ mm²

*Refers to the treatment used for walls with openings: In the 'solid' treatment any openings present were entirely ignored. In the 'longer side' treatment the wall was treated as if it had a free vertical edge at the boundary of the opening.

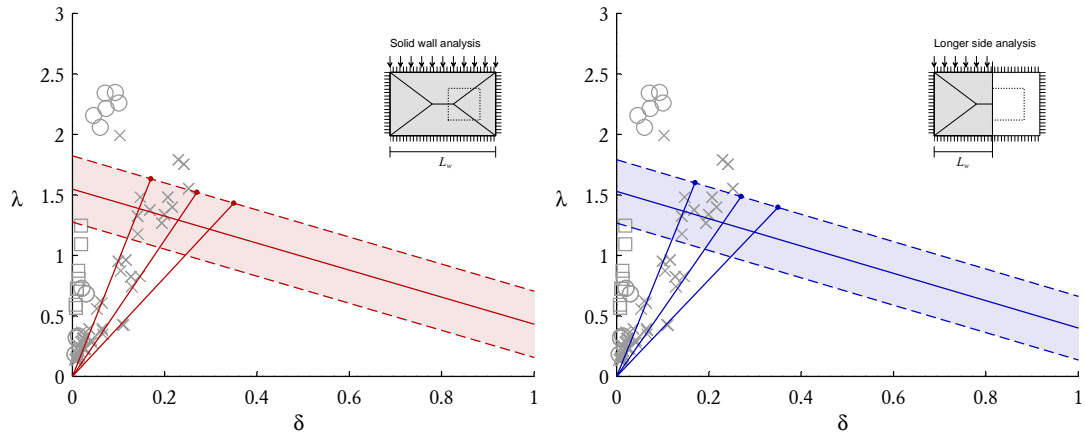


(a) Wall D1

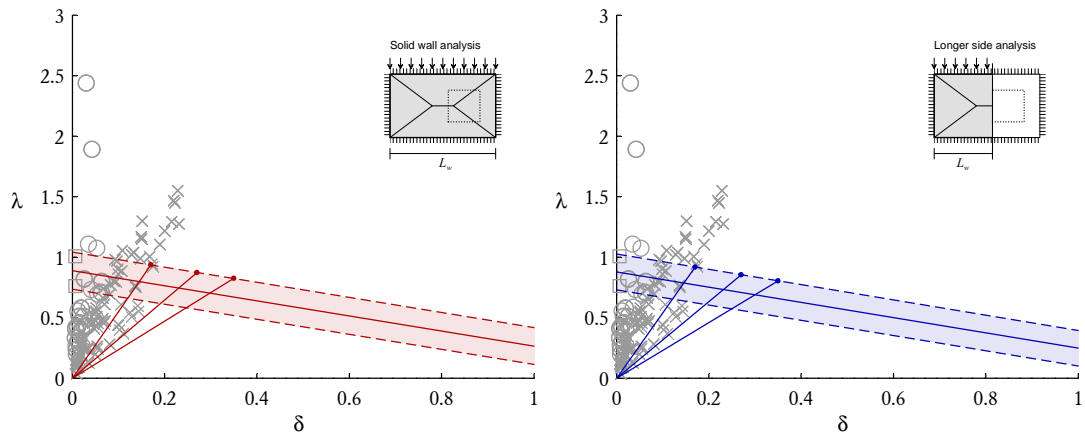


(b) Wall D2

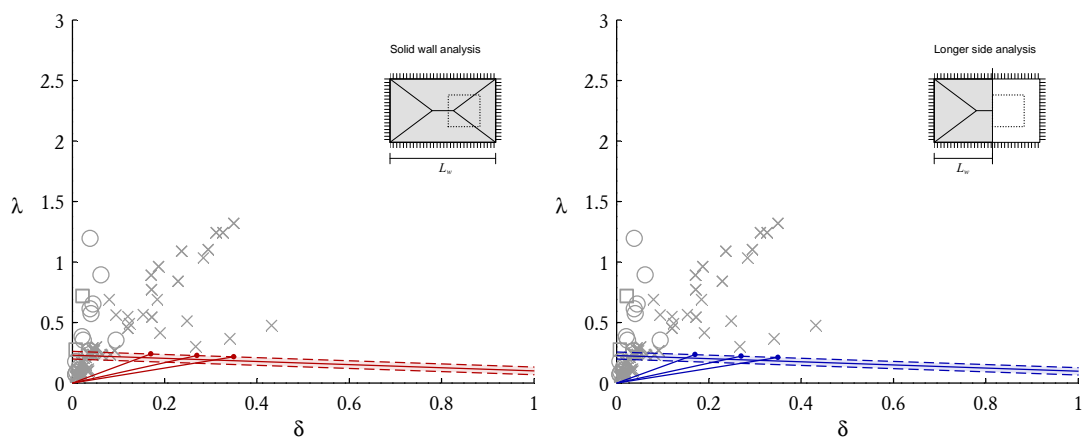
Figure 7.6: Comparison of theoretical behaviour and experimental response for shaketable test walls D1–D5. The experimental response, shown using grey markers, corresponds to the largest amplitude cycles measured during individual test runs (refer to Figure 3.17; marker legend defined in Table 3.6).



(c) Wall D3



(d) Wall D4



(e) Wall D5

Figure 7.6: (cont'd).

irregularities in the shape of the brick units, and consequently, the walls could be considered representative of very poor quality masonry construction. Loading of the walls was conducted in displacement control using airbags. The test procedure consisted of subjecting the wall to some displacement and then unloading, which was generally repeated a few times in order to study the walls' hysteretic behaviour. During the course of testing, the maximum displacements imposed on the walls were fairly large, ranging between approximately $0.5 < \max \delta < 1$. A total of three walls were tested, each at three different levels of vertical precompression.

A summary of the basic calculations to obtain nominal capacities using the equations in Tables 7.1 and 7.3 is presented in Table 7.6. The nominal load capacities λ_{r0} and λ_{h0} were further factored to account for the fact that airbags used did not cover the entire wall face, but were instead concentrated toward the centre of the wall. These load modification factors were computed using the virtual work approach as the ratio of the average virtual displacements along the loaded area in the two respective loading scenarios. Note that, unlike the load capacities, the positioning of the airbags does not affect the rocking displacement capacity δ_{ru} , as this is based on the stability criterion at zero applied load. A summary of the modified load capacities, including comparison to the peak measured load during the experiments, is given in Table 7.7. Graphical comparison of the predicted model response incorporating the modified load capacities and the experimentally measured load-displacement behaviour is presented in Figure 7.7.

From Figure 7.7 it can be seen that the experimental response of the walls is highly hysteretic (inelastic), indicating that some modes of frictional resistance were activated. Each of the experimental curves clearly exhibits a peak load followed by a softening branch, which is consistent with the general form of the proposed load-displacement model. On the basis of this observation, it appears that any arching in these walls was minimal, in stark contrast to the response of the full-scale walls where arching effects were significant (Section 7.3.1). The difference in this behaviour is likely to result from the different type of masonry used for these two sets of walls, that is, dry stack masonry as opposed to mortar-bonded masonry.

Interestingly, the calculated load capacities overpredict the measured strength for every one of these walls. This is believed to be a result of the poor quality of masonry construction, as stated previously. As seen from Figure 7.1, in the trilinear load-displacement model by *Doherty et al.* [2002], the ratio of the peak load of the real system to the idealised rigid body load capacity is effectively $1 - \delta_2$. Therefore, from Doherty's empirically derived δ limits (Table 7.2) this ratio would be expected to be approximately 50% for severely degraded masonry, which is comparable to the values quantified (Table 7.7). It should also be noted that the vertical edges

Table 7.6: Details of analyses performed on half-scale dry-stack masonry test walls F8–F10 [from *Vaculik et al., 2003*].

Wall	Treatment*	Input parameters				Intermediate variables						Calculated capacities						
		L_t [mm]	H_t [mm]	σ_{vo} [MPa]	ϵ	R_{os}	L_c [mm]	H_c [mm]	β	α	a	r	ψ	ζ_{hi}	Mech.	δ_{ru}	λ_{ro}	λ_{ho}
F8	solid	2180	960	0.036	0.5	1	1090	480	2.27	1.18	0.16	-	1.86	-	K2 _x	1.39	1.21	0.20
				0.046									2.37			1.37	1.45	0.24
				0.066									3.40			1.35	1.95	0.33
F9	solid	1720	960	0.034	0.5	1	860	480	1.79	0.93	-	0.07	1.75	1	K2 _y	1.61	1.29	0.28
				0.055									2.84			1.57	1.87	0.42
				0.080								4.13			1.55	2.56	0.58	
F10	solid	1950	750	0.028	0.5	1	975	375	2.60	1.36	0.26	-	1.85	-	K2 _x	1.27	1.47	0.21
				0.050									3.30			1.24	2.31	0.34
				0.072									4.75			1.23	3.16	0.47

Input constants

Unit geometry: $l_u = 115$ mm, $t_u = 55$ mm, $h_u = 30$ mm, $t_j = 0$ mm

Material properties: $\gamma = 20.2 \times 10^{-6}$ N/mm³, $\mu_m = 0.761$

Dependent constants

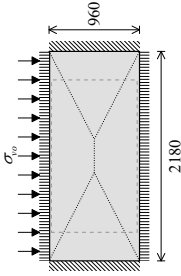
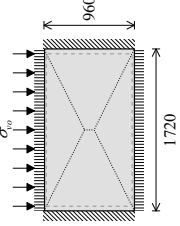
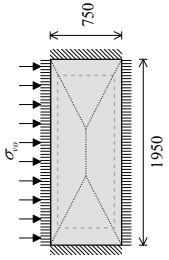
Natural diagonal slope: $G_n = 0.5217$

Bed joint overlap: $s_b = 57.5$ mm; Overlap ratio: $r_o = 1.045$; Plastic torque coefficient: $k_{bp} = 0.4091$

Moment moduli: $\bar{Z}_v = 1513$ mm²; $\bar{Z}_h = 1727$ mm²

*Refers to the treatment used for walls with openings: In the 'solid' treatment any openings present were entirely ignored. In the 'longer side' treatment, the wall was treated as if it had a free vertical edge at the boundary of the opening.

Table 7.7: Summary of the experimental method and results in the study by *Vaculik et al. [2003]*, including modification of the predicted capacities to account for non-uniformity of the applied load in the tests.

Wall	Configuration*		Wall/Mech dimensions		Airbag dimensions		Axial loading		Peak measured strength λ_{test}	Nominal predicted capacities [†]		Modified predicted load capacities [‡]		Peak strength ratios		
	L_w [mm]	H_w [mm]	L [mm]	H [mm]	σ_{vo}	ψ	λ_{ro}	δ_{tu}		λ_{ro}	mod factor	λ_{ho}	λ_{ro}	λ_{ho}	$\frac{\lambda_{test}}{\lambda_{ro}}$	$\frac{\lambda_{test}}{\lambda_{ro} + \lambda_{ho}}$
F8	2180	960	1600	900	0.036	1.86	1.21	1.39	0.24	1.21	1.39	0.92	0.15	0.26	22%	
					0.046	2.37	1.45	1.37	0.38	1.45	1.37	1.11	0.18	0.34	29%	
					0.066	3.40	1.95	1.35	0.48	1.95	1.35	1.48	0.25	0.32	27%	
																
F9	1720	960	1600	900	0.034	1.75	1.29	1.61	0.58	1.29	1.61	1.14	0.25	0.51	42%	
					0.055	2.84	1.87	1.57	0.55	1.87	1.57	1.64	0.37	0.34	27%	
					0.080	4.13	2.56	1.55	0.83	2.56	1.55	2.25	0.51	0.37	30%	
																
F10	1950	750	1600	600	0.028	1.85	1.47	1.27	0.57	1.47	1.27	1.08	0.15	0.53	46%	
					0.050	3.30	2.31	1.24	0.80	2.31	1.24	1.70	0.25	0.47	41%	
					0.072	4.75	3.16	1.23	1.13	3.16	1.23	2.33	0.34	0.49	42%	
																

*Dashed outline indicates airbag coverage during testing.

[†]Nominal capacities were calculated using the equations in Tables 7.1 and 7.3, which assume uniform loading over the entire wall face.

[‡]Modified capacities account for airbag loading being concentrated nearer to the centre of the wall, and are obtained as the nominal capacities multiplied by the capacity modification factor. This factor may be calculated as the ratio of the average virtual displacements along the loaded area in the two respective loading scenarios.

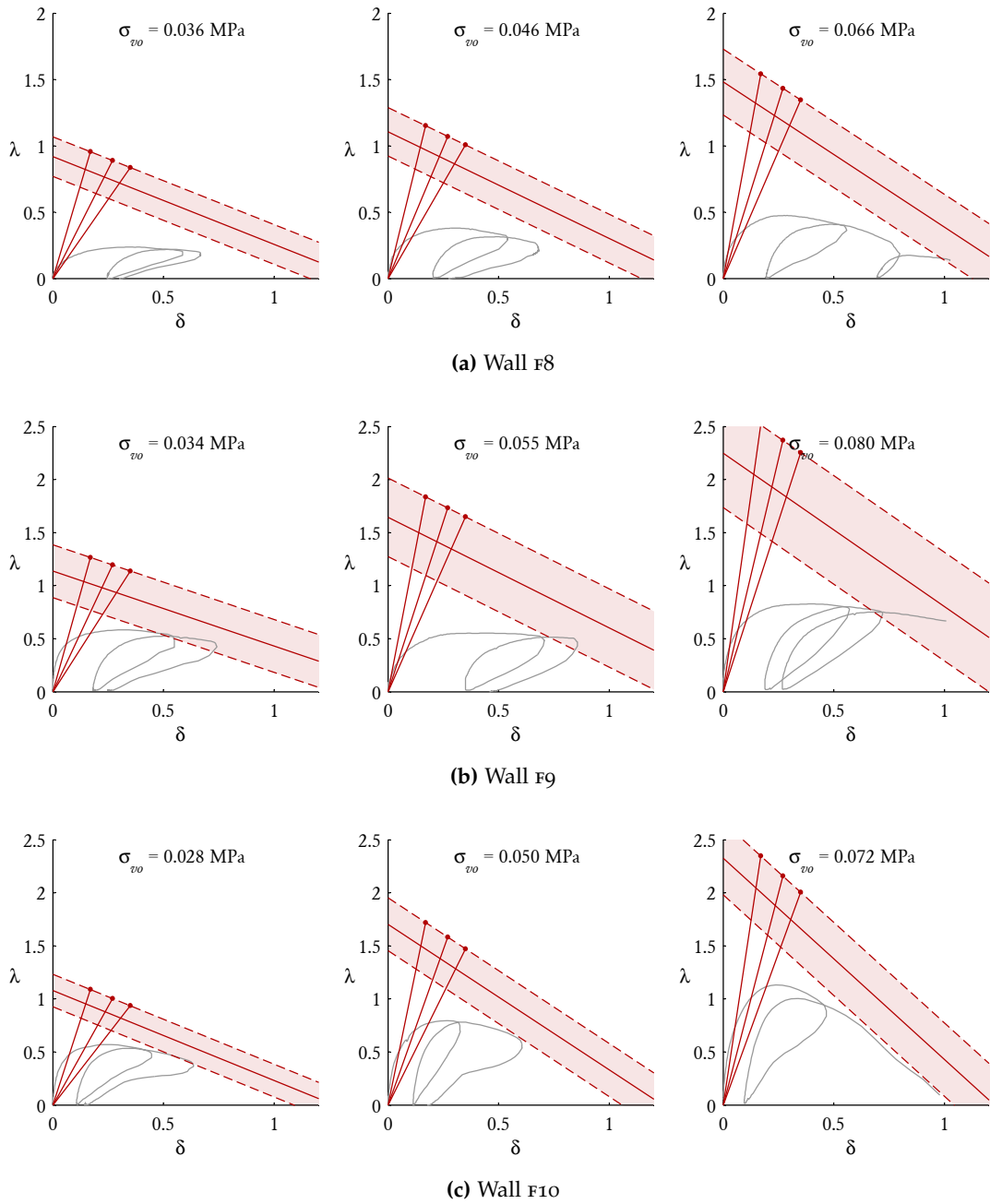


Figure 7.7: Comparison of theoretical behaviour and experimental response for reduced-scale dry-stack masonry walls tested by *Vaculik et al. [2003]*.

of the walls, while being restrained against lateral displacement, did not have full rotational restraint. As a result, it is expected that their overall behaviour lay somewhere between pure rocking response (λ_r) and response inclusive of the full horizontal bending contribution ($\lambda_r + \lambda_h$).

Although the test walls were not pushed up to the point of collapse, the graphical comparisons in Figure 7.7 suggest that if the softening branches of the experimentally measured load-displacement curves were extrapolated, then in most cases, the predicted displacement capacity (δ_{ru}) would provide a conservative estimate of the experimental (extrapolated) capacities.

7.4 DISPLACEMENT-BASED SEISMIC ASSESSMENT

This section demonstrates implementation of the proposed load-displacement model into a displacement-based seismic assessment procedure using the substitute structure approach—an approximate technique for estimation of the maximum displacement demands of nonlinear structural systems subjected to seismic excitations. The method was originally proposed by *Gülkan and Sozen* [1974] [also *Shibata and Sozen*, 1976] and has since been developed for various structural systems and nonlinear load-displacement behaviour types [e.g. *Moehle*, 1992; *Priestley*, 1997; *Magenes and Calvi*, 1997; *Medhekar and Kennedy*, 2000; *Kowalsky*, 2002], including vertically spanning walls subjected to out-of-plane actions [*Doherty et al.*, 2002; *Griffith et al.*, 2003].

The basic steps in the method can be summarised as follows:

1. The actual multi-degree-of-freedom (MDOF) structure (in this case the wall), whose mass and displacement are both spatially distributed, is transformed into an equivalent single-degree-of-freedom (SDOF) system with a lumped effective mass M^* and effective displacement u (Section 7.4.1).
2. The structure's nonlinear F - Δ behaviour is replaced by an equivalent linear system characterised by an effective stiffness K_e and equivalent viscous damping ζ_e . Properties K_e and M^* are then used to determine an effective vibrational period T_e (Section 7.4.2).
3. Finally, the maximum displacement demand of the structure, u_d , to a particular earthquake is estimated by entering the effective dynamic properties T_e and ζ_e (as determined in Step 2) into the earthquake's elastic spectrum. In the case of design, a code-prescribed design spectrum is used. While numerous alternative approaches exist for undertaking this step, the approach demonstrated will be the capacity spectrum (CS) method (Section 7.4.3).

In its present state, implementation of the proposed F - Δ model into the substitute structure method is as yet unverified, in that the accuracy of the resulting approach has not been tested by comparing its displacement demand predictions to those of nonlinear time-history analyses. It is anticipated that such a verification process, conducted for a range of values of the input parameters in the proposed F - Δ model, can be a focus for future research.

7.4.1 SDOF Transformation

The first step of the substitute structure approach involves transforming the masonry wall from a MDOF system into an equivalent SDOF system with lumped displacement and mass properties. These transformations are based on standard modal analysis [see for instance *Clough and Penzien, 1993; Chopra, 2000*], which fundamentally requires the structure to deform according to a predominant displacement pattern (mode shape). This assumption seems reasonable for a masonry wall in flexure, whose primary mode shape is characterised by the collapse mechanism.

Effective Displacement

In standard modal analysis, the modal participation factor Γ is defined as

$$\Gamma = \frac{\sum_{i=1}^n m_i \varphi_i}{\sum_{i=1}^n m_i \varphi_i^2}, \quad (7.35)$$

where i denotes indices of nodes in the MDOF structure with a total of n nodes, φ_i is the mode shape function at each node, and m_i is the mass at each node.

By defining a particular control node in the MDOF structure such that the value of the mode shape function at the control node is φ_c [as used during the calculation of Γ by Eq. (7.35)], the relationship between effective SDOF system displacement u and the displacement at the control node, Δ_c , becomes

$$u = \frac{\Delta_c}{\varphi_c \Gamma}. \quad (7.36)$$

Based on these formulae, it is possible to derive a displacement transformation relationship for any wall collapse mechanism by considering its deflected shape. To define such a relationship for the type K family of mechanisms (Figures 6.16

and 6.17), let us firstly define a modified normalised aspect ratio α_s , such that

$$\alpha_s = \text{greater of } \begin{cases} \alpha, \\ 1/\alpha, \end{cases} \quad (7.37)$$

where α is the normalised aspect ratio calculated using Eq. (6.44). From this, the ratio of the effective displacement and the maximum surface displacement (indicated by Δ' in Figures 6.16 and 6.17) in any of the type K mechanisms, including K1_x, K1_y, K2_x or K2_y, becomes

$$\frac{u}{\Delta} = \frac{2\alpha_s - 1}{3\alpha_s - 1}. \quad (7.38)$$

For consistency, this equation uses the same reference displacement (Δ) in each of the mechanisms as the load-displacement relationships in Section 7.2.

Note that Eq. (7.38) is only applicable to solid walls. Furthermore, in the case of type K1 mechanisms, it assumes that any OBL present is restrained from lateral movement ($\Phi = 0$). For walls with openings or for type K1 mechanisms with an unrestrained OBL ($\Phi = 1$), which acts as additional concentrated mass along the top edge of the wall, the ratio u/Δ may be determined from first principles using Eqs. (7.35) and (7.36).

Since α_s may assume values between 1 and ∞ , the ratio u/Δ calculated using Eq. (7.38) can range between 1/2 and 2/3. The latter corresponds to the wall becoming sufficiently long or tall to be treated as one-way spanning and is consistent with the value determined by *Doherty et al.* [2002] for vertically spanning walls.

The ratio u/Δ together with Eq. (2.2) may subsequently be used for transformation of the various displacement properties in the load-displacement model between the δ , Δ and u domains. For example, the rocking instability displacements δ_{ru} , Δ_{ru} and u_{ru} are related by

$$\Delta_{ru} = t_u \cdot \delta_{ru}, \quad \text{and} \quad u_{ru} = \frac{u}{\Delta} \cdot \Delta_{ru}.$$

Other displacement properties may also be converted in a similar manner.

Effective Mass

Based on modal analysis, the effective mass of the equivalent SDOF system (i.e. the modal mass) is calculated as

$$M^* = \frac{\left(\sum_{i=1}^n m_i \varphi_i \right)^2}{\sum_{i=1}^n m_i \varphi_i^2}, \quad (7.39)$$

with m_i and φ_i as defined previously. The actual mass of the structure is

$$M = \sum_{i=1}^n m_i. \quad (7.40)$$

Therefore, the ratio of the effective and actual mass becomes

$$\frac{M^*}{M} = \frac{\left(\sum_{i=1}^n m_i \varphi_i \right)^2}{\left(\sum_{i=1}^n m_i \right) \left(\sum_{i=1}^n m_i \varphi_i^2 \right)}. \quad (7.41)$$

For the type K mechanisms, including $K1_x$, $K1_y$, $K2_x$ and $K2_y$, this ratio becomes

$$\frac{M^*}{M} = \frac{9\alpha_s^2 - 6\alpha_s + 1}{12\alpha_s^2 - 6\alpha_s}, \quad (7.42)$$

where α_s is obtained by Eq. (7.37). Note that the actual mass (M) in the above equation refers to the mass of the wall over the height of the mechanism, H_t , as illustrated in Figures 6.16 and 6.17. Applicability of Eq. (7.42) is subject to the same limitations as discussed previously in relation to Eq. (7.38).

As α_s can range between 1 and ∞ , the ratio M^*/M obtained using Eq. (7.42) may assume values between 2/3 and 3/4. The latter is consistent with the value provided by *Doherty et al.* [2002] for vertically spanning walls.

7.4.2 Equivalent Linearisation

This step of the substitute structure approach involves replacing the nonlinear F - Δ behaviour by an effective linear system with an effective stiffness K_e and equivalent viscous damping ξ_e . The criterion for ideal selection of K_e and ξ_e is that an inelastic time-history analysis (THA) incorporating the actual nonlinear F - Δ behaviour will produce the same maximum structural displacement as a THA of the equivalent

linear system, when subjected to the same earthquake motion. Achieving this will realistically require an extensive calibration process of formulae for determining these linear properties on the basis of the different input properties of the proposed F - Δ rule. This, however, is a major task and is outside the scope of this thesis. Therefore, a simplified procedure will instead be outlined, in which the equivalent stiffness is obtained using the usual secant approach and the effective damping by the hysteretic area approach.

Effective Stiffness

The first step in determining the secant stiffness at a particular displacement is to define the pushover (capacity) curve of the structure. In analysis of MDOF structures, determination of the capacity curve is typically carried out by subjecting the system to a load shape function based on its modal inertia distribution (i.e. mode shape function \times mass distribution).⁴ The capacity relationships presented in Section 7.2, however, are based on the assumption that the acting load is distributed directly according to the wall's mass. This therefore requires us to convert the derived nominal load capacities (λ_o or F_o) to equivalent force capacities based on a modal inertia load shape (denoted by λ_o^* or F_o^*).

Using the fundamental assumption of independence between the mode shape and the loading function, it follows that irrespective of the loading function, the wall performs the same amount of internal work. From this, it can be demonstrated that

$$\frac{F_o^*}{F_o} = \frac{M^*}{M} \quad (7.43)$$

(refer to Appendix H.2). The significance of this will now be demonstrated.

As seen from Figure 7.8, according to the secant approach the effective stiffness is taken as

$$K_e = \frac{F^*\langle u \rangle}{u}, \quad (7.44)$$

where $F^*\langle u \rangle$ is the effective force resistance based on the wall's capacity envelope curve at an arbitrarily chosen value of the effective displacement u .

From basic dynamics principles, the modal angular frequency is

$$\omega_e = \sqrt{\frac{K_e}{M^*}} = \sqrt{\frac{F^*\langle u \rangle}{u M^*}}, \quad (7.45)$$

⁴Other, more adverse approaches in terms of the resulting load capacity are also sometimes used for determination of the pushover curve, such as applying a point load at the position of maximum displacement [see e.g. *Chopra and Goel, 1999*].

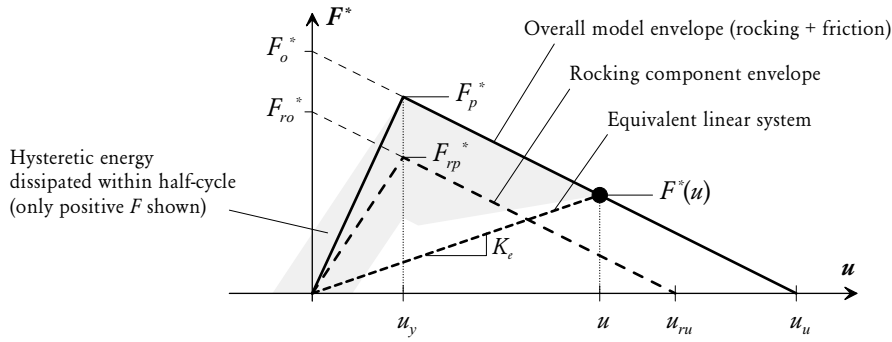


Figure 7.8: Effective stiffness K_e of equivalent linear system obtained using the secant approach at an arbitrary effective displacement u .

which, by noting Eq. (7.43), is equivalent to

$$\omega_e = \sqrt{\frac{F\langle u \rangle}{u M}}, \quad (7.46)$$

where $F\langle u \rangle$ is simply the force resisted at the effective displacement u , assuming a mass-proportional load shape distribution. The significance of this result is that the effective mass calculation [as per Eqs. (7.39) and (7.42)] effectively becomes redundant if one uses the load capacity expressions presented in Tables 7.1 and 7.3.

Since $F\langle u \rangle / M$ is equivalent to the static acceleration of the wall, Eq. (7.46) can be written as

$$\omega_e = \sqrt{\frac{\lambda\langle u \rangle g}{u}}, \quad (7.47)$$

where $\lambda\langle u \rangle$ is the load multiplier at the effective displacement u as defined by the capacity curve, and g is gravitational acceleration. From this, the wall's effective period T_e and frequency f_e are related by

$$T_e = \frac{1}{f_e} = \frac{2\pi}{\omega_e}. \quad (7.48)$$

Equivalent Viscous Damping

A conventional method of quantifying the equivalent hysteretic damping ζ_{hyst} of an inelastic F - Δ system is by the hysteretic area approach, which accounts for the amount of energy dissipated in a full deformation cycle at a given displacement amplitude (e.g. see Figure 3.8 and the accompanying discussion in Section 3.3.2 for further detail). This approach, originally proposed by *Jacobsen* [1930, 1960], is based on the notion that the inelastic system dissipates the same amount of energy by hysteresis as a replacement linear system does by viscous (velocity-proportional)

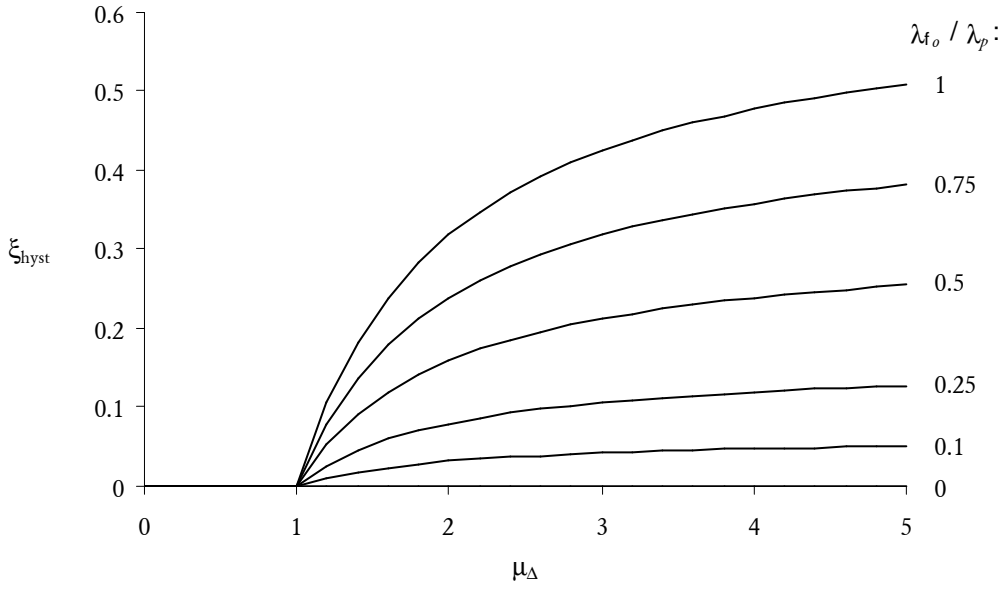


Figure 7.9: Hysteretic damping ζ_{hyst} as a function of the displacement ductility μ_{Δ} , for different ratios of the inelastic strength λ_{f_0} to the overall peak strength λ_p .

damping, and furthermore, the assumption that both systems undergo steady-state sinusoidal response at resonance [see e.g. *Clough and Penzien, 1993*]. As per Eq. (3.11), the corresponding equivalent viscous damping is calculated as

$$\zeta_{\text{hyst}} = \frac{2}{\pi} \frac{U_{\text{loop}}}{U_{\text{box}}},$$

with U_{loop} and U_{box} as defined in Figure 3.8.

Denoting the displacement cycle amplitude (δ_{amp} in Figure 7.4) simply as δ , the equivalent viscous damping in the proposed load-displacement model becomes

$$\zeta_{\text{hyst}}(\delta) = \begin{cases} 0 & \text{for } \delta \leq \delta_{fy} \text{ (pre-yield),} \\ \frac{2}{\pi} \frac{\lambda_{f_0} (\delta - \delta_{fy})}{\lambda_p \delta} & \text{for } \delta > \delta_{fy} \text{ (post-yield),} \end{cases} \quad (7.49)$$

where δ_{fy} is the yield displacement of the combined frictional component [Eq. (7.29)], and λ_p is the overall peak force resistance [Eq. (7.34)]. Note that this calculation implicitly assumes a higher value of the effective stiffness in terms of the resulting internal strain energy compared to Eq. (7.44), thus leading to a lower (more conservative) value of ζ_{hyst} .

By introducing a displacement ductility parameter μ_{Δ} according to its conven-

tional definition as the ratio of the cycle displacement to the yield displacement:

$$\mu_{\Delta} = \frac{\delta}{\delta_{fy}}, \quad (7.50)$$

the post-yield equivalent hysteretic damping in Eq. (7.49) can also be written in the alternative form

$$\tilde{\zeta}_{\text{hyst}} = \frac{2}{\pi} \frac{\lambda_{fo}}{\lambda_p} \left(1 - \frac{1}{\mu_{\Delta}} \right). \quad (7.51)$$

Figure 7.9 plots the resulting relationship between $\tilde{\zeta}_{\text{hyst}}$ and μ_{Δ} for different values of the ratio λ_{fo}/λ_p .

The total effective viscous damping ζ_e is subsequently obtained as the sum of the nominal viscous damping ζ_{nom} (typically taken between 0.03 to 0.05) and the equivalent hysteretic damping:

$$\zeta_e = \zeta_{\text{nom}} + \tilde{\zeta}_{\text{hyst}}. \quad (7.52)$$

At this point, it is important to emphasise that $\tilde{\zeta}_{\text{hyst}}$ based on the hysteretic area approach is known to overestimate damping of certain types of systems when subjected to realistic earthquake motions, particularly systems with a high inelastic energy absorption [Chopra and Goel, 2001; Dwairi and Kowalsky, 2004; Priestley et al., 2007]. This is because real accelerograms contain a broad spectrum of frequencies, as opposed to a single excitation frequency as assumed by the Jacobsen damping approach. A common way of addressing this is to apply a reduction factor to the area-based $\tilde{\zeta}_{\text{hyst}}$ term in Eq. (7.52), where the factor is typically expressed as a function of the initial value of $\tilde{\zeta}_{\text{hyst}}$ and characteristics of the hysteresis rule [ATC, 1996; Chopra and Goel, 2000; Priestley et al., 2007]. This further underlines the necessity for development of an expression for calculating a suitable value of the equivalent damping in the proposed F - Δ model, as an alternative to Eq. (7.49). Such a calibration process may be performed using methods similar to those employed for various types of hysteresis rules by Grant et al. [2005] and Dwairi et al. [2007].

7.4.3 Prediction of the Displacement Demand

Having transformed the wall from a MDOF system to a SDOF system (Section 7.4.1) and replaced its nonlinear inelastic F - Δ behaviour with equivalent linear dynamic properties (Section 7.4.2), the displacement response of the wall with respect to a particular design earthquake is determined from the elastic design spectrum. This will now be demonstrated using the capacity spectrum (CS) method, as originally

proposed by *Freeman et al.* [1975] [also described in *Freeman, 2004*], which provides a convenient graphical implementation of DB assessment.

The method consists of the following steps:

1. The elastic design spectrum is obtained from the relevant earthquake loading standard for a particular limit state (e.g. serviceability or ultimate limit state). It is convenient to discretise the period domain into a finely spaced grid over the range of interest. At each value of period T , the elastic spectral acceleration and displacement, $S_{ae}\langle T \rangle$ and $S_{de}\langle T \rangle$, are determined. This step assumes the usual spectral ordinate dependency

$$S_{ae}\langle T \rangle = \left(\frac{2\pi}{T} \right)^2 S_{de}\langle T \rangle. \quad (7.53)$$

2. The elastic spectrum is converted into an inelastic spectrum by accounting for hysteretic damping in the specific wall under consideration. It is common to perform this reduction using a spectrum reduction factor R_{ξ} formulated in terms of the equivalent viscous damping. A number of alternative expressions for calculating R_{ξ} are described by *Priestley et al.* [2007], which for illustrative purposes, Eurocode 8 [*Comité Européen de Normalisation, 2004*] prescribes as

$$R_{\xi}\langle \xi_e \rangle = \left(\frac{0.10}{0.05 + \xi_e} \right)^{1/2}, \quad \text{subject to } 0.55 \leq R_{\xi}\langle \xi_e \rangle \leq 1, \quad (7.54)$$

where ξ_e is the total damping inclusive of both nominal and hysteretic damping. This equation assumes nominal damping to be $\xi_{\text{nom}} = 0.05$, so that the resulting factor becomes applicable to the 5% damped elastic spectrum.

From this, the spectrum reduction factor, R_T , at a given period is determined as

$$R_T\langle T \rangle = R_{\xi}\langle \xi_e \rangle, \quad \text{by satisfying } S_{de}\langle T \rangle \cdot R_{\xi}\langle \xi_e \langle u \rangle \rangle = u. \quad (7.55)$$

Because of the circular dependency between R_{ξ} , ξ_e and u , solution for $R_T\langle T \rangle$ may be obtained by numerical iteration.

The inelastic spectral ordinates at each period T are then calculated as

$$S_{di}\langle T \rangle = R_T\langle T \rangle \cdot S_{de}\langle T \rangle, \quad (7.56)$$

and

$$S_{ai}\langle T \rangle = R_T\langle T \rangle \cdot S_{ae}\langle T \rangle. \quad (7.57)$$

3. The inelastic spectrum and the capacity envelope curve of the wall are plotted together on the same set of axes in the acceleration-displacement format. It is

up to the user to decide the normalisation for each axis, but in the author's opinion, it is convenient to plot normalised acceleration on the y-axis (S_a/g for the spectrum and λ for the capacity curve) and effective displacement on the x-axis (S_d for the spectrum and u for the capacity curve). This requires the capacity envelope, given by Eq. (7.31), to be converted into the λ - u format using Eqs. (2.2) and (7.38).

The wall's displacement response (demand) u_d is subsequently obtained as the displacement at the intersection of the two curves, referred to as the performance point. In the event that the curves do not intersect, the wall is deemed to fail. Because of the softening nature of the capacity curve in the proposed model, it is possible in some circumstances for multiple intersections to occur. In such an instance, the solution is taken as the intersection point at the lowest displacement.

Finally, to assess the structural adequacy of the wall, the displacement demand u_d is compared to an acceptable deformation limit. For example, in ultimate limit state design (against collapse) the user may deem as acceptable any demand within a certain percentage of the available rocking displacement capacity (u_{ru}), such that

$$\text{capacity utilisation ratio} = u_d/u_{ru}. \quad (7.58)$$

It should be noted that when using the CS method, it is not necessary to explicitly calculate the wall's effective stiffness nor period [given by Eqs. (7.44) and (7.48)], as this information is effectively stored in the acceleration-displacement diagram itself. These properties are, however, required when using the secant stiffness approach [e.g. *Doherty et al., 2002*].

7.5 EXAMPLES

Several examples will now be provided to demonstrate the application of the proposed F - Δ model as part of a DB seismic assessment using the CS method. The influence of various aspects of the boundary conditions on the resulting capacities will also be demonstrated.

7.5.1 Assumptions and Generalities

CAPACITY RELATED Consider walls comprising standard Australian clay brick masonry with $230 \times 110 \times 76$ mm bricks and 10 mm mortar joints, with values of

material properties and other dependent properties as walls s1–s8 (summarised in Table 7.4). Let us treat each wall as being constructed with mortar, and therefore, as per the lessons learnt from the parametric studies in Section 6.7, assume that: (i) the span of the mechanism utilises the full length and height of the wall, and (ii) type K mechanisms will be favoured over other mechanisms such as type G.⁵ From this, the precise mechanism applied to each wall becomes immediately defined from the start of the analysis based on the wall's dimensions and support shape, and capacities λ_{ro} , δ_{ru} and λ_{ho} are obtained using the relevant equations in Tables 7.1 and 7.3. To account for capacity reduction effects due to non-idealised behaviour [as discussed throughout Section 7.2; see for example Eq. (7.21)], let us apply a capacity reduction factor of 0.9 to each of the aforementioned capacities. The yield displacement for both the rocking and frictional components is estimated using Doherty's empirical value for the most degraded state, which from Table 7.2 gives $\delta_y = 0.35$ and therefore $\Delta_y = 0.35 \times 110 \text{ mm} = 38.5 \text{ mm}$ for each wall, regardless of its configuration.

SPECTRUM RELATED To define the elastic design spectrum, let us use the Australian earthquake loading standard AS 1170.4 [*Standards Australia, 2007*] and assume a 1/500 year return period, type D soil class (deep or soft soil) and location within the Adelaide region. This results in an elastic spectrum with the characteristics: $PGA = 0.11 \text{ g}$, $PSA = 0.37 \text{ g}$, $PSV = 0.31 \text{ m/s}$, and $PSD = 0.074 \text{ m}$. Conversion of the elastic spectrum to an inelastic spectrum is performed based on each wall's damping function [Eq. (7.49)] combined with the Eurocode 8 spectrum reduction formula [Eq. (7.54)].

7.5.2 Results

The CS method examples, whose results are shown in Figures 7.10, 7.11 and 7.12, all consider an identically sized wall with dimensions $4080 \times 2494 \times 110 \text{ mm}$ ($L \times H \times t$), subjected to different types of boundary conditions.

In the respective diagrams, three performance points are plotted for each wall configuration: (i) total capacity versus the inelastic spectrum, (ii) total capacity versus the elastic spectrum, and (iii) elastic capacity versus the elastic spectrum. The first case represents the primary solution of the analysis. The second and third cases are used to provide an upper-bound prediction of the displacement demand that would result if the elastic spectrum was not reduced to account for inelastic

⁵Note that despite any initial ultimate strength obtained from mortar bond contribution, which may be calculated using the methodology dealt with in Chapter 4, the DB analysis undertaken here effectively assumes bond strength to be zero.

Table 7.8: Legend for Figures 7.10, 7.11 and 7.12.

Capacity curves	
-----	Elastic capacity (rocking only)
————	Total capacity (rocking + inelastic)
Spectrum curves	
————	Elastic spectrum
————	Inelastic spectrum
Performance points	
●	Total capacity vs. Inelastic spectrum
□	Total capacity vs. Elastic spectrum
×	Elastic capacity vs. Elastic spectrum

effects. For each performance point plotted in these figures, the percentage value indicates the utilisation of the wall's displacement capacity relative to the rocking instability displacement [as per Eq. (7.58)].

As a matter of terminology, note that in the following discussions, 'displacement capacity' refers to the rocking instability displacement δ_{ru} and not the additional enhanced capacity δ_u that is obtained from inelastic contributions (refer to Figure 7.4 for an illustration of both).

Example set 1—Influence of vertical edge support

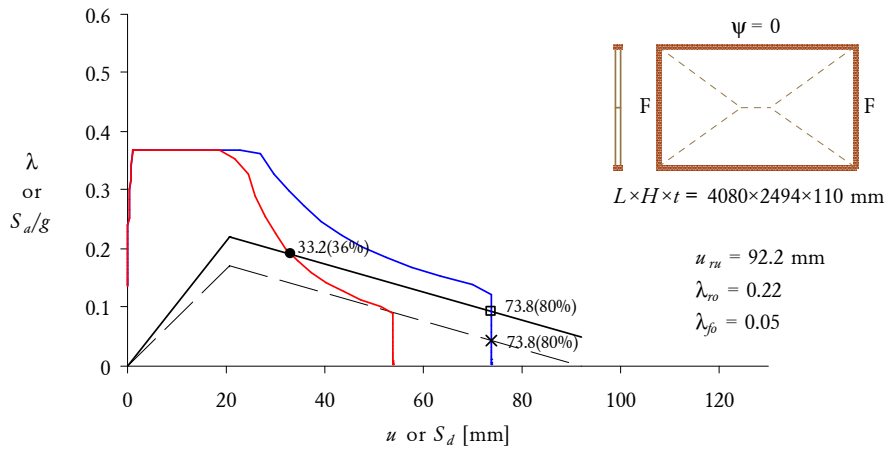
Figure 7.10 demonstrates the predicted response for a wall with: (a) O-shaped support with full moment restraint at the vertical edges, (b) O-shaped support with only simple support at the vertical edges, and (c) both vertical edges unsupported.

Comparison of cases (a) and (b) shows that a significant improvement to the wall's seismic resistance is gained from having its vertical edges fixed against rotation. This is due to not only an increase in the wall's load capacity, but also a reduction of the spectrum due to inelastic resistance along these edges.

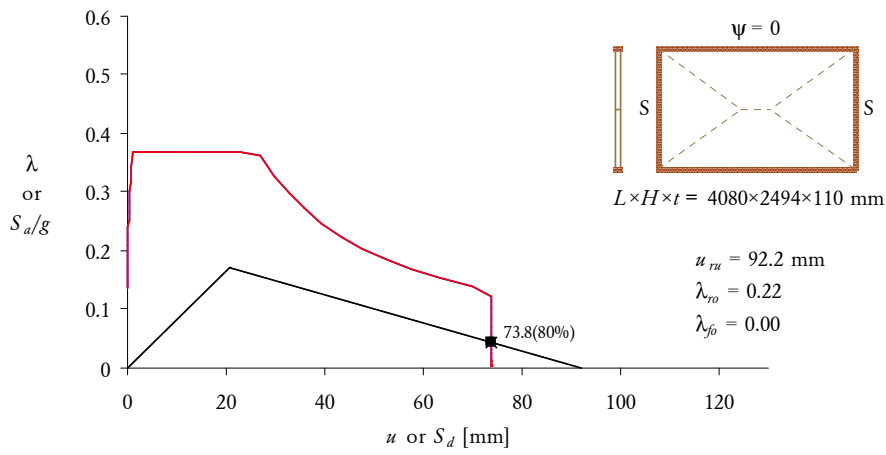
Comparing cases (b) and (c) demonstrates that despite both systems being elastic and therefore being subject to the same unfactored spectrum, a wall with two-way support performs significantly better than a vertically spanning wall, due to an enhancement of both its load and displacement capacities.

Example set 2—Influence of precompression and overburden load eccentricity

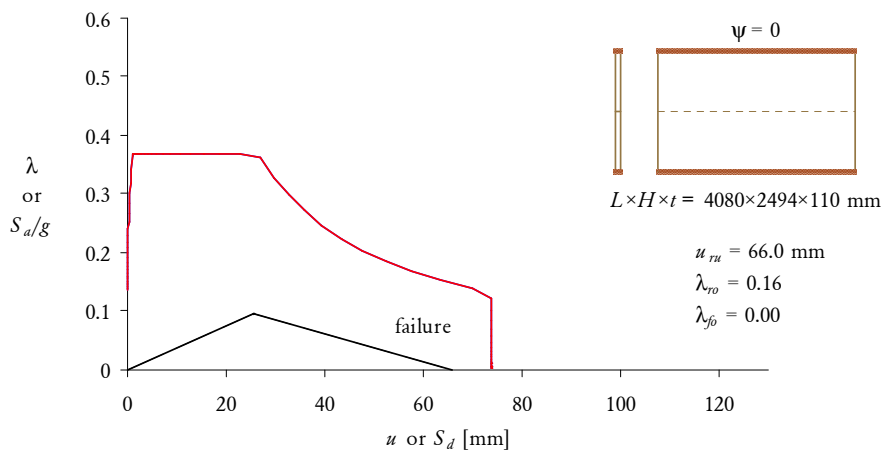
Figure 7.11 shows the predicted response for a wall with 0.05 MPa precompression, which is equivalent to an overburden weight ratio of $\psi = 1.06$. Parts (a) and (b) of the figure demonstrate the effect of the OBL eccentricity, which is controlled by the property ϵ (defined in Figure 6.6 and Figure 6.7b for type-2 mechanisms).



(a) Fully fixed vertical edges ($R_{vs} = 1$).

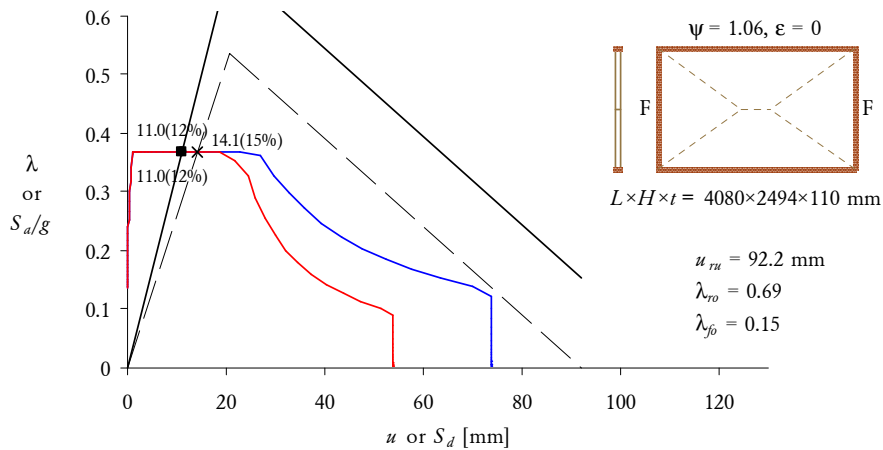


(b) Simply supported vertical edges ($R_{vs} = 0$).

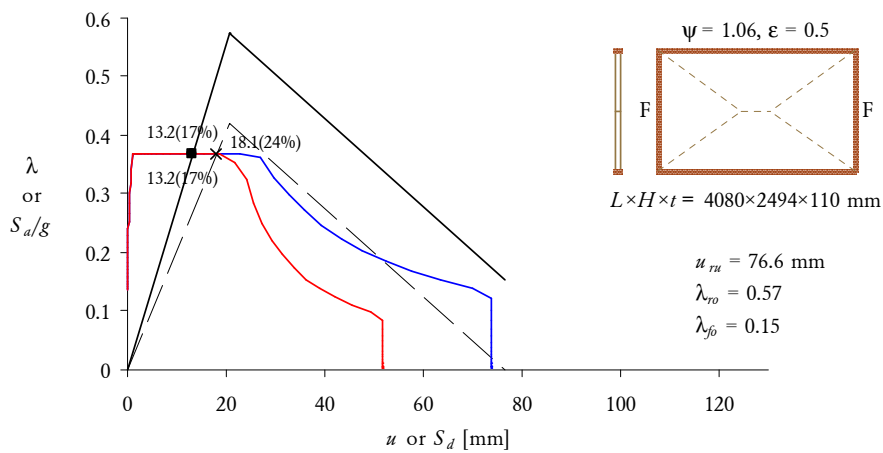


(c) Unsupported vertical edges.

Figure 7.10: CS method examples—Influence of vertical edge support. Legend in Table 7.8.



(a) OBL acting at upward-deflecting point ($\epsilon = 0$).



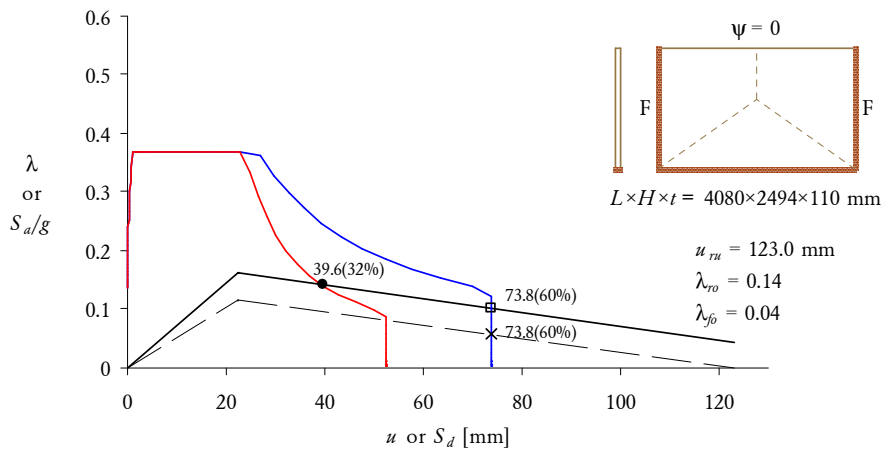
(b) OBL acting at wall's centreline ($\epsilon = 0.5$).

Figure 7.11: CS method examples—Influence of an applied overburden load and its eccentricity. Refer to Figure 7.10a for case without precompression. Legend in Table 7.8.

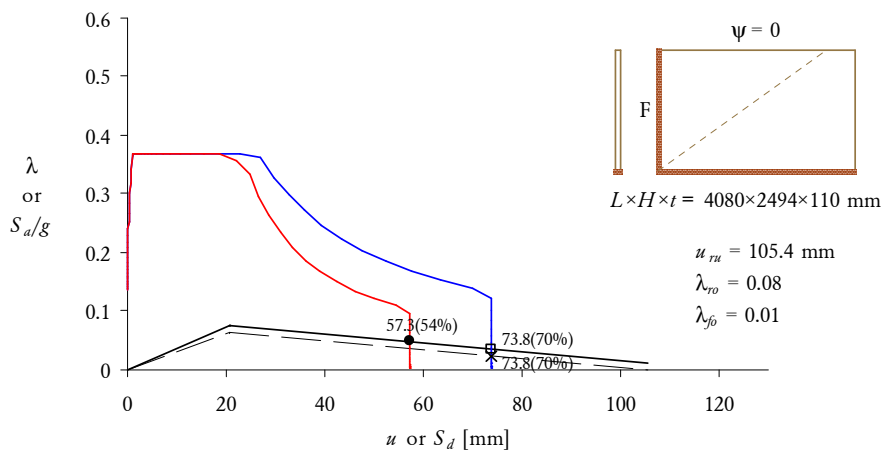
In part (a), the load is concentrated at the upward-deflecting point of the wall's cross section ($\epsilon = 0$), while in part (b), the load acts at the wall's centreline ($\epsilon = 0.5$). For reference, Figure 7.10a shows the response of a control wall without any precompression.

Comparison of Figures 7.10a and 7.11a demonstrates that if the OBL acts at the upward-deflecting point ($\epsilon = 0$), an increase in the applied precompression will enhance the load capacity, but will have no influence on the displacement capacity.

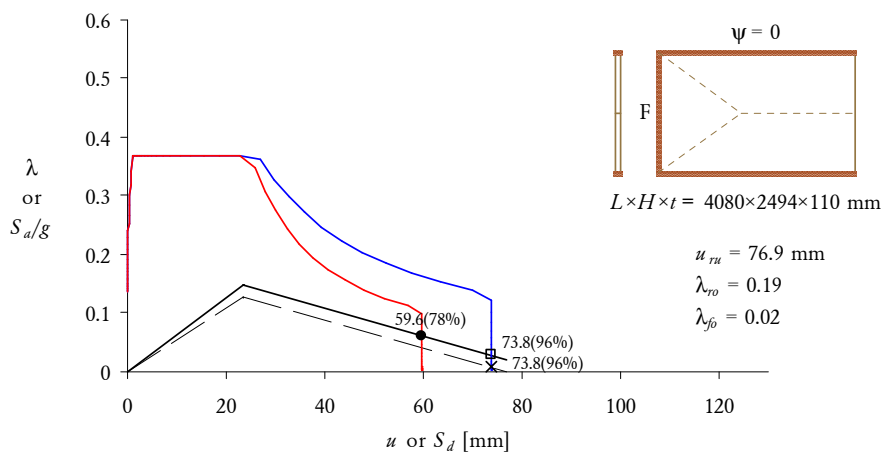
On the other hand, comparison of Figures 7.10a and 7.11b shows that when the OBL acts at the centreline ($\epsilon = 0.5$), an increase in the precompression will lead to better overall load capacity but poorer displacement capacity. The latter occurs due



(a) U-shaped support.



(b) L-shaped support.



(c) C-shaped support.

Figure 7.12: CS method examples—Influence of wall support shape. Also refer to Figure 7.10a for case with O-shaped support. Legend in Table 7.8.

to the destabilising moment resulting from the position of the OBL.

For a constant value of precompression (ψ), variation of the eccentricity influences the load and displacement capacities such that the softening slope of the capacity curve remains unaltered. This can be seen by comparing parts (a) and (b) of Figure 7.11, which show that a more eccentric load (higher ϵ) reduces the load and displacement capacities in equal proportion. The most favourable condition therefore results when the OBL acts at the upward-deflecting point ($\epsilon = 0$), which is analogous to a slab connection (as illustrated by Figure 6.8). It is worth noting that the eccentricity can only influence the rocking load and displacement capacities and not the inelastic load capacities.

Example set 3—Influence of support shape (O, U, C or L)

Figure 7.12 demonstrates the predicted response for a wall with: (a) U-shaped support, (b) L-shaped support, and (c) C-shaped support. For reference, Figure 7.10a shows the response of a control wall with O-shaped support.

The examples demonstrate the expected influence of the support shape on the load capacity, in that providing any wall with additional supported edges will act to enhance its strength. This is seen by an increase in strength by modifying the support shape from L to U (Figures 7.12b and 7.12a), from L to C (Figures 7.12b and 7.12c), from U to O (Figures 7.12a and 7.10a), and from C to O (Figures 7.12c and 7.10a).

However, these examples also demonstrate another very interesting prediction—that removal of support along the top horizontal edge, while reducing the wall's load capacity, actually acts to increase displacement capacity. This is evident by comparing O-shaped support with U-shaped support (Figures 7.10a and 7.12a), and C with L (Figures 7.12c and 7.12b). The reason for this somewhat counterintuitive result is that removing the top edge support causes a greater proportion of the wall to undergo rotation about the vertical axis, thus making it less prone to rocking destabilisation (or P-Delta effect) which only influences the mechanism sub-plates rotating horizontally. In fact, the governing equations in Table 7.1 predict that in the absence of precompression ($\psi = 0$), the instability displacement in each of the type K mechanisms becomes dependent only on the normalised aspect ratio α [Eq. (6.44)], such that a lower value of α will lead to a higher displacement capacity. Furthermore, the equations predict that the theoretical upper limit to the displacement capacity occurs in mechanisms K1_y and K2_y, where δ_{ru} can approach a value of 2, that is, a displacement equal to twice the wall thickness. By contrast, the well known upper limit for vertically spanning walls is equal to 1. Note that

this prediction is also consistent with behaviour observed in the quasistatic cyclic tests (Chapter 2), where the U-shaped wall s6 appeared to have a considerably higher displacement capacity than the identically sized O-shaped walls s1–s5.

7.6 CONCLUSIONS

A nonlinear inelastic load-displacement model has been proposed for modelling the behaviour of two-way walls subjected to out-of-plane loading. The model treats the wall as possessing zero bond strength and assumes that its response consists of several independently acting resistance sources whose load contributions can be superimposed at any value of the wall's displacement. These include the rocking component, modelled by a bilinear elastic softening rule; and frictional components due to horizontal bending and overburden load friction, both modelled by elastoplastic rules.

Analytical expressions have been derived for calculating the load and displacement capacities of the rocking component, for the various possible forms of type K mechanisms, which are the mechanisms most commonly associated with two-way URM walls. It is possible, however, to employ the same techniques to derive such expressions for other types of mechanisms, such as type G, which, although being more favoured in dry walls, should probably also not be overlooked for mortar-bonded walls. Expressions for the load capacities of the inelastic capacities were obtained using the virtual work approach. By contrast, a mechanics-based approach to calculating the initial loading stiffness or yield displacement of the wall is still lacking.

Comparisons of the proposed model with experimentally observed behaviour have been shown to be largely favourable. While the model does not account for the initial ultimate strength that uncracked walls gain from tensile bond strength, nor effects such as strength degradation and arching, it is conceptually possible to account for such effects by the inclusion of additional resistance components. Nonetheless, in its current form, the model appears to provide a reasonable albeit conservative representation of observed behaviour.

Implementation of the model into a DB seismic assessment approach using the substitute structure method has also been demonstrated. The parameters necessary to perform the relevant displacement and mass transformations to convert the system from MDOF to SDOF were presented for the type K mechanisms. By contrast, only simplified techniques were demonstrated for estimating the effective stiffness and equivalent viscous damping, based on the secant stiffness and hysteretic area based damping methods, respectively. It is anticipated that performing an extensive

set of parametric THA studies using the proposed F - Δ model is the next necessary step toward developing a reliable DB assessment technique.

CONCLUSION

8.1 EXPERIMENTAL WORK

A pair of complimentary experimental studies have been performed on two-way spanning unreinforced masonry (URM) walls: quasistatic cyclic tests on full-scale walls (Chapter 2), and shaketable tests on half-scale walls (Chapter 3).

The quasistatic tests demonstrated that two-way walls, in addition to possessing greater strength than vertically spanning walls, also possess a substantially higher displacement capacity that is in excess of the wall thickness (as validated by the load-displacement model developed in Chapter 7). Good energy dissipation characteristics due to frictional modes of resistance were also observed, which are further beneficial to a wall's seismic resistance. The tests also demonstrated, however, that it is possible for the out-of-plane wall to separate from the connecting return walls when a significant proportion of brick units along the wall's vertical edge undergo line failure. This can be of some concern, since loss of functionality by the vertical edges can cause a two-way wall to revert to a vertical one-way collapse mechanism, thus losing the aforementioned benefits.

The shaketable tests were not able to achieve the same levels of wall displacement as in the quasistatic tests, mainly because of performance limitations of the shaketable. However, they were still able to verify the main trends in wall behaviour, including hysteretic energy dissipation and the ability to displace beyond the peak load capacity. Furthermore, both sets of studies demonstrated consistency between the walls' observed failure mechanisms and patterns generally associated with mortar-bonded walls (i.e. type K mechanisms, see Figure 4.1), thus laying the foundation for the subsequent development of analytical methods.

8.2 ANALYTICAL WORK

In this thesis, the development of analytical techniques was tackled on several fronts: Chapters 4 and 6 dealt with prediction of the wall's load capacity by respectively including and ignoring, the presence of tensile bond strength. Chapter 5 developed a probabilistic approach in relation to the possible failure modes in horizontal bending, with implications toward both the ultimate and residual load capacity. And finally, Chapter 7 developed a load-displacement capacity model and demonstrated its implementation into a prototype displacement-based (DB) analysis procedure. It is envisaged that these methodologies, with some further development, can be assimilated into a multi-tiered design/assessment approach incorporating both force-based (FB) and DB components, as shown by the flowchart in Figure 8.1

8.2.1 Force-Based Methodology

Prediction of Ultimate Strength

Chapter 4 provided further development of the current state-of-the-art methodology for calculating the ultimate strength of walls possessing tensile bond strength, including refinements to existing models for predicting the ultimate moment capacities in horizontal bending (particularly stepped failure) and diagonal bending. Advances were also made in Chapter 5 through quantification of the strength reduction expected in the ultimate horizontal bending moment capacity, as a result of weak link effects associated with the combined possibility of the stepped and line failure modes.

Ultimate moment capacity expressions were fed into the virtual work (VW) approach to predict the load capacity of overall walls. Comparisons of the predictions with the measured wall strength (from Chapter 2) demonstrated that if we assume the fundamental models for horizontal and diagonal bending moment capacities to be accurate, then it is unlikely that diagonal and vertical cracks in the mechanism achieve their peak moments simultaneously as assumed by the current AS 3700 design approach. This conclusion was also supported by observations of crack patterns during the tests. It was also demonstrated that inclusion of some residual (post-cracking) moment capacity along horizontal crack lines in the mechanism reduced the overall scatter in the predictions. In its present form, the AS 3700 approach neglects any such moment capacities.

Since rigid plastic analysis (the VW method) is well known to be fundamentally flawed with regard to URM, in that it is extremely unlikely that all cracks within

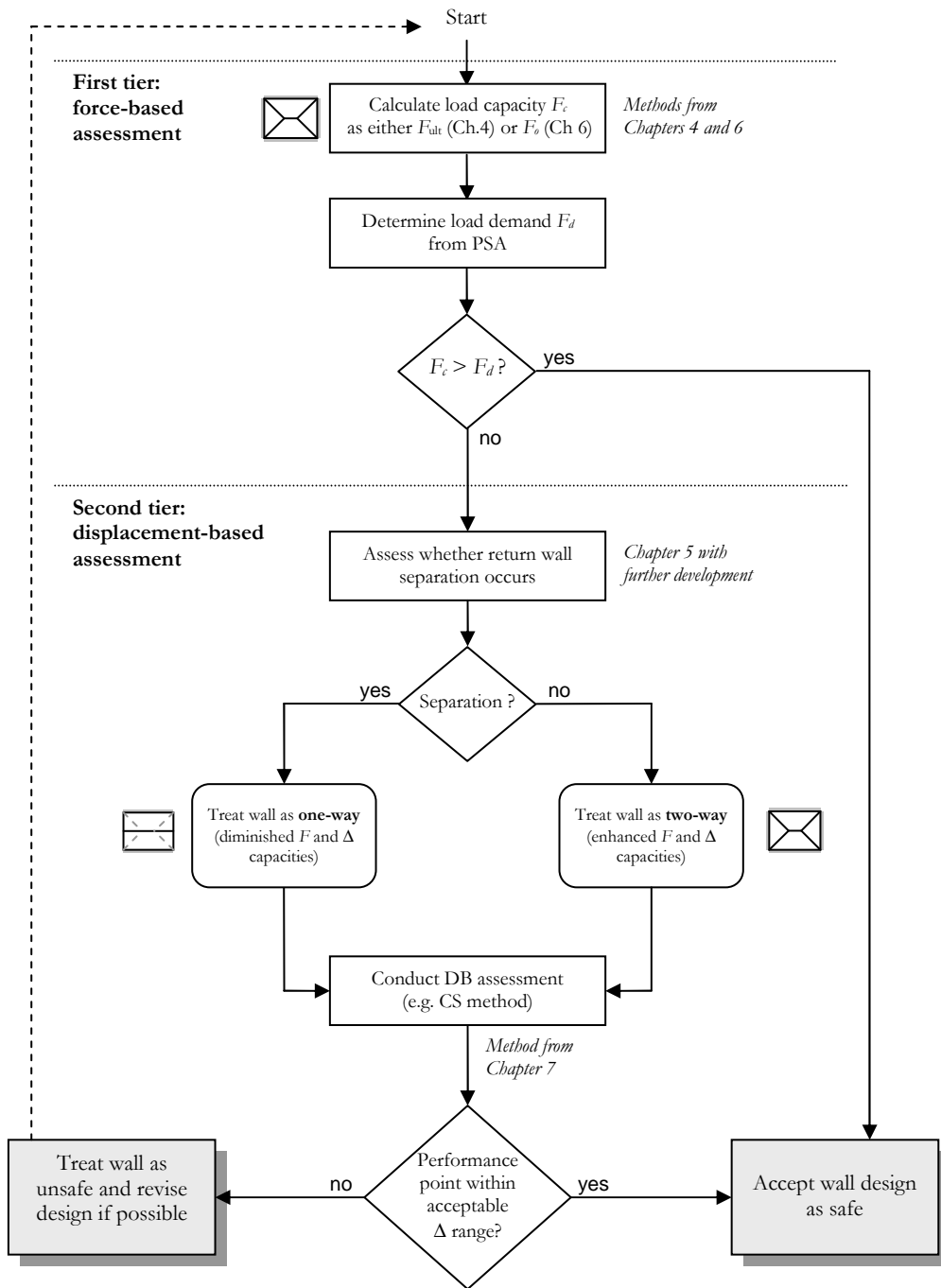


Figure 8.1: Multi-tier design flowchart.

the mechanism could achieve their moment capacities simultaneously, it would be reasonable to accept that a *rational* design approach requires some level of empiricism to account for the discrepancy between actual and idealised behaviour. This could be accomplished, for example, by implementation of internal work reduction factors to the respective crack lines, to address issues such as: (i) moments along different types of cracks not peaking simultaneously, and (ii) weak link effects due to variability in material properties.

In addition, there is still a significant scope for further development of the fundamental models for the different types of bending (vertical, horizontal and diagonal), including:

- The need for additional diagonal bending test data, as the present models by Willis [Griffith *et al.*, 2005] and the refined approach developed in this thesis have so far been calibrated using only a handful of tests;
- Calibration of an ultimate shear stress expression [see Eq. (4.24)] to different types of brick units (e.g. perforated, frogged or solid) through further bed joint torsion tests; and
- Further wallette testing and development of moment-rotation models for the different types of bending. It is believed that such models could be used to make the transition from one-way bending in wallettes to two-way bending in actual walls.

Prediction of Residual (Post-Cracking) Strength

An alternative, conservative approach to predicting a wall's load capacity is to assume that the masonry possesses zero tensile bond strength and that it derives its strength purely from gravity effects. Chapter 6 focused on the development of such methodology. The various refinements incorporated into the method were: (i) inclusion of rotational friction resistance along vertical cracks, (ii) characterisation of several additional collapse mechanisms, including hybrid mechanisms incorporating both out-of-plane and in-plane components, and (iii) development of a frictional shear model for the participating in-plane walls. A detailed account of various effects relating to overburden loads (OBLs) was also provided, including the possibility of the OBL being restrained or unrestrained, as well as eccentricity effects. The developed approach showed good correlation compared to experimentally tested dry-stack masonry (DSM) walls with regard to both their strength and the critical collapse mechanisms.

Whilst an analysis that ignores bond strength will generally result in lower (more conservative) calculations of strength compared to the ‘ultimate strength’ analysis, which includes the benefit of bond cohesion, its main advantage is that it bypasses the difficulty of having to determine the material tensile strength properties of the masonry. This makes it a particularly appealing tool for **FB** assessment of walls in existing **URM** buildings, where it is especially difficult to quantify these properties reliably. It is expected that this approach could be used as an alternative to the ultimate strength prediction method (from Chapter 4) within the overall design procedure, as shown in Figure 8.1.

8.2.2 Displacement-Based Methodology

As shown by Figure 8.1, it is believed that **DB** assessment can form a second tier of the multi-tiered design approach, that would only be called upon should the wall fail the first (**FB**) check.

Chapter 7 developed a load-displacement capacity model for representing the nonlinear inelastic behaviour of two-way walls. The basis of the model is similar to the strength prediction methodology in Chapter 6, in that it treats the wall as having zero tensile bond strength. The model assumes that the overall load resistance of the wall can be obtained by superimposing the load contributions of several independently acting sources, including: (i) a rocking component modelled by a bilinear elastic softening rule; and (ii) frictional components due to rotational and translational friction sources, both modelled using elastoplastic rules. Analytical expressions for calculating the load and displacement capacities were derived for the type K family of mechanisms. The various considerations relating to **OBLs**, as described previously, were also catered for in the derived relationships. Comparisons of the proposed model with measured experimental $F-\Delta$ response (using data from Chapters 2 and 3) were shown to be largely favourable, in that the model appears to provide a reasonable albeit conservative representation of the observed behaviour.

Implementation of the model into a **DB** seismic assessment based on the substitute structure method was also demonstrated (in Chapter 7). The parameters necessary to transform the wall from a multi- to single-degree-of-freedom system were derived for the type K mechanisms. By contrast, replacement of the nonlinear $F-\Delta$ behaviour with an equivalent linear elastic system was performed using standard procedures—namely the secant approach to estimating the effective stiffness, and the hysteretic area based approach to estimating the equivalent viscous damping. In its present form, this procedure is as yet unverified, in that its displacement demand predictions have not been validated with the demand

predictions of nonlinear time-history analyses. It is anticipated that such a verification process, conducted for a realistic range of input parameters, can be a focus for future research.

A necessary intermediate step before undertaking a displacement-based design check (Figure 8.1) is to establish whether return wall separation is likely to occur. As identified through testing, this is an important consideration as it determines whether the wall continues to respond in two-way bending at larger displacements, or if it reverts to vertical one-way bending due to loss of connection at the edges. At the present stage, the analytical tools to make such an assessment are not yet fully developed. It is believed however, that the stochastic methodology developed in Chapter 5, for estimating the expected likelihood of stepped versus line failure in horizontal bending, can provide the basis for development of such a method.

8.3 TOPICS FOR FUTURE RESEARCH

The following topics also require further research attention:

- Interaction between combined in-plane and out-of-plane wall response;
- Development of floor spectra accounting for filtration of the ground motion by the building itself, to serve as the input motion for out-of-plane walls at different levels in the building; This is especially important toward DB assessment;
- Influence of connecting in-plane walls and flexible floor/roof diaphragms, which may cause an out-of-plane wall to receive different input excitations at these boundaries; and
- Further wall testing with various realistic types of boundary conditions.

REFERENCES

- Abramowitz, M., and Stegun, I. A. (1964), *Handbook of mathematical functions with formulas, graphs, and mathematical tables*, Applied Mathematics Series 55, tenth printing, Dec 1972 ed., U.S. Govt. Print. Off, Washington. ⟨cited p. 554⟩
- Abrams, D. (1996), Effects of scale and loading rate with tests of concrete and masonry structures, *Earthq. Spectra*, 12(1), 13–28. ⟨cited p. 16⟩
- Abrams, D. P. (2001), Performance-based engineering concepts for unreinforced masonry building structures, *Prog. Struct. Engng. Mater.*, 3(1), 48–56. ⟨cited pp. 2, 6⟩
- Abrams, D. P., Angel, R., and Uzarski, J. (1996), Out-of-plane strength of unreinforced masonry infill panels, *Earthq. Spectra*, 12(4), 825–844. ⟨cited pp. 6, 18, 119, 199⟩
- Anderson, C. (1976), Lateral loading tests on concrete block walls, *Struct. Eng.*, 54(7), 239–246. ⟨cited p. 18⟩
- Anderson, C. (1985), Tests on walls subjected to uniform lateral loading and edge loading, in *Proc. 7th International Brick Masonry Conference*, Melbourne, Australia. ⟨cited p. 18⟩
- Anderson, C., and Bright, N. J. (1976), Behaviour of non-loadbearing block walls under windloading, *Concrete*, 10(9), 27–30. ⟨cited pp. 119, 199⟩
- Andreaus, U. (1996), Failure criteria for masonry panels under in-plane loading, *J. Struct. Eng.*, 122(1), 37–46. ⟨cited p. 1⟩
- Anthoine, A., Magonette, G., and Magenes, G. (1994), Shear-compression testing and analysis of brick masonry walls, in *Proc. 10th European Conference on Earthquake Engineering*, vol. 3, pp. 1657–1662, Vienna, Austria. ⟨cited p. 1⟩
- ATC (1996), Seismic Evaluation and Retrofit of Concrete Buildings, Volume 1, *Tech. Rep. ATC-40*, Applied Technology Council. ⟨cited p. 296⟩

- Bakeer, T. (2011), Theoretical verification of existing solutions on lateral loading of masonry infill walls, *Mauerwerk*, 15(1), 35–42. <cited p. 122>
- Baker, C., Chen, B., and Drysdale, R. (2005), Failure line method applied to walls with openings, in *Proc. 10th Canadian Masonry Symposium*, Banff, Alberta, Canada. <cited pp. 18, 118, 121, 123, 199>
- Baker, L. R. (1973), Structural action of brickwork panels subjected to wind loads, *J. Aust. Ceram. Soc.*, 9(1), 8–13. <cited pp. 118, 119, 199>
- Baker, L. R. (1979), A failure criterion for brickwork in bi-axial bending, in *Proc. 5th International Brick Masonry Conference*, pp. 71–78, Washington, U. S. <cited pp. 120, 135, 557, 558>
- Baker, L. R. (1984), Concrete masonry wall panels subjected to lateral loads, *Durac report MRC-11*, Deakin University. <cited p. 18>
- Baker, L. R., and Franken, G. L. (1976), Variability aspects of the flexural strength of brickwork, in *Proc. 4th International Brick Masonry Conference*, Brussels. <cited p. 162>
- Baker, L. R., Gairns, D. A., Lawrence, S. J., and Scrivener, J. C. (1985), Flexural behaviour of masonry panels—A state of the art, in *Proc. 7th International Brick Masonry Conference*, pp. 27–55, Melbourne, Australia. <cited pp. 118, 130>
- Base, G. D., and Baker, L. R. (1973), Fundamental properties of structural brickwork, *J. Aust. Ceram. Soc.*, 9(1), 1–6. <cited p. 130>
- Bazzurro, P., et al. (2009), Learning from earthquakes: The Mw 6.3 Abruzzo, Italy, earthquake of April 6, 2009, *EERI Special Earthquake Report*, Earthquake Engineering Research Institute. <cited p. 1>
- Benedetti, D., Carydis, P., and Pezzoli, P. (1998), Shaking table tests on 24 simple masonry buildings, *Earthq. Eng. Struct. Dyn.*, 27(1), 67–90. <cited p. 17>
- Bertero, R. D., and Bertero, V. V. (2002), Performance-based seismic engineering: The need for a reliable conceptual comprehensive approach, *Earthq. Eng. Struct. Dyn.*, 31(3), 627–652. <cited p. 6>
- British Standards Institution (2005), *Code of practice for use of masonry, Part 1: Structural use of unreinforced masonry (BS 5628-1:2005)*, BSI, London. <cited p. 119>
- Bruneau, M. (1994), State-of-the-art report on seismic performance of unreinforced masonry buildings, *J. Struct. Eng.*, 120(1), 230–251. <cited p. 2>

- Brunsdon, D. (1994), Study group on earthquake risk buildings 1993/94 report, in *Proc. Technical Conference of the New Zealand National Society for Earthquake Engineering*, pp. 1–6. [⟨cited p. 2⟩](#)
- Calvi, G. M. (1999), A displacement-based approach for vulnerability evaluation of classes of buildings, *J. Earthq. Eng.*, 3(3), 411–438. [⟨cited p. 2⟩](#)
- Calvi, G. M., Kingsley, G. R., and Magenes, G. (1996), Testing of masonry structures for seismic assessment, *Earthq. Spectra*, 12(1), 145–162. [⟨cited p. 16⟩](#)
- Canadian Standards Association (2004), *CSA Standard: Design of masonry structures (S304.1-04)*, CSA, Mississauga, Ontario. [⟨cited p. 121⟩](#)
- Candy, C. C. E., Carrick, J. W., and Shackel, B. (1989), An evaluation of the energy line method for predicting ultimate load capacity from tests of minimally supported wall panels subjected to lateral loading, *Tech. Rep. R3271*, The Concrete Masonry Association of Australia. [⟨cited p. 18⟩](#)
- Casapulla, C. (1999), Resistenze attrittive in una parete muraria soggetta ad azioni normali al suo piano medio, in *Proc. L'Ingegneria Sismica in Italia, Atti IX Convegno Nazionale ANIDIS*, Torino. [⟨cited p. 238⟩](#)
- Casapulla, C. (2008), Lower and upper bounds in closed form for out-of-plane strength of masonry structures with frictional resistances, in *Proc. 6th International Conference on Structural Analysis of Historical Constructions*, Bath, UK. [⟨cited pp. 195, 241, 270⟩](#)
- Casolo, S., and Milani, G. (2010), A simplified homogenization-discrete element model for the non-linear static analysis of masonry walls out-of-plane loaded, *Eng. Struct.*, 32(8), 2352–2366. [⟨cited p. 114⟩](#)
- Cecchi, A., and Milani, G. (2008), A kinematic FE limit analysis model for thick English bond masonry walls, *Int. J. Solids Struct.*, 45(5), 1302–1331. [⟨cited p. 194⟩](#)
- Cecchi, A., Milani, G., and Tralli, A. (2007), A Reissner-Mindlin limit analysis model for out-of-plane loaded running bond masonry walls, *Int. J. Solids Struct.*, 44(5), 1438–1460. [⟨cited pp. 114, 194⟩](#)
- Ceradini, V. (1992), Modellazione e sperimentazione per lo studio della struttura muraria storica, PhD thesis, Università degli Studi di Roma “La Sapienza”. [⟨cited p. 198⟩](#)
- Chen, B. (2002), Masonry walls with openings under out-of-plane loading, Masters thesis, McMaster University. [⟨cited p. 18⟩](#)

- Chong, V. L. (1993), The behaviour of laterally loaded masonry panels with openings, PhD thesis, University of Plymouth. <cited pp. 18, 119, 199>
- Chopra, A. K. (2000), *Dynamics of Structures: Theory and Applications to Earthquake Engineering*, second ed., Prentice-Hall, Upper Saddle River, New Jersey. <cited p. 290>
- Chopra, A. K., and Goel, R. K. (1999), Capacity-demand-diagram methods based on inelastic design spectrum, *Earthq. Spectra*, 15(4), 637–655. <cited p. 293>
- Chopra, A. K., and Goel, R. K. (2000), Evaluation of NSP to estimate seismic deformation: SDF systems, *J. Struct. Eng.*, 126(4), 482–490. <cited p. 296>
- Chopra, A. K., and Goel, R. K. (2001), Direct displacement-based design: Use of inelastic vs. elastic design spectra, *Earthq. Spectra*, 17(1), 47–64. <cited p. 296>
- Clough, R. W., and Penzien, J. (1993), *Dynamics of Structures*, second ed., McGraw-Hill, New York. <cited pp. 290, 295>
- Comité Européen de Normalisation (2004), *Eurocode 8, Design of Structures for Earthquake Resistance—Part 1: General rules, seismic actions and rules for buildings*, EN 1998-1:2004 (E) ed., CEN, Brussels, Belgium. <cited p. 297>
- Comité Européen de Normalisation (2005), *Eurocode 6, Design of Masonry Structures—Part 1-1: General rules for reinforced and unreinforced masonry structures*, EN 1996-1-1:2005 (E) ed., CEN, Brussels, Belgium. <cited p. 119>
- Dafnis, A., Kolsch, H., and Reimerdes, H.-G. (2002), Arching in masonry walls subjected to earthquake motions, *J. Struct. Eng.*, 128(2), 153–159. <cited p. 17>
- D’Ayala, D., and Speranza, E. (1999), Identificazione dei meccanismi di collasso per la stima della vulnerabilità sismica di edifici in centri storici, in *Proc. IX Convegno Nazionale L’Ingegneria Sismica in Italia*, Torino. <cited p. 194>
- D’Ayala, D., and Speranza, E. (2002), An integrated procedure for the assessment of seismic vulnerability of historic buildings, in *Proc. 12th European Conference on Earthquake Engineering*, London, UK. <cited p. 194>
- D’Ayala, D., and Speranza, E. (2003), Definition of collapse mechanisms and seismic vulnerability of historic masonry buildings, *Earthq. Spectra*, 19(3), 479–509. <cited pp. xiv, 194, 195, 198, 199, 241, 245, 255>
- de Felice, G. (1999), Le strutture murarie: dall’osservazione alla previsione del danno sismico, in *Codice di pratica per la sicurezza e la conservazione del centro storico di Palermo*, edited by A. Giuffrè and C. Carocci, first ed., p. 200, Laterza, Bari. <cited p. 238>

- de Felice, G., and Giannini, R. (2001), Out-of-plane seismic resistance of masonry walls, *J. Earthq. Eng.*, 5(2), 253–271. <cited p. 194>
- de Riggi, T. (1999), Il comportamento della parete muraria soggetta ad azioni perpendicolari al proprio piano: Il caso della frattura triangolare, in *Proc. L'Ingegneria Sismica in Italia, Atti IX Convegno Nazionale ANIDIS*, Torino. <cited p. 238>
- de Vekey, R. C., Bright, N. J., Luckin, K. R., and Arora, S. K. (1986), The resistance of masonry to lateral loading, Part 3: Research results on autoclaved aerated concrete blockwork, *Struct. Eng.*, 64A(11), 332–340. <cited p. 18>
- Derakhshan, H., Ingham, J. M., and Griffith, M. C. (2009), Tri-linear force-displacement models representative of out-of-plane unreinforced masonry wall behaviour, in *Proc. 11th Canadian Masonry Symposium*, Toronto, Ontario. <cited pp. 265, 266>
- Derakhshan, H., Griffith, M. C., and Ingham, J. M. (2011), Out-of-plane behavior of one-way spanning unreinforced masonry walls, *J. Eng. Mech.*, *in press*. <cited pp. 40, 260, 266>
- Doherty, K. (2000), An investigation of the weak links in the seismic load path of unreinforced masonry buildings, PhD thesis, University of Adelaide. <cited pp. xiv, 2, 72, 205, 332>
- Doherty, K., Griffith, M. C., Lam, N., and Wilson, J. (2002), Displacement-based seismic analysis for out-of-plane bending of unreinforced masonry walls, *Earthq. Eng. Struct. Dyn.*, 31(4), 833–850. <cited pp. 4, 6, 7, 40, 258, 260, 265, 266, 267, 285, 289, 291, 292, 298>
- Drysdale, R. G., and Baker, C. A. (2003), Failure line design of unreinforced masonry walls subject to out-of-plane loading, *Tech. rep.*, Centre for Effective Design of Structures, McMaster University. <cited pp. 118, 121>
- Drysdale, R. G., and Essawy, A. S. (1988), Out-of-plane bending of concrete block walls, *J. Struct. Eng.*, 114(1), 121–133. <cited pp. 18, 118, 119, 123, 199>
- Drysdale, R. G., Hamid, A. A., and Baker, L. R. (1994), *Masonry Structures: Behaviour and Design*, Prentice-Hall, Englewood Cliffs, New Jersey. <cited p. 4>
- Dwairi, H., and Kowalsky, M. (2004), Investigation of Jacobsen's equivalent viscous damping approach as applied to displacement-based seismic design, in *Proc. 13th World Conference on Earthquake Engineering*, Vancouver, B.C., Canada. <cited p. 296>

- Dwairi, H. M., Kowalsky, M. J., and Nau, J. M. (2007), Equivalent damping in support of direct displacement-based design, *J. Earthq. Eng.*, 11(4), 512–530. <cited p. 296>
- Edgell, G. J. (2005), Masonry, *Struct. Eng.*, 83(9), 27–31. <cited pp. 119, 199>
- Edgell, G. J., and Kjær, E. (2000), Lateral load behaviour of walls with openings, in *Proc. 12th International Brick and Block Masonry Conference*, vol. 1, pp. 537–544, Madrid, Spain. <cited pp. 18, 119, 199>
- Ehsani, M. R., Saadatmanesh, H., and Velazquez-Dimas, J. I. (1999), Behavior of retrofitted URM walls under simulated earthquake loading, *J. Compos. Constr.*, 3(3), 134–142. <cited p. 17>
- Ewing, R. D., and Kariotis, J. C. (1981), Methodology for mitigation of seismic hazards in existing unreinforced masonry buildings: Wall testing, out-of-plane, *Tech. Rep. ABK-TR-04*, ABK, A Joint Venture, El Segundo, California. <cited pp. 4, 17, 40, 260>
- Fajfar, P. (2000), Nonlinear analysis method for performance-based seismic design, *Earthq. Spectra*, 16(3), 573–592. <cited p. 6>
- Freeman, S. A. (2004), Review of the development of the capacity spectrum method, *ISET J. Earthq. Tech.*, 41(1), 1–13. <cited pp. 8, 297>
- Freeman, S. A., Nicoletti, J. P., and Tyrell, J. V. (1975), Evaluations of existing buildings for seismic risk—A case study of Puget Sound Naval Shipyard, Bremerton, Washington, in *Proc. 1st U.S. National Conference on Earthquake Engineering*, pp. 113–122, Berkeley, California. <cited p. 297>
- Gairns, D. A. (1983), Flexural behaviour of concrete blockwork panels, Masters thesis, University of Melbourne. <cited pp. 18, 130>
- Gairns, D. A., and Scrivener, J. C. (1987), The flexural strength of concrete block and clay brick masonry panels, in *Proc. First National Structural Engineering Conference*, Melbourne, Australia. <cited p. 18>
- Gazzola, E. A., Drysdale, R. G., and Essawy, A. S. (1985), Bending of concrete masonry walls at different angles to the bed joints, in *Proc. 3rd North American Masonry Conference*, Arlington, Texas, USA. <cited p. 123>
- Ghobarah, A., and El Mandooh Galal, K. (2004), Out-of-plane strengthening of unreinforced masonry walls with openings, *J. Compos. Constr.*, 8(4), 298–305. <cited pp. 18, 19>

- Giuffrè, A. (1990), *Lecture sulla meccanica delle murature storiche*, Roma. <cited p. 194>
- Giuffrè, A. (Ed.) (1993), *Sicurezza e conservazione dei centri storici. Il caso Ortigia*, Laterza, Bari. <cited pp. 194, 198>
- Gülkan, P., and Sozen, M. A. (1974), Inelastic responses of reinforced concrete structures to earthquake motions, *ACI Struct. J.*, 71(12), 604–610. <cited p. 289>
- Golding, J. M. (1991), Practical design of laterally loaded masonry panels, *Struct. Eng.*, 59(4), 55–66. <cited p. 120>
- Grant, D. N., Blandon, C. A., and Priestley, M. J. N. (2005), Modelling inelastic response in direct displacement-based design, *Tech. Rep. ROSE 2005/03*, IUSS Press, Pavia. <cited p. 296>
- Griffith, M. C. (2000), Experimental study of the flexural strength of URM (brick) walls, *Tech. Rep. R 169*, Department of Civil and Environmental Engineering, University of Adelaide. <cited pp. 18, 27, 119, 123, 199>
- Griffith, M. C., Magenes, G., Melis, G., and Picchi, L. (2003), Evaluation of out-of-plane stability of unreinforced masonry walls subjected to seismic excitation, *J. Earthq. Eng.*, 7(S1), 141–169. <cited p. 289>
- Griffith, M. C., Lam, N. T. K., Wilson, J. L., and Doherty, K. (2004), Experimental investigation of unreinforced brick masonry walls in flexure, *J. Struct. Eng.*, 130(3), 423–432. <cited pp. 4, 17, 46, 265>
- Griffith, M. C., Lawrence, S. J., and Willis, C. R. (2005), Diagonal bending of unreinforced clay brick masonry, *Mas. Intl.*, 18(3), 125–138. <cited pp. 114, 120, 124, 134, 135, 137, 310>
- Hagsten, L. G., and Nielsen, M. P. (2000), Laterally loaded masonry, in *Proc. 12th International Brick and Block Masonry Conference*, vol. 2, pp. 841–858, Madrid, Spain. <cited p. 135>
- Haseltine, B. A., and Tutt, J. N. (1986), The resistance of masonry to lateral loading, Part 4: Implications of research on design recommendations, *Struct. Eng.*, 64A(11), 341–350. <cited pp. 18, 118>
- Haseltine, B. A., West, H. W. H., and Tutt, J. N. (1977), The resistance of brickwork to lateral loading, Part 2: Design of walls to resist lateral loads, *Struct. Eng.*, 55(10), 422–430. <cited p. 118>
- Haseltine, B. A., West, H. W. H., Hodgkinson, H. R., and Tutt, J. N. (1978), The resistance of brickwork to lateral loading—Discussion, *Struct. Eng.*, 56A(12), 363–374. <cited p. 18>

- Heffler, L. M., Stewart, M. G., Masia, M. J., and Correa, M. R. S. (2008), Statistical analysis and spatial correlation of flexural bond strength for masonry walls, *Mas. Intl.*, 21(2), 59–70. <cited p. 161>
- Hendry, A. W. (1973), The lateral strength of unreinforced brickwork, *Struct. Eng.*, 51(2), 43–50. <cited p. 18>
- Hendry, A. W., Sinha, B. P., and Davies, S. R. (1997), *Design of Masonry Structures*, third ed., E & FN Spon, London. <cited p. 121>
- Hodgkinson, H. R., Haseltine, B. A., and West, H. W. H. (1982a), In-situ lateral loading tests on a 10-year-old brickwork building, *Br. Ceram. Proc.*, 30. <cited pp. 119, 199>
- Hodgkinson, H. R., Haseltine, B. A., and West, H. W. H. (1982b), Structural tests on single-leaf two-storey brick masonry structures, *Br. Ceram. Proc.*, 30. <cited pp. 18, 119, 199>
- Hogan, S. J. (1989), On the dynamics of rigid-block motion under harmonic forcing, *Proc. R. Soc. Lond. A*, 425(1869), 441–476. <cited p. 262>
- Housner, G. W. (1963), The behaviour of inverted pendulum structures during earthquakes, *Bull. Seismol. Soc. Am.*, 53(2), 403–417. <cited p. 262>
- Ingham, J. M., and Griffith, M. C. (2011a), Performance of unreinforced masonry buildings during the 2010 Darfield (Christchurch, NZ) earthquake, *Aust. J. Struct. Eng.*, 11(3), 207–224. <cited p. 1>
- Ingham, J. M., and Griffith, M. C. (2011b), The performance of unreinforced masonry buildings in the 2010/2011 Canterbury earthquake swarm, *Tech. rep.*, Canterbury Earthquakes Royal Commission of Inquiry. <cited p. 1>
- Jacobsen, L. S. (1930), Steady forced vibrations as influenced by damping, *Trans. ASME*, 52, 169–181. <cited pp. 294, 296>
- Jacobsen, L. S. (1960), Damping in composite structures, in *Proc. 2nd World Conference on Earthquake Engineering*, vol. 2, Tokyo and Kyoto, Japan. <cited p. 294>
- Jaramillo, J. D. (2002), Mecanismo de transmision de cargas perpendiculares al plano del muro en muros de mamposteria no reforzada, *Revista de Ingeniería Sísmica*, 67, 53–78. <cited pp. 4, 19, 119, 199>
- Johansen, K. W. (1962), *Yield-Line Theory*, first ed., Cement and Concrete Association, London. <cited pp. 118, 119, 199>

- Kappos, A. J., Penelis, G. G., and Drakopoulos, C. G. (2002), Evaluation of simplified models for lateral load analysis of unreinforced masonry buildings, *J. Struct. Eng.*, 128(7), 890–897. ⟨cited p. 114⟩
- König, G., Mann, W., and Ötes, A. (1988), Experimental investigations on the behaviour of unreinforced masonry walls under seismically induced loads and lessons derived, in *Proc. 9th World Conference on Earthquake Engineering*, vol. 8, pp. 1117–1122, Tokyo-Kyoto, Japan. ⟨cited p. 1⟩
- Korany, Y. (2004), Rehabilitation of masonry walls using unobtrusive FRP techniques for enhanced out-of-plane seismic resistance, PhD thesis, McMaster University. ⟨cited pp. 18, 119, 199⟩
- Kowalsky, M. J. (2002), A displacement-based approach for the seismic design of continuous concrete bridges, *Earthq. Eng. Struct. Dyn.*, 31(3), 719–747. ⟨cited pp. 6, 289⟩
- Lawrence, S. (1991), Stochastic analysis of masonry structures, in *Proc. International Symposium on Computer Methods in Structural Masonry*, pp. 104–113, Swansea, United Kingdom. ⟨cited p. 157⟩
- Lawrence, S., and Marshall, R. (2000), Virtual work design method for masonry panels under lateral load, in *Proc. 12th International Brick and Block Masonry Conference*, vol. 2, pp. 1063–1072, Madrid, Spain. ⟨cited pp. 17, 25, 114, 118, 122⟩
- Lawrence, S. J. (1975), Flexural strength of brickwork normal to and parallel to the bed joints, *J. Aust. Ceram. Soc.*, 11(1), 5–6. ⟨cited pp. 128, 546⟩
- Lawrence, S. J. (1983), Behaviour of brick masonry walls under lateral loading, PhD thesis, The University of New South Wales. ⟨cited pp. 18, 36, 39, 118, 119, 123, 130, 161, 163, 199⟩
- Lawrence, S. J. (1995), The behaviour of masonry in horizontal flexure, in *Proc. 7th Canadian Masonry Symposium*, pp. 525–536, Hamilton, Ontario. ⟨cited p. 130⟩
- Lawrence, S. J., and Cao, H. T. (1988), Cracking of non-loadbearing masonry walls under lateral forces, in *Proc. 8th International Brick and Block Masonry Conference*, pp. 1184–94, Dublin. ⟨cited p. 157⟩
- Lawrence, S. J., and Lu, J. P. (1991), An elastic analysis of laterally loaded masonry walls with openings, in *Proc. International Symposium on Computer Methods in Structural Masonry*, pp. 39–48, Swansea, United Kingdom. ⟨cited p. 154⟩

- Lawrence, S. J., and Marshall, R. (1998), The new AS 3700 approach to lateral load design, in *Proc. 5th Australasian Masonry Conference*, Gladstone, Queensland, Australia. <cited pp. 114, 118, 122>
- Lawrence, S. J., and Marshall, R. J. (1996), Virtual work approach to design of masonry walls under lateral loading, *Tech. Rep. DRM429*, CSIRO Division of Building, Construction and Engineering. <cited pp. xiv, 18, 114, 116, 118, 122, 134, 199, 207, 547, 548>
- Lawrence, S. J., and Page, A. W. (1999), *Manual 4: Design of Clay Masonry for Wind and Earthquake*, CBPI Technical Manuals, Clay Brick and Paver Institute (CBPI). <cited p. 116>
- Lee, J. S., Pande, G. N., Middleton, J., and Kralj, B. (1996), Numerical modelling of brick masonry panels subject to lateral loadings, *Comput. Struct.*, 61(4), 735–745. <cited p. 114>
- Lourenço, P. B. (2000), Anisotropic softening model for masonry plates and shells, *J. Struct. Eng.*, 126(9), 1008–1016. <cited p. 114>
- Lourenço, P. B. (2002), Computations on historic masonry structures, *Prog. Struct. Engng. Mater.*, 4(3), 301–319. <cited pp. 114, 194>
- Lovegrove, R. (1988), A discussion of ‘yieldlines’ in unreinforced masonry, *Struct. Eng.*, 66(22), 371–375. <cited pp. 118, 322>
- Lovegrove, R., Beal, A. N., and Lawrence, S. J. (1989), Correspondence regarding the paper “A discussion of ‘yieldlines’ in unreinforced masonry” by *Lovegrove [1988]*, *Struct. Eng.*, 67(8), 143–144. <cited p. 118>
- Lu, J. P., and Lawrence, S. J. (1991), Cracking of laterally loaded masonry walls with openings, in *Proc. 9th International Brick and Block Masonry Conference*, pp. 1087–94, Berlin, Germany. <cited p. 157>
- Maffei, J., Comartin, C. D., Kehoe, B., Kingsley, G. R., and Lizundia, B. (2000), Evaluation of earthquake damaged concrete and masonry wall buildings, *Earthq. Spectra*, 16(1), 263–283. <cited p. 2>
- Magenes, G., and Calvi, G. M. (1997), In-plane seismic response of brick masonry walls, *Earthq. Eng. Struct. Dyn.*, 26(11), 1091–1112. <cited pp. 1, 6, 289>
- Maluf, D. R., Parsekian, G. A., and Shrive, N. G. (2008), An investigation of out-of-plane loaded unreinforced masonry walls design criteria, in *Proc. 14th International Brick and Block Masonry Conference*, Sydney, Australia. <cited p. 118>

- Martini, K. (1998), Finite element studies in the two-way out-of-plane failure of unreinforced masonry, in *Proc. 6th U.S. National Conference on Earthquake Engineering*, Seattle, Washington, U.S. ⟨cited p. 114⟩
- Mathew, A., Kumar, B., Sinha, B. P., and Pedreschi, R. F. (1999), Analysis of masonry panel under biaxial bending using ANNs and CBR, *J. Comput. Civ. Eng.*, 13(3), 170–177. ⟨cited p. 114⟩
- McNeilly, T., Scrivener, J., Lawrence, S., and Zsembery, S. (1996), A site survey of masonry bond strength, *Australian Civ./Struct. Engrg. Trans.*, CE38(2, 3 & 4), 103–109. ⟨cited pp. 162, 176⟩
- Medhekar, M. S., and Kennedy, D. J. L. (2000), Displacement-based seismic design of buildings—Application, *Eng. Struct.*, 22(3), 210–221. ⟨cited pp. 6, 289⟩
- Milani, G. (2008), 3D upper bound limit analysis of multi-leaf masonry walls, *Int. J. Mech. Sci.*, 50(4), 817–836. ⟨cited p. 194⟩
- Milani, G., Lourenço, P., and Tralli, A. (2006), Homogenization approach for the limit analysis of out-of-plane loaded masonry walls, *J. Struct. Eng.*, 132(10), 1650–1663. ⟨cited p. 114⟩
- Milani, G., Lourenço, P., and Tralli, A. (2007), 3D homogenized limit analysis of masonry buildings under horizontal loads, *Eng. Struct.*, 29(11), 3134–3148. ⟨cited p. 194⟩
- Moehle, J. P. (1992), Displacement-based design of RC structures subjected to earthquakes, *Earthq. Spectra*, 8(3), 403–427. ⟨cited p. 289⟩
- Ng, C. L. (1996), Experimental and theoretical investigation of the behaviour of brickwork cladding panel subjected to lateral loading, PhD thesis, University of Edinburgh. ⟨cited pp. 114, 119, 199⟩
- Orduña, A., and Lourenço, P. B. (2005a), Three-dimensional limit analysis of rigid blocks assemblages. Part I: Torsion failure on frictional interfaces and limit analysis formulation, *Int. J. Solids Struct.*, 42(18-19), 5140–5160. ⟨cited pp. 134, 194, 552⟩
- Orduña, A., and Lourenço, P. B. (2005b), Three-dimensional limit analysis of rigid blocks assemblages. Part II: Load-path following solution procedure and validation, *Int. J. Solids Struct.*, 42(18-19), 5161–5180. ⟨cited p. 194⟩
- Oyarzo-Vera, C., and Griffith, M. C. (2009), The Mw 6.3 Abruzzo (Italy) earthquake of April 6th, 2009: On site observations, *Bull. New. Zeal. Soc. Earthquake Eng.*, 42(4), 302–307. ⟨cited p. 1⟩

- Page, A. W. (1992), The design, detailing and construction of masonry—The lessons from the Newcastle earthquake, *Civil Engrg. Trans., I.E. Aust., CE34(4)*, 343–353. [⟨cited p. 1⟩](#)
- Page, A. W. (1995), Unreinforced masonry structures—An Australian overview (Keynote address), in *Proc. Pacific Conference on Earthquake Engineering*, vol. 3, pp. 1–16, Parkville, Victoria, Australia. [⟨cited p. 1⟩](#)
- Paquette, J., and Bruneau, M. (2003), Pseudo-dynamic testing of unreinforced masonry building with flexible diaphragm, *J. Struct. Eng.*, 129(6), 708–716. [⟨cited p. 1⟩](#)
- Paquette, J., Bruneau, M., and Filiatrault, A. (2001), Out-of-plane seismic evaluation and retrofit of turn-of-the-century North American masonry walls, *J. Struct. Eng.*, 127(5), 561–569. [⟨cited p. 17⟩](#)
- Paulay, T., and Priestley, M. J. N. (1992), *Seismic Design of Reinforced Concrete and Masonry Buildings*, John Wiley and Sons, New York. [⟨cited p. 2⟩](#)
- Picchi, L. (2002), Risposta sismica per azioni fuori dal piano di parete murarie, Thesis for Laurea degree in Civil Engineering, Università degli Studi di Pavia. [⟨cited p. 238⟩](#)
- Priestley, M. J. N. (1985), Seismic behaviour of unreinforced masonry walls, *Bull. New. Zeal. Natl. Soc. Earthquake Eng.*, 18(2), 191–205. [⟨cited p. 6⟩](#)
- Priestley, M. J. N. (1997), Displacement-based seismic assessment of reinforced concrete buildings, *J. Earthq. Eng.*, 1(1), 157–192. [⟨cited pp. 6, 289⟩](#)
- Priestley, M. J. N. (2000), Performance based seismic design, in *Proc. 12th World Conference on Earthquake Engineering*, pp. 325–346, Auckland, New Zealand. [⟨cited p. 6⟩](#)
- Priestley, M. J. N., Calvi, G. M., and Kowalsky, M. J. (2007), *Displacement-Based Seismic Design of Structures*, IUSS Press, Pavia, Italy. [⟨cited pp. 296, 297⟩](#)
- Rneckis, D., LaFave, J. M., and Clarke, W. M. (2004), Out-of-plane performance of brick veneer walls on wood frame construction, *Eng. Struct.*, 26(8), 1027–1042. [⟨cited p. 17⟩](#)
- Restrepo Vélez, L. F. (2004), Seismic risk of unreinforced masonry buildings, PhD thesis, ROSE School, Università degli Studi di Pavia. [⟨cited pp. 195, 198, 234, 235, 244, 245, 247, 255⟩](#)

- Restrepo Vélez, L. F., and Magenes, G. (2009), Static tests on dry stone masonry and evaluation of static collapse multipliers, *Tech. Rep. ROSE 2009/02*, IUSS Press, Pavia. ⟨cited pp. [xiv](#), [195](#), [234](#), [239](#), [241](#), [243](#), [634](#), [638](#)⟩
- Rondelet, J. B. (1802), *Traité théorique et pratique de l'art de bâtir*, Chez l'auteur, Paris. ⟨cited p. [194](#)⟩
- Satti, K. M. H. (1972), Model brickwork wall panels under lateral loading, PhD thesis, The University of Edinburgh. ⟨cited p. [18](#)⟩
- Schueremans, L., and Gemert, D. V. (2006), Probability density functions for masonry material parameters—A way to go?, in *Proc. 5th International Conference on Structural Analysis of Historical Constructions*, New Delhi, India. ⟨cited pp. [154](#), [156](#)⟩
- Scrivener, J. C. (1993), Masonry structures—Earthquake resistant design and construction, in *Proc. Earthquake Engineering and Disaster Reduction Seminar*, pp. 39–44, Melbourne, Australia. ⟨cited p. [1](#)⟩
- Shi, Y., D'Ayala, D., and Jain, P. (2008), Analysis of out-of-plane damage behaviour of unreinforced masonry walls, in *Proc. 14th International Brick and Block Masonry Conference*, Sydney, Australia. ⟨cited p. [198](#)⟩
- Shibata, A., and Sozen, M. A. (1976), Substitute-structure method for seismic design in R/C, *J. Struct. Div.*, *102*(1), 1–18. ⟨cited p. [289](#)⟩
- Simon, M. K. (2002), *Probability Distributions Involving Gaussian Random Variables: A Handbook for Engineers and Scientists*, Springer, New York. ⟨cited p. [169](#)⟩
- Sinha, B. P. (1978), A simplified ultimate load analysis of laterally loaded model orthotropic brickwork panels of low tensile strength, *Struct. Eng.*, *56B*(4), 81–84. ⟨cited pp. [118](#), [121](#), [199](#)⟩
- Sinha, B. P. (1980), An ultimate load analysis of laterally loaded brickwork panels, *Int. J. Masonry Constr.*, *1*(2), 57–61. ⟨cited pp. [118](#), [121](#)⟩
- Sinha, B. P., Ng, C. L., and Pedreschi, R. F. (1997), Failure criterion and behavior of brickwork in biaxial bending, *J. Mater. Civ. Eng.*, *9*(2), 70–75. ⟨cited pp. [120](#), [135](#), [558](#)⟩
- Southcombe, C., and Tapp, A. (1988), An investigation of laterally loaded brickwork panels with openings, *Mas. Int.*, *2*, 112–114. ⟨cited p. [18](#)⟩
- Southcombe, C., May, I. M., and Chong, V. L. (1995), The behaviour of brickwork panels with openings under lateral load, *Proc. Brit. Mas. Soc.*, *7*, 105–110. ⟨cited pp. [114](#), [118](#)⟩

- Standards Australia (2001), *Masonry Structures (AS 3700—2001)*, SA, Homebush, NSW. ⟨cited pp. 6, 20, 27, 68, 114, 122, 155, 199, 258, 545⟩
- Standards Australia (2007), *Structural design actions, Part 4: Earthquake actions in Australia (AS 1170.4—2007)*, SA, Sydney, NSW. ⟨cited pp. 5, 299⟩
- Stewart, M. G., and Lawrence, S. J. (2002), Structural reliability of masonry walls in flexure, *Mas. Intl.*, 15(2), 48–52. ⟨cited pp. 154, 156⟩
- Tapp, A. (1985), An investigate of laterally loaded fenestrated masonry panels, Masters of Philosophy Transfer Report, Polytechnic South West. ⟨cited pp. 18, 119, 199⟩
- Timoshenko, S. P., and Goodier, J. N. (1934), *Theory of Elasticity*, third (1970) ed., McGraw-Hill Book Company, New York. ⟨cited pp. 131, 547, 549⟩
- Tomažević, M., and Klemenc, I. (1997), Seismic behaviour of confined masonry walls, *Earthq. Eng. Struct. Dyn.*, 26(10), 1059–1071. ⟨cited p. 1⟩
- Vaculik, J., and Griffith, M. C. (2008), Time-history analysis for unreinforced masonry walls in two-way bending, in *Proc. 14th World Conference on Earthquake Engineering*, Beijing, China. ⟨cited p. 66⟩
- Vaculik, J., Hogarth, B., and Todd, J. (2003), Experimental and analytical investigation of the flexural response of brick masonry, Honours degree thesis, School of Civil and Environmental Engineering, The University of Adelaide. ⟨cited pp. 19, 25, 275, 281, 286, 287, 288, 551⟩
- Vaculik, J., Griffith, M. C., Hogarth, B., and Todd, J. (2004), Out-of-plane flexural response tests using dry-stack masonry, in *Proc. Australian Earthquake Engineering Society Conference*, Mt Gambier, South Australia. ⟨cited pp. 5, 19, 198, 281⟩
- Vasconcelos, G., and Lourenço, P. B. (2009), In-plane experimental behavior of stone masonry walls under cyclic loading, *J. Struct. Eng.*, 135(10), 1269–1277. ⟨cited p. 1⟩
- West, H. W. H., Hodgkinson, H. R., and Haseltine, B. A. (1977), The resistance of brickwork to lateral loading, Part 1: Experimental methods and results of tests on small specimens and full sized walls, *Struct. Eng.*, 55(10), 411–421. ⟨cited pp. 18, 119, 199⟩
- West, H. W. H., Hodgkinson, H. R., and de Vekey, R. C. (1979a), The lateral resistance of cavity walls with different types of wall ties, in *Proc. 5th International Brick Masonry Conference*, pp. 387–390, Washington, United States. ⟨cited pp. 18, 119, 199⟩

- West, H. W. H., Hodgkinson, H. R., and Haseltine, B. A. (1979b), The lateral resistance of walls with one free vertical edge, in *Proc. 5th International Brick Masonry Conference*, pp. 382–386, Washington, United States. ⟨cited pp. 18, 119, 199⟩
- West, H. W. H., Hodgkinson, H. R., Haseltine, B. A., and de Vekey, R. C. (1986), The resistance of masonry to lateral loading, Part 2: Research results on brickwork and aggregate blockwork since 1977, *Struct. Eng.*, 64A(11), 320–331. ⟨cited p. 18⟩
- Willis, C. R. (2004), Design of unreinforced masonry walls for out-of-plane loading, PhD thesis, University of Adelaide. ⟨cited pp. xiv, 114, 122, 124, 129, 131, 134, 135, 136, 180, 181, 182, 184, 192, 310, 332, 548, 550, 558, 560, 563, 567⟩
- Willis, C. R., Griffith, M. C., and Lawrence, S. J. (2004), Horizontal bending of unreinforced clay brick masonry, *Mas. Intl.*, 17(3), 109–121. ⟨cited pp. 114, 129, 155, 165, 166, 180, 181, 548, 550⟩
- Xue, Q., and Chen, C.-C. (2003), Performance-based seismic design of structures: A direct displacement-based approach, *Eng. Struct.*, 25(14), 1803–1813. ⟨cited p. 6⟩
- Zeiny, A. (2003), Evaluation of the seismic performance of brick walls retrofitted and repaired by expansive epoxy, *TMS J.*, 21(1), 55–68. ⟨cited p. 17⟩

